A strain gradient approach to the mechanics of micro and nanocrystals

Nicolas Cordero

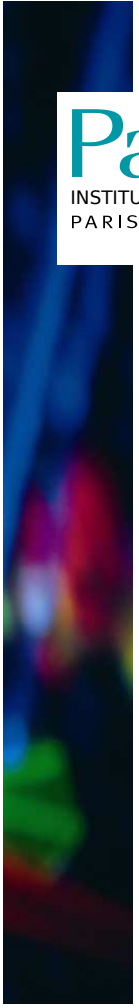

ParisTech
INSTITUT DES SCIENCES ET TECHNOLOGIES
PARIS INSTITUTE OF TECHNOLOGY

MINES ParisTech

École doctorale n°432 :
Science des Métiers de l'Ingénieur

Doctorat ParisTech

T H È S E

pour obtenir le grade de docteur délivré par

l'École nationale supérieure des mines de Paris

Spécialité « Sciences et Génie des Matériaux »

présentée et soutenue publiquement par

Nicolas CORDERO

le 30 septembre 2011

Gradients de Déformation en Mécanique des Micro et Nanocristaux

~ ~ ~

A Strain Gradient Approach to the Mechanics of Micro and Nanocrystals

Directeurs de thèse : **Esteban P. BUSSO**
Samuel FOREST

Jury

Marc G.D. GEERS, Professeur, Eindhoven University of Technology	Rapporteur
David L. MCDOWELL, Professeur, Georgia Institute of Technology	Rapporteur
Stéphane BERBENNI, Chargé de recherche, CNRS / Arts et Métiers ParisTech	Examinateur
Mohammed CHERKAOUI, Professeur, Georgia Institute of Technology	Examinateur
Bob SVENDSEN, Professeur, RWTH Aachen University	Président & Examinateur
Esteban P. BUSSO, Professeur, Centre des Matériaux, Mines ParisTech	Directeur de thèse
Samuel FOREST, Professeur, Centre des Matériaux, Mines ParisTech	Directeur de thèse

T H È S E

MINES ParisTech
Centre des Matériaux
CNRS UMR 7633, BP 87, 91003 Evry cedex, France

Résumé

Le comportement des matériaux dont la microstructure est ultra–fine ou nanométrique est un sujet de recherche qui passionne une partie de la communauté scientifique. Cependant, malgré les progrès réalisés dans ce domaine, il n'est toujours pas possible de prévoir et de décrire de manière précise le comportement en déformation de ce type de matériau. A cause de la complexité des approches expérimentales nécessaires et des défauts souvent constatés dans ces matériaux, peu de données fiables sont disponibles dans la littérature. Ajouté à cela, les techniques de modélisation discrètes telles que les approches atomistiques ont une utilité limitée en raison des échelles spatiale et temporelle accessibles qui sont souvent inadaptées pour représenter les phénomènes physiques sur lesquels cette étude se concentre.

Dans cette thèse de doctorat, un cadre théorique est proposé pour étudier le comportement en déformation de matériaux polycristallins ayant des grains ultra–fins ou nanométriques. Pour cela, des modèles continus capables de reproduire les effets de taille de microstructure provenant de mécanismes intervenant aux interfaces (par exemple, aux joints de grains) ou aux surfaces sont proposés. Ces modèles continus permettent de traiter des éléments de volume suffisamment grands pour être représentatifs. Il sont formulés de manière à être calibrés à partir de résultats obtenus par des simulations atomistiques ou de dynamique des dislocations discrètes et par des résultats expérimentaux.

Dans un premier temps, un modèle micromorphe de plasticité cristalline, le modèle "*microcurl*", basé sur le tenseur de densité de dislocations est proposé. Il régularise la réponse de modèles de plasticité de type Gurtin en présence d'interfaces. Les effets de taille générés sont caractérisés par la valeur globale de la contrainte interne provenant des contraintes d'ordre supérieur. Le modèle *microcurl* est particulièrement bien adapté pour simuler le comportement de polycristaux dont les tailles de grain varient entre quelques centaines de microns et quelques dizaines de nanomètres et il est capable de reproduire une large gamme de lois d'échelle dont l'effet Hall–Petch. Il peut aussi simuler l'influence de la taille de la microstructure sur les champs de déformation. L'évolution de la distribution des dislocations géométriquement nécessaires (GNDs) et des épaisseurs de leurs empilements aux joints de grains sont aussi étudiées.

La seconde partie de cette thèse se concentre sur des échelles plus petites et plus particulièrement sur des phénomènes liés aux surfaces et interfaces apparaissant à une échelle nanométrique : l'énergie de surface et la contrainte de surface. Un approche continue faisant intervenir le second gradient de la déformation (ou de manière équivalente, le troisième gradient du champ de déplacement) est proposée pour introduire ces effets de surface sans différencier les propriétés de la surface de celles du matériau. Après avoir démontré qu'une théorie d'un tel ordre est nécessaire, des cas simples pour lesquels le déplacement des atomes peut être résolu analytiquement sont considérés pour valider cette théorie et en décrire les principales caractéristiques. Le modèle proposé s'appuie sur une approche micromorphe. Il est d'abord formulé et décrit en détail puis implémenté numériquement dans un code éléments finis. Différents cas sont alors considérés dont le comportement mécanique apparent de nanofils.

Mots clés: Gradients de déformation, Modèle micromorphe, Milieux continus d'ordre supérieur, Effets d'échelle, Effets de surface, Plasticité cristalline, Grains ultra–fins, Matériaux nanocristallins

Abstract

The influence of grain size on the strength of ultra–fine grained and nanocrystalline materials is the subject of an increasing number of scientific studies. However, despite the progress made in this field, it is not yet possible to predict accurately and model the deformation behaviour of this type of materials. Few reliable data are available in the literature due to the complexity of the required experiments and to the high defect densities that some of these materials are known to contain. Moreover, the use of discrete modelling techniques such as atomistic approaches has a limited utility as the temporal and spatial scales are often unsuitable to address the real physical phenomena of interest in this work.

In this doctoral thesis, a theoretical framework is proposed to study the deformation behaviour of polycrystalline materials with ultra–fine or nano–sized microstructures. To that purpose, continuum models able to produce size effects arising from mechanisms that are predominant at interfaces (i.e., grain boundaries) or surfaces are proposed. These models, which enable the study of large representative volume elements, have been formulated so as to be calibrated using results from atomistic and discrete dislocation dynamics simulations and experimental work.

A micromorphic crystal plasticity model based on the dislocation density tensor, referred to as "*microcurl*", is first proposed. It regularises the response of Gurtin–type strain gradient plasticity models in the presence of material interfaces. The resulting size effects are characterised by the overall additional back–stress component resulting from the action of higher order stresses. This model is well adapted to simulate the deformation behaviour of polycrystals with grain sizes ranging from hundreds of microns to tens of nanometers, and it is shown to be capable of modelling a range of scaling laws, such as the Hall–Petch effect. It can also simulate the effect of the microstructure's dominant length scales on the strain fields. The evolution of the distribution of the geometrically necessary dislocations (GNDs) and of the thickness of the GND pileups at grain boundaries are also studied.

In order to address the size effects at the nanoscale arising from surface/interface phenomena, the second part of this thesis focuses on the role of surface energy and surface stress. A continuous method involving the third gradient of displacement is proposed to introduce surface effects without distinguishing between the properties of the surface/interface from those of the bulk. After discussing the need of such a higher order theory, simple cases for which an analytical solution for the displacement of atoms is known are considered to validate it and to describe its main features. The proposed model, based on a micromorphic approach, is formulated and numerically implemented using the finite element method. Various cases are considered, in particular, the apparent stiffening or softening of nano–wires.

Keywords: Strain gradient approach, Micromorphic model, Higher order continua, Size effects, Surface effects, Crystal plasticity, Ultra–fine grained materials, Nanocrystalline materials

Remerciements

On pense parfois que je suis solitaire et peu expansif. La fin de ma thèse (les trois dernières années), passée devant un écran d'ordinateur ou bien à griffonner des équations sur du papier, a sans doute participé à cette image. Si cela était vrai, la combinaison de ces deux traits de caractère aurait forcément eu des effets terribles sur les remerciements qui vont suivre à savoir qu'il n'aurait subsisté que quelques banalités, figures imposées par le contexte, la politesse et le bon sens. Alors, les conséquences auraient été à la hauteur de l'événement: frustration du lecteur cherchant un peu d'humanité entre le résumé de la thèse un peu mystérieux et la table des matières pas beaucoup plus explicite, sentiment d'abandon des anciens collègues avec les risques que cela comporte pour les plus fragiles d'entre eux (en cours de rédaction), révolte des directeurs de thèse excédés par tant d'ingratitude, panique dans la famille... Heureusement cela est faux, et si quelques banalités demeurent forcément dans ce qui suit, celles-ci sont toutes profondément sincères et n'ont pas été imposées par quoi que ce soit. Il y aura aussi sans doute quelques oubliés, que ceux-ci me pardonnent, auxquels j'adresse un message spécial: si vous pensez avoir votre place ici, alors je vous remercie et vous invite à inscrire votre nom dans la marge en face du paragraphe où vous pensez devoir apparaître.

Il est temps pour moi, en quelques mots, de rendre hommage à ceux qui m'ont accompagné pendant ces trois années. Certains d'entre eux sont toujours là, d'autres ne sont pas bien loin, certains n'ont fait que passer, d'autres sont partis pour plus ou moins longtemps.

Je remercie mes deux chers directeurs de thèse, Esteban Busso et Samuel Forest, de m'avoir fait confiance et accueilli au Centre des Matériaux. Au-delà de leur grande expérience, de la finesse de leur analyse et de leurs profondes connaissances qu'ils ont su partager avec moi et dont j'ai profité quotidiennement, c'est surtout leurs qualités humaines que je souhaite saluer ici. Le flegme d'Esteban et sa vision pleine de bon sens et de recul resteront pour moi un exemple. Ses conseils se sont toujours avérés utiles et m'ont permis d'aborder certaines périodes délicates avec sérénité. La fougue, l'énergie et l'enthousiasme communicatifs de Samuel ont été une source de motivation incroyable du premier au dernier jour de cette thèse. Sa gentillesse et sa disponibilité font de lui une personne à part que je suis fier d'avoir eu la chance de rencontrer.

Je remercie Marc Geers et David McDowell d'avoir accepté d'être les rapporteurs du présent manuscrit. J'ai eu la chance de les croiser à plusieurs reprises pendant ma thèse et d'échanger avec eux. Leurs conseils m'ont fait prendre beaucoup de recul et ont largement participé à l'amélioration de mon travail. Merci à Bob Svendsen d'avoir présidé mon jury de soutenance et bravo à lui d'avoir habilement surmonté les quelques changements de dernière minute. Merci à Mohammed Cherkaoui de m'avoir accompagné pendant ces trois ans et d'avoir accepté de participer au jury. Je tiens à remercier tout particulièrement Stéphane Berbenni qui, par ses conseils et son analyse minutieuse, a été un acteur important de ma thèse et de ma soutenance dont il a été un examinateur attentif et pointu.

Je remercie le personnel du Centre des Matériaux pour son travail et le cadre favorable qu'il m'a offert. Je tiens notamment à citer Grégory, Liliane, Olivier et Véronique et à les remercier pour leur aide précieuse. Mention spéciale à Konaly qui, en plus de m'avoir aidé à soigner mes défaillances chroniques pour tout ce qui touche aux documents administratifs, a été une présence amicale et chaleureuse.

La liste est longue, mais je remercie les membres du CdM. D'abord Anaïs et Goimul avec qui j'ai eu le plaisir de travailler, nos articles resteront les souvenirs des longues heures passées à triturer nos modèles.
Pour les moments inoubliables que nous avons partagés ensemble, un peu au CDM mais surtout en dehors, je remercie Angélique, Bahram, João, Laurent, Leandro et Savio. A nous de faire en sorte qu'il y en ait encore beaucoup d'autres.
Parce que passer beaucoup de temps dans un espace restreint ça crée des liens, je tiens à saluer chaleureusement Guillaume, Özgur, Martin, Édouard, Bahram, Justin et Damien. Notre bureau, pour tous les moments d'échanges divers et variés et d'entraide que nous y avons vécus, restera un souvenir fantastique.
Je remercie aussi Antoine, Djamel, Henri, Konstantin, Michel, Philippe, Thilo, Thomas, Yoann... compagnons de navette, de tarot, de Zebulon, de début de soirée, de fin de soirée, de cafet', de piscine, de rugby...

Je remercie celles et ceux qui m'ont apporté leur aide, logistique et morale, le jour de la soutenance. Je pense notamment à la famille de Jeanne.

Je remercie ma famille et tout particulièrement mes parents pour tout ce qu'ils m'ont apporté et tout ce qu'ils m'apportent chaque jour. Au-delà du fait que bien sûr "techniquement" je ne serais pas là sans eux, je n'en serais pas là non plus sans l'environnement idéal qu'ils m'ont offert, parfait dosage de libertés et de pragmatisme dont la recette subtile repose sur beaucoup de confiance, énormément de soutien, pas mal de conseils, de la patience et sans doute quelques sacrifices. Cela fait 28 ans que ça dure et c'est toujours aussi efficace, les mots me manquent pour témoigner tout le bien que je pense d'eux.
Être son grand frère est une source d'inspiration et de fierté, c'est pourquoi ma sœur Laura tient une place toute particulière. Il est vrai que cette thèse nous a éloignés géographiquement mais elle reste ma plus proche confidente et ses avis directs et sincères me sont indispensables.

Pour finir, j'adresse un énorme "merci" à Jeanne. Support technique et moral indispensable en période de rédaction, organisatrice de pots de thèse hors pair, je la remercie très chaleureusement pour sa patience, son soutien, son dynamisme et son humour à toute épreuve qui vont bien au-delà du cadre de la thèse. Toujours surprenante, c'est sans nul doute la colocataire idéale.

Nicolas Cordero, le 30 décembre 2011

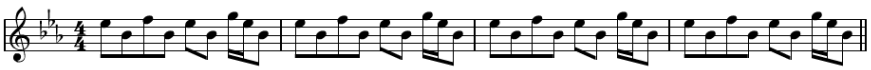

Corgan W., *Today* (1993).

Contents

Introduction

Mechanical behaviour at small scales

The influence of an object's dimensions or of characteristic microstructural length scales exhibited by a material is a fundamental aspect to understand and predict their mechanical behaviour. This influence is even more important at small length scales as specific deformation mechanisms, generally ignored at larger sizes, become predominant. Consequently, predicting the deformation behaviour of micro and nano–objects or of micro and nano–structured materials is a challenging task. Indeed, the role of grain size on the strength of ultra–fine grained and nanocrystalline materials is the subject of an increasing number of scientific studies. However, despite the progress made in this field, it is not yet possible to predict accurately and model the deformation behaviour of this type of materials. Few reliable data are available in the literature due to the complexity of the required experiments and to the high defect densities that some of these materials are known to contain. Moreover, discrete modelling techniques such as atomistic approaches have limited utility as the temporal and spatial scales are often unsuitable to address the real physical phenomena of interest.

Conventional continuum constitutive models based on crystal plasticity principles are common tools in computational mechanics but do not account for size dependency so that the modelled macroscopic response as well as the modelled fields are size independent. A generalisation of these classical models to enable them to model size effects is then required. To that purpose, one can decide that the absolute grain size should arise naturally from the gradient fields. For instance, the dislocation density tensor characterising plastic deformation incompatibilities is directly related to the plastic strain gradient and can therefore be relied upon to introduce strain gradient effects in continuum crystal plasticity simulations. A physical interpretation of the dislocation density tensor is to link it to density of Geometrically Necessary Dislocations (GNDs). In fact, at the onset of plastic deformation in a polycrystalline aggregate, it is commonly assumed that some grains with favourable orientations start yielding by dislocation glide. The corresponding GNDs form pileups when they reach a grain boundary (GB) and the resulting stress field affects further yielding within the grain and its neighbours. The back–stress arising from the pileups effectively reduces the magnitude of the stress required for further glide. The effective stress is increased by the forward stress produced in the neighbouring grains, slip is increased and plastic deformation spreads over the whole microstructure. This mechanism is commonly used to explain the Hall–Petch effect (Hall, 1951; Petch, 1953), which predicts a scaling power law exponent equal to $-1/2$ in the relationship between yield strength and grain size. The Hall–Petch relationship has been verified experimentally over a wide range of metals and grain sizes, and slightly different values of the scaling power law exponent have therefore been observed. Finite element simulations of polycrystals based on strain gradient plasticity models have revealed significant grain size effects, at least in a qualitative manner. One of the major advantage of these simulations is the large representative volume elements that can be studied. However, evidence that strain gradient plasticity models are able to predict the Hall–Petch behaviour from full field simulations remains scarce.

The elementary mechanisms occurring at surfaces or GBs, such as surface/GB motion and GB sliding or dislocation absorption, transmission and emission at GBs, become predominant when the microstructure size decreases below some tens of nanometers. These mechanisms are not directly taken into account in continuum crystal plasticity and have to be derived from atomistic simulations (McDowell, 2008). Results from atomistic simulations can be used to formulate and calibrate more realistic continuum crystal plasticity models by improving the representation of the grain boundary behaviour.

At the nanoscale, elasticity effects should also be considered as plastic slip is either severely restricted or non–existent in such small volumes. In fact, the different equilibrium interatomic

distances and bond strength between surface (or interface) atoms are known to significantly affect the apparent elastic material behaviour of nano–objects and nano–structured materials (Cammarata, 1994; Müller and Saúl, 2004).

The "Nanocrystals" project

This thesis is part of the ANR project "Nanocrystals" (ANR–07–BLAN–0186) which is a collaboration between the Centre des Matériaux of Mines ParisTech and the CNRS UMI (UMI CNRS-GeorgiaTech 2958) located on the European campus of the Georgia Institute of Technology, Georgia Tech–Lorraine, in Metz, France. The objective of this ANR project is to develop an effective framework to study the mechanical behaviour of nanocrystalline materials. To that purpose, multiple approaches have to be considered and a framework that can bridge scales ranging from the atomistic grain boundary structure to the continuum is required. Figure .1 presents the scales involved in the multiscale modelling approach dealt within the "Nanocrystals" project. The project is organised in two main tasks conducted in

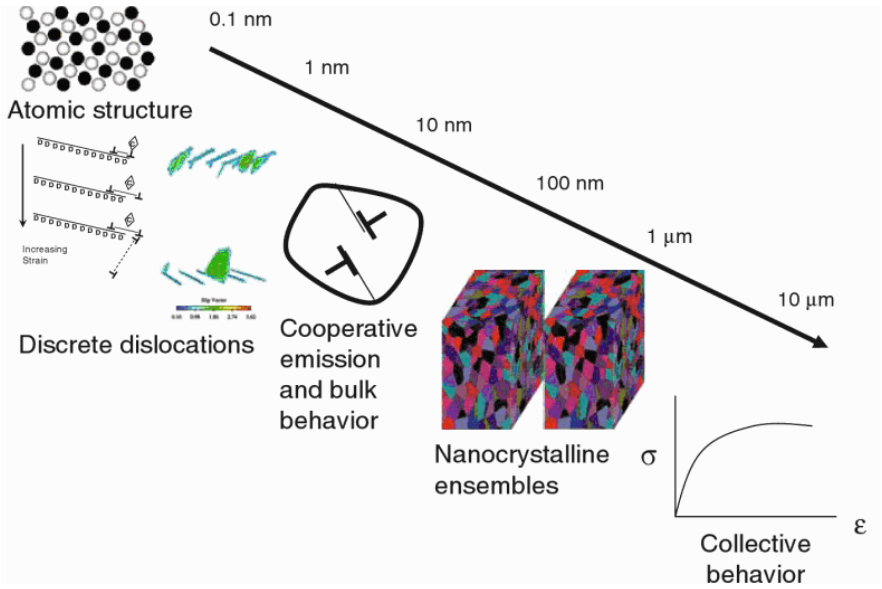

Figure .1 : Multiple length scales to be considered in mechanism–based self–consistent multiscale modeling of nanocrystalline materials (Atomistic and Continuum Modeling of Nanocrystalline Materials: Deformation Mechanisms and Scale Transition, Cherkaoui and Capolungo, 2009).

parallel between GeorgiaTech and Mines ParisTech:

- Task I: Atomistic studies of GBs and Nanocrystals
- Task II: Incorporation of elementary mechanisms into continuum modeling

The results of Task I provide descriptions of the elementary mechanisms occurring at the surfaces or GBs used in Task II to improve the representation of the grain boundary behaviour in enhanced continuum models. The work done in this thesis focuses on Task II.

This doctoral thesis is also open to neighbouring projects and groups which made possible some interesting and fulfilling collaborations. The main one was with the "Cat–Size" project (ANR–07–MAPR–0023–04) which led to the discrete dislocation dynamics part of this manuscript. The CNRS research groups "Mecano" and "NanoMines" also provided opportunities to present our work in front of the wider scientific community.

Thesis main objective

The main objective of this doctoral thesis is to develop a theoretical framework to study the deformation behaviour of polycrystalline materials with ultra–fine or nano–sized microstructures. To that purpose, continuum models able to model size effects arising from mechanisms that are predominant at interfaces (i.e., grain boundaries) or surfaces are proposed. These models, which enable the study of large representative volume elements, are formulated so as to be calibrated using results from experimental work and atomistic and discrete dislocation dynamics simulations.

The proposed approaches are mechanically rigorous but relatively simple. Such approaches have been shown to capture size effects at least in a qualitative way. In fact, the continuum models formulated in the thesis take into account the local and global behaviour and are then able to model intragranular fields and overall size effects. The choice of continuous models is motivated by two main reasons. A physically relevant one: it is possible to carry out continuum descriptions of elasticity surface effects (Mindlin, 1965) and of plastic interaction effects at GBs (Forest *et al.*, 1997; Busso *et al.*, 2000). And a pragmatic one: continuum models are well suited to study large material volumes through the use of finite element techniques. Micromorphic generalisations of the studied models are formulated and used as suitable frameworks for their numerical implementations.

Outline

The manuscript follows the scales of the structures and objects of interest, starting from the largest – the macroscale – to the smallest – the nanoscale. This progression, which also corresponds to the chronology of the work done during the thesis, stands out for two reasons. One one hand, it starts with the more common concepts and methods to set the background of the study and to also highlight the limitations that arise when the length scales of interest reach the nanoscale. On the other hand, there is an inherent increasing level of complexity as we study physical phenomena at lower scales. Thus, in this thesis microplasticity is treated before nanoelasticity, each one defines the two main parts of the document.

Part A is dedicated to microplasticity and to the presentation, formulation, calibration and application of a micromorphic crystal plasticity model referred to as the *microcurl* model. Part A deals with length scales ranging from hundreds of microns to tens of nanometers. The background, context and objectives of this part of the thesis are first introduced in Chapter I. The *microcurl* model, proposed to regularise the response of a strain gradient plasticity model, is formulated and described in Chapter II; the solutions of a boundary value problem are explored for various classes of models. The *microcurl* model is then calibrated and compared with Discrete Dislocation Dynamics in Chapter III. This model is well adapted to simulate the deformation behaviour of polycrystals with grain sizes ranging from hundreds of microns to tens of nanometers. For that purpose, it is numerically implemented using the finite element method. It is shown in Chapter IV that the *microcurl* model is capable of predicting a range of scaling laws, such as that proposed by Hall and Petch. Simulations of the microstructural

length scale effects on (i) the strain fields, (ii) the evolution of the geometrically necessary dislocations and (iii) the thickness of the GND pileups at grain boundaries are presented in Chapter V. The main results of this part are finally recalled in Chapter VI, followed by some concluding remarks.

Part B focuses on nanoelasticity and is dedicated to study surface effects which are localised at a few nanometers from the surface. To that purpose, a continuous method involving the third gradient of displacement is used. This part is introduced by Chapter VII. A discussion about the need of such a higher order theory is done in Chapter VIII and a micromorphic generalisation of Mindlin's model for fluids (Mindlin, 1965) is proposed. The case of elastic solids is treated in Chapter IX and a corresponding second order micromorphic approach is formulated and numerically implemented in order to simulate complex boundary value problems. The resulting surface effects are described in Chapter X by considering simple cases for which analytical solutions for the displacement of atoms are known. The numerical implementation of the model allows the simulations of complex boundary value problems such as the size–dependent apparent elastic properties of nano–wires. Chapter XI presents the main conclusions from this last part of the thesis.

General conclusions and recommendations for future work are finally proposed.

References

Busso E.P., Meissonier F.T., and O'Dowd N.P. (2000). *Gradient-dependent deformation of two-phase single crystal.* Journal of Mechanics and Physics of Solids, vol. 48 n° 11, pp 2333–2361.

Cammarata R.C. (1994). *Surface and interface stress effects in thin films.* Progress in surface science, vol. 46 n° 1, pp 1–38.

Cherkaoui M. and Capolungo L. (2009). *Atomistic and Continuum Modeling of Nanocrystalline Materials: Deformation Mechanisms and Scale Transition.* Springer Verlag.

Forest S., Cailletaud G., and Sievert R. (1997). *A Cosserat theory for elastoviscoplastic single crystals at finite deformation.* Archives of Mechanics, vol. 49 n° 4, pp 705–736.

Hall E.O. (1951). *The deformation and ageing of mild steel: III discussion of results.* Proceedings of the Physical Society. Section B, vol. 64, pp 747.

McDowell D.L. (2008). *Viscoplasticity of heterogeneous metallic materials.* Materials Science and Engineering R, vol. 62, pp 67–123.

Mindlin R.D. (1965). *Second gradient of strain and surface–tension in linear elasticity.* Int. J. Solids Structures, vol. 1, pp 417–438.

Müller P. and Saúl A. (2004). *Elastic effects on surface physics.* Surface Science Reports, vol. 54 n° 5-8, pp 157–258.

Petch N.J. (1953). *The cleavage strength of polystrals.* J. Iron Steel Inst, vol. 173, pp 25–28.

Part A

Microplasticity

Chapter -I-

Introduction

Contents

I.1 Context

Classical continuum crystal plasticity theory incorporates internal variables associated with scalar dislocations densities in order to describe the hardening behaviour of single crystals and polycrystals (McDowell, 2008). The modelling of size effects observed in crystalline solids, such as grain or precipitate size effects, has been addressed by adding strain gradient variables into the constitutive framework, either in an explicit way as in Acharya and Beaudoin (2000), Busso *et al.* (2000) and Bassani (2001) or by means of additional degrees of freedom associated with new boundary and interface conditions (Forest *et al.*, 1997; Shu, 1998). Motivations for introducing strain gradients in continuum modelling stem from the multiscale analysis of micromechanics, as reviewed in Ghoniem *et al.* (2003). The resulting strain gradient components are related to the dislocation density tensor as introduced by Nye (1953). The dislocation density tensor is computed from the rotational part of the gradient of plastic deformation, so that the partial differential equations to be solved generally are of higher order than those used in classical mechanics. That is why it is usually necessary to resort to the mechanics of generalised continua in order to properly formulate models that incorporate extra–hardening effects associated with the dislocation density tensor. Generalised crystal plasticity models developed in the past forty years can be classified into two main groups:

- Strain gradient plasticity models involving either the rotational part of plastic deformation or its full gradient (Aifantis, 1984, 1987; Steinmann, 1996; Fleck and Hutchinson, 1997; Gurtin, 2002; Cheong *et al.*, 2005; Lele and Anand, 2008),

- Generalised continuum theories with additional degrees of freedom accounting for rotation or full deformation of a triad of crystal directors and the effect of their gradients on hardening: Cosserat models (Kröner, 1963; Forest *et al.*, 2000; Clayton *et al.*, 2006), and models based on micromorphic theory (Eringen and Claus, 1970; Bammann, 2001).

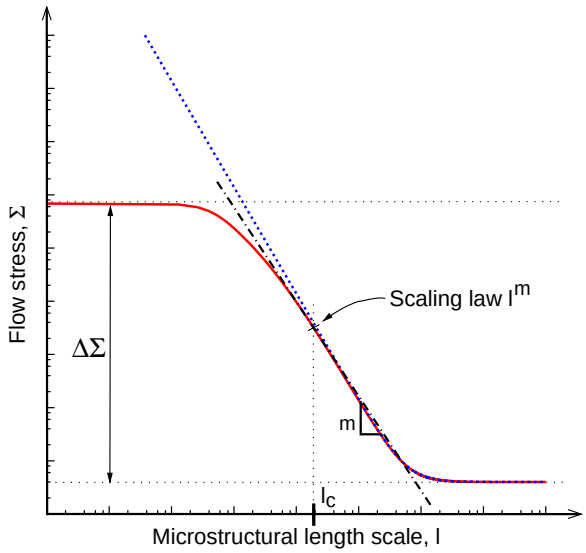

Figure I.1 : Description of two different profiles of the macroscopic flow stress that can be obtained with the different groups of models: size effect with two asymptotic regimes (solid line), unbounded extra–stress for small sizes (dotted line), definition of the scaling law in the transition domain (dot–dashed line).

Most of these phenomenological theories have been shown to capture size effects at least in a qualitative way. However, clear demonstrations that they can reproduce the scaling laws expected in precipitate hardening or grain size effect, namely Orowan and Hall–Petch laws, have not been yet provided.

The extra–hardening effects modelled by generalised continuum crystal plasticity models can be summarised in the main features identified in Fig. I.1, which shows schematically in a log–log diagram the effect of the microstructural length scale l (grain or precipitate size) on flow stress. These three main characteristics are the stress range, $\Delta\Sigma$, the characteristic length, l_c, and the scaling law, $\Sigma \propto l^m$ when $l \approx l_c$. Here, $\Delta\Sigma$ also corresponds to the highest extra–stress reached for small microstructural length scales, that is why $\Delta\Sigma$ is also called the extra–stress in this work. Fig. I.1 shows that when the characteristic size of the microstructure decreases, the material strengthens. For large values of l, the asymptotic behaviour corresponds to the size–independent response of conventional crystal plasticity models. In contrast, for small values of l, a bounded or unbounded asymptotic behaviour can be obtained, depending on the model considered. The Cosserat crystal plasticity model proposed by Forest *et al.* (2000), for instance, models an asymptotically saturated extra–stress $\Delta\Sigma$ (see Fig. I.1). In the intermediate region around the characteristic length l_c, the size–dependent response can be characterised by the scaling law, $\Sigma \propto l^m$, in the proximity of $l = l_c$. The objective of the present work is to derive explicitly the characteristics $\Delta\Sigma$, l_c and m, for models representative of the above classes of generalised material models.

An analytic description of the size–dependent behaviour of materials is possible only in some special simplified geometrical situations. For instance the prediction of the shearing of a single crystal layer under single (or double) slip for strain gradient plasticity models was treated in Shu *et al.* (2001), Bittencourt *et al.* (2003), Bardella (2007) and Hunter and Koslowski (2008). Single slip in a two–phase laminate microstructure was considered in Sedláček and Forest (2000), Forest and Sedláček (2003) and Forest (2008). Here, the plastic slip distributions were compared with those obtained from the continuous dislocation line

tension model, considered as a reference, and Cosserat and strain gradient plasticity models, including that proposed by Aifantis (1987). This simple situation is considered again in the present work in order to derive explicit expressions for the overall extra–hardening, the characteristic length scale l_c and the $\Sigma - l$ scaling law, which had not been done in previous work.

In the crystal plasticity theory at small deformation, the gradient of the velocity field can be decomposed into the elastic and plastic deformation rates:

$$\dot{\underset{\sim}{\boldsymbol{H}}} = \underline{\dot{\boldsymbol{u}}} \otimes \boldsymbol{\nabla} = \dot{\underset{\sim}{\boldsymbol{H}}}^e + \dot{\underset{\sim}{\boldsymbol{H}}}^p, \tag{I.1}$$

where

$$\dot{\underset{\sim}{\boldsymbol{H}}}^p = \sum_\alpha \dot{\gamma}^\alpha \underline{\boldsymbol{l}}^\alpha \otimes \underline{\boldsymbol{n}}^\alpha, \tag{I.2}$$

with, $\underline{\boldsymbol{u}}$ the displacement field, α the number of slip systems, $\dot{\gamma}^\alpha$ the slip rate for the slip system α, $\underline{\boldsymbol{l}}$ the slip direction and $\underline{\boldsymbol{n}}$ the normal to the slip plane. The elastic deformation $\underset{\sim}{\boldsymbol{H}}^e$ bridges the gap between the compatible total deformation $\underset{\sim}{\boldsymbol{H}}$ and the incompatible plastic deformation $\underset{\sim}{\boldsymbol{H}}^p$. Applying the curl operator to a compatible field gives zero so that:

$$\operatorname{curl} \dot{\underset{\sim}{\boldsymbol{H}}} = 0 = \operatorname{curl} \dot{\underset{\sim}{\boldsymbol{H}}}^e + \operatorname{curl} \dot{\underset{\sim}{\boldsymbol{H}}}^p. \tag{I.3}$$

The incompatibility of plastic deformation is characterised by its curl part called dislocation density tensor $\underset{\sim}{\boldsymbol{\Gamma}}$ (Nye, 1953; Steinmann, 1996; Forest *et al.*, 1997; Acharya and Bassani, 2000; Cermelli and Gurtin, 2001; Svendsen, 2002) defined here as

$$\underset{\sim}{\boldsymbol{\Gamma}} = -\operatorname{curl} \underset{\sim}{\boldsymbol{H}}^p = \operatorname{curl} \underset{\sim}{\boldsymbol{H}}^e. \tag{I.4}$$

The tensors $\underset{\sim}{\boldsymbol{H}}, \underset{\sim}{\boldsymbol{H}}^e, \underset{\sim}{\boldsymbol{H}}^p$, generally non–symmetric, can be decomposed into their symmetric and skew–symmetric parts:

$$\underset{\sim}{\boldsymbol{H}} = \underset{\sim}{\boldsymbol{\varepsilon}} + \underset{\sim}{\boldsymbol{\omega}}, \quad \underset{\sim}{\boldsymbol{H}}^e = \underset{\sim}{\boldsymbol{\varepsilon}}^e + \underset{\sim}{\boldsymbol{\omega}}^e, \quad \underset{\sim}{\boldsymbol{H}}^p = \underset{\sim}{\boldsymbol{\varepsilon}}^p + \underset{\sim}{\boldsymbol{\omega}}^p. \tag{I.5}$$

Then Eq. (I.3) becomes:

$$0 = \operatorname{curl} \underset{\sim}{\boldsymbol{\varepsilon}}^e + \operatorname{curl} \underset{\sim}{\boldsymbol{\omega}}^e + \operatorname{curl} \underset{\sim}{\boldsymbol{H}}^p. \tag{I.6}$$

Neglecting the curl part of the elastic strain, $\underset{\sim}{\boldsymbol{\varepsilon}}^e$, leads to the following approximation to the dislocation density tensor derived by Nye:

$$\underset{\sim}{\boldsymbol{\Gamma}} = \operatorname{curl} \underset{\sim}{\boldsymbol{H}}^e = \operatorname{curl} \underset{\sim}{\boldsymbol{\varepsilon}}^e + \operatorname{curl} \underset{\sim}{\boldsymbol{\omega}}^e \simeq \operatorname{curl} \underset{\sim}{\boldsymbol{\omega}}^e. \tag{I.7}$$

Nye's formula sets a linear relationship between this approximation of the dislocation density tensor and lattice curvature. The Cosserat crystal plasticity theory developed in Forest *et al.* (1997) incorporates the effect of lattice curvature on crystal hardening behaviour. It requires three additional degrees of freedom associated with the lattice rotation $\underset{\sim}{\boldsymbol{\omega}}^e$. In contrast, the theories proposed by Gurtin (2002) and Svendsen (2002), for example, include the full curl of the plastic deformation. This requires in general nine additional degrees of freedom associated with the generally non–symmetric plastic deformation tensor $\underset{\sim}{\boldsymbol{H}}^p$. We will call this sub–class of models "$curl H^p$".

A consequence of neglecting the curl of elastic strain tensor in the Cosserat model is that Cosserat effects can arise even in the elastic regime as soon as a gradient of "elastic" rotation exists. Indeed, the $\operatorname{curl} \underset{\sim}{\boldsymbol{\omega}}^e \neq 0$ as soon as $\operatorname{curl} \underset{\sim}{\boldsymbol{\varepsilon}}^e \neq 0$. In contrast, in the $curl H^p$ theory, strain gradient effects arise only when plastic deformation has developed. As it will be shown in this work, this leads to different modelled behaviour at the interface between an elastic and a plastic phase.

This interface configuration can be found at the grain boundaries of polycrystals. The behaviour of a polycrystalline material is notably dependent on grain size. Finite element simulations of polycrystals based on classical continuum crystal plasticity do not account for this dependence so that the modelled macroscopic response as well as the modelled fields inside the aggregates are size independent (Mika and Dawson, 1998; Barbe *et al.*, 2001; St-Pierre *et al.*, 2008). As it would be irrelevant to enter the grain size into the constitutive model explicitly, its effects should arise from the gradient fields. Some finite element simulations on a limited number of grains are provided in (Forest *et al.*, 2000; Bayley *et al.*, 2007; Bargmann *et al.*, 2010). However, due to the high non–linearity of the models and the number of additional degrees of freedom, only coarse meshes were used so that only poor description of the gradient fields are given. Most contributions were dedicated to the prediction of the grain size–dependent overall response of polycrystals and to the derivation of Hall–Petch–like relationships. This is also done in the present work, but in addition, we want to show how the grain size also affects the intragranular fields of plastic strains and of dislocation density tensor. For that purpose, a micromorphic crystal plasticity model, called *microcurl*, closely related to the $curlH^p$ theory and belonging to the class of generalised continuum models with additional degrees of freedom as presented in Eringen (1999) and Forest (2009) is implemented.

I.2 Aims and outline

The work presented here is organised as follows. Chapter II focuses on the formulation and the description of a micromorphic crystal plasticity model proposed to regularise the response of a strain gradient plasticity model. For that, strain / stress fields and the back stress in a laminate microstructure, made of a hard elastic and a soft plastic phase, submitted to simple shear are derived for the Cosserat theory in Section II.1 and for a "$curlH^p$" type model in Section II.2. It will be shown that a jump in the generalised tractions arises at the interface according to the latter approach, due to the presence of a purely elastic phase. A regularisation method is proposed in Section II.3 by introducing the *microcurl* model. A finite deformation extension of this model is also given in Appendix A.5. The size effects given by the Cosserat and *microcurl* models are compared in Section II.4. In Section II.5, we discuss how our results could be used to identify strain gradient plasticity parameters from experimentally observed size effects, such as precipitate size effects in two–phase single crystal nickel based superalloys published by Busso *et al.* (2000), Forest *et al.* (2000) and Tinga *et al.* (2008). The solution is finally extended to the case of symmetric double slip. It is shown that very similar size effects as those for the single slip case are found, opening the way to further multislip generalisations of the models.

In Chapter III, size effects induced by multilayer pileups are investigated in terms of plastic slip distribution and overall work–hardening using discrete dislocation dynamics (DDD) and the *microcurl* model. Double ended stacked pileups of edge dislocations and pileups on inclined slip planes in a channel are considered. The channel size effects on the mechanical responses obtained with the two models are analysed and compared using analytical and numerical solutions.

The *microcurl* model is used simulate the behaviour of polycrystalline aggregates with various microstructure sizes in Chapter IV. The continuity requirements at grain boundaries are introduced in Section IV.1 and their role in the size effects is studied. As an illustration, finite element simulations of the simple shear response of a polycrystalline aggregate with a relatively small number of grains (24 grains) are first performed to have an overview of the size effects produced by the model. Various microstructure sizes are investigated and a virtual material is considered with various intrinsic length scales. It is shown in particular that, even

when no classical isotropic hardening is introduced, the linear kinematic hardening produced by the *microcurl* model is sufficient to reproduce scaling laws observed in grain size effects. This first set of simulations also serves as a basis for the identification of the intrinsic material parameters. Finite element simulations of the simple shear response of a larger idealised aluminium aggregate are performed in Section IV.2. The impact of the microstructure size on the overall response is investigated.

Finally, in Chapter V, the *microcurl* model is used to explore the grain size effects on the fields of plastic strain and of the dislocation density tensors in two–dimensional polycrystals. The dependence of the overall response and of fields on the grain size are shown in Sections V.1, V.2 and V.3.

The notation used hereafter are given in Appendix A.1.

References

Acharya A. and Bassani J.L. (2000). *Lattice incompatibility and a gradient theory of crystal plasticity.* Journal of the Mechanics and Physics of Solids, vol. 48, pp 1565–1595.

Acharya A. and Beaudoin A.J. (2000). *Grain size effects in viscoplastic polycrystals at moderate strains.* Journal of the Mechanics and Physics of Solids, vol. 48, pp 2213–2230.

Aifantis E.C. (1984). *On the microstructural origin of certain inelastic models.* Journal of Engineering Materials and Technology, vol. 106, pp 326–330.

Aifantis E.C. (1987). *The physics of plastic deformation.* International Journal of Plasticity, vol. 3, pp 211–248.

Bammann D.J. (2001). *A model of crystal plasticity containing a natural length scale.* Materials Science and Engineering A, vol. 309–310, pp 406–410.

Barbe F., Decker L., Jeulin D., and Cailletaud G. (2001). *Intergranular and intragranular behavior of polycrystalline aggregates. Part 1: FE model.* International Journal of Plasticity, vol. 17, pp 513–536.

Bardella L. (2007). *Some remarks on the strain gradient crystal plasticity modelling, with particular reference to the material length scales involved.* International Journal of Plasticity, vol. 23, pp 296–322.

Bargmann S., Ekh M., Runesson K., and Svendsen B. (2010). *Modeling of polycrystals with gradient crystal plasticity: A comparison of strategies.* Philosophical Magazine, vol. 90 n° 10, pp 1263–1288.

Bassani J.L. (2001). *Incompatibility and a simple gradient theory of plasticity.* J. Mech. Physics of Solids, vol. 49, pp 1983–1996.

Bayley C.J., Brekelmans W.A.M., and Geers M.G.D. (2007). *A three–dimensional dislocation field crystal plasticity approach applied to miniaturized structures.* Philosophical Magazine, vol. 87, pp 1361–1378.

Bittencourt E., Needleman A., Gurtin M.E., and Van der Giessen E. (2003). *A comparison of nonlocal continuum and discrete dislocation plasticity predictions.* Journal of the Mechanics and Physics of Solids, vol. 51 n° 2, pp 281 – 310.

Busso E.P., Meissonier F.T., and O'Dowd N.P. (2000). *Gradient-dependent deformation of two-phase single crystal.* Journal of Mechanics and Physics of Solids, vol. 48 n° 11, pp 2333–2361.

Cermelli P. and Gurtin M.E. (2001). *On the characterization of geometrically necessary dislocations in finite plasticity.* Journal of the Mechanics and Physics of Solids, vol. 49, pp 1539–1568.

Cheong K.S., Busso E.P., and Arsenlis A. (2005). *A study of microstructural length scale effects on the behavior of FCC polycrystals using strain gradient concepts.* International Journal of Plasticity, vol. 21, pp 1797–1814.

Clayton J.D., McDowell D.L., and Bammann D.J. (2006). *Modeling dislocations and disclinations with finite micropolar elastoplasticity.* International Journal of Plasticity, vol. 22, pp 210–256.

Eringen A.C. and Claus W.D. (1970). *A micromorphic approach to dislocation theory and its relation to several existing theories.* In : Fundamental Aspects of Dislocation Theory, éds. Simmons J.A., de Wit R., and Bullough R., pp 1023–1062. Nat. Bur. Stand. (US) Spec. Publ. 317, II.

Eringen A. C. (1999). *Microcontinuum field theories.* Springer, New York.

Fleck N.A. and Hutchinson J.W. (1997). *Strain gradient plasticity.* Adv. Appl. Mech., vol. 33, pp 295–361.

Forest S. (2008). *Some links between Cosserat, strain gradient crystal plasticity and the statistical theory of dislocations.* Philosophical Magazine, vol. 88, pp 3549–3563.

Forest S. (2009). *Micromorphic Approach for Gradient Elasticity, Viscoplasticity, and Damage.* Journal of Engineering Mechanics, vol. 135, pp 117–131.

Forest S., Barbe F., and Cailletaud G. (2000). *Cosserat Modelling of Size Effects in the Mechanical Behaviour of Polycrystals and Multiphase Materials.* International Journal of Solids and Structures, vol. 37, pp 7105–7126.

Forest S., Cailletaud G., and Sievert R. (1997). *A Cosserat theory for elastoviscoplastic single crystals at finite deformation.* Archives of Mechanics, vol. 49 n° 4, pp 705–736.

Forest S. and Sedláček R. (2003). *Plastic slip distribution in two–phase laminate microstructures: Dislocation–based vs. generalized–continuum approaches.* Philosophical Magazine A, vol. 83, pp 245–276.

Ghoniem N.M., Busso E.P., Kioussis N., and Huang H. (2003). *Multiscale modelling of nanomechanics and micromechanics: an overview.* Philosophical Magazine, vol. 83, pp 3475–3528.

Gurtin M.E. (2002). *A gradient theory of single–crystal viscoplasticity that accounts for geometrically necessary dislocations.* Journal of the Mechanics and Physics of Solids, vol. 50, pp 5–32.

Hunter A. and Koslowski M. (2008). *Direct calculations of material parameters for gradient plasticity.* Journal of the Mechanics and Physics of Solids, vol. 56 n° 11, pp 3181–3190.

Kröner E. (1963). *On the physical reality of torque stresses in continuum mechanics.* Int. J. Engng. Sci., vol. 1, pp 261–278.

Lele S.P. and Anand L. (2008). *A small-deformation strain-gradient theory for isotropic viscoplastic materials.* Philosophical Magazine, vol. 88, pp 3655–3689.

McDowell D.L. (2008). *Viscoplasticity of heterogeneous metallic materials.* Materials Science and Engineering R, vol. 62, pp 67–123.

Mika D. P. and Dawson P. R. (1998). *Effects of grain interaction on deformation in polycrystals.* Materials Science and Engineering, vol. A257, pp 62–76.

Nye J.F. (1953). *Some geometrical relations in dislocated crystals.* Acta Metall., vol. 1, pp 153–162.

Sedláček R. and Forest S. (2000). *Non-local plasticity at microscale : A dislocation-based model and a Cosserat model.* physica status solidi (b), vol. 221, pp 583–596.

Shu J.Y. (1998). *Scale–dependent deformation of porous single crystals.* International Journal of Plasticity, vol. 14, pp 1085–1107.

Shu J.Y., Fleck N.A., Van der Giessen E., and Needleman A. (2001). *Boundary layers in constrained plastic flow : comparison of non local and discrete dislocation plasticity.* Journal of the Mechanics and Physics of Solids, vol. 49, pp 1361–1395.

St-Pierre L., Héripré E., Dexet M., Crépin J., Bertolino G., and Bilger N. (2008). *3D simulations of microstructure and comparison with experimental microstructure coming from OIM analysis.* International Journal of Plasticity, vol. 24, pp 1516–1532.

Steinmann P. (1996). *Views on multiplicative elastoplasticity and the continuum theory of dislocations.* International Journal of Engineering Science, vol. 34, pp 1717–1735.

Svendsen B. (2002). *Continuum thermodynamic models for crystal plasticity including the effects of geometrically-necessary dislocations.* J. Mech. Phys. Solids, vol. 50, pp 1297–1329.

Tinga T., Brekelmans W.A.M., and Geers M.G.D. (2008). *Incorporating strain gradient effects in a multiscale constitutive framework for nickel-base superalloys.* Philosophical Magazine, vol. 88, pp 3793–3825.

Chapter -II-

Size effects in generalised continuum crystal plasticity for two–phase laminates

Abstract

In this chapter, the solutions of a boundary value problem are explored for various classes of generalised crystal plasticity models including Cosserat, strain gradient and micromorphic crystal plasticity. A micromorphic crystal plasticity model, called *microcurl*, based on the dislocation density tensor is proposed. The considered microstructure consists of a two–phase laminate containing a purely elastic and an elasto–plastic phase undergoing single or double slip. The local distributions of plastic slip, lattice rotation and stresses are derived when the microstructure is subjected to simple shear. The arising size effects are characterised by the overall extra back stress component resulting from the action of higher order stresses, a characteristic length l_c describing the size–dependent domain of material response, and by the corresponding scaling law l^n as a function of microstructural length scale, l. Explicit relations for these quantities are derived and compared for the different models. The conditions at the interface between the elastic and elasto–plastic phases are shown to play a major role in the solution. A range of material parameters is shown to exist for which the Cosserat and the *microcurl* model exhibit the same behaviour. The models display in general significantly different asymptotic regimes for small microstructural length scales. Scaling power laws with the exponent continuously ranging from 0 to -2 are obtained depending on the values of the material parameters. The unusual exponent value -2 is obtained for the strain gradient plasticity model, denoted "$curl H^p$" in this work. These results provide guidelines for the identification of higher order material parameters of crystal plasticity models from experimental data, such as precipitate size effects in precipitate strengthened alloys.

Contents

Preamble: The work presented in this chapter has been published in the "*Journal of the Mechanics and Physics of Solids*" in a paper entitled "*Size effects in generalised continuum crystal plasticity for two–phase laminates*" (Cordero *et al.*, 2010). It was done in collaboration with Anaïs Gaubert, former PhD student of Samuel Forest.

II.1 Cosserat modelling of simple shear in a two–phase laminate

Simple shear of a two–phase laminate was considered first in Sedláček and Forest (2000) and then explored in more details in Forest and Sedláček (2003) and Forest (2008) from the point of view of the continuum theory of dislocations, on the one hand, and for Cosserat and strain gradient continuum plasticity models, on the other hand. Analytic solutions of the boundary value problem were derived for the stress, strain and plastic slip profiles in the microstructure. According to the Cosserat model presented in Forest (2008), a back stress intrinsically arises from the skew symmetric contribution of the stress and orientation tensors, when writing Schmid law. The objective of this section is to recall the main features of the

Cosserat approach, and to derive the main characteristics of the size effect, given by the maximum stress amplitude, $\Delta\Sigma$, the characteristic length scale of the transition zone, l_c, and the scaling law exponent, m.

II.1.1 The Cosserat formulation

A Cosserat continuum is described by a displacement field $\underline{\boldsymbol{u}}$ and an independent microrotation field, represented by its axial vector, $\underline{\boldsymbol{\phi}}$. Two deformation measures are then defined:

$$\underset{\sim}{\boldsymbol{e}} = \underline{\boldsymbol{u}} \otimes \boldsymbol{\nabla} + \underset{\sim}{\boldsymbol{\epsilon}}.\underline{\boldsymbol{\phi}}, \quad e_{ij} = u_{i,j} + \epsilon_{ijk}\phi_k, \tag{II.1}$$

$$\underset{\sim}{\boldsymbol{\kappa}} = \underline{\boldsymbol{\phi}} \otimes \boldsymbol{\nabla}, \quad \kappa_{ij} = \phi_{i,j}, \tag{II.2}$$

where $\underset{\sim}{\boldsymbol{e}}$ represents the relative deformation tensor and $\underset{\sim}{\boldsymbol{\kappa}}$ the curvature tensor. The stress tensors associated with the previous deformation and curvature are the force stress tensor, $\underset{\sim}{\boldsymbol{\sigma}}$, and the couple stress tensor, $\underset{\sim}{\boldsymbol{m}}$. Both have to fulfil the balance of momentum and balance of moment of momentum equations:

$$\operatorname{div} \underset{\sim}{\boldsymbol{\sigma}} = 0, \quad \sigma_{ij,k} = 0, \tag{II.3}$$

$$\operatorname{div} \underset{\sim}{\boldsymbol{m}} + 2\,\overset{\times}{\underline{\boldsymbol{\sigma}}} = 0, \quad m_{ij,j} - \epsilon_{ijk}\sigma_{jk} = 0. \tag{II.4}$$

Note that volume forces and couples are not considered for simplicity. In Eq. (II.4), $\overset{\times}{\underline{\boldsymbol{\sigma}}}$ is the axial vector associated with the skew-symmetric part of the stress tensor,

$$\overset{\times}{\underline{\boldsymbol{\sigma}}} = -\frac{1}{2}\,\underset{\sim}{\boldsymbol{\epsilon}} : \underset{\sim}{\boldsymbol{\sigma}}. \tag{II.5}$$

Moreover, the boundary conditions for the traction and couple stress vectors are

$$\underline{\boldsymbol{t}} = \underset{\sim}{\boldsymbol{\sigma}}.\underline{\boldsymbol{n}}, \quad t_i = \sigma_{ij}n_j, \tag{II.6}$$

$$\underline{\boldsymbol{m}} = \underset{\sim}{\boldsymbol{m}}.\underline{\boldsymbol{n}}, \quad m_i = m_{ij}n_j, \tag{II.7}$$

where $\underline{\boldsymbol{n}}$ is the unit normal vector to the boundary of the considered domain. The deformation can be decomposed into its elastic and plastic parts,

$$\underset{\sim}{\boldsymbol{e}} = \underset{\sim}{\boldsymbol{e}}^e + \underset{\sim}{\boldsymbol{H}}^p. \tag{II.8}$$

Plastic deformation is due to slip processes and the evolution of $\underset{\sim}{\boldsymbol{H}}^p$ is still given by Eq. (I.2). The constitutive equations for isotropic Cosserat elasticity can be expressed as,

$$\underset{\sim}{\boldsymbol{\sigma}} = \lambda(\operatorname{tr}\underset{\sim}{\boldsymbol{e}}^e)\underset{\sim}{\mathbf{1}} + 2\mu\underset{\sim}{\boldsymbol{e}}^{es} + 2\mu_c\underset{\sim}{\boldsymbol{e}}^{ea}, \tag{II.9}$$

$$\underset{\sim}{\boldsymbol{m}} = \alpha(\operatorname{tr}\underset{\sim}{\boldsymbol{\kappa}})\underset{\sim}{\mathbf{1}} + 2\beta\underset{\sim}{\boldsymbol{\kappa}}^s + 2\gamma\underset{\sim}{\boldsymbol{\kappa}}^a, \tag{II.10}$$

where λ and μ are the classical Lamé constants, and μ_c, α, β and γ are four additional elastic constants. In a 2D situation, as it is the case in this work, the constant α is not relevant and we choose $\beta = \gamma$ for simplicity. The size effects exhibited by the solutions of boundary value problems involving such a model are related to an intrinsic length scale, typically defined as,

$$l_\omega = \sqrt{\frac{\beta}{\mu}}. \tag{II.11}$$

In the present work, the constraint

$$\mu/\mu_c \ll 1 \tag{II.12}$$

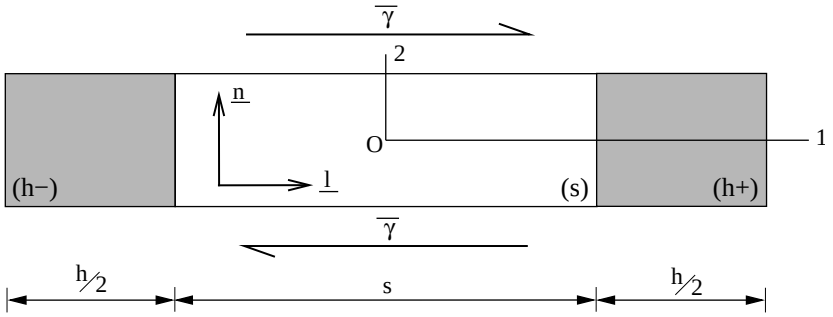

Figure II.1 : Single slip in a two–phase periodic microstructure under simple shear: the grey phase (h) displays a purely linear elastic behaviour whereas the inelastic deformation of the white elasto–plastic phase (s) is controlled by a single slip system $(\underline{\boldsymbol{n}}, \underline{\boldsymbol{l}})$.

is enforced. This condition implies that $\underset{\sim}{\boldsymbol{e}}^e$ is almost symmetric and therefore means that the Cosserat microrotation almost coincides with the lattice rotation. The parameter μ_c can be seen as a penalty factor that constrains the Cosserat directors to be lattice vectors (Forest *et al.*, 2001). The curvature tensor $\underset{\sim}{\boldsymbol{\kappa}}$ is then directly related to the curl $\underset{\sim}{\boldsymbol{\omega}}^e$ through Nye's formula (Forest, 2008). It follows that the curvature tensor of the Cosserat theory stands as an approximation to the dislocation density tensor.

Here the Schmid criterion is used as the yield criterion, computed with the generally non–symmetric force stress tensor. Furthermore, the critical resolved shear stress, τ_c, is taken to be constant for the analytic developments of this work (thus no strain–hardening is considered). The generalised resolved shear stress for the slip system α, defined by its slip plane normal vector $\underline{\boldsymbol{n}}^\alpha$, and its slip direction vector $\underline{\boldsymbol{l}}^\alpha$, is obtained from

$$\tau^\alpha = \underset{\sim}{\boldsymbol{\sigma}} : \underset{\sim}{\boldsymbol{P}}^\alpha = \underset{\sim}{\boldsymbol{\sigma}}^s : \underset{\sim}{\boldsymbol{P}}^{\alpha s} + \underset{\sim}{\boldsymbol{\sigma}}^a : \underset{\sim}{\boldsymbol{P}}^{\alpha a} = \tau^\alpha_{sym} - x^\alpha, \tag{II.13}$$

where $\underset{\sim}{\boldsymbol{P}}^\alpha = \underline{\boldsymbol{l}}^\alpha \otimes \underline{\boldsymbol{n}}^\alpha$ is the orientation tensor. The first term in the generalised resolved shear stress is the classical resolved shear stress τ^α_{sym}. The second term is a back stress, x^α, which is related to the divergence of the couple stress tensor. Recalling Eq. (II.4):

$$x^\alpha = -\frac{1}{2}(\operatorname{div} \underset{\sim}{\boldsymbol{m}}).(\underline{\boldsymbol{l}}^\alpha \times \underline{\boldsymbol{n}}^\alpha). \tag{II.14}$$

The slip system is activated when the resolved shear stress reaches the threshold, τ_c, so that the yield criterion reads,

$$|\tau^\alpha| = |\tau^\alpha_{sym} - x^\alpha| \leq \tau_c. \tag{II.15}$$

It has been shown in Forest (2008) that this back stress component leads to linear kinematic hardening in single slip under simple shear.

II.1.2 Application to a two-phase periodic microstructure under simple shear

We consider a two–phase periodic microstructure under simple shear as studied in Forest and Sedláček (2003) and Forest (2008). This microstructure, described in Fig. II.1, is composed of a hard purely elastic phase (h) and a soft elasto–plastic single crystal phase (s). One single slip system is considered in the soft phase (s), with slip direction normal to the interface plane (h)/(s). This periodic unit cell is subjected to a mean simple glide $\bar{\gamma}$ in the crystal slip direction of the phase (s). We look for a displacement and micro-rotation

fields of the form,

$$u_1 = \bar{\gamma}\ x_2, \quad u_2(x_1) = u(x_1), \quad u_3 = 0, \tag{II.16}$$

$$\phi_1 = \phi_2 = 0, \quad \phi_3 = \phi(x_1). \tag{II.17}$$

Consequently, the Cosserat deformation and curvature tensors become

$$\underset{\sim}{\boldsymbol{e}} = \begin{bmatrix} 0 & \bar{\gamma} + \phi(x_1) & 0 \\ u_{,1} - \phi(x_1) & 0 & 0 \\ 0 & 0 & 0 \end{bmatrix} \quad , \quad \underset{\sim}{\boldsymbol{\kappa}} = \begin{bmatrix} 0 & 0 & 0 \\ 0 & 0 & 0 \\ \phi_{,1} & 0 & 0 \end{bmatrix} \tag{II.18}$$

The solution for $\underline{\boldsymbol{\phi}}$ in the elastic phase (h) can be found in Forest and Sedláček (2003). The micro-rotation exhibits a hyperbolic profile, given by

$$\phi^{(h+)} = a^h \cosh\left(\omega^h \left(x_1 - \frac{s+h}{2}\right)\right) + d^h \quad \text{for} \quad s/2 < x < (s+h)/2, \tag{II.19}$$

$$\phi^{(h-)} = a^h \cosh\left(\omega^h \left(x_1 + \frac{s+h}{2}\right)\right) + d^h \quad \text{for} \quad -(s+h)/2 < x < -s/2, \tag{II.20}$$

with

$$\omega^{h\,2} = \frac{2\mu^h \mu_c^h}{\beta^h(\mu^h + \mu_c^h)}, \tag{II.21}$$

and with a^h and d^h being two integration constants. The following relations are obtained for the deformation tensor:

$$e_{21}^{(h+)} = -\frac{\mu^h - \mu_c^h}{\mu^h + \mu_c^h}\phi^{h+} + \bar{\gamma} + d^h \frac{2\mu^h}{\mu^h + \mu_c^h}, \tag{II.22}$$

$$e_{21}^{(h-)} = -\frac{\mu^h - \mu_c^h}{\mu^h + \mu_c^h}\phi^{h-} + \bar{\gamma} + d^h \frac{2\mu^h}{\mu^h + \mu_c^h}. \tag{II.23}$$

In the plastic phase, the solution is derived here for the yield criterion (II.15). We compute successively,

$$\underset{\sim}{\boldsymbol{e}}^p = \gamma \underline{\boldsymbol{l}} \otimes \underline{\boldsymbol{n}} = \begin{bmatrix} 0 & \gamma & 0 \\ 0 & 0 & 0 \\ 0 & 0 & 0 \end{bmatrix} \quad \underset{\sim}{\boldsymbol{e}}^e = \begin{bmatrix} 0 & e_{12}^e & 0 \\ e_{21}^e & 0 & 0 \\ 0 & 0 & 0 \end{bmatrix}, \tag{II.24}$$

which results into two non-zero components for the stress tensor,

$$\sigma_{12} = \mu^s(e_{12}^e + e_{21}^e) + \mu_c^s(e_{12}^e - e_{21}^e), \tag{II.25}$$

$$\sigma_{21} = \mu^s(e_{12}^e + e_{21}^e) + \mu_c^s(e_{21}^e - e_{12}^e), \tag{II.26}$$

and one non-zero component for the couple-stress tensor,

$$m_{31} = 2\beta^s \kappa_{31}. \tag{II.27}$$

The balance equations yield,

$$\sigma_{21,1} = 0, \tag{II.28}$$

$$m_{31,1} - (\sigma_{12} - \sigma_{21}) = 0. \tag{II.29}$$

The resolved shear stress is given by

$$\tau = \underset{\sim}{\boldsymbol{\sigma}} : \underset{\sim}{\boldsymbol{P}} = \sigma_{12}. \tag{II.30}$$

Combining Eqs. (II.28), (II.29), (II.30) and the yield condition (II.15), we obtain the following equation for the micro-rotation axial vector in the (s) phase

$$\phi^s_{,111} = 0. \tag{II.31}$$

The integration of Eq. (II.31) leads to a parabolic profile for ϕ^s

$$\phi^s = a^s x_1^2 + d^s, \tag{II.32}$$

where a^s and d^s are two integration constants.

The determination of the four integration constants, a^s, d^s, a^h, d^h, is done after taking interface and periodicity boundary conditions into account:

- Continuity of ϕ at $x_1 = s/2$:

$$a^s \frac{s^2}{4} + d^s = a^h \cosh\left(\omega^h \frac{h}{2}\right) + d^h. \tag{II.33}$$

- Continuity of m_{31} at $x_1 = s/2$:

$$\beta^s a^s s = -\beta^h a^h \omega^h \sinh\left(\omega^h \frac{h}{2}\right). \tag{II.34}$$

- Continuity of σ_{21} at $x_1 = s/2$ in the phase (s),

$$\sigma_{21} = m_{31,1} + \sigma_{12}, \tag{II.35}$$

  which implies that

$$\sigma_{21} = 4\beta^s a^s + \tau_c. \tag{II.36}$$

  In the phase (h), one finds that

$$\sigma_{21} = \mu^h(\bar{\gamma} + \phi + e_{21}) + \mu_c^h(\bar{\gamma} + \phi - e_{21}) = 2\mu^h(\bar{\gamma} + d^h). \tag{II.37}$$

  Combining the two previous equations, we obtain

$$4\beta^s a^s + \tau_c = 2\mu^h(\bar{\gamma} + d^h). \tag{II.38}$$

- Periodicity of u_2. We use the property $\langle e_{21}\rangle = \langle u_{,1} - \phi\rangle = -\langle\phi\rangle$.
  In the phase (h), one finds

$$e_{21} = \frac{2\mu_c^h}{\mu^h + \mu_c^h} a^h \cosh\left(\omega^h \left(x_1 - \frac{s+h}{2}\right)\right) + \bar{\gamma} + 2d^h, \tag{II.39}$$

  and in the phase (s):

$$e_{21} = e^e_{21} = \frac{\tau_c}{2\mu} + \frac{\beta^s a^s(\mu^s + \mu_c^s)}{\mu^s \mu_c^s}, \tag{II.40}$$

  which gives the following relationships between the integration constants

$$s\left(\frac{\tau_c}{2\mu} - \frac{\beta^s a^s(\mu^s + \mu_c^s)}{\mu^s \mu_c^s} + d^s\right) + a^s \frac{s^3}{12} + \frac{4\mu_c^h a^h}{\mu^h + \mu_c^h} \sinh\left(\omega^h \frac{h}{2}\right) + h(2d^h + \bar{\gamma}) = 0. \tag{II.41}$$

By solving Eqs. (II.33) to (II.41) analytically, the following expression for the constant a^s is obtained:

$$a^s = \frac{\bar{\gamma} - \dfrac{\tau_c}{2\mu^h}\left(f_s + 2(1-f_s) + f_s\dfrac{\mu^h}{\mu^s}\right)}{-\dfrac{f_s^3}{6}l^2 - \beta^s\dfrac{f_s^2}{\beta^h\omega^h}l\ \coth\left(\omega^h\dfrac{l(1-f_s)}{2}\right) - \beta^s\left(f_s\dfrac{\mu^s+\mu_c^s}{\mu^s\mu_c^s} + \dfrac{4}{\mu^h}\right)}. \tag{II.42}$$

In Eq. (II.42), f_s represents the fraction of phase (s), $f_s = s/l$. The remaining constants can be determined in terms of a^s:

$$a^h = \frac{-s\beta^s a^s}{\beta^h\omega^h\ \sinh\left(\omega^h\frac{h}{2}\right)}, \tag{II.43}$$

$$d^h = -\frac{4\beta^s a^s - \tau_c}{2\mu^h} - \bar{\gamma}, \tag{II.44}$$

$$d^s = -\frac{4\beta^s a^s - \tau_c}{2\mu^h} - \bar{\gamma} - \frac{s\beta^s a^s}{\beta^h\omega^h}\coth\left(\omega^h\frac{h}{2}\right) - a^s\frac{s^2}{4}. \tag{II.45}$$

Fig. II.2 illustrates the micro-rotation profile in the two–phase laminate for a fraction of phase (s) equal to 0.7, and for three different sets of material parameters. The first one clearly shows the continuity of the micro–rotation at the interface while the two others, introducing a stronger mismatch between the two phases, show sharper profiles at the interfaces. The set of material parameters (a) has been chosen in order to clearly show the parabolic profile in the soft phase and the hyperbolic one in the hard phase. Note that if l is changed into $l/10$, values of $\beta^{h,s}/100$ will provide the same curves.

II.2 Strain gradient plasticity: The "$curlH^p$" model

We consider now a strain gradient plasticity theory which includes the full curl of the plastic deformation tensor, $\underset{\sim}{\boldsymbol{H}}^p$. This approach, herefrom to be referred to as the "$curlH^p$" model, was proposed by Gurtin (2002) and applied to a constrained layer and a composite problem in Bittencourt *et al.* (2003). The balance and constitutive equations are first recalled and recast into the notation used throughout this work. Then the model is applied to a crystal undergoing single slip. It will be shown that a specific form of the back stress arises from this application. As it was done with the Cosserat model, the "$curlH^p$" model is finally applied to the two–phase microstructure illustrated in Fig. II.1.

II.2.1 Balance equations

Following Gurtin (2002), we consider a continuum whose power density of internal forces takes the form:

$$p^{(i)} = \underset{\sim}{\boldsymbol{\sigma}} : \dot{\underset{\sim}{\boldsymbol{H}}} + \underset{\sim}{\boldsymbol{s}} : \dot{\underset{\sim}{\boldsymbol{H}}}^p + \underset{\sim}{\boldsymbol{M}} : \operatorname{curl}\dot{\underset{\sim}{\boldsymbol{H}}}^p. \tag{II.46}$$

For objectivity reasons, the stress tensor $\underset{\sim}{\boldsymbol{\sigma}}$ is symmetric whereas the micro–stress tensor $\underset{\sim}{\boldsymbol{s}}$ and the double–stress tensor $\underset{\sim}{\boldsymbol{M}}$ are generally asymmetric. The total power of internal forces in a domain V, with boundary ∂V, is

$$\begin{aligned}
\mathcal{P}^{(i)} &= \int_V \left(\underset{\sim}{\boldsymbol{\sigma}} : \dot{\underset{\sim}{\boldsymbol{H}}} + \underset{\sim}{\boldsymbol{s}} : \dot{\underset{\sim}{\boldsymbol{H}}}^p + \underset{\sim}{\boldsymbol{M}} : \operatorname{curl}\dot{\underset{\sim}{\boldsymbol{H}}}^p\right) dV, \\
&= \int_V \left(\left(\sigma_{ij}\dot{u}_i\right)_{,j} + \left(M_{ij}\epsilon_{jkl}\dot{H}^p_{ik}\right)_{,l}\right) dV + \int_V \left(-\sigma_{ij,j}\dot{u}_i + s_{ij}\dot{H}^p_{ij} - \epsilon_{jkl}M_{ij,l}\dot{H}^p_{ik}\right) dV, \\
&= -\int_V \left(\sigma_{ij,j}\dot{u}_i - (\epsilon_{kjl}M_{ik,l} - s_{ij})\dot{H}^p_{ij}\right) dV + \int_{\partial V}\left(\sigma_{ij}n_j\dot{u}_i + \int_{\partial V}\epsilon_{jkl}M_{ij}n_l\dot{H}^p_{ik}\right) dS.
\end{aligned}$$

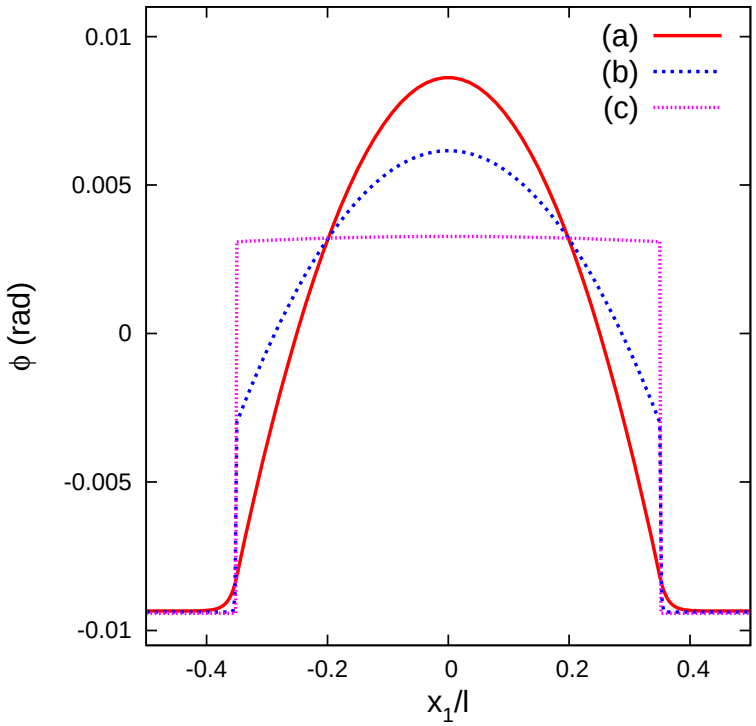

Figure II.2 : Profiles of the lattice rotation angle ϕ (radians) in the two–phase microstructure modelled by the Cosserat model: (a) with a set of material parameters giving clearly visible parabolic and hyperbolic profiles ($\mu = 35000$ MPa, $\mu_c^h = \mu_c^s = 10^6$ MPa, $\beta^h = \beta^s = 10^{-5}$ MPa mm^2 and $\tau_c = 40$ MPa), (b) with a stronger mismatch between the moduli of the two phases $\beta^h = 10^{-7}$ MPa mm^2 and $\beta^s = 10^{-5}$ MPa mm^2 and (c) $\beta^h = 10^{-11}$ MPa mm^2 and $\beta^s = 10^{-5}$ MPa mm^2, which leads to sharper interface profiles. In all three cases, $f_s = 0.7$ and the $\beta^{h,s}$ values are chosen for $l = 1$ μm.

The power density of contact forces is taken as

$$p^{(c)} = \underline{\boldsymbol{t}}.\dot{\underline{\boldsymbol{u}}} + \underset{\sim}{\boldsymbol{m}} : \dot{\underset{\sim}{\boldsymbol{H}}}^p, \tag{II.47}$$

where $\underline{\boldsymbol{t}}, \underset{\sim}{\boldsymbol{m}}$ are, respectively, the surface simple and double tractions. Volume forces are not written for simplicity. The method of virtual power can be used to derive the field equations governing the continuum, based on the virtual motions $\dot{\underline{\boldsymbol{u}}}$ and $\dot{\underset{\sim}{\boldsymbol{H}}}^p$:

$$\mathrm{div}\, \underset{\sim}{\boldsymbol{\sigma}} = 0, \quad \sigma_{ij,j} = 0, \tag{II.48}$$

$$\mathrm{curl}\, \underset{\sim}{\boldsymbol{M}} + \underset{\sim}{\boldsymbol{s}} = 0, \quad \epsilon_{jkl} M_{ik,l} + s_{ij} = 0, \tag{II.49}$$

for all regular points of the domain V. Furthermore, the following boundary conditions on ∂V can be derived:

$$\underline{\boldsymbol{t}} = \underset{\sim}{\boldsymbol{\sigma}}.\underline{\boldsymbol{n}}, \quad t_i = \sigma_{ij} n_j, \tag{II.50}$$

$$\underset{\sim}{\boldsymbol{m}} = \underset{\sim}{\boldsymbol{M}}.\underset{\approx}{\boldsymbol{\epsilon}}.\underline{\boldsymbol{n}}, \quad m_{ij} = M_{ik} \epsilon_{kjl} n_l. \tag{II.51}$$

II.2.2 Energy and entropy principles: Constitutive equations

Under isothermal conditions, the energy balance in its local form states that:

$$\rho \dot{e} = p^{(i)}, \tag{II.52}$$

where e is the internal energy density function and, ρ, the mass density. The entropy principle is formulated as

$$\rho(\dot{e} - \dot{\psi}) \geq 0 \tag{II.53}$$

where ψ is the Helmholtz free energy function. The free energy is taken as a function of the elastic strain, $\underset{\sim}{\boldsymbol{\varepsilon}}^e$, the dislocation density tensor, or curl $\underset{\sim}{\boldsymbol{H}}^p$, and a generic internal hardening variable, q, viz. $\psi(\underset{\sim}{\boldsymbol{\varepsilon}}^e, \operatorname{curl} \underset{\sim}{\boldsymbol{H}}^p, q)$. As a result, the Clausius–Duhem inequality becomes

$$\left(\underset{\sim}{\boldsymbol{\sigma}} - \rho\frac{\partial\psi}{\partial\underset{\sim}{\boldsymbol{\varepsilon}}^e}\right) : \dot{\underset{\sim}{\boldsymbol{\varepsilon}}}^e + \left(\underset{\sim}{\boldsymbol{M}} - \rho\frac{\partial\psi}{\partial\operatorname{curl}\underset{\sim}{\boldsymbol{H}}^p}\right) : \operatorname{curl}\dot{\underset{\sim}{\boldsymbol{H}}}^p + (\underset{\sim}{\boldsymbol{\sigma}} + \underset{\sim}{\boldsymbol{s}}) : \dot{\underset{\sim}{\boldsymbol{H}}}^p - \rho\frac{\partial\psi}{\partial q}\dot{q} \geq 0. \tag{II.54}$$

Here, the constitutive assumption is made that the two first terms in the previous inequality are non dissipative and therefore should vanish. Then,

$$\underset{\sim}{\boldsymbol{\sigma}} = \rho\frac{\partial\psi}{\partial\underset{\sim}{\boldsymbol{\varepsilon}}^e}, \quad \underset{\sim}{\boldsymbol{M}} = \rho\frac{\partial\psi}{\partial\operatorname{curl}\underset{\sim}{\boldsymbol{H}}^p}. \tag{II.55}$$

It follows that the residual dissipation rate is

$$D = (\underset{\sim}{\boldsymbol{\sigma}} + \underset{\sim}{\boldsymbol{s}}) : \dot{\underset{\sim}{\boldsymbol{H}}}^p - R\dot{q} \geq 0, \tag{II.56}$$

where $R = \rho\partial\psi/\partial q$ is the thermodynamic force associated with the internal variable, q. The existence of a dissipation potential, namely $\Omega(\underset{\sim}{\boldsymbol{\sigma}} + \underset{\sim}{\boldsymbol{s}}, R)$, is postulated so that

$$\dot{\underset{\sim}{\boldsymbol{H}}}^p = \frac{\partial\Omega}{\partial\left(\underset{\sim}{\boldsymbol{\sigma}} + \underset{\sim}{\boldsymbol{s}}\right)}, \quad \dot{q} = -\frac{\partial\Omega}{\partial R}. \tag{II.57}$$

II.2.3 Application of the "$curlH^p$" model to a single slip problem

For a crystal deforming under single slip conditions, the plastic deformation rate is given by:

$$\dot{\underset{\sim}{\boldsymbol{H}}}^p = \dot{\gamma}\underset{\sim}{\boldsymbol{P}} = \dot{\gamma}\underline{\boldsymbol{l}} \otimes \underline{\boldsymbol{n}}\,, \tag{II.58}$$

where $\underset{\sim}{\boldsymbol{P}} = \underline{\boldsymbol{l}} \otimes \underline{\boldsymbol{n}}$ is the orientation tensor, $\underline{\boldsymbol{l}}$ is the slip direction and $\underline{\boldsymbol{n}}$ the normal to the slip plane. The dissipation rate can then be expressed as,

$$(\tau + \underline{\boldsymbol{l}}\,.\underset{\sim}{\boldsymbol{s}}.\underline{\boldsymbol{n}})\dot{\gamma} - R\dot{q} \geq 0, \tag{II.59}$$

where $\tau = \underline{\boldsymbol{l}}\,.\underset{\sim}{\boldsymbol{\sigma}}.\underline{\boldsymbol{n}}$ is the resolved shear stress. In the absence of a hardening variable, q, for simplicity, the following generalised Schmid law can be defined (for positive $\dot{\gamma}$):

$$|\tau - x| = \tau_c, \quad \text{with} \quad x = -\underline{\boldsymbol{l}}\,.\underset{\sim}{\boldsymbol{s}}.\underline{\boldsymbol{n}}\,, \tag{II.60}$$

meaning that plastic flow occurs when the effective resolved shear stress $|\tau - x|$ reaches the critical resolved shear stress τ_c. A kinematic hardening component, x, naturally arises in the formulation for which a more specific form is given next. The curl of the plastic deformation is then given by

$$\operatorname{curl}\underset{\sim}{\boldsymbol{H}}^p = \underline{\boldsymbol{l}} \otimes (\underline{\boldsymbol{n}} \times \boldsymbol{\nabla}\gamma). \tag{II.61}$$

For a two–dimensional case, one finds

$$\left[\operatorname{curl}\underset{\sim}{\boldsymbol{H}}^p\right] = \begin{bmatrix} 0 & 0 & \gamma_{,2}n_1n_2 - \gamma_{,1}n_2^2 \\ 0 & 0 & -\gamma_{,2}n_1^2 + \gamma_{,1}n_1n_2 \\ 0 & 0 & 0 \end{bmatrix}. \tag{II.62}$$

In the particular case when $\underline{\boldsymbol{l}} = \underline{\boldsymbol{e}}_1$, $\underline{\boldsymbol{n}} = \underline{\boldsymbol{e}}_2$, the only non–vanishing component of the dislocation density tensor is

$$(\operatorname{curl} \underset{\sim}{\boldsymbol{H}}^p)_{13} = -\gamma_{,1}. \tag{II.63}$$

Let us consider at this stage the simple quadratic potential:

$$\rho\psi(\underset{\approx}{\boldsymbol{\varepsilon}}^e, \operatorname{curl} \underset{\sim}{\boldsymbol{H}}^p) = \frac{1}{2}\underset{\approx}{\boldsymbol{\varepsilon}}^e : \underset{\approx}{\boldsymbol{\Lambda}} : \underset{\approx}{\boldsymbol{\varepsilon}}^e + \frac{1}{2} A \left(\operatorname{curl} \underset{\sim}{\boldsymbol{H}}^p\right) : \left(\operatorname{curl} \underset{\sim}{\boldsymbol{H}}^p\right), \tag{II.64}$$

so that

$$\underset{\sim}{\boldsymbol{\sigma}} = \underset{\approx}{\boldsymbol{\Lambda}} : \underset{\approx}{\boldsymbol{\varepsilon}}^e, \quad \underset{\sim}{\boldsymbol{M}} = A \operatorname{curl} \underset{\sim}{\boldsymbol{H}}^p, \tag{II.65}$$

where $\underset{\approx}{\boldsymbol{\Lambda}}$ is the four–rank tensor of the elastic moduli, assumed isotropic hereafter, and A is a higher order modulus. According to the balance equation (II.49), it follows that

$$\underset{\approx}{\boldsymbol{s}} = -\operatorname{curl} \underset{\sim}{\boldsymbol{M}} = -\operatorname{curl}\operatorname{curl} \underset{\sim}{\boldsymbol{H}}^p. \tag{II.66}$$

For single slip, the double curl of plastic deformation is defined as

$$\operatorname{curl}\operatorname{curl} \underset{\sim}{\boldsymbol{H}}^p = \underline{\boldsymbol{l}} \otimes ((\underline{\boldsymbol{n}} \times \gamma_{,ij} \underline{\boldsymbol{e}}_i) \times \underline{\boldsymbol{e}}_j). \tag{II.67}$$

In the particular case of $\underline{\boldsymbol{l}} = \underline{\boldsymbol{e}}_1$, $\underline{\boldsymbol{n}} = \underline{\boldsymbol{e}}_2$, we obtain

$$\operatorname{curl}\operatorname{curl} \underset{\sim}{\boldsymbol{H}}^p = \gamma_{,12} \underline{\boldsymbol{e}}_1 \otimes \underline{\boldsymbol{e}}_1 - \gamma_{,11} \underline{\boldsymbol{e}}_1 \otimes \underline{\boldsymbol{e}}_2, \tag{II.68}$$

so that the back stress takes the form

$$x = A(\operatorname{curl}\operatorname{curl} \underset{\sim}{\boldsymbol{H}}^p) : (\underline{\boldsymbol{l}} \otimes \underline{\boldsymbol{n}}) = -A\gamma_{,11}. \tag{II.69}$$

II.2.4 Application to a two–phase periodic microstructure under simple shear

We consider the same two–phase periodic microstructure under simple shear illustrated in Fig. II.1. When the previously described "*curl*H^p" continuum plasticity theory is applied to the laminate problem shown in Section II.1.2, the main unknowns are the component of displacement, u_2, and the H^p_{12} component of plastic deformation:

$$u_1 = \bar{\gamma} x_2, \quad u_2(x_1) = u(x_1), \quad u_3 = 0, \quad H^p_{12}(x_1). \tag{II.70}$$

Recalling,

$$\underset{\sim}{\boldsymbol{H}}^p = \gamma \underline{\boldsymbol{l}} \otimes \underline{\boldsymbol{n}} = \gamma \underline{\boldsymbol{e}}_1 \otimes \underline{\boldsymbol{e}}_2, \tag{II.71}$$

we obtain

$$\left[\underset{\sim}{\boldsymbol{H}}\right] = \begin{bmatrix} 0 & \bar{\gamma} & 0 \\ u_{,1} & 0 & 0 \\ 0 & 0 & 0 \end{bmatrix}, \quad \left[\underset{\sim}{\boldsymbol{H}}^p\right] = \begin{bmatrix} 0 & \gamma & 0 \\ 0 & 0 & 0 \\ 0 & 0 & 0 \end{bmatrix}, \quad \left[\underset{\sim}{\boldsymbol{H}}^e\right] = \begin{bmatrix} 0 & \bar{\gamma} - \gamma & 0 \\ u_{,1} & 0 & 0 \\ 0 & 0 & 0 \end{bmatrix} \tag{II.72}$$

$$\left[\operatorname{curl} \underset{\sim}{\boldsymbol{H}}^p\right] = \begin{bmatrix} 0 & 0 & -\gamma_{,1} \\ 0 & 0 & 0 \\ 0 & 0 & 0 \end{bmatrix}. \tag{II.73}$$

The resulting stress tensors are

$$\left[\underset{\sim}{\boldsymbol{\sigma}}\right] = \mu \begin{bmatrix} 0 & \bar{\gamma} - \gamma + u_{,1} & 0 \\ \bar{\gamma} - \gamma + u_{,1} & 0 & 0 \\ 0 & 0 & 0 \end{bmatrix}, \quad \left[\underset{\sim}{\boldsymbol{M}}\right] = A \begin{bmatrix} 0 & 0 & -\gamma_{,1} \\ 0 & 0 & 0 \\ 0 & 0 & 0 \end{bmatrix}, \tag{II.74}$$

$$\left[\operatorname{curl} \underset{\sim}{\boldsymbol{M}}\right] = A \begin{bmatrix} 0 & -\gamma_{,11} & 0 \\ 0 & 0 & 0 \\ 0 & 0 & 0 \end{bmatrix}. \tag{II.75}$$

The balance equations (II.48) and (II.49) imply that:

$$\sigma_{12,1} = 0 \quad \Longrightarrow \quad -\gamma_{,1} + u_{,11} = 0, \tag{II.76}$$

and

$$s_{12} = -(\operatorname{curl} \underset{\sim}{\boldsymbol{M}})_{12} \quad \Longrightarrow \quad s_{12} = A\gamma_{,11}. \tag{II.77}$$

Thus, the shear stress component, σ_{12}, is constant. For this particular case, Schmid law is written as

$$\tau - x = \sigma_{12} - x = \tau_c, \tag{II.78}$$

with

$$x = A(\operatorname{curl}\operatorname{curl} \underset{\sim}{\boldsymbol{H}}^p)_{12} = -A\gamma_{,11}. \tag{II.79}$$

As the shear stress σ_{12} is constant, so is the corresponding back stress,

$$x_{,1} = \gamma_{,111} = 0. \tag{II.80}$$

The slip profile is therefore parabolic in the plastic phase. In the elastic zone, all the variables, $H^p_{12}, M_{13}, \gamma, x$, vanish.

We now enforce continuity requirements at the interface between both phases for the plastic slip, in addition to the continuity of displacement and simple traction vector. The continuity condition of plastic slip at $x_1 = \pm s/2$ is

$$H^p_{12} = \gamma = 0. \tag{II.81}$$

The condition of continuity of the double traction tensor, (II.51), at the interface needs to be considered next. Here,

$$m_{12} = M_{13}\epsilon_{321}n_1 = -M_{13} = A\gamma_{,1}, \tag{II.82}$$

which implies the continuity of the double stress component, M_{13}. In the elastic phase, the couple stress component M_{13} is not defined since no plastic deformation takes place. If we impose the condition that $M_{13} = m_{12} = 0$ at the interface, it will imply that the first derivative, $\gamma_{,1}$, also vanishes. This latter condition requires that the full parabolic function γ should also vanish, so that no plastic strain could develop in the plastic zone. In fact, according to such a plastic strain gradient model, higher order stresses exhibit a jump at the interface between an elastic and a plastic phase. This discontinuity of the generalised traction prompts us to introduce, in the next section, a regularised model which is closely related to the "*curl*H^p" model but which offers a complete solution to the elastic/plastic laminate boundary value problem. On the other hand, it must be noted that a complete solution can be worked out with the "*curl*H^p" model when both phases are elasto–plastic without any indeterminacy (see Appendix A.2). The regularised model presented next will give us a way to find a valid interface condition and to derive the jump condition for generalised tractions (see Appendix A.3).

II.3 Formulation of the *microcurl* model

An alternative model will now be proposed in order to circumvent the discontinuity of the generalised traction observed in the boundary value problem of interest, thus representing a regularisation of the "*curl*H^p" model. This model, called here *microcurl*, is based on a

micromorphic approach that falls in the class of generalised continuum models presented in Forest (2009). The theory is first described in terms of the balance and constitutive equations. An internal constraint controlling the plastic micro–deformation is then introduced. Finally an application of the model to the two–phase laminate problem of Fig. II.1 is presented. Finally, it will be shown that the "*curl*H^p" model can be obtained as a special limiting case of the *microcurl* formulation proposed here. A finite deformation extension of this model is given in Appendix A.5.

II.3.1 Balance equations

We introduce a plastic micro–deformation variable, $\underset{\sim}{\boldsymbol{\chi}}^p$, as a second–rank generally non–symmetric tensor. It is distinct from the plastic deformation $\underset{\sim}{\boldsymbol{H}}^p$ which is still treated as an internal variable. Then the degrees of freedom of the theory are:

$$DOF = \{\underline{\boldsymbol{u}}\,, \underset{\sim}{\boldsymbol{\chi}}^p\} \tag{II.83}$$

The components of $\underset{\sim}{\boldsymbol{\chi}}^p$ are introduced as independent degrees of freedom. In the three–dimensional case, there are nine such components and the micro-deformation field is generally incompatible. We assume that only the curl part of the gradient of plastic micro–deformation plays a role in the power of internal forces. Then, in the same way as in Eq. (II.46), we assume that

$$p^{(i)} = \underset{\sim}{\boldsymbol{\sigma}} : \dot{\underset{\sim}{\boldsymbol{H}}} + \underset{\sim}{\boldsymbol{s}} : \dot{\underset{\sim}{\boldsymbol{\chi}}}^p + \underset{\sim}{\boldsymbol{M}} : \operatorname{curl} \dot{\underset{\sim}{\boldsymbol{\chi}}}^p. \tag{II.84}$$

The total power of internal forces over the domain V is then given by

$$\begin{aligned} -\mathcal{P}^{(i)} &= \int_V p^{(i)}\, dV = \int_V \left(\underset{\sim}{\boldsymbol{\sigma}} : \dot{\underset{\sim}{\boldsymbol{H}}} + \underset{\sim}{\boldsymbol{s}} : \dot{\underset{\sim}{\boldsymbol{\chi}}}^p + \underset{\sim}{\boldsymbol{M}} : \operatorname{curl} \dot{\underset{\sim}{\boldsymbol{\chi}}}^p \right) dV, \\ &= \int_V \left((\sigma_{ij}\dot{u}_i)_{,j} + \left(M_{ij}\epsilon_{jkl}\dot{\chi}^p_{ik}\right)_{,l} \right) dV + \int_V \left(-\sigma_{ij,j}\dot{u}_i + s_{ij}\dot{\chi}^p_{ij} - \epsilon_{jkl}M_{ij,l}\dot{\chi}^p_{ik} \right) dV, \\ &= -\int_V \sigma_{ij,j}\dot{u}_i\, dV - \int_V \left(\epsilon_{kjl}M_{ik,l} - s_{ij}\right) \dot{\chi}^p_{ij}\, dV + \int_{\partial V} \sigma_{ij}n_j\dot{u}_i\, dS + \int_{\partial V} \epsilon_{jkl}M_{ij}n_l\dot{\chi}^p_{ik}\, dS. \end{aligned}$$

The method of virtual power is used to derive the generalised balance of momentum equations. Assuming no volume forces for simplicity, one finds

$$\operatorname{div} \underset{\sim}{\boldsymbol{\sigma}} = 0, \quad \operatorname{curl} \underset{\sim}{\boldsymbol{M}} + \underset{\sim}{\boldsymbol{s}} = 0. \tag{II.85}$$

The corresponding boundary conditions are,

$$\underline{\boldsymbol{t}} = \underset{\sim}{\boldsymbol{\sigma}}.\underline{\boldsymbol{n}}\,, \quad \underset{\sim}{\boldsymbol{m}} = \underset{\sim}{\boldsymbol{M}}.\underset{\sim}{\boldsymbol{\epsilon}}.\underline{\boldsymbol{n}}\,, \tag{II.86}$$

where $\underline{\boldsymbol{t}}$ and $\underset{\sim}{\boldsymbol{m}}$ are the simple and double tractions at the boundary.

II.3.2 Constitutive equations

The free energy function is assumed to have the following arguments:

$$\psi\left(\underset{\sim}{\boldsymbol{\varepsilon}}^e, \quad \underset{\sim}{\boldsymbol{e}}^p := \underset{\sim}{\boldsymbol{H}}^p - \underset{\sim}{\boldsymbol{\chi}}^p, \quad \underset{\sim}{\boldsymbol{\Gamma}}_\chi := \operatorname{curl} \underset{\sim}{\boldsymbol{\chi}}^p\right) \tag{II.87}$$

where $\underset{\sim}{\boldsymbol{e}}^p$ is the relative plastic strain measuring the difference between plastic deformation and the plastic microvariable.

The reduced entropy inequality reads:

$$\left(\underset{\sim}{\boldsymbol{\sigma}} - \rho\frac{\partial\psi}{\partial\underset{\sim}{\boldsymbol{\varepsilon}}^e}\right) : \dot{\underset{\sim}{\boldsymbol{\varepsilon}}}^e - \left(\underset{\sim}{\boldsymbol{s}} + \rho\frac{\partial\psi}{\partial\underset{\sim}{\boldsymbol{e}}^p}\right) : \dot{\underset{\sim}{\boldsymbol{e}}}^p + \left(\underset{\sim}{\boldsymbol{M}} - \rho\frac{\partial\psi}{\partial\underset{\sim}{\boldsymbol{\Gamma}}_\chi}\right) : \dot{\underset{\sim}{\boldsymbol{\Gamma}}}_\chi + \left(\underset{\sim}{\boldsymbol{\sigma}} + \underset{\sim}{\boldsymbol{s}}\right) : \dot{\underset{\sim}{\boldsymbol{H}}}^p \geq 0. \tag{II.88}$$

Furthermore, the following state laws are adopted:

$$\underset{\sim}{\boldsymbol{\sigma}} = \rho\frac{\partial\psi}{\partial\underset{\sim}{\boldsymbol{\varepsilon}}^e}, \quad \underset{\sim}{\boldsymbol{s}} = -\rho\frac{\partial\psi}{\partial\underset{\sim}{\boldsymbol{e}}^p}, \quad \underset{\sim}{\boldsymbol{M}} = \rho\frac{\partial\psi}{\partial\underset{\sim}{\boldsymbol{\Gamma}}_\chi}, \tag{II.89}$$

so that the residual intrinsic dissipation rate is defined as,

$$D = (\underset{\sim}{\boldsymbol{\sigma}} + \underset{\sim}{\boldsymbol{s}}) : \dot{\underset{\sim}{\boldsymbol{H}}}^p \geq 0. \tag{II.90}$$

Assuming a quadratic potential in Eq. (II.89), the following linear relationships are obtained:

$$\underset{\sim}{\boldsymbol{\sigma}} = \underset{\approx}{\boldsymbol{\Lambda}} : \underset{\sim}{\boldsymbol{\varepsilon}}^e, \quad \underset{\sim}{\boldsymbol{s}} = -H_\chi\underset{\sim}{\boldsymbol{e}}^p, \quad \underset{\sim}{\boldsymbol{M}} = A\underset{\sim}{\boldsymbol{\Gamma}}_\chi, \tag{II.91}$$

where H_χ and A are the generalised moduli. The size effects exhibited by the solutions of boundary value problems involving such a model are related to an intrinsic length scale, typically defined as

$$l_\omega = \sqrt{\frac{A}{H_\chi}}. \tag{II.92}$$

The flow rule can be derived from a viscoplastic potential, $\Omega(\underset{\sim}{\boldsymbol{\sigma}} + \underset{\sim}{\boldsymbol{s}})$, expressed in terms of the effective stress, $(\underset{\sim}{\boldsymbol{\sigma}} + \underset{\sim}{\boldsymbol{s}})$, that intervenes in the dissipation rate, see Eq. (II.90). Then,

$$\dot{\underset{\sim}{\boldsymbol{H}}}^p = \frac{\partial\Omega}{\partial(\underset{\sim}{\boldsymbol{\sigma}} + \underset{\sim}{\boldsymbol{s}})} \tag{II.93}$$

For a crystal undergoing single slip, Eq. (II.58) is still valid. The dissipation takes the form:

$$D = (\tau + \underset{\sim}{\boldsymbol{s}} : (\underline{\boldsymbol{l}} \otimes \underline{\boldsymbol{n}}))\dot{\gamma} \geq 0 \tag{II.94}$$

The generalised Schmid criterion then becomes

$$|\tau + \underset{\sim}{\boldsymbol{s}} : (\underline{\boldsymbol{l}} \otimes \underline{\boldsymbol{n}})| = \tau_c \tag{II.95}$$

where τ_c is the critical resolved shear stress. Accordingly, a back stress component naturally arises in the yield function $f(\tau, \underset{\sim}{\boldsymbol{s}}) = |\tau + \underset{\sim}{\boldsymbol{s}} : (\underline{\boldsymbol{l}} \otimes \underline{\boldsymbol{n}})| - \tau_c$, in the same way as in the Cosserat and "*curl* H^p" models. Closely related back stresses are presented in Kuroda and Tvergaard (2006, 2008a,b), and in Evers *et al.* (2004a,b); Bayley *et al.* (2006, 2007); Erturk *et al.* (2009) where explicit expressions are given.

II.3.3 Internal constraint

The modulus H_χ in Eq. (II.91) introduces a coupling between the macro and micro–variables. It could also be interpreted as a penalty factor that constrains the relative plastic deformation $\underset{\sim}{\boldsymbol{e}}^p$ to remain sufficiently small. Equivalently, a high value of the coupling modulus, H_χ, forces the plastic micro–deformation to be as close as possible to the macroscopic plastic deformation, $\underset{\sim}{\boldsymbol{H}}^p$. In the limit, the use of a Lagrange multiplier instead of the penalty factor, H_χ, is necessary to enforce the internal constraint that

$$\underset{\sim}{\boldsymbol{\chi}}^p \equiv \underset{\sim}{\boldsymbol{H}}^p \tag{II.96}$$

In that case, the power of the internal forces, Eq. (II.84), coincides with that defined in Eq. (II.46). As a result, the *microcurl* model degenerates into the curl $\underset{\sim}{\boldsymbol{H}}^p$ theory described in Section II.2. In Eringen's and Mindlin's micromorphic theory, the microdeformation can be constrained to be as close as possible to the macrodeformation, represented by the usual

deformation gradient tensor. Then, the micromorphic model reduces to Mindlin's second gradient theory. We adopt here a similar constraint such that the *microcurl* model degenerates into Gurtin's strain gradient plasticity model. The curl of microdeformation, $\underset{\sim}{\boldsymbol{\Gamma}}_{\chi}$ coincides with the dislocation density tensor only when this constraint is enforced. This suggests that, in the general unconstrained case, the microdeformation $\underset{\sim}{\boldsymbol{\chi}}^p$ should not depart too much from the plastic deformation for the $\underset{\sim}{\boldsymbol{\Gamma}}_{\chi}$ measure to still have the physical meaning of a quantity close to the dislocation density tensor. The departure of the microdeformation from the plastic deformation introduces a new constitutive ingredient in the model that remains however of a purely phenomenological nature. This constitutive law, embodied by the additional parameter H_χ, is shown in what follows to lead to more general scaling laws than the original strain gradient plasticity model.

The micromorphic model can also be seen as a regularisation of the curl $\underset{\sim}{\boldsymbol{H}}^p$ theory which displays some indeterminacy at the interface between the elastic and the elasto–plastic zones. Another way of solving the indeterminacy problem is to track the limit of the elastic domain and to enforce an *a priori* condition of vanishing double traction (Liebe *et al.*, 2003) on this surface. However, with such conditions, it has been shown that the laminate boundary value problem of interest does not admit any non trivial solution.

II.3.4 Application to a two–phase periodic microstructure under simple shear

Contrary to the curl $\underset{\sim}{\boldsymbol{H}}^p$ theory, plastic micro–deformation can develop even in the absence of macroscopic plastic strain. In particular, double stresses that may arise in a plastic phase can be transmitted to an elastic phase through the interface.

Let us consider again the two–phase microstructure under simple shear of Section II.2 and apply the *microcurl* model to that problem. We consider a slip system whose slip direction is along the axis 1, i.e., the shear direction in Fig. II.1. The unknowns of the problem are one component of the displacement vector and two components of the plastic micro–deformation tensor, namely,

$$u_1 = \bar{\gamma} x_2, \quad u_2(x_1), \quad u_3 = 0, \quad \chi^p_{12}(x_1), \quad \chi^p_{21}(x_1), \tag{II.97}$$

$$\left[\underset{\sim}{\boldsymbol{H}}\right] = \begin{bmatrix} 0 & \bar{\gamma} & 0 \\ u_{,1} & 0 & 0 \\ 0 & 0 & 0 \end{bmatrix}, \quad \left[\underset{\sim}{\boldsymbol{H}}^p\right] = \begin{bmatrix} 0 & \gamma & 0 \\ 0 & 0 & 0 \\ 0 & 0 & 0 \end{bmatrix}, \quad \left[\underset{\sim}{\boldsymbol{H}}^e\right] = \begin{bmatrix} 0 & \bar{\gamma}-\gamma & 0 \\ u_{2,1} & 0 & 0 \\ 0 & 0 & 0 \end{bmatrix}, \tag{II.98}$$

$$\left[\underset{\sim}{\boldsymbol{\chi}}^p\right] = \begin{bmatrix} 0 & \chi^p_{12}(x_1) & 0 \\ \chi^p_{21}(x_1) & 0 & 0 \\ 0 & 0 & 0 \end{bmatrix}, \quad \left[\operatorname{curl} \underset{\sim}{\boldsymbol{\chi}}^p\right] = \begin{bmatrix} 0 & 0 & -\chi^p_{12,1} \\ 0 & 0 & 0 \\ 0 & 0 & 0 \end{bmatrix}. \tag{II.99}$$

The resulting stress tensors are

$$\left[\underset{\sim}{\boldsymbol{\sigma}}\right] = \mu \begin{bmatrix} 0 & \bar{\gamma}-\gamma+u_{2,1} & 0 \\ \bar{\gamma}-\gamma+u_{2,1} & 0 & 0 \\ 0 & 0 & 0 \end{bmatrix}, \quad \left[\underset{\sim}{\boldsymbol{s}}\right] = -H_\chi \begin{bmatrix} 0 & \gamma-\chi^p_{12} & 0 \\ -\chi^p_{21} & 0 & 0 \\ 0 & 0 & 0 \end{bmatrix}, \tag{II.100}$$

$$\left[\underset{\sim}{\boldsymbol{M}}\right] = \begin{bmatrix} 0 & 0 & -A\chi^p_{12,1} \\ 0 & 0 & 0 \\ 0 & 0 & 0 \end{bmatrix}, \quad \left[\operatorname{curl} \underset{\sim}{\boldsymbol{M}}\right] = \begin{bmatrix} 0 & -A\chi^p_{12,11} & 0 \\ 0 & 0 & 0 \\ 0 & 0 & 0 \end{bmatrix}. \tag{II.101}$$

The balance equation, $\underset{\sim}{\boldsymbol{s}} = -\mathrm{curl}\,\underset{\sim}{\boldsymbol{M}}$, gives:

$$\chi^p_{21} = 0, \quad H_\chi(\gamma - \chi^p_{12}) = -A\chi^p_{12,11}. \tag{II.102}$$

Furthermore, the plasticity criterion stipulates that

$$\sigma_{12} + s_{12} = \sigma_{12} + A\chi^p_{12,11} = \tau_c. \tag{II.103}$$

The force stress balance equation requires that σ_{12} be constant. It follows that

$$\chi^p_{12,111} = 0, \tag{II.104}$$

and the plastic micro–deformation profile in the soft phase is therefore parabolic:

$$\chi^{ps}_{12} = a^s x_1^2 + c, \tag{II.105}$$

where symmetry conditions have already been taken into account ($\chi^{ps}_{12}(-s/2) = \chi^{ps}_{12}(s/2)$), and a^s and c are constants to be determined. The plastic slip can be computed from Eq. (II.102). In the elastic domain, the balance equation (II.102) is still valid with vanishing plastic slip so that the profile of plastic micro–deformation is hyperbolic:

$$\chi^{ph}_{12} = a^h \cosh\left(\omega^h\left(x_1 - \frac{s+h}{2}\right)\right), \quad \text{with} \quad \omega^h = \sqrt{\frac{H^h_\chi}{A^h}}, \tag{II.106}$$

for $s/2 \le |x_1| \le (s+h)/2$. Note that symmetry conditions have already been taken into account ($\chi^{ph}_{12}(s/2) = \chi^{ph}_{12}(s/2+h)$). The identification of the coefficients, a^h, a^s, c, is possible by means of the following interface and periodicity conditions:

- Continuity of χ^p_{12} at $x_1 = s/2$:

$$a^s\left(\frac{s}{2}\right)^2 + c = a^h \cosh\frac{\omega^h h}{2}. \tag{II.107}$$

  The periodicity condition for χ^p_{12} at $x_1 = -s/2$ and $x_1 = s/2 + h$ leads to the same equation.

- Continuity of the double traction $m_{12} = -M_{13}$ at $x_1 = s/2$, according to Eq. (II.86):

$$M^h_{13} = -A^h\chi^{ph}_{12,1} = -a^h A^h \omega^h \sinh\left(x_1 - \frac{s+h}{2}\right) \;=\; M^s_{13} = -A^s\chi^{ps}_{12,1} = -2a^s A^s x_1. \tag{II.108}$$

  so that,

$$2A^s a^s \frac{s}{2} = -A^h a^h \omega^h \sinh\frac{\omega^h h}{2}. \tag{II.109}$$

  Likewise, the periodicity condition for M_{13} at $x_1 = -s/2$ and $x_1 = (s/2 + h)$ leads to the same equation as above.

- The plasticity condition in the soft phase provides the value of the constant stress component:

$$\sigma_{12} = \tau_c - 2A^s a^s. \tag{II.110}$$

- Consequence of the periodicity of the displacement component u_2. We start from

$$\sigma_{12} = \mu(\bar{\gamma} - \gamma + u_{2,1}) \Longrightarrow u^s_{2,1} = \frac{\sigma_{12}}{\mu} + \gamma - \bar{\gamma}, \tag{II.111}$$

so that,

$$u^s_{2,1} = \frac{\sigma_{12}}{\mu} - \bar{\gamma} + a^s x_1^2 + c - \frac{2A^s a^s}{H^s_\chi} \tag{II.112}$$

in the plastic phase. In contrast, in the elastic phase, we have:

$$u^h_{2,1} = \frac{\sigma_{12}}{\mu} - \bar{\gamma}. \tag{II.113}$$

We compute the average:

$$\int_{-s/2}^{s/2+h} u_{2,1}\, dx_1 = 0, \tag{II.114}$$

which vanishes for periodicity reasons and gives:

$$\left(\frac{\sigma_{12}}{\mu} - \bar{\gamma}\right)(s+h) + \left(c - \frac{2A^s a^s}{H^s_\chi}\right) s + \frac{2}{3} a^s \left(\frac{s}{2}\right)^3 = 0 \tag{II.115}$$

The solutions of Eqs. (II.107) to (II.115) are

$$a^s = (s+h)\left(\bar{\gamma} - \frac{\tau_c}{\mu}\right)\left(-\frac{2A^s}{\mu}(s+h) - \left(\left(\frac{s}{2}\right)^2 + \frac{sA^s}{\omega^h A^h}\coth\frac{\omega^h h}{2}\right) s - \frac{2A^s s}{H^s_\chi} + \frac{2}{3}\left(\frac{s}{2}\right)^3\right)^{-1}, \tag{II.116}$$

$$a^h = -\frac{1}{\sinh\frac{\omega^h h}{2}}\,\frac{sA^s}{\omega^h A^h} a^s, \tag{II.117}$$

$$c = -\left(\left(\frac{s}{2}\right)^2 + \frac{sA^s}{\omega^h A^h}\coth\frac{\omega^h h}{2}\right) a^s. \tag{II.118}$$

The corresponding profiles of plastic micro–deformation are illustrated in Fig. II.3 for three different sets of material parameters. The first parameters are chosen to clearly visualize the parabolic profile in the soft phase and the hyperbolic profiles in the elastic phase. When $A^s = A^h$, the slope of the plastic micro–deformation is continuous at the interface, as can be seen in Fig. II.3(a). The two other sets of material parameters introduce a stronger mismatch between the moduli A^h and A^s. Accordingly, the micro-variable χ^p decreases rapidly in the elastic phase, while it is still continuous at the interface. The profile of Fig. II.3(c) is almost flat. In all cases, the coupling modulus has been taken high enough so as the plastic micro–deformation almost coincides with the plastic slip in the soft phase.

II.4 Overall size effects modelled by the Cosserat, *microcurl* and "$curlH^p$" models

Based on the non–homogeneous distribution of mechanical variables in a two–phase laminate undergoing simple shear as determined for the Cosserat and the *microcurl* models, see Sections II.1.2 and II.3.4, we now study more specifically the macroscopic response of the laminate and the macroscopic size effects given by the two models. Due to the similarity of the models, their responses are analysed in parallel. Differences however exist and will be pointed out. This section is organised as follows. First, the macroscopic stress strain curve is calculated for the laminate material. The overall hardening moduli are also determined. The second subsection analyses the modelled size effects. For simplicity, we assume here that the shear moduli of the two phases are equal: $\mu_s = \mu_h = \mu$.

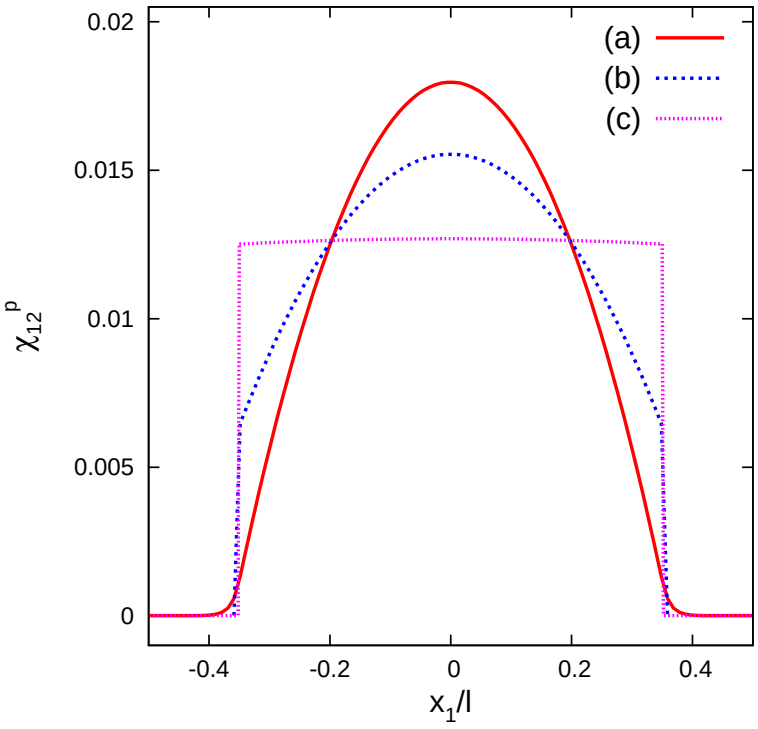

Figure II.3 : Profiles of plastic micro–deformation χ_{12}^p in the two–phase microstructure with the *microcurl* model: (a) obtained with a set of material parameters to visualize the smooth transition at the elasto–plastic interface ($\mu = 35000$ MPa, $H_\chi^h = H_\chi^s = 133829$ MPa, $A^h = A^s = 2.10^{-5}$ MPa mm^2 and $\tau_c = 40$ MPa); (b) with a stronger mismatch between the moduli of the two phases $A^h = 2.10^{-7}$ MPa mm^2 and $A^s = 2.10^{-5}$ MPa and (c) $A^h = 2.10^{-11}$ MPa mm^2 and $A^s = 2.10^{-5}$ MPa mm^2, which leads to sharper profiles at the interfaces. In all three cases, $f_s = 0.7$ and the $A^{h,s}$ values are chosen for $l = 1$ μm.

II.4.1 Predicted macroscopic stress-strain response and kinematic hardening modulus

When deriving the overall properties of a periodic generalised medium, the development of specific homogenisation tools are required. Such methods were developed for heterogeneous strain gradient and Cosserat media in Smyshlyaev and Fleck (1996) and Forest *et al.* (2001), respectively. The effective material is regarded here as a classical Cauchy material endowed with effective elasto–plastic properties. We derive the expression of the macroscopic Cauchy stress tensor component, Σ_{12}, defined as the mean value of the stress component σ_{12} over the unit cell of size $l = (s + h)$:

$$\Sigma_{12} =< \sigma_{12} >= \frac{1}{l} \int_{-\frac{l}{2}}^{\frac{l}{2}} \sigma_{12} dx_1. \tag{II.119}$$

Note that for the Cosserat model, the local stress tensor is non symmetric, even though for the simple shear boundary value problem considered here, we find that the average stress component $\langle \sigma_{12} \rangle = \langle \sigma_{21} \rangle = \Sigma_{12}$. Expressions for the local stress σ_{12} were derived in Sections II.1.2 and II.3.4, in terms of the coefficients (a^s, d^s, a^h, d^h). The following form can be

adopted for the coefficient, a^s, which is valid for both the Cosserat and the *microcurl* models,

$$a^s = \frac{\mathcal{A}}{\mathcal{B}l^2 + \mathcal{C}l \ \coth\left(\omega^h \frac{l(1-f_s)}{2}\right) + \mathcal{D}}, \tag{II.120}$$

Table II.1 gives the values of $\mathcal{A}$, $\mathcal{B}$, $\mathcal{C}$, $\mathcal{D}$ introduced in Eq. (II.120) for both models. An equivalence can be found between Cosserat and *microcurl* material parameters, which is valid for the boundary value problem of interest here,

$$A \equiv 2\beta, \tag{II.121}$$

$$H_\chi \equiv 4\frac{\mu\mu_c}{\mu+\mu_c}. \tag{II.122}$$

However, identification of μ_c for a given value of H_χ is not always possible due to the non linear relation, Eq. (II.122), that allows only values of H_χ smaller than

$$\lim_{\mu_c\to\infty} 4\frac{\mu\mu_c}{\mu+\mu_c} = 4\mu \tag{II.123}$$

Next, results are presented for the *microcurl* model. The corresponding expressions for the Cosserat model can be obtained using the previous equivalence relations. The macroscopic stress component, Σ_{12}, can be obtained knowing the applied shear strain, $\overline{\gamma}$, and mean plastic slip, $<\gamma>$. Recalling Eq. (II.110),

$$\Sigma_{12} = \frac{1}{l}\int_{-l/2}^{l/2} \sigma_{12} dx_1 = \tau_c - 2A^s a^s = \mu\left(\overline{\gamma} - \frac{\langle\gamma\rangle}{f_s}\right), \tag{II.124}$$

The mean plastic slip is determined from Eq. (II.102) as follows,

$$\begin{aligned}
\langle\gamma\rangle &= \left\langle \chi^p_{12} - \frac{A^s}{H^s_\chi}\chi^p_{12,11}\right\rangle \\
&= \frac{1}{l}\int_{-s/2}^{s/2}\left(a^s\left(x_1^2 - \frac{2A^s}{H^s_\chi}\right) + c\right)dx_1 \\
&= \frac{1}{l}\left(a^s\frac{s^3}{12} + s\left(c - \frac{2A^s a^s}{H^s_\chi}\right)\right).
\end{aligned} \tag{II.125}$$

Accordingly, an alternative expression of a^s as a function of mean plastic strain is obtained

$$a^s = \frac{\mathcal{A}'}{\mathcal{B}'l^2 + \mathcal{C}'l\coth\left(\omega^h\frac{l(1-f_s)}{2}\right) + \mathcal{D}'}, \tag{II.126}$$

where coefficients $\mathcal{A}'$, $\mathcal{B}'$, $\mathcal{C}'$, $\mathcal{D}'$ are given in Table II.2 for both the *microcurl* and Cosserat models.

for a microstructural length scale of size $l = s+h = 10^{-3}$ mm, and the material parameters from Table II.3, is shown in Fig. II.4. To obtain the curves of Fig. II.4, the laminate microstructure of Fig. II.1 has been subjected to cyclic shear loading, controlled by the mean shear deformation $\bar{\gamma}$. The average stress component Σ_{12} has been then computed. The modelled response clearly exhibits pure linear kinematic hardening, in contrast to that obtained with the perfectly plastic classical crystal plasticity model that does not incorporate the higher order back stress component. Such kinematic hardening components are usually introduced directly into the constitutive equations of classical crystal plasticity, as done in Busso *et al.* (2000). The expression for the kinematic hardening modulus H can be obtained

Table II.1 : Coefficients needed to determine the integration constant a^s from Eq. (II.120), as a function of the applied shear strain $\overline{\gamma}$ for both the Cosserat and *microcurl* models.

Model		Cosserat	*microcurl*
$a^s(\overline{\gamma})$	$\mathcal{A}$	$\frac{\tau_c}{\mu} - \overline{\gamma}$	$\frac{\tau_c}{\mu} - \overline{\gamma}$
	$\mathcal{B}$	$\frac{f_s^3}{6}$	$\frac{f_s^3}{6}$
	$\mathcal{C}$	$\frac{f_s^2 \beta^s}{\beta^h \omega^h}$	$\frac{f_s^2 A^s}{A^h \omega^h}$
	$\mathcal{D}$	$\beta^s \left(f_s \frac{\mu + \mu_c}{\mu \mu_c} + \frac{4}{\mu} \right)$	$A^s \left(\frac{2 f_s}{H_\chi^s} + \frac{2}{\mu} \right)$

Table II.2 : Coefficients needed to determine the integration constant a^s from Eq. (II.126), as a function of the mean plastic deformation, $< \gamma >$, for both the Cosserat and *microcurl* models.

Model		Cosserat	*microcurl*
$a^s(\langle\gamma\rangle)$	$\mathcal{A}'$	$-\langle\gamma\rangle$	$-\langle\gamma\rangle$
	$\mathcal{B}'$	$\frac{f_s^3}{6}$	$\frac{f_s^3}{6}$
	$\mathcal{C}'$	$\frac{f_s^2 \beta^s}{\beta^h \omega^h}$	$\frac{f_s^2 A^s}{A^h \omega^h}$
	$\mathcal{D}'$	$f_s \beta^s \frac{\mu + \mu_c}{\mu \mu_c}$	$\frac{2 f_s A^s}{H_\chi^s}$

using Eqs. (II.124) and (II.126):

$$H = \frac{2A^s}{\mathcal{B}' l^2 + \mathcal{C}' l \ \coth\left(\omega^h \frac{l(1-f_s)}{2}\right) + \mathcal{D}'}. \tag{II.127}$$

This expression clearly shows that the hardening modulus is size–dependent for both the Cosserat and *microcurl* models. At the limit of vanishingly small microstructural size, l, for fixed intrinsic lengths of the generalised continua and fixed soft phase volume fraction, f_s,

Table II.3 : Set of material parameters satisfying the equivalence conditions (II.121) and (II.122) between the *microcurl* and the Cosserat models. The intrinsic length scales, defined as $\sqrt{A/H_\chi}$ or $\sqrt{\beta/\mu}$, induced by these parameters are of the order of 10 nm for the elastic phase (h) and 500 nm for the plastic phase (s).

Coefficient			Cosserat	*microcurl*	Cosserat	*microcurl*
	μ [MPa]	τ_c [MPa]	μ_c [MPa]	H_χ [MPa]	β [MPa mm^2]	A [MPa mm^2]
Phase (s)	35000	40	10^6	133829	10^{-2}	2.10^{-2}
Phase (h)	35000	-	10^6	133829	10^{-5}	2.10^{-5}

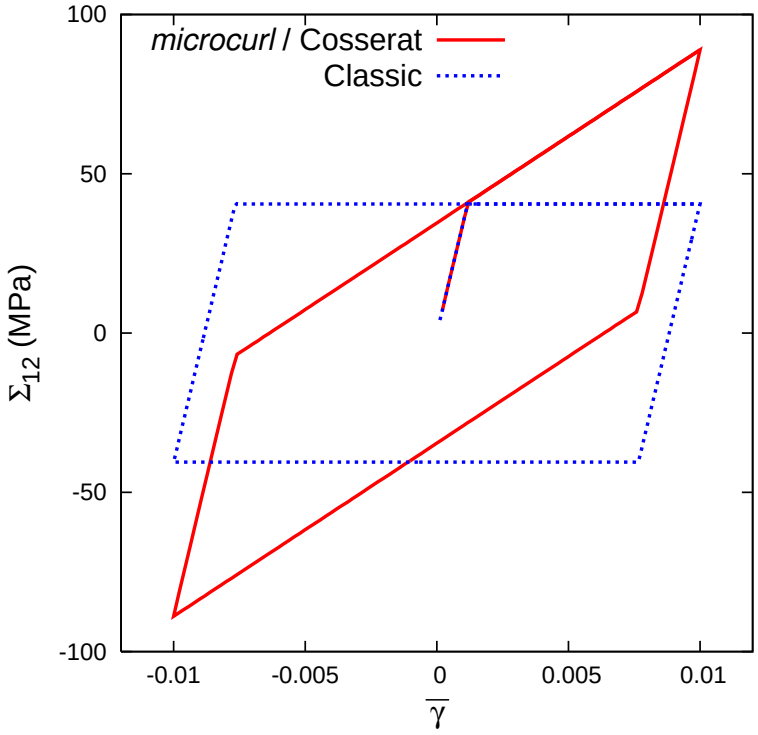

Figure II.4 : Macroscopic stress–strain response of the laminate microstructure under cyclic shear loading conditions: comparison between the kinematic hardening modelled by both the *microcurl* and Cosserat models in comparison and the behaviour from a conventional crystal plasticity theory for $l = 10^{-3}$ mm (the material parameters used are given in Table II.3).

the following value of the hardening modulus is obtained:

$$\lim_{l\to 0} H = \frac{1-f_s}{\dfrac{f_s^2}{H_\chi^h} + \dfrac{f_s(1-f_s)}{H_\chi^s}}. \tag{II.128}$$

In the specific case when $H_\chi^h = H_\chi^s = H_\chi$, the limit becomes

$$\lim_{l\to 0} H = \frac{1-f_s}{f_s} H_\chi \tag{II.129}$$

for the *microcurl*, and

$$\lim_{l\to 0} H = \frac{1-f_s}{f_s}\frac{4\mu\mu_c}{\mu+\mu_c}. \tag{II.130}$$

for Cosserat. Eqs. (II.129) and (II.130) reveal a major difference between the two models. In the *microcurl* model, the limiting hardening modulus depends only on the parameter H_χ, whereas Cosserat depends on both the classical shear modulus, μ, and the Cosserat coupling modulus, μ_c. Moreover, taking into account the condition $\mu \ll \mu_c$ chosen for the Cosserat continuum, see Eq. (II.12), we find that, in that case, the limit hardening modulus saturates at

$$\lim_{l\to 0} H = \frac{1-f_s}{f_s} 4\mu. \tag{II.131}$$

In contrast, the kinematic hardening modulus in the *microcurl model* linearly increases with the coupling modulus H_χ.

The existence of such a back stress contribution from the dislocation density tensor was anticipated by Steinmann (1996), derived from statistical mechanical arguments by Groma *et al.* (2003) and simulated for a two–phase microstructure in Forest (2008). However, the previous analytical expressions of the hardening modulus were derived in none of these publications.

II.4.2 Modelled size–dependent macroscopic flow stress

The previous results make it possible to study the dependence of the flow stress at $<\gamma>=0.002$ as a function of the microstructural length scale $l=(s+h)$ for a given volume fraction of the soft phase, f_s. The overall flow stress is obtained by setting $\langle\gamma\rangle=0.002$ in Eq. (II.124). Fig. II.5 presents the modelled evolution of the flow stress as a function of l in a log–log diagram using the numerical values from Table II.3 and for different values of the coupling modulus, $H_\chi^h=H_\chi^s=H_\chi$. All other material parameters are kept fixed, in particular, the intrinsic lengths associated with the moduli A^s and A^h (resp. β^s,β^h), which are assumed to be independent of l. The two lower curves in Fig. II.5 are obtained for values of the coupling moduli lying in the range of equivalence between the Cosserat and *microcurl* models (i.e. satisfying the equivalence condition (II.122)). The dotted curve, obtained with $\mu_c=\infty$, shows the upper limit reached by the Cosserat model. The curves above are obtained for higher values of the coupling modulus H_χ.

For finite values of the coupling modulus, the curves exhibit a typical *tanh*–shape with a saturation for large ($l>10^{-2}$ mm for the chosen parameters) and small ($l<10^{-6}$ mm) values of l. Between these two asymptotic regimes, there is a transition domain for which significant size dependence is observed. This zone is situated between approximately $l=10^{-5}$ mm and $l=10^{-3}$ mm. The asymptotic values, the width of the transition zone, and the scaling law exponent in the transition regime are directly related to the material parameters used in both the Cosserat and *microcurl* models. The main characteristics of the *tanh*–curves are analysed in the two following subsections.

II.4.2.1 Asymptotic regimes and maximal size effect modelled by the models

When the size of the elasto–plastic phase becomes large compared to the intrinsic model material length scale, l_ω, strain gradients are small and the kinematic hardening contribution to the overall stress tends to vanish. In such case, the models reduce to classical crystal plasticity theory. The 0.2% macroscopic flow stress then evolves towards the critical resolved shear stress:

$$\lim_{l\to\infty}\Sigma_{12|0.2}=\tau_c. \tag{II.132}$$

In contrast, for small microstructure sizes, l, compared to the intrinsic material length scale, l_ω, the strain gradient effects dominate. The maximum size effect generated by the *microcurl* model is obtained for sizes lower than a critical value. For smaller and smaller microstructures, the stress at a given mean plastic strain $<\gamma>$ saturates at

$$\lim_{l\to 0}\Sigma_{12}(<\gamma>)=\tau_c+\frac{1-f_s}{f_s}\frac{H_\chi^hH_\chi^s\langle\gamma\rangle}{H_\chi^h(1-f_s)+H_\chi^sf_s}. \tag{II.133}$$

If the two coupling moduli are assumed equal, $H_\chi=H_\chi^s=H_\chi^h$, this limit becomes:

$$\lim_{l\to 0}\Sigma_{12}(<\gamma>)=\tau_c+\frac{1-f_s}{f_s}H_\chi\langle\gamma\rangle. \tag{II.134}$$

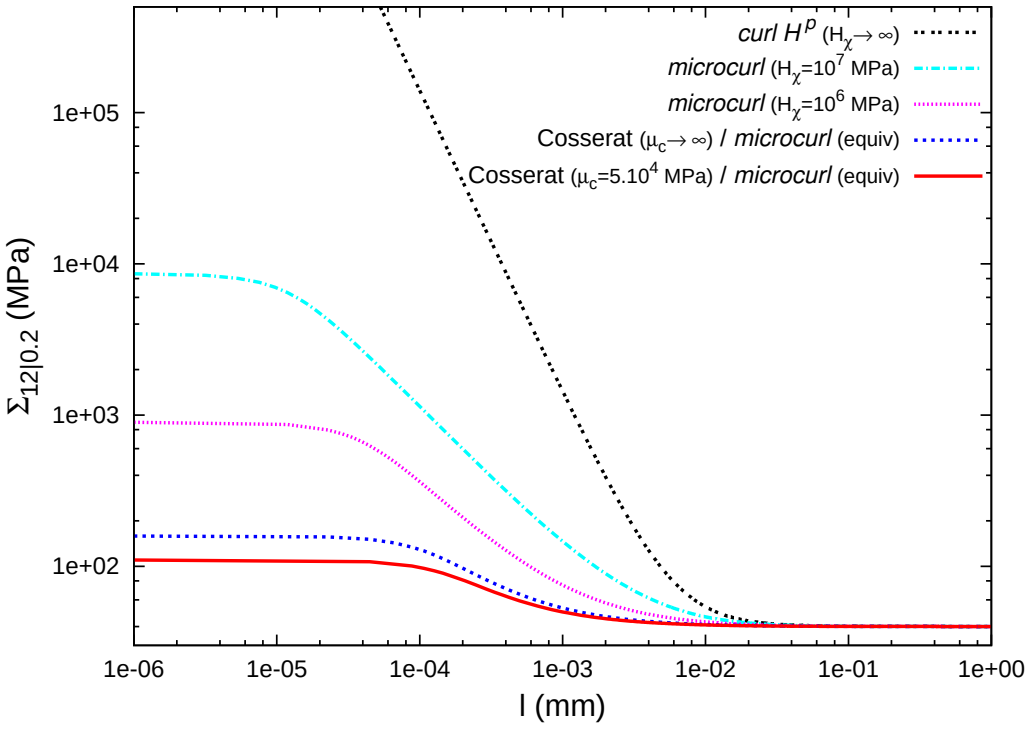

Figure II.5 : Evolution of the macroscopic flow stress $\Sigma_{12|0.2}$ at 0.2% plastic strain as a function of the microstructure length scale l, plotted for different coupling moduli H_χ and μ_c of the Cosserat and *microcurl* models respectively.

As a result, for a fixed $< \gamma >$ value, there exists a maximum extra–stress $\Delta\Sigma$ induced by strain gradient effects according to the *microcurl* model:

$$\Delta\Sigma = \lim_{l\to 0} \Sigma_{12}(< \gamma >) - \tau_c = \frac{1-f_s}{f_s} H_\chi \langle\gamma\rangle \,. \tag{II.135}$$

The maximum macroscopic extra–stress reachable by the model depends on the volume fraction, f_s, the mean plastic slip, $\langle\gamma\rangle$, and the coupling modulus, H_χ. Note that, for f_s and $\langle\gamma\rangle$ fixed, we can compute the following limit:

$$\lim_{H_\chi\to\infty} \left(\lim_{l\to 0} \Sigma_{12} \right) = \infty. \tag{II.136}$$

A similar expression for the maximum extra–stress modelled by the Cosserat model is

$$\Delta\Sigma = \frac{1-f_s}{f_s} \frac{4\mu\mu_c}{\mu+\mu_c} \langle\gamma\rangle \tag{II.137}$$

which, when μ_c goes to infinity, tends to:

$$\Delta\Sigma^\infty = \frac{1-f_s}{f_s} 4\mu \langle\gamma\rangle \,. \tag{II.138}$$

This expression clearly shows that the maximal size effect given by the Cosserat model is bounded, in contrast to that given by the *microcurl* model. Consequently, as noted in the previous subsection about the hardening modulus, the Cosserat and *microcurl* models behave

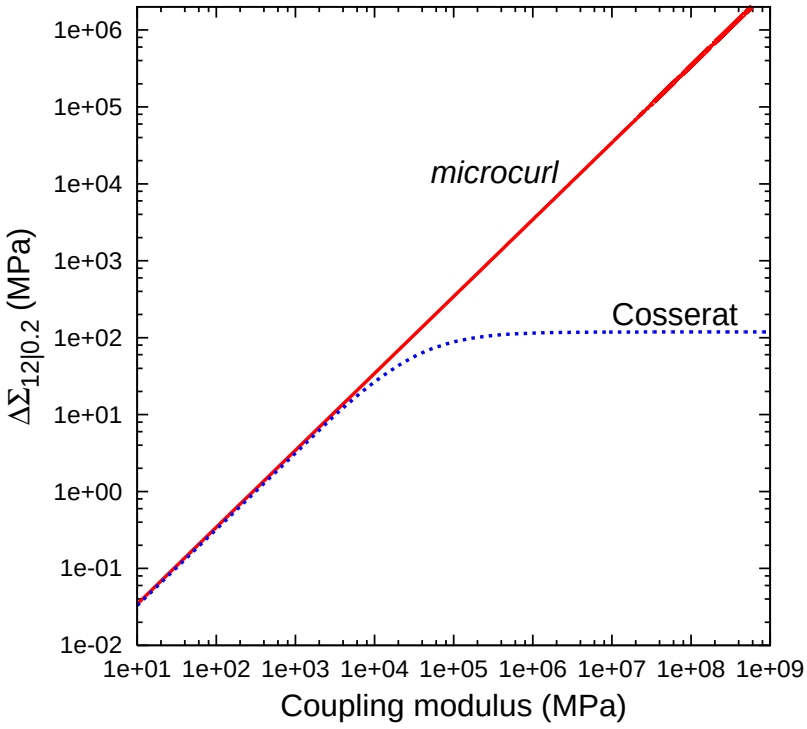

Figure II.6 : Evolution of the 0.2% macroscopic flow stress, $\Delta\Sigma_{12|0.2}$, as a function of the coupling modulus for the Cosserat and *microcurl* models. The abscissa corresponds to H_χ for the *microcurl* model and to $4\mu_c$ for the Cosserat model (first order Taylor approximation of Eq. (II.122) for μ_c near zero). The material parameters considered for each phase are given in Table II.3.

differently for small values of l. The Cosserat maximum size effect is intrinsically limited by the elastic properties for a given fraction of the phase (s), whereas the maximum size effect predicted by the *microcurl* model is entirely controlled by the H_χ coefficient.

These different responses are illustrated by Fig. II.6, where the extra–stress at 0.2% plastic strain is plotted as a function of the coupling modulus for the two models. As it was shown in Section II.4.1 and in Fig. II.5, the two models considered here are equivalent for sufficiently small values of the coupling modulus, according to the expression (II.122).

II.4.2.2 Modelled transition zone and scaling law

The transition domain between the size–independent and dependent flow stress can be characterised by two main parameters, see Fig. I.1. A critical value of l, denoted l_c, is defined as the inflection point of the $\log l - \log \Sigma_{0.2}$ curve. The inflection point l_c can be computed, for instance, for all the curves of Fig. II.5. Moreover, the scaling law, of the form l^m, is defined by the first derivative of the curve, $\log l - \log \Sigma_{0.2}$ at $l = l_c$. The values l_c and m are determined numerically. For the material parameters given in Table II.3, we found $l_c \simeq 2.24\ 10^{-5}$ mm and the slope at this point is $m \simeq -0.46$.

Next, we present the model predictions of the evolution of l_c as a function of the material parameters. For a fixed modulus, $A^s = 10^{-1}$ MPa mm^2, the microstructure size dependence of the flow stress is plotted in Fig. II.7(a) for different values of A^h. The other parameters are taken equal to their values in Table II.3. These curves show that the transition zone is

translated towards smaller microstructural length scales when A^h is decreased. Similar results hold for the $\beta^{h,s}$ values in the Cosserat model. For a fixed modulus $A^h = 10^{-1}$ MPa mm^2, the microstructural length scale dependence of the flow stress is plotted in Fig. II.7(b) for different values of A^s. The translation of the transition zone is still observed.

From these curves, the characteristic length scale, l_c, and the scaling law exponent, m, can be determined and plotted as functions of A^h and A^s, see Fig. II.8. The characteristic length l_c increases with $A^{s,h}$, and eventually saturates. For the chosen parameters, the scaling power law remains close to $m = -0.5$. The values of l_c and m also depend on that of the coupling modulus. Fig. II.9(a) gives the dependence of the inflection point of the curves of Fig. II.5 with respect to the values of the coupling moduli μ_c and H_χ, for fixed values of the remaining parameters, especially $A^{h,s}$ which describe the gradient effect. The predictions of the *microcurl* model shown in Fig. II.9 are obtained analytically. A bump is observed on the l_c curve for the *microcurl* model. It seems to be the result of two competing effects of material parameters. On the one hand, increasing H_c leads to a translation of the inflection point to the left in Fig. 6. When $H_\chi \to \infty$, there is no longer an inflection point, this is the reason why the red curve converges toward zero for large values of the coupling modulus. On the other hand, increasing H_χ leads to an increase in the slope of the quasi–linear part of the $\log \Sigma_{0.2} = f(\log l)$ curve, which in turn tends to slightly move the inflection point to the right in Fig. 6. We find that there exists a domain of H_χ values for which the second effect becomes dominant. This non–linear effect remains limited. Probably, there exists a combination of parameters H_χ and A that would lead to a monotonic decrease of l_c. Fig. II.9(b) shows that the coupling modulus has a major effect on the scaling law for both models. In contrast, it has a limited effect on the size–dependent region location since it is generally taken around an equivalent value of 10^6 MPa. It turns out that, for the chosen material parameters, the Cosserat model provides power law exponent values that saturate close to $m = -0.5$ in the highly constrained case. In contrast, the asymptotic power law for the *microcurl* model is close to $m = -2$. Indeed, when the coupling modulus H_χ tends to infinity, we can derive an asymptotic expression for a^s. In Eq. (II.126), the $\mathcal{C}'$ and $\mathcal{D}'$ coefficients tend to zero and the coth function tends toward 1. In that specific case, the flow stress becomes

$$\lim_{H_\chi \to \infty} \Sigma_{12} = \tau_c + \frac{12 A^s \langle \gamma \rangle}{f_s^3 l^2}. \tag{II.139}$$

This expression indicates a $m = -2$ scaling law. Fig. II.10 presents the effect of the volume fraction f_s on the scaling law for the constrained Cosserat and *microcurl* models, i.e., for high values of the coupling moduli, μ_c and H_χ, respectively. According to the *microcurl* model, f_s has no effect on the asymptotic power law exponent of $m = -2$. For the Cosserat model, the effect of volume fraction is strong and dominates when the coupling modulus μ_c is high. The range of reachable scaling laws lies between 0 and -1. The -1 scaling law is obtained when the fraction of the soft phase tends to 0, i.e., when the microstructure is mainly constituted by hard obstacles. In this case, the Cosserat model delivers the same scaling law as the Orowan effect for precipitate hardening:

$$\Sigma_{12} - \tau_c \propto \frac{1}{l} \tag{II.140}$$

An approximation of the flow stress can be derived when f_s tends to 0. In the transition zone we have checked that the coth term in Eq. (II.126) is close to 1. Consequently,

$$\lim_{f_s \to 0} \Sigma_{12} = \tau_c + \beta^s \frac{\mathcal{A}'}{\mathcal{C}' l + \mathcal{D}'} \tag{II.141}$$

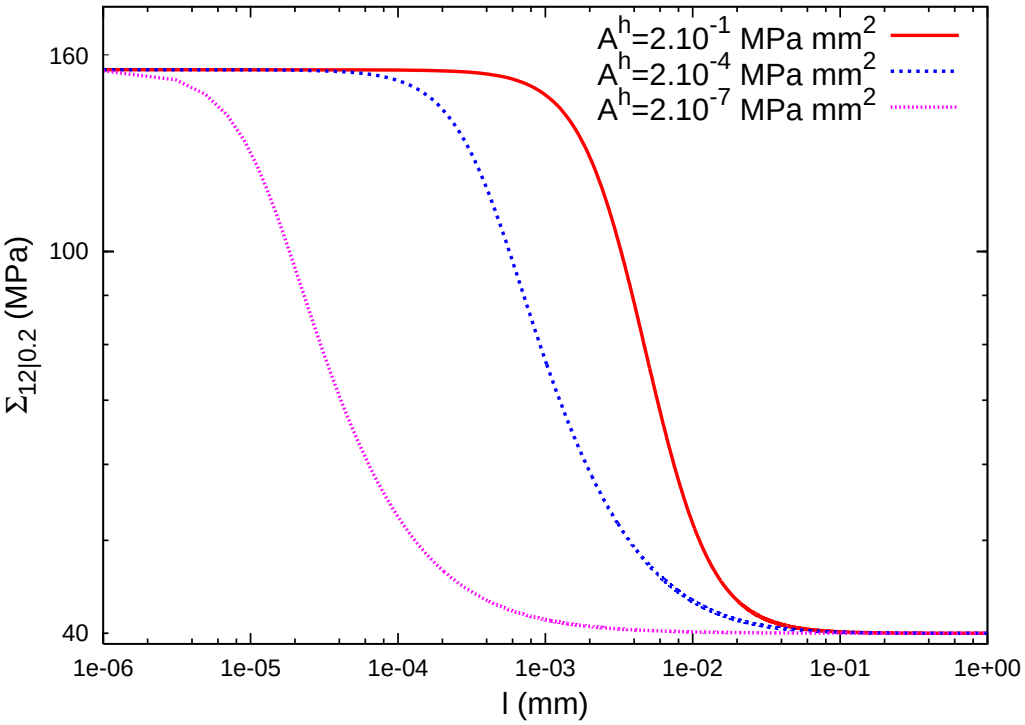

(a)

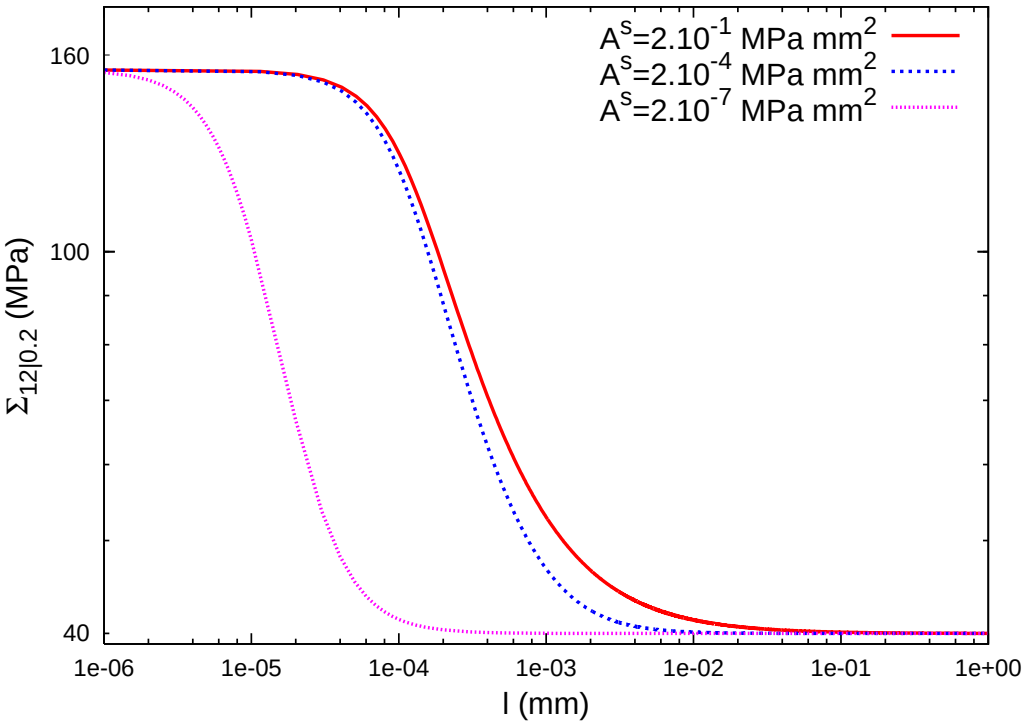

(b)

Figure II.7 : Effect of the higher order moduli A^h and A^s on the evolution of the macroscopic 0.2% flow stress $\Sigma_{12|0.2}$, as a function of the microstructural length scale l for: (a) different values of A^h (or β^h), and $A^s = 10^{-1}$ MPa mm^2; (b) different values of A^s (or β^s), and $A^h = 10^{-1}$ MPa mm^2.

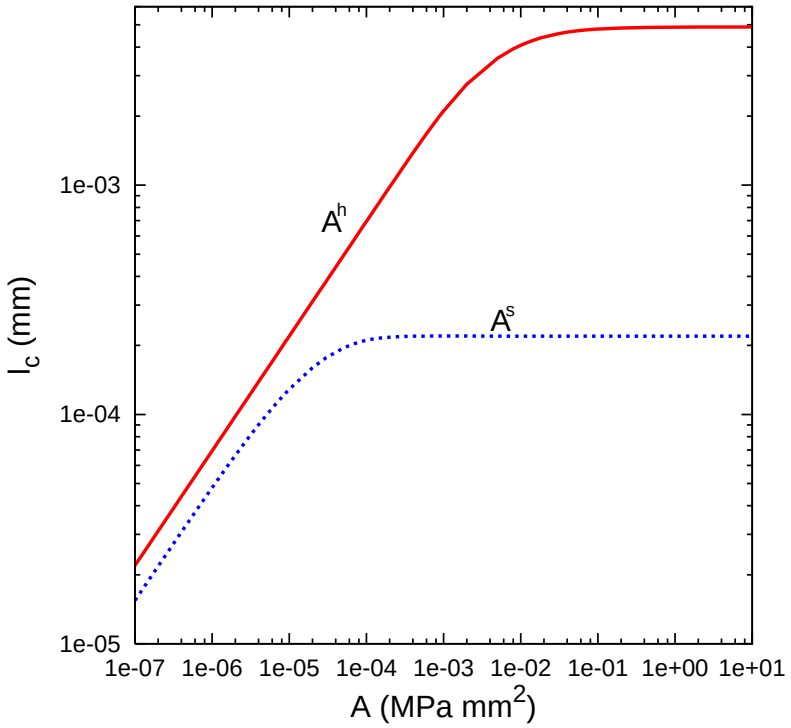

(a)

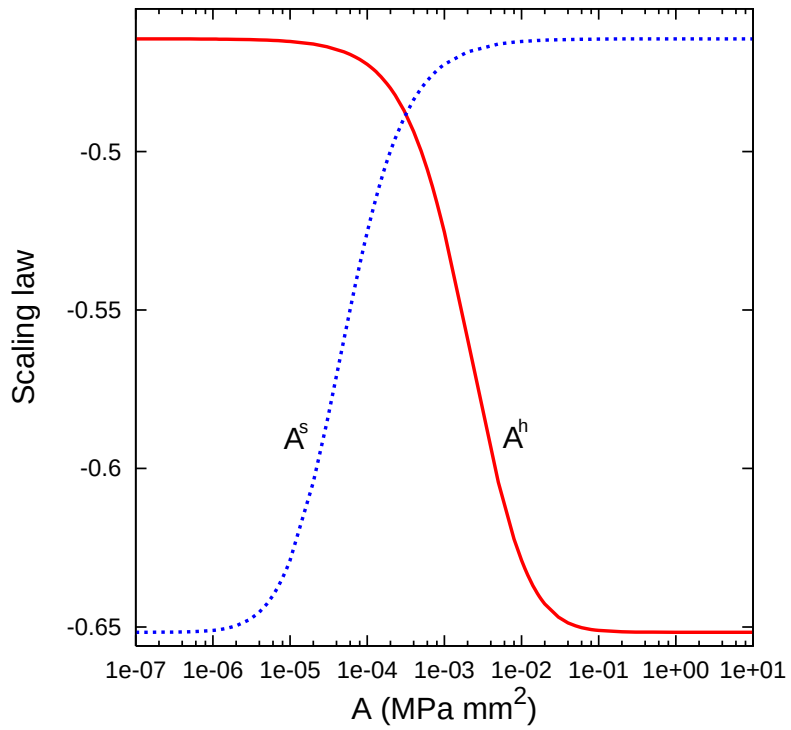

(b)

Figure II.8 : Effect of the higher order moduli A^h and A^s on (a) the location l_c of the size–dependent region, and (b) the scaling power law exponent m. These evolutions are plotted as functions of one higher order modulus (A^h or A^s) while the other one is fixed.

This expression can be simplified considering that μ_c goes to ∞ :

$$\lim_{f_s \to 0} \Sigma_{12} = \tau_c + \frac{\langle \gamma \rangle}{\frac{f_s^2}{\sqrt{2}} \frac{l_\omega l}{\beta^h} + \frac{f_s}{4\mu}} \tag{II.142}$$

where l_ω is the characteristic length of the phase (h) defined by Eq. (II.11). Eq. (II.142) confirms the scaling law exponent of $m = -1$ modelled by the Cosserat model when f_s tends to 0.

The physical implications of these findings will be discussed in Section II.5.

II.5 Discussion

The objective of this section is to discuss the previous results and to compare the pro and cons of the three models, namely the Cosserat, "*curl*H^p" and *microcurl*. In particular, we insist on the major importance of the interface conditions in the evaluation of the different approaches. As an illustration, it is shown that the explicit relations obtained for the main characteristics of the size–dependent model responses in the case of simple shear of a laminate, could be used for the identification of material parameters for a real two–phase material. Finally, the obtained results are proved to hold also in the case of a laminate microstructure endowed with two symmetric slip systems and undergoing simple shear.

II.5.1 Towards an identification of material parameters

The main features of the scaling behaviour of Cosserat, micromorphic and strain gradient plasticity models have been quantitatively described in the special case of a two–phase laminate microstructure. Explicit formula or numerical estimates of the extra–hardening associated with plastic strain gradients, asymptotic behaviour and scaling laws have been provided for this specific case. A parametric study has shown that a large range of size effects can be explored depending on the higher order theories' material parameters. The previous analyses therefore set guidelines for the identification of such material parameters to describe specific size effects. Simple analytical situations like the one proposed in this work can help to estimate the order of magnitude of such parameters, see also Hunter and Koslowski (2008). The targeted phenomena are precipitate hardening and grain size effects. Generalisations of the approach will be necessary to tackle more realistic microstructures. This will also require intensive numerical simulations.

Depending on the amplitude and the range of observed size effects, the Cosserat and *microcurl* theories are suitable models to predict the size–dependent response of elasto–(visco)plastic crystalline solids. The Cosserat formulation has the particular advantage of requiring three additional degrees of freedom in contrast to the nine required by the micromorphic approach. However, it has been shown in Section II.4.2.1 that the Cosserat crystal plasticity model may not be sufficient to account for large amplitude extra–hardening over a broad range of length scales, see Eq. (II.138).

Experimental results on size effects are generally available for a limited range of length scales. The transition domain between the two asymptotic regimes of the flow stress curve as a function of microstructure length scale, see Fig. II.9, can therefore be calibrated in order to coincide with the measured experimental range. The existence of a saturated asymptotic regime below the experimentally investigated length scales, i.e., below l_c, can be seen as the limit of the continuum approach. That is why predictive extrapolations to smaller scales of the generalised continuum models should not be expected.

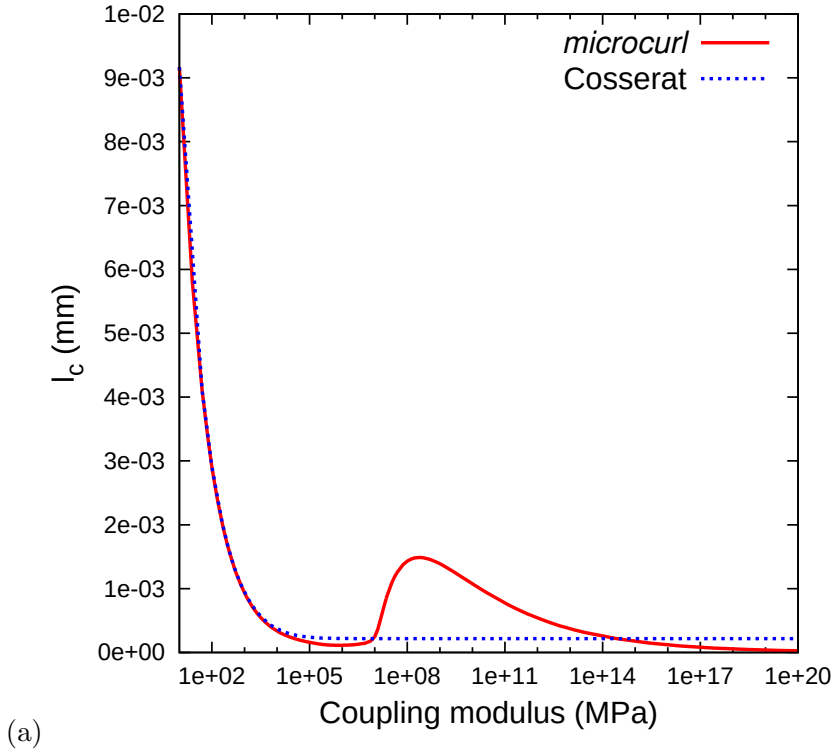

(a)

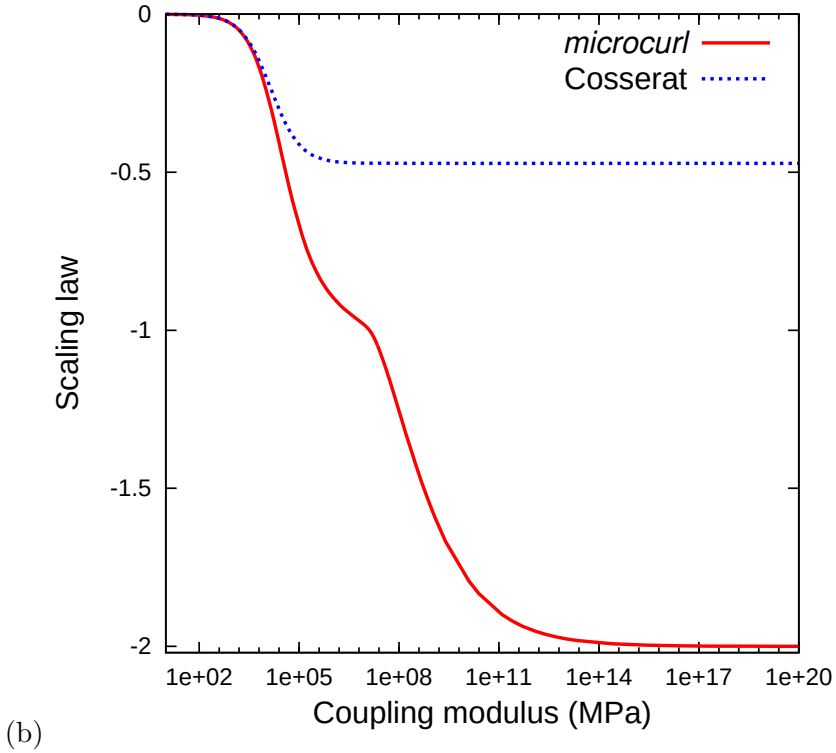

(b)

Figure II.9 : Effect of the coupling moduli μ_c and H_χ on (a) the location l_c of the size–dependent transition zone, and (b) the scaling power law exponent m. The abscissa corresponds to H_χ for the *microcurl* model and to $4\mu_c$ for the Cosserat model (first order Taylor approximation of Eq. (II.122) when μ_c nears zero).

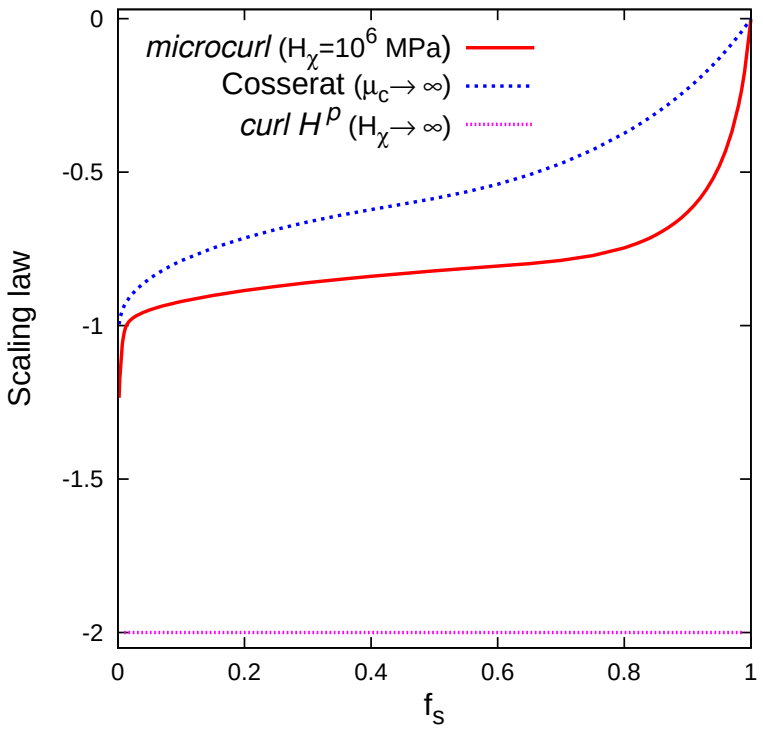

Figure II.10 : Effect of the volume fraction f_s on the scaling law reachable by each model (obtained for high values of the coupling moduli).

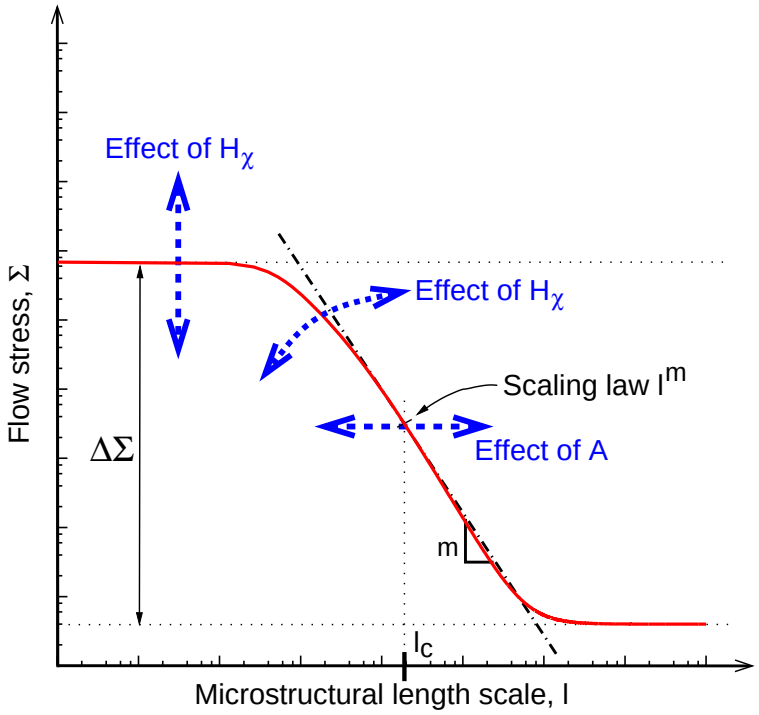

Figure II.11 : Influence of each material parameter on the size effect given by the considered model.

The power law exponent m of the Cosserat and *microcurl* models is not intrinsic to the form of the chosen constitutive equations but rather strongly depends on the values of the material parameters. It can be calibrated from experimental results in the range $-2 \leq m \leq 0$. These models can therefore be used to describe mixed Hall–Petch and Orowan effects. In contrast, the "$curl H^p$" model, regarded as the limiting case of the *microcurl* model for large values of H_χ, systematically leads to a power law exponent $m = -2$, which does not correspond to any known physical situation in crystal plasticity, to the best of our knowledge.

For the transmission of higher order tractions at the interface between elastic and elasto–plastic phases, it has been necessary to introduce higher order moduli like A^s and A^h in both phases. The absence of such transmission rules leads to a discontinuity of generalised tractions in the strict strain gradient plasticity theory. These higher order moduli can be seen as representing intrinsically non local effects that work at different length scales. Non local elasticity effects are expected at very low length scales, typically 10 nm, which motivates low values of the parameter A^h. In contrast, the volume element of a generalised crystal plasticity model must contain a sufficient number of dislocations for a continuum theory to apply. Non local micro-plasticity effects occur at scales ranging typically from 0.3 to 10 μm in FCC metals. So we expect that $A^h \ll A^s$. These remarks set guidelines for the identification procedure and motivates the selected values of the material parameters in the examples provided in the previous sections (see Table II.3).

As a formal exercise and with a view to setting guidelines for the identification of a more realistic model in the future, we propose in this section to calibrate the parameters $A^{h,s}, H_\chi$ etc., of the *microcurl* (and Cosserat) models from experimental results for a material which shares some common features with the ideal laminate microstructures. Such experimental results in the form of precipitate size effects in single crystal nickel base superalloys can be found in Duhl (1987). Here, the microstructure consists of a quasi–periodic distribution of cuboidal γ' precipitates coherently embedded in the γ matrix. In a certain range of temperature and strain rate, the precipitates can be regarded as elastic whereas the matrix displays a complex elasto-viscoplastic behaviour. The narrow channels of γ phase are reminiscent of the ideal laminate microstructure of Fig. II.1.

The precipitate size effect in such quasi–periodic microstructures has been modelled by means of periodic homogenisation techniques based on cubic unit cells, and using generalised continuum models by Busso *et al.* (2000), Forest *et al.* (2000) and more recently by Tinga *et al.* (2008). In the two first references, the size effect is entirely accounted for by the strain gradient approach, whereas the strain gradient plasticity model used by Tinga *et al.* (2008), also includes the Orowan law explicitly introduced in the constitutive model. In the context of the simple laminate model considered here, we will try to identify the higher order material parameters so as to describe the experimental precipitate hardening effect without including explicitly Orowan's law in the model. As it will be shown, the Orowan effect will arise naturally as a result of the generalised crystal plasticity formulation. This formal identification aims at discriminating the ability of the Cosserat and *microcurl* models to account for significant additional hardening due to strain gradient effects. The identification remains somehow idealised since we consider only single slip, which is not the dominant deformation mode in real superalloys. The slip geometry is also different from the reality, even though the soft phase of the laminate model mimics a γ–channel. Finally, the size effect observed in tension along the [001] crystallographic orientation is converted in terms of the resolved shear stress and slip amount, τ/γ, on one of the eight systems that are activated for this tensile test, see Fig. II.12. Fig. II.12 shows that the *microcurl* model is able to simulate an Orowan–like scaling law, that is when $m \sim -1$. Moreover, the identified characteristic length, $l_c = 200nm$, is approximately the matrix channels width in Ni-base superalloys. The calibrated parameters are given in the caption of Fig. II.12. For an unambiguous

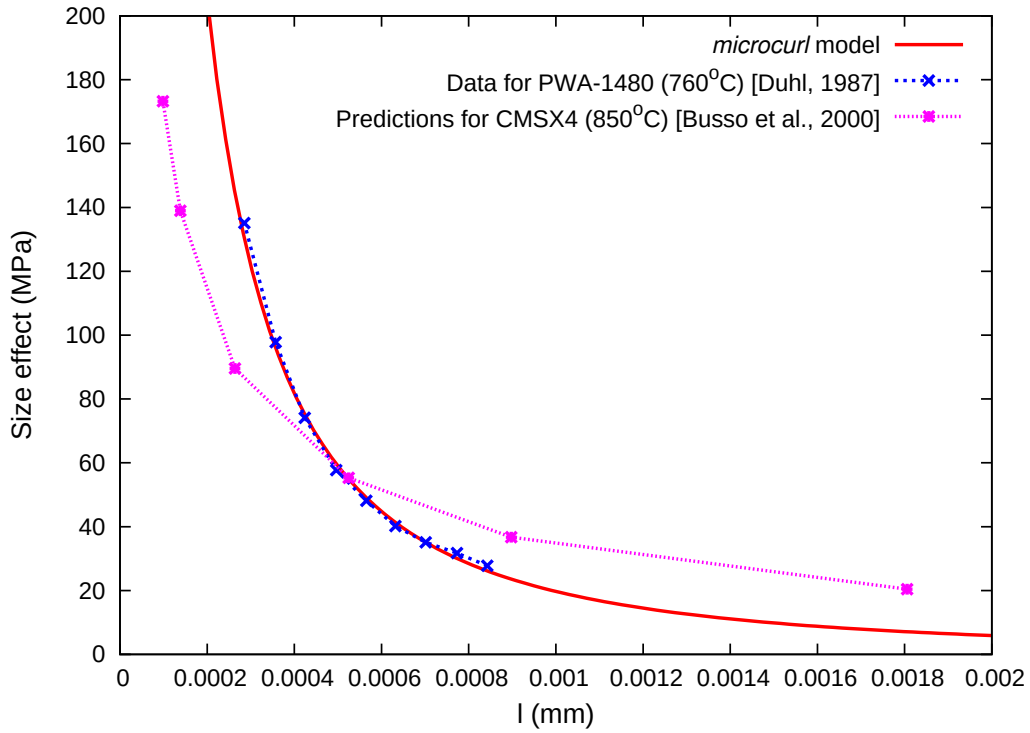

Figure II.12 : Comparison between experimental data, in the form of precipitate size vs. size effect strengthening (extra–stress above the size–independent value) published for a two–phase material (γ matrix phase elasto-viscoplastic and quasi–elastic γ' precipitates) from Duhl (1987), the prediction of Busso *et al.* (2000) and that obtained using the *microcurl* model. The volume fraction of precipitates is $f_h = 68\%$, critical resolved shear stress of the matrix phase $\tau_c = 59$ MPa, $\mu = 100000$ MPa, $H^h_\chi = H^s_\chi = 7.10^5$ MPa, $A^h = 3.5.10^{-6}$ MPa mm^2 and $A^s = 4.10^{-5}$ MPa mm^2.

identification, we have adopted $H^s_\chi = H^h_\chi = H_\chi$. This leaves three parameters that have been identified in order to account for the three characteristics of the size effect, namely $\Delta\Sigma$, l_c and m, see Fig. II.11. The experimental results are available only over a narrow window of precipitate sizes, from 0.2 μm to 2 μm, so that the calibration of the three parameters leads to correct description of the experimental curve. The predicted ratio, $A^s/A^h \approx 10$, confirms the difference in characteristic lengths for the elastic and plastic phases. The relatively high value found for A^h shows the important role of the double traction transfer at the interface. The identified value of the parameter H_χ is such that an equivalence with the Cosserat model is possible. As a result, both the Cosserat and *microcurl* models are suitable to describe the superalloy behaviour. More detailed comparisons with experiment would be necessary to further study both approaches.

II.5.2 Extension to double slip

The Cosserat and *microcurl* models have common features with the statistical model of dislocations developed for single slip by Groma *et al.* (2003) as well as with results obtained from discrete dislocation dynamics simulations in Yefimov *et al.* (2004). The strain gradient plasticity model used in the two latter references has been extended for multiple slip situations using purely phenomenological arguments in Yefimov and Van der Giessen

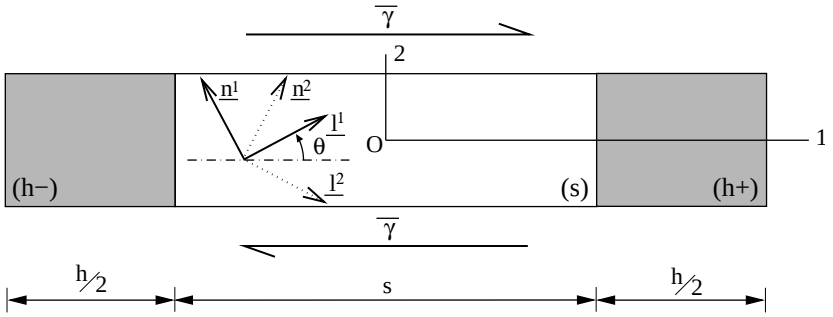

Figure II.13 : Double slip in a two–phase periodic laminate microstructure under simple shear.

(2005) and Bardella (2007). In the same way, the Cosserat and *microcurl* models possess a straightforward phenomenological generalisation for multiple slip, without introducing either additional ingredients nor parameters, but without confirmation that it is indeed consistent with the actual multislip behaviour of crystals. This formulation is illustrated for symmetric double slip in the laminate microstructure under shear loading conditions. Two slip systems, symmetric with respect to direction 1 and inclined at an angle $\pm\theta$ with respect to direction 1 are taken into account in the soft phase (s), as shown in Fig. II.13. The main unknowns remain the same as in Section II.3.4, see Eq. (II.97). Following the same procedure as in the case of single slip, one obtains:

$$\left[\underset{\sim}{\boldsymbol{H}}\right] = \begin{bmatrix} 0 & \bar{\gamma} & 0 \\ u_{2,1} & 0 & 0 \\ 0 & 0 & 0 \end{bmatrix}, \quad \left[\underset{\sim}{\boldsymbol{H}}^p\right] = \begin{bmatrix} 0 & H^p_{12} & 0 \\ H^p_{21} & 0 & 0 \\ 0 & 0 & 0 \end{bmatrix}, \quad \left[\underset{\sim}{\boldsymbol{H}}^e\right] = \begin{bmatrix} 0 & \bar{\gamma} - H^p_{12} & 0 \\ u_{2,1} - H^p_{21} & 0 & 0 \\ 0 & 0 & 0 \end{bmatrix}. \tag{II.143}$$

As the two slip systems are symmetric, the associated plastic slips are equal $\gamma^1 = \gamma^2 = \gamma$. Then the non–zero components of the plastic deformation are:

$$H^p_{12} = 2\gamma \cos^2\theta, \quad H^p_{21} = -2\gamma \sin^2\theta. \tag{II.144}$$

The plastic micro–deformation tensor takes the same form as that in Section II.3.4. However, in contrast to the case of single slip, we expect the component χ^p_{21} of the plastic micro–deformation not to vanish. The matrix expressions (II.99) are still valid in the double slip context. In particular, there is still one single non–zero component in the curl of plastic micro–deformation. The resulting stress tensors are:

$$\left[\underset{\sim}{\boldsymbol{\sigma}}\right] = \mu \begin{bmatrix} 0 & \bar{\gamma} - H^p_{12} - H^p_{21} + u_{2,1} & 0 \\ \bar{\gamma} - H^p_{12} - H^p_{21} + u_{2,1} & 0 & 0 \\ 0 & 0 & 0 \end{bmatrix}, \tag{II.145}$$

$$\left[\underset{\approx}{\boldsymbol{s}}\right] = -H_\chi \begin{bmatrix} 0 & H^p_{12} - \chi^p_{12} & 0 \\ H^p_{21} - \chi^p_{21} & 0 & 0 \\ 0 & 0 & 0 \end{bmatrix}, \tag{II.146}$$

$$\left[\underset{\sim}{\boldsymbol{M}}\right] = \begin{bmatrix} 0 & 0 & -A\chi^p_{12,1} \\ 0 & 0 & 0 \\ 0 & 0 & 0 \end{bmatrix}, \quad \left[\operatorname{curl}\underset{\sim}{\boldsymbol{M}}\right] = \begin{bmatrix} 0 & -A\chi^p_{12,11} & 0 \\ 0 & 0 & 0 \\ 0 & 0 & 0 \end{bmatrix}. \tag{II.147}$$

Consequently, the double stress has only one non–vanishing component related to χ^p_{12} as in the case of single slip. Therefore the balance equation, $\underset{\sim}{\boldsymbol{s}} = -\mathrm{curl}\,\underset{\sim}{\boldsymbol{M}}$, becomes:

$$\begin{cases} -H_\chi\,(H^p_{12} - \chi^p_{12}) = A\chi^p_{12,11}, \\ H^p_{21} - \chi^p_{21} = 0. \end{cases} \tag{II.148}$$

It is also found that the component χ^p_{21} does not contribute to the dislocation density tensor. It is bound to coincide with the plastic deformation H^p_{21}, according to the second balance equation. This will be due to the fact that no contribution of the component χ^p_{21} will appear in the back stress, as it is shown by the plasticity criterion $|\underset{\sim}{\boldsymbol{\sigma}} : \underset{\sim}{\boldsymbol{P}}^\alpha + \underset{\sim}{\boldsymbol{s}} : \underset{\sim}{\boldsymbol{P}}^\alpha| = \tau_c$:

$$|\sigma_{12}\left(\cos^2\theta - \sin^2\theta\right) + s_{12}\,\cos^2\theta| = |\sigma_{12}\left(\cos^2\theta - \sin^2\theta\right) + A\chi^p_{12,11}\,\cos^2\theta| = \tau_c. \tag{II.149}$$

In the same way as for the single slip case, the profile of χ^p_{12} is parabolic in the plastic phase. It is computed as in Eq. (II.105), which involves integration constants that can be identified as in Section II.3.4 based on interface conditions. The resulting plastic slip is:

$$\gamma = \frac{1}{2\cos^2\theta}\left(\chi^{ps}_{12} - \frac{A^s}{H^s_\chi}\chi^{ps}_{12,11}\right). \tag{II.150}$$

Since we have $\chi^{ps}_{21} = -2\gamma\,\sin^2\theta$, the profile of χ^p_{21} is parabolic in the plastic phase as well. In the elastic phase, the balance equations (II.148) are still valid with vanishing plastic slip. Then, one obtains,

$$\begin{cases} \chi^{ph}_{12} = \dfrac{A^h}{H^h_\chi}\chi^p_{12,11}, \\ \chi^{ph}_{21} = 0. \end{cases} \tag{II.151}$$

Therefore, the component χ^p_{12} has a hyperbolic profile in the hard phase and can be computed as in Eq. (II.106); and its profile over the whole structure is similar to the single slip case. In addition, the component χ^p_{21} vanishes in the elastic domain and it cannot be continuous at the interface as soon as $\gamma \neq 0$. Accordingly, the *microcurl* model only ensures the continuity of the component χ^p_{12}, which contributes to the dislocation density tensor. Here the complete analytical solution with χ^p_{21} discontinuous at the interface between the two phases has been obtained. The expressions of the integration constants as functions of $\bar{\gamma}$ are

$$a^s = \frac{\dfrac{\tau_c}{\cos^2\theta - \sin^2\theta} - \bar{\gamma}}{(1-\tan^2\theta)\left(\dfrac{l^2 f_s^3}{6} + \dfrac{l f_s^2 A^s \coth(\dfrac{\omega^h h}{2})}{A^h\omega^h} + \dfrac{2f_s A^s}{H^s_\chi} + \dfrac{2f_s A^s}{\mu(1-\tan^2\theta)^2}\right)}, \tag{II.152}$$

$$a^h = -\frac{a^s A^s s}{A^h\omega^h \sinh(\dfrac{\omega^h h}{2})}, \tag{II.153}$$

$$c = -a^s\left(\frac{s^2}{4} + \frac{A^s s\coth(\dfrac{\omega^h h}{2})}{A^h\omega^h}\right). \tag{II.154}$$

Fig. II.14 illustrates the continuity of χ^p_{12} and the discontinuity of χ^p_{21} at the interface. The problem of interface conditions in strain gradient plasticity has already been pointed out, for example in Aifantis and Willis (2005) and Gurtin and Needleman (2005). In these

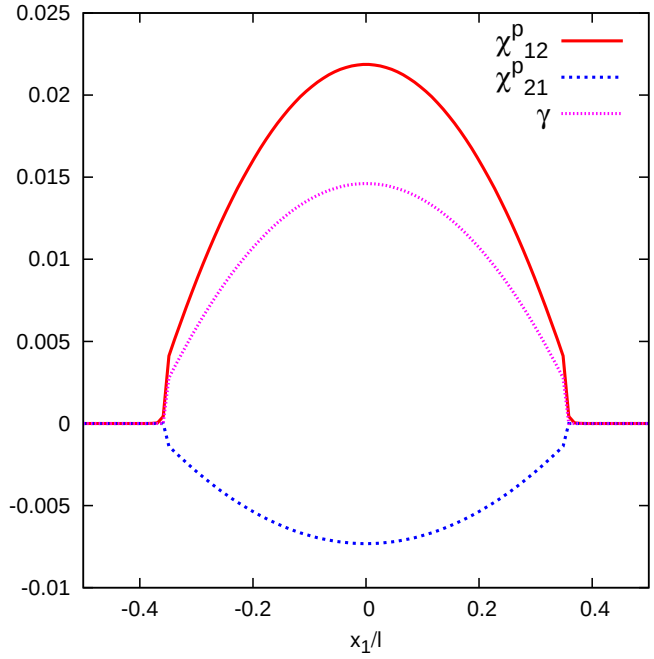

Figure II.14 : Profiles of plastic micro–deformation χ^p_{12} and χ^p_{21} and of the plastic slip γ in the two–phase microstructure with the *microcurl* model, for symmetric double slip with $\theta = 30°$. The material parameters used in this case are: $\mu = 35000$ MPa, $H^h_\chi = H^s_\chi = 133829$ MPa, $A^h = 2.10^{-6}$ MPa mm^2, $A^s = 2.10^{-5}$ MPa mm^2 and $\tau_c = 40$ MPa. $f_s = 0.7$ and the values of $\beta^{h,s}$ are chosen for $l = 1$ μm. This figure shows that in the case of double slip, χ^p_{12} is continuous at the interface while χ^p_{21} is discontinuous.

publications, jump conditions at interfaces are discussed. Here, no jump condition is imposed on χ^p_{21} at the interface, instead, continuity requirements for χ^p_{12} and the double traction tensor are enforced. In order to illustrate the size effects obtained with double symmetric slip, the integration constant a^s has been obtained as a function of $\langle H^p_{12} \rangle$. It materialises that we find the same expression than in single slip, a^s being still given by Eq. (II.126). The Cosserat model also gives the same expression for a^s as a function of $\langle H^p_{12} \rangle$. The macroscopic stress Σ_{12} can be expressed by

$$\Sigma_{12} = \frac{\tau_c}{\cos^2\theta - \sin^2\theta} - \frac{2A^s a^s}{1 - \tan^2\theta}. \tag{II.155}$$

Fig. II.15 presents the modelled size effects in double symmetric slip for angles θ ranging from 0^o and 90^o. For the particular case of $\theta = 45°$, no plastic slip is activated since the Schmid factors vanish. Note also that for the specific case of $\theta = 90°$, no hardening effect is found. Indeed, in that situation, one single effective slip system is obtained. Under shear, one slip band forms parallel to the interface for a vanishing dislocation density tensor, that is curl $\underset{\sim}{\boldsymbol{H}}^p = 0$. It can therefore be concluded that the generalised crystal plasticity models based on the dislocation density tensor do not regularise this strain localisation problem.

In order to sum up the influence of θ on size effects, the maximal size effect modelled by the models is calculated. For large microstructural length scales compared to the characteristic length, the macroscopic stress becomes:

$$\lim_{l \to \infty} \Sigma_{12} = \frac{\tau_c}{\cos^2\theta - \sin^2\theta}, \tag{II.156}$$

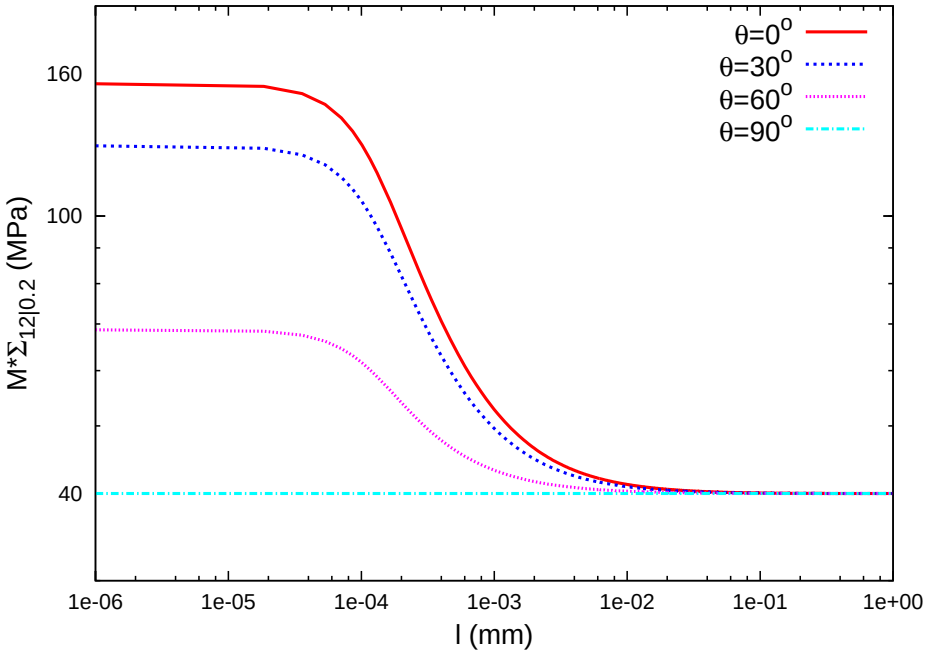

Figure II.15 : Evolution of the macroscopic flow stress $\Sigma_{12|0.2}$ multiplied by the Schmid factor $M = \cos^2\theta - \sin^2\theta$ at $\langle H_{12}^p \rangle = 0.002$ as a function of θ. The material parameters considered for each phase are given in Table II.3.

as in classical crystal plasticity. On the other hand, for small microstructural length scales,

$$\lim_{l\to 0} \Sigma_{12} = \frac{\tau_c}{\cos^2\theta - \sin^2\theta} + \frac{1-f_s}{f_s}\frac{1}{1-\tan^2\theta} H_\chi \langle\gamma\rangle. \tag{II.157}$$

Consequently, the maximal extra–stress reads

$$\Delta\Sigma = \frac{1-f_s}{f_s}\frac{1}{1-\tan^2\theta} H_\chi \langle\gamma\rangle. \tag{II.158}$$

The maximal size effect as a function of θ predicted by the models is presented in Fig. II.16.

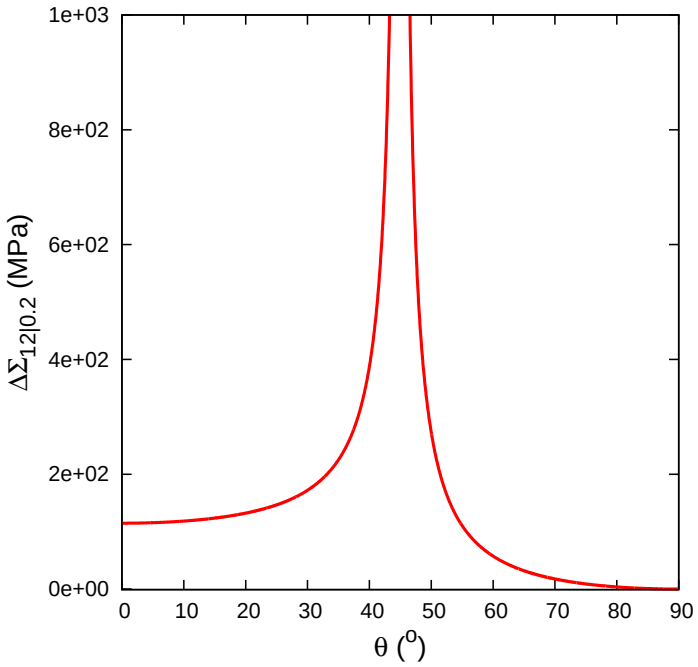

Figure II.16 : Evolution of the macroscopic yield stress $\Delta\Sigma_{12|0.2}$ as a function of θ. The material parameters considered for each phase are given in Table II.3.

References

Aifantis K.E. and Willis J.R. (2005). *The role of interfaces in enhancing the yield strength of composites and polycrystals.* Journal of the Mechanics and Physics of Solids, vol. 53, pp 1047–1070.

Bardella L. (2007). *Some remarks on the strain gradient crystal plasticity modelling, with particular reference to the material length scales involved.* International Journal of Plasticity, vol. 23, pp 296–322.

Bayley C.J., Brekelmans W.A.M., and Geers M.G.D. (2006). *A comparison of dislocation induced back stress formulations in strain gradient crystal plasticity.* International Journal of Solids and Structures, vol. 43, pp 7268–7286.

Bayley C.J., Brekelmans W.A.M., and Geers M.G.D. (2007). *A three–dimensional dislocation field crystal plasticity approach applied to miniaturized structures.* Philosophical Magazine, vol. 87, pp 1361–1378.

Bittencourt E., Needleman A., Gurtin M.E., and Van der Giessen E. (2003). *A comparison of nonlocal continuum and discrete dislocation plasticity predictions.* Journal of the Mechanics and Physics of Solids, vol. 51 n° 2, pp 281 – 310.

Busso E.P., Meissonier F.T., and O'Dowd N.P. (2000). *Gradient-dependent deformation of two-phase single crystal.* Journal of Mechanics and Physics of Solids, vol. 48 n° 11, pp 2333–2361.

Cordero N.M., Gaubert A., Forest S., Busso E.P., Gallerneau F., and Kruch S. (2010). *Size effects in generalised continuum crystal plasticity for two–phase laminates.* Journal of the Mechanics and Physics of Solids, vol. 58, pp 1963–1994.

Duhl D.N. (1987). *Directionally solidified superalloys.* In : Superalloys II–High Temperature Materials for Aerospace and Industrial Power, pp 189–214. Wiley-Interscience, John Wiley and Sons.

Erturk I., Dommelen J.A.W.V., and Geers M.G.D. (2009). *Energetic dislocation interactions and thermodynamical aspects of strain gradient crystal plasticity theories.* Journal of the Mechanics and Physics of Solids, vol. 57, pp 1801–1814.

Evers L.P., Brekelmans W.A.M., and Geers M.G.D. (2004a). *Non-local crystal plasticity model with intrinsic SSD and GND effects.* Journal of the Mechanics and Physics of Solids, vol. 52 n° 10, pp 2379–2401.

Evers L.P., Brekelmans W.A.M., and Geers M.G.D. (2004b). *Scale dependent crystal plasticity framework with dislocation density and grain boundary effects.* International journal of solids and structures, vol. 41 n° 18-19, pp 5209–5230.

Forest S. (2008). *Some links between Cosserat, strain gradient crystal plasticity and the statistical theory of dislocations.* Philosophical Magazine, vol. 88, pp 3549–3563.

Forest S. (2009). *Micromorphic Approach for Gradient Elasticity, Viscoplasticity, and Damage.* Journal of Engineering Mechanics, vol. 135, pp 117–131.

Forest S., Barbe F., and Cailletaud G. (2000). *Cosserat Modelling of Size Effects in the Mechanical Behaviour of Polycrystals and Multiphase Materials.* International Journal of Solids and Structures, vol. 37, pp 7105–7126.

Forest S., Pradel F., and Sab K. (2001). *Asymptotic analysis of heterogeneous Cosserat media.* International Journal of Solids and Structures, vol. 38, pp 4585–4608.

Forest S. and Sedláček R. (2003). *Plastic slip distribution in two–phase laminate microstructures: Dislocation–based vs. generalized–continuum approaches.* Philosophical Magazine A, vol. 83, pp 245–276.

Groma I., Csikor F.F., and Zaiser M. (2003). *Spatial correlations and higher-order gradient terms in a continuum description of dislocation dynamics.* Acta Materialia, vol. 51, pp 1271–1281.

Gurtin M.E. (2002). *A gradient theory of single–crystal viscoplasticity that accounts for geometrically necessary dislocations.* Journal of the Mechanics and Physics of Solids, vol. 50, pp 5–32.

Gurtin M.E. and Needleman A. (2005). *Boundary conditions in small-deformation single crystal plasticity that account for the Burgers vector.* Journal of the Mechanics and Physics of Solids, vol. 53, pp 1–31.

Hunter A. and Koslowski M. (2008). *Direct calculations of material parameters for gradient plasticity.* Journal of the Mechanics and Physics of Solids, vol. 56 n° 11, pp 3181–3190.

Kuroda M. and Tvergaard V. (2006). *Studies of scale dependent crystal viscoplasticity models.* Journal of the Mechanics and Physics of Solids, vol. 54 n° 9, pp 1789–1810.

Kuroda M. and Tvergaard V. (2008a). *A finite deformation theory of higher-order gradient crystal plasticity.* Journal of the Mechanics and Physics of Solids, vol. 56 n° 8, pp 2573–2584.

Kuroda M. and Tvergaard V. (2008b). *On the formulations of higher-order strain gradient crystal plasticity models.* Journal of the Mechanics and Physics of Solids, vol. 56 n° 4, pp 1591–1608.

Liebe T., Menzel A., and Steinmann P. (2003). *Theory and numerics of geometrically non-linear gradient plasticity.* International Journal of Engineering Science, vol. 41, pp 1603–1629.

Sedláček R. and Forest S. (2000). *Non-local plasticity at microscale : A dislocation-based model and a Cosserat model.* physica status solidi (b), vol. 221, pp 583–596.

Smyshlyaev V.P. and Fleck N.A. (1996). *The role of strain gradients in the grain size effect for polycrystals.* Journal of the Mechanics and Physics of Solids, vol. 44, pp 465–495.

Steinmann P. (1996). *Views on multiplicative elastoplasticity and the continuum theory of dislocations.* International Journal of Engineering Science, vol. 34, pp 1717–1735.

Tinga T., Brekelmans W.A.M., and Geers M.G.D. (2008). *Incorporating strain gradient effects in a multiscale constitutive framework for nickel-base superalloys.* Philosophical Magazine, vol. 88, pp 3793–3825.

Yefimov S., Groma I., and Van der Giessen E. (2004). *A comparison of a statistical-mechanics based plasticity model with discrete dislocation plasticity calculations.* J. Mech. Phys. Solids, vol. 52, pp 279–300.

Yefimov S. and Van der Giessen E. (2005). *Multiple slip in a strain-gradient plasticity model motivated by a statistical-mechanics description of dislocations.* International Journal of Solids and Structures, vol. 42, pp 3375–3394.

Résumé

Dans ce chapitre, les solutions d'un problème aux limites sont étudiées pour différents modèles de plasticité cristalline : modèle de Cosserat, modèle à gradient de déformation et une approche micromorphe. Un modèle de plasticité cristalline micromorphe, appelé *microcurl*, prenant en compte le tenseur de densité de dislocations est proposé. La microstructure considérée comporte une phase purement élastique et une phase élasto–plastique soumise à du glissement simple ou double. Les distributions locales de glissement plastique, de rotation de réseau et des contraintes sont obtenues analytiquement pour une microstructure soumise à un cisaillement simple. Les effets de taille générés par le modèle sont caractérisés par trois éléments : la valeur globale de la contrainte interne provenant de l'action de contraintes d'ordre supérieur (back stress), la longueur caractéristique l_c décrivant le domaine où la réponse du matériau dépend de la taille, et la loi d'échelle l^n correspondante qui est fonction de la longueur caractéristique de la microstructure, l. Les expressions analytiques de ces éléments sont dérivées et comparées pour les différents modèles. Il est montré que les conditions d'interface entre la phase élastique et la phase élasto–plastique jouent un rôle majeur dans la solution. Cette étude montre aussi qu'il existe une gamme de paramètres matériau pour lesquels le modèle Cosserat et le modèle *microcurl* produisent des résultats équivalents. Des valeurs de l'exposant de la loi d'échelle, n, allant de 0 à -2 sont obtenues en fonction des valeurs des paramètres matériau. La valeur inhabituelle de -2 est notamment obtenue avec le modèle à gradient de déformation plastique, appelé modèle "$curl H^p$" dans ce travail. Ces résultats fournissent des directions pour identifier les paramètres matériau d'ordre supérieur des modèles de plasticité cristalline à partir de données expérimentales telles que l'effet de la taille des précipités dans les alliages renforcés.

Chapter -III-

Comparing strain gradient plasticity and discrete dislocation dynamics for multilayer pileups

Abstract

In this chapter, size effects induced by multilayer pileups are investigated in terms of plastic slip distribution and overall work–hardening using discrete dislocation dynamics (DDD) and the *microcurl* model. To that purpose, double ended stacked pileups of edge dislocations and pileups on inclined slip planes in a channel are considered. The channel size effects on the mechanical responses obtained with the two models are analysed and compared using analytical and numerical solutions. Hardenings by pileups on single layer and by neighbouring slip planes are both taken into account in this study.

It is shown that the intrinsic lengths considered in the models, thus representing very different concepts, both have a major impact on the plastic slip distribution and the overall work–hardening. In DDD, the intrinsic length, l, represents the distance between active neighbouring slip planes while the intrinsic length of the *microcurl* model, l_{SGP}, characterises the ratio of the higher order moduli of the model, A and H_χ. It is found, for a fixed coupling modulus, H_χ, that the higher order modulus, A, can be calibrated for each intrinsic length used in the DDD simulations so that the two models give similar overall behaviour and local distributions. Consequently, it is shown that results from DDD simulations and from the *microcurl* model are equivalent when l_{SGP} is approximately ten times smaller than l. Furthermore, a correlation is found between the thickness of the boundary layer and the distance between active neighbouring slip planes.

Contents

Preamble: The work presented in this chapter was done in collaboration with Hyung–Jun Chang, post–doc at the Centre des Matériaux in 2010. He conducted the three–dimensional discrete dislocation dynamics simulations presented here and took part in the discussions about the method and the results of this study. This part of the thesis is a cooperation with the ANR project Cat–Size (ANR–07–MAPR–0023–04) and will be published in a future paper.

III.1 Motivation

Dislocation pileups, resulting in a non–vanishing field of the dislocation density tensor at interfaces in Section II, are essential to account for size effects (Hall, 1951; Petch, 1953). Pileups at boundaries and their induced stress field affect dislocations motion and then give rise to extra work–hardening. Consequently, the role of boundaries constraining dislocation pileups is of great interest to analyse size effects.

It has been shown that the motion of dislocation ensembles simulated with Discrete Dislocation Dynamics (DDD) leads directly to size effect predictions (Mughrabi, 1983; Aifantis, 1984; Ortiz *et al.*, 2000; Busso *et al.*, 2000). A detailed comparison of DDD simulations with those using the *microcurl* model introduced in Chapter II is then a suitable way to identify and assess the higher order material parameters of the latter method. Such comparison was first carried out by Bassani *et al.* (2001) and many alternative formulations have then been evaluated by DDD simulations (Shu *et al.*, 2001; Bittencourt *et al.*, 2003; Yefimov *et al.*, 2004; Yefimov and Van der Giessen, 2005; Baskaran *et al.*, 2010). However, most of these studies have been supported by two–dimensional DDD computations (Shu *et al.*, 2001; Cleveringa *et al.*, 1997, 1998, 1999).

In this chapter, size effects induced by multilayer pileups are investigated in terms of plastic slip distribution and overall work–hardening using three–dimensional (3D) DDD and Chapter's II *microcurl* model. Double ended stacked pileups of edge dislocations in a channel are first considered, followed by pileups on inclined slip planes. The mechanical responses obtained with DDD are analysed in terms of channel size effect and compared, qualitatively and quantitatively, with results obtained with the *microcurl* model using both analytical and numerical solutions.

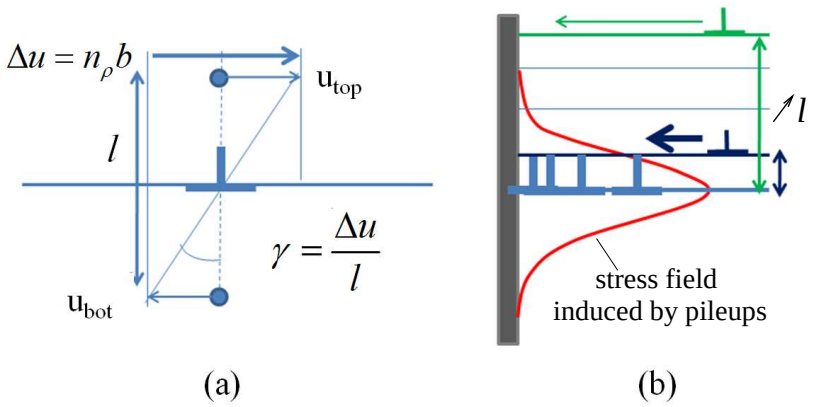

Figure III.1 : Schematic illustrations of the effects of the distance, l, between neighbouring slip layers (a) The amount of plastic slip, γ, is directly calculated from l and the displacement difference, Δu. (b) The stress field induced by pileups (red line) affects the dislocations moving on the neighbouring slip planes. This effect is also related to the distance l.

III.2 Three–dimensional discrete dislocation dynamics

III.2.1 A short presentation of the theory

Three–dimensional DDD deals with full physical phenomena resulting from collective motions of realistic dislocations in a three dimensional framework. This approach is expected to provide a full description of physically–based plasticity. For instance, only such computations can provide line tension induced dislocation motion and relaxation due to extension of screw dislocations (Shu *et al.*, 2001). Several codes for three dimensional DDD have been developed (Kubin *et al.*, 1992; Zbib *et al.*, 1998; Ghoniem and Sun, 1999; Weygand *et al.*, 2001) and applied to a wide range of dislocation related problems (Kubin *et al.*, 1992; Fivel *et al.*, 1998; Madec *et al.*, 2003; Shin *et al.*, 2003; Déprés *et al.*, 2004; Kim *et al.*, 2010). The code used in the present work was used in H.J. Chang's PhD thesis (Chang, 2009; Chang *et al.*, 2010) and modified during his postdoctoral researches at the Centre des Matériaux (Chang *et al.*, 2011).

DDD simulations are based on dynamic states (out of equilibrium) inducing instabilities and time dependencies. However, it is possible to obtain quasi–static dislocation distributions. For that, the external loading has to be increased step by step, the next step being computed only after the dislocations have reached equilibrium positions at the current step. Then, the post–processing of dislocation distributions was carried out to calculate the plastic slip distributions and stress–strain curves based on quasi–static states. Finally, the overall work–hardening was derived from the linear slope of the stress–plastic strain curves.

The distance between active neighbouring slip planes is considered in the DDD simulations as an intrinsic length, l, and plays a key role in size effects for the two reasons illustrated in Fig. III.1. First, the amount of plastic slip, γ, is directly calculated from l and the displacement difference, Δu (Fig.III.1(a)). Here, Δu comes from the dislocation motion, it is a function of their number, n_p, and of Burgers vectors, b,

$$\Delta u = n_p\, b. \tag{III.1}$$

The amount of plastic slip between adjacent slip planes is determined as

$$\gamma = \frac{\Delta u}{l} = \frac{n_p\, b}{l}. \tag{III.2}$$

The intrinsic length, l, also determines how the stress field induced by pileups affects the motion of dislocations on neighbouring slip planes. The stress field of an array of parallel dislocation pileups is studied in Schouwenaars *et al.* (2010). The red line in Fig.III.1(b) represents schematically the magnitude of hindrance to the dislocation motion induced by dislocation pileups. The magnitude is maximum at the layer of the considered pileup and decreases exponentially away from this layer. Hence, a dislocation (represented in green) moving on a slip plane far from the pileup feels no or very weak hindrance from the pileup, while a dislocation (represented in dark blue) moving on a slip plane close to the pileup is strongly affected. Consequently, the intrinsic length between slip layers, l, is strongly related to the hardening induced by multilayer pileups. Mura (see Forest and Sedláček, 2003) has suggested a simple solution for multilayer pileups without considering the effect of neighbouring slip layers (see also Evers *et al.*, 2004a,b), while Déprés (2004) has incorporated this effect in an alternative approach presented later in this chapter.

III.2.2 Presentation of the boundary value problem

The 3D boundary value problems simulated with DDD are described in Fig. III.2. A channel whose height, h, and depth, w, are set to $10\,\mu$m in the simulations is considered. Various widths, s, ranging from 1 to $5\,\mu$m are set to analyse the channel size effects. Periodic boundary conditions are considered at the top and bottom faces to represent an infinite channel along the Z–direction. The other four faces are assumed impenetrable by dislocations, i.e., dislocations are constrained inside the channel. Single slip systems are taken into account. The slip planes can be orthogonal to the boundary (Fig. III.2(a)) or inclined by an angle θ with respect to the Y–axis (Fig. III.2(b)). In the case of double slip, the global axes, X, Y and Z are parallel to (110), $(\bar{1}1\bar{1})$ and $(\bar{1}12)$ orientations, respectively. The two slip systems correspond to systems B4 ($b := (\bar{1}01), n := (111)$) and C1($b := (011), n := (\bar{1}\bar{1}1)$) according to the Schmid–Boas notation (Fig. III.2(c)). As the double slip case is still under investigation, the simulations are not presented in this work. Franck–Read sources are randomly distributed on equidistant slip planes and the distance between them is the intrinsic length l taken between $l = 0.01$ and $10\,\mu$m. Each slip plane has a $0.1\,\mu$m Franck–Read source. Note that, as the height of the simulated channel is set to $h = 10\,\mu$m, the number of slip planes in the channel depends on the intrinsic length. Consequently, $l = 10\,\mu$m is a limiting case where only one slip plane is embedded in the center of the channel structure.

Elastic properties of the modelled channel are assumed isotropic with $\mu = 42$ GPa and $\nu = 0.31$. A local shear stress, τ, up to 600 MPa is applied. In order to simplify the calculations and analyses, cross slip is avoided and image forces of the boundaries are not taken into account.

III.2.3 Analytical expressions of the multilayer pileup hardening

Work–hardening induced by non–interacting pileups has been derived analytically from continuum dislocation dynamics. Mura suggested a simple solution for work–hardening by multilayer pileups (Forest and Sedláček, 2003).

$$H_{Mura} = \frac{4\mu\, l}{\pi\,(1-\nu)\, s}. \tag{III.3}$$

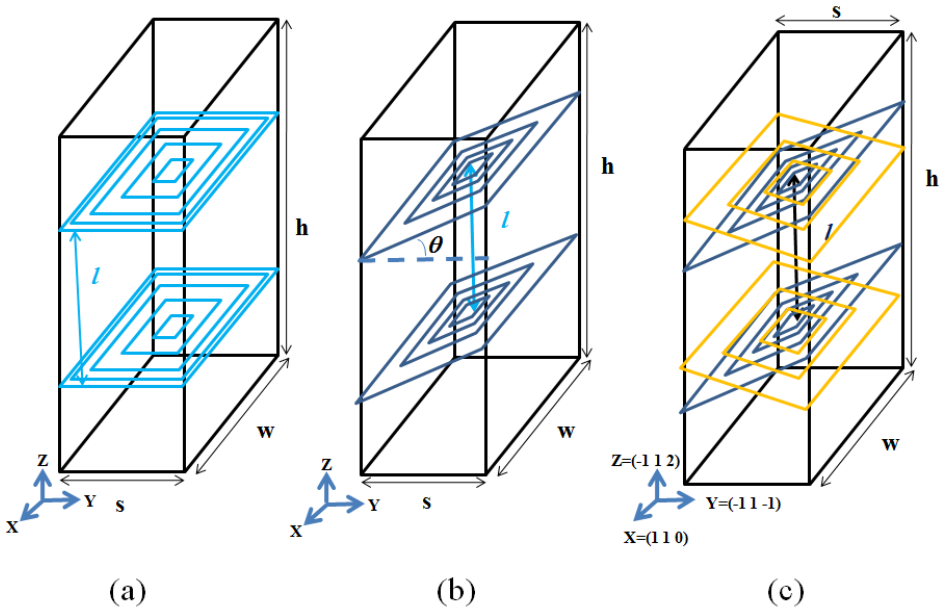

Figure III.2 : Description of the boundary value problems simulated with DDD. A channel, infinite along the Z–direction and of various widths, s, is considered with: (a) single slip systems and slip planes orthogonal to the boundaries; (b) single slip systems and slip planes inclined by an angle θ with respect to the Y–axis and (c) double slip systems. The case (c) of double slip is still under investigation and is not presented in this work. The distance between two neighbouring slip layers is the intrinsic length, l.

It assumes that dislocations moving on a slip plane are only affected by pileups on the same slip plane. Additional stresses induced by dislocations on other slip planes are ignored. Hence, Eq. (III.3) is similar to a solution for single layer pileups. Accordingly, this works reasonably for large intrinsic lengths l (see Fig. III.1(b)).

Déprés (2004) proposed an alternative model where the additional stresses from pileups on neighbouring slip planes are considered as well as those induced by single layer pileups. The additional stresses decrease exponentially for larger values of l (see the red line in Fig. III.1(b)). This approach can be applied to analyse multilayer pileup hardening without any limitation. We have

$$H_{Déprés} = \frac{4\mu\left[1+\exp\left(-k\frac{l}{s}\right)\right]}{\pi\left(1-\nu\right)\left\{2+\left(\frac{s}{l}-2\right)\left[1-\exp\left(-k\frac{l}{s}\right)\right]\right\}}, \tag{III.4}$$

where k is a parameter setting the magnitude of the additional work–hardening, increasing k leads to wider zones affected by the additional stress field. This formula is an interpolation function identified from DDD calculations. Here, the calibrated value $k = 2.0$ is taken to fit the results of DDD simulations. Déprés' expression exhibits two kinds of limiting cases: Mura's solution is one of these limiting cases for large enough l due to vanishingly small exponential terms in Eq. (III.4). The other limiting case, obtained for vanishingly small intrinsic lengths, l, or infinite widths of the channel, s, is

$$\lim_{l/s\to 0} H_{Déprés} = \frac{8\mu}{\pi\left(1-\nu\right)\left(k+2\right)}. \tag{III.5}$$

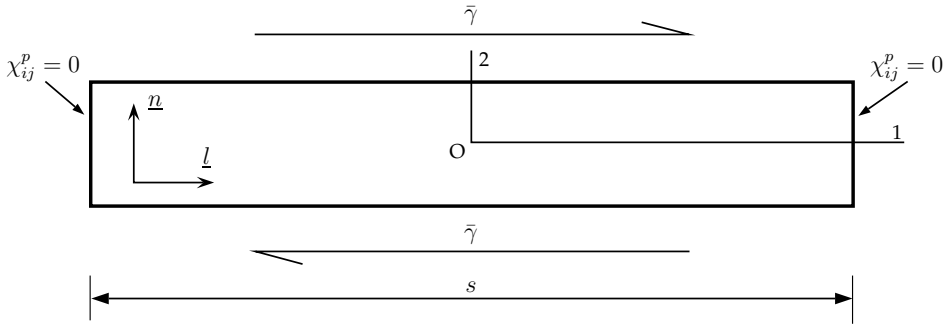

Figure III.3 : Single slip in the elasto–plastic channel under simple shear studied with the *microcurl* model.

Note that in this limiting case ($l/s \to 0$), the work–hardening is not affected by any size, s nor is l.

III.3 Application of the *microcurl* model to an elasto–plastic channel under simple shear

The elasto–plastic channel under simple shear described in Fig. III.3 is considered with the components of the plastic micro–deformation, χ^p_{ij}, vanishing at both ends and with periodic boundary conditions at the top and bottom of the channel. This boundary value problem has been chosen in order to have similar boundary conditions to the ones applied in DDD. Indeed, imposing χ^p_{ij} to vanish at the ends of the channel leads to a constraint of the dislocations inside the channel. In the same way as in Section II.3.4, where the *microcurl* model is applied to a two–phase periodic microstructure under simple shear, the model is now used for a channel. The unknowns of the problem within the context of small deformation theory remain as in Eq. (II.97),

$$u_1 = \bar{\gamma} x_2, \quad u_2(x_1), \quad u_3 = 0, \quad \chi^p_{12}(x_1), \quad \chi^p_{21}(x_1), \tag{III.6}$$

i.e., one component of the displacement vector and two components of the plastic micro–deformation tensor. Recalling that,

$$\underset{\sim}{\boldsymbol{H}}^p = \gamma \underline{\boldsymbol{l}} \otimes \underline{\boldsymbol{n}} = \gamma \underline{\boldsymbol{e}}_1 \otimes \underline{\boldsymbol{e}}_2, \tag{III.7}$$

we have

$$\left[\underset{\sim}{\boldsymbol{H}}\right] = \begin{bmatrix} 0 & \bar{\gamma} & 0 \\ u_{,1} & 0 & 0 \\ 0 & 0 & 0 \end{bmatrix}, \quad \left[\underset{\sim}{\boldsymbol{H}}^p\right] = \begin{bmatrix} 0 & \gamma & 0 \\ 0 & 0 & 0 \\ 0 & 0 & 0 \end{bmatrix}, \quad \left[\underset{\sim}{\boldsymbol{H}}^e\right] = \begin{bmatrix} 0 & \bar{\gamma}-\gamma & 0 \\ u_{2,1} & 0 & 0 \\ 0 & 0 & 0 \end{bmatrix}, \tag{III.8}$$

and

$$\left[\underset{\sim}{\boldsymbol{\chi}}^p\right] = \begin{bmatrix} 0 & \chi^p_{12}(x_1) & 0 \\ \chi^p_{21}(x_1) & 0 & 0 \\ 0 & 0 & 0 \end{bmatrix}, \quad \left[\operatorname{curl} \underset{\sim}{\boldsymbol{\chi}}^p\right] = \begin{bmatrix} 0 & 0 & -\chi^p_{12,1} \\ 0 & 0 & 0 \\ 0 & 0 & 0 \end{bmatrix}. \tag{III.9}$$

The resulting stress tensors are

$$\left[\underset{\sim}{\boldsymbol{\sigma}}\right] = \mu \begin{bmatrix} 0 & \bar{\gamma}-\gamma+u_{2,1} & 0 \\ \bar{\gamma}-\gamma+u_{2,1} & 0 & 0 \\ 0 & 0 & 0 \end{bmatrix}, \quad \left[\underset{\approx}{\boldsymbol{s}}\right] = -H_\chi \begin{bmatrix} 0 & \gamma-\chi^p_{12} & 0 \\ -\chi^p_{21} & 0 & 0 \\ 0 & 0 & 0 \end{bmatrix}, \tag{III.10}$$

$$\left[\underset{\sim}{\boldsymbol{M}}\right] = \begin{bmatrix} 0 & 0 & -A\chi^p_{12,1} \\ 0 & 0 & 0 \\ 0 & 0 & 0 \end{bmatrix}, \quad \left[\operatorname{curl}\underset{\sim}{\boldsymbol{M}}\right] = \begin{bmatrix} 0 & -A\chi^p_{12,11} & 0 \\ 0 & 0 & 0 \\ 0 & 0 & 0 \end{bmatrix}. \tag{III.11}$$

The balance equation previously given in Eq. (II.85), $\underset{\sim}{\boldsymbol{s}} = -\operatorname{curl}\underset{\sim}{\boldsymbol{M}}$, gives $\chi^p_{21} = 0$ and the micro–plastic slip result,

$$\gamma = \chi^p_{12} - \frac{A}{H_\chi}\chi^p_{12,11}. \tag{III.12}$$

The intrinsic length defined in Eq. (II.92) of Chapter II is still valid and is denoted

$$l_{SGP} = \sqrt{\frac{A}{H_\chi}} \tag{III.13}$$

in order to be distinguished from the intrinsic length of DDD, l. In the channel, the plasticity criterion stipulates that

$$\sigma_{12} + s_{12} = \tau_c + \bar{H}\,\gamma, \tag{III.14}$$

where $\bar{H}$ is an additional linear hardening modulus considered in this case as in Aslan *et al.* (2011). The plasticity criterion gives the second order differential equation for the micro–deformation variable, χ^p_{12},

$$\frac{1}{\omega^2}\,\chi^p_{12,11} - \chi^p_{12} = \frac{\tau_c - \sigma_{12}}{\bar{H}}, \quad \text{with} \quad \omega = \sqrt{\frac{H_\chi \bar{H}}{A\left(H_\chi + \bar{H}\right)}}, \tag{III.15}$$

where $1/\omega$ is the characteristic length of this boundary value problem:

$$l_{BVP} = \frac{1}{\omega}. \tag{III.16}$$

The force stress balance equation requires σ_{12} to be constant. It follows that the non–homogeneous part of the differential equation is constant and then the profile of χ^p_{12} is hyperbolic :

$$\chi^p_{12} = a\cosh(\omega x) + c. \tag{III.17}$$

Here, a and c are constants to be determined assuming the following symmetry conditions ($\chi^p_{12}(-s/2) = \chi^p_{12}(s/2)$). Note that the additional linear hardening considered in this case leads to a different profile of the micro–deformation variable from the parabolic profile found in the soft phase of the periodic microstructure considered in Section II.3.4. In what follows, we will see that this additional linear hardening affects the local and macroscopic behaviour while the main effects of the *microcurl* model presented in Cordero *et al.* (2010) (and in Chapter II) remain.

The coefficients a and c can be identified using the following boundary and periodicity conditions:

- Boundary conditions at both ends of the channel, $\chi^p_{12}(\pm s/2) = 0$:

$$a\cosh\left(\omega\frac{s}{2}\right) + c = 0. \tag{III.18}$$

- Periodicity of displacement component u_2. The constant stress component is

$$\sigma_{12} = \mu(\bar{\gamma} - \gamma + u_{2,1}), \tag{III.19}$$

its value is obtained from the plasticity criterion given in Eq. III.14:

$$\sigma_{12} = \tau_c + \bar{H}\,\gamma - A\chi^p_{12,11}. \tag{III.20}$$

It follows that

$$u_{2,1} = \frac{\sigma_{12}}{\mu} - \bar{\gamma} + \gamma = \frac{\tau_c}{\mu} - \bar{\gamma} + \frac{A\,\omega^2 a}{\bar{H}}\cosh(\omega x) + \frac{\bar{H}+\mu}{\mu}c. \tag{III.21}$$

The average on the channel vanishes,

$$\int_{-s/2}^{s/2} u_{2,1}\,dx = 0, \tag{III.22}$$

and gives

$$\left(\frac{\tau_c}{\mu} - \bar{\gamma}\right)s + \frac{2A\,\omega\,a}{\bar{H}}\sinh\left(\omega\frac{s}{2}\right) + \frac{\left(\bar{H}+\mu\right)s}{\mu}c = 0. \tag{III.23}$$

The resolution of Eqs. (III.18) and (III.23) gives a and c:

$$a = \left(\frac{\tau_c}{\mu} - \bar{\gamma}\right)\left[\frac{A\,\omega\sinh\left(\omega\frac{s}{2}\right)}{s}\left(\frac{\left(\bar{H}+\mu\right)\coth\left(\omega\frac{s}{2}\right)s}{A\,\omega\,\mu} - \frac{2}{\bar{H}}\right)\right]^{-1}, \tag{III.24}$$

$$c = -a\cosh\left(\omega\frac{s}{2}\right). \tag{III.25}$$

The macroscopic stress tensor component Σ_{12} is defined as the mean value of the stress component σ_{12} over the channel size, s. Its expression is derived from Eq. (III.20):

$$\Sigma_{12} = <\sigma_{12}> = \frac{1}{s}\int_{-s/2}^{s/2}\sigma_{12}\,dx = \tau_c + \bar{H}\langle\gamma\rangle - A\langle\chi^p_{12,11}\rangle, \tag{III.26}$$

where brackets $<>$ denote the average values over the microstructure unit cell. The mean plastic slip is obtained from Eq. (III.12):

$$\langle\gamma\rangle = \left\langle\chi^p_{12} - \frac{A}{H_\chi}\chi^p_{12,11}\right\rangle = \frac{2A\,\omega\,a\,\sinh\left(\omega\frac{s}{2}\right)}{\bar{H}\,s} + c. \tag{III.27}$$

From this equation we obtain alternative expressions of a and c expressed as functions of $\langle\gamma\rangle$,

$$a = -\langle\gamma\rangle\left[A\,\omega\sinh\left(\omega\frac{s}{2}\right)\left(\frac{\coth\left(\omega\frac{s}{2}\right)}{A\,\omega} - \frac{2}{\bar{H}\,s}\right)\right]^{-1}, \tag{III.28}$$

$$c = \langle\gamma\rangle\left(1 - \frac{2A\,\omega}{\coth\left(\omega\frac{s}{2}\right)\bar{H}\,s}\right)^{-1} \tag{III.29}$$

and of the macroscopic stress

$$\Sigma_{12} = \tau_c + \bar{H}\,c. \tag{III.30}$$

It should be noted that the hardening produced by the model is a combination of the kinematic hardening arising from the higher order back–stress component and the linear isotropic hardening introduced in Eq. (III.14). Its modulus, H_{SGP}, is size–dependent and is obtained using Eqs. (III.29) and (III.30):

$$H_{SGP} = \bar{H}\left[1 - \frac{2A\,\omega}{\coth\left(\omega\frac{s}{2}\right)\bar{H}\,s}\right]^{-1}. \tag{III.31}$$

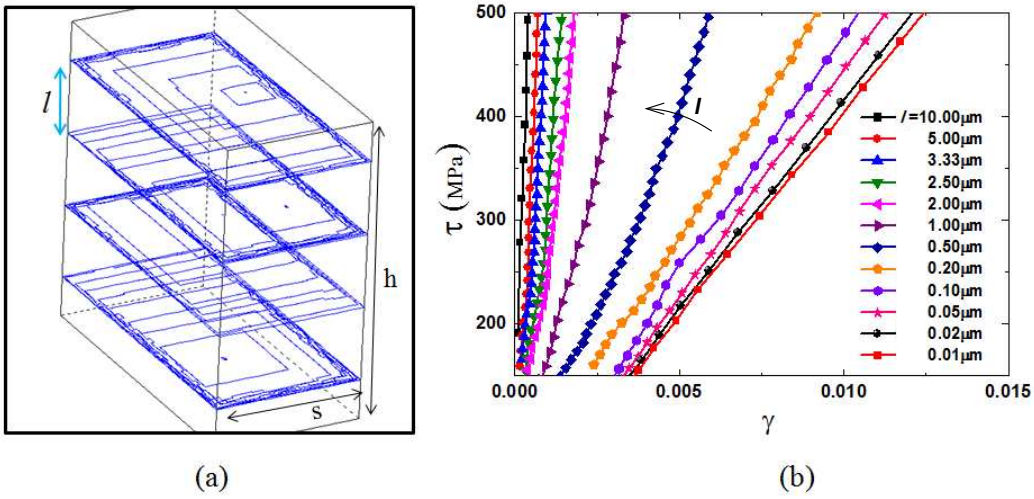

Figure III.4 : (a) Dislocation structures in the case of single slip with slip planes orthogonal to the boundaries (described in Fig. III.2(a)) under a local shear stress $\tau = 200$ MPa, in a channel of width $s = 5\,\mu$m and with an intrinsic length $l = 2.5\,\mu$m. (b) Local stress–plastic slip curves for different intrinsic lengths, l, and a fixed channel width of $s = 1\,\mu$m.

III.4 Results and discussion

Results obtained from 3D DDD simulations and with the *microcurl* model (analytically and from finite element simulations) are compared and discussed in this section. The three boundary value problems simulated with 3D DDD and presented in Fig. III.2 are also studied with the *microcurl* model using a two–dimensional boundary value problem with specific boundary conditions as presented in Fig. III.3. An analytical solution was derived for the most simple case of single slip with slip planes orthogonal to the boundaries in Section III.3 and is used in what follows to obtain the overall size–dependent work–hardening and the plastic slip distribution. The *microcurl* model is numerically implemented and finite element simulations of the more complex cases are conducted under generalised plane strain conditions.

III.4.1 Work–hardening by multilayer pileups

III.4.1.1 Single slip case with slip planes orthogonal to the boundaries

Dislocation structures generated by a given applied stress are directly provided by DDD simulations of multilayer pileups. Figure III.4(a) presents these dislocation structures in a channel of width $s = 5\,\mu$m under a local shear stress $\tau = 200$ MPa and with an intrinsic length $l = 2.5\,\mu$m. A pileup structure is generated from the Frank–Read sources in each slip plane. The local stress–plastic slip curves presented in Fig. III.4(b) are obtained from DDD simulations using intrinsic lengths l ranging from 0.01 to $10\,\mu$m. As the amount of slip is proportional to the number of moving dislocations, it is directly related to the number of slip planes in the channel which is equal to h/l. Accordingly, smaller values of l increase the amount of slip at a given stress. However, this effect saturates since smaller values of l also increase the hindrance to dislocation motions caused by pileups on neighbouring slip planes, as already discussed earlier in this chapter.

The effect of the ratio s/l between the channel width and the distance between the slip

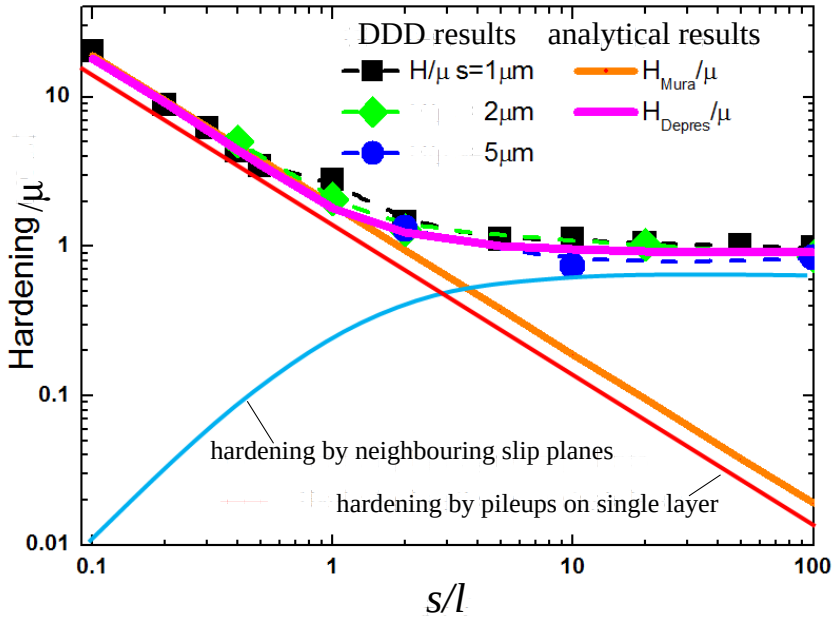

Figure III.5 : Relative work–hardening, H/μ, as a function of the ratio s/l with various intrinsic lengths $l = 0.01$ to $10\,\mu$m and channel widths $s = 1$, 3 and $5\,\mu$m. These results are obtained from DDD simulations (H), Mura's (H_{Mura}) and Déprés' ($H_{Déprés}$) solutions in the case of single slip with slip planes orthogonal to the boundaries (described in Fig. III.2(a)) and with $\mu = 42$ GPa and $\nu = 0.31$. The obtained work–hardening can be divided in two distinct parts: one is from pileups on single layers (red line) and the other is from neighbouring slip planes (light blue line).

planes on the overall work–hardening simulated with DDD is presented in a log–log diagram in Fig. III.5 and compared with the analytical expressions from Mura and Déprés (see Eqs. (III.3) and (III.4)). Two different regimes can be noted from the simulated work–hardening. When the channel width, s, is small compared to the intrinsic length, l, (i.e., $s/l < 1$), both DDD and the analytical results estimate a size dependent work–hardening that increases for decreasing values of the ratio s/l. If s is high compared to l (i.e., $s/l > 1$), results from DDD simulations and Déprés' analytical expression show that the work–hardening saturates and becomes size–independent. The simple model of Mura does not exhibit this second regime and the relation between the work–hardening and the ratio s/l remains the same. The effect of the ratio s/l on the work–hardening can be explained by two types of internal stresses that affect the motions of dislocations. On the one hand, moving dislocations on a slip plane are restricted by pileups on the same slip plane. The resulting hardening is called "hardening by pileups on single layer" and is represented with a red line in Fig. III.5. It gives a linear inverse relation close to Mura's model (in which only this type of hardening is considered as mentioned earlier in this chapter). On the other hand, moving dislocations are also restricted by the pileups of neighbouring slip planes. The resulting hardening is called "hardening by neighbouring slip planes" and is represented by the blue curved line in Fig. III.5. This hardening vanishes for small values of s/l. Indeed, when the distance between the slip planes is large, moving dislocations are not affected by pileups on neighbouring slip planes. The hardening–by–neighbouring slip planes saturates for large values of s/l as shown by Déprés (2004) (see the limit given in Eq. (III.5)). Consequently, the total work–hardening is mainly affected by single layer pileups in the size–dependent regime, when $s/l < 1$, and is more and

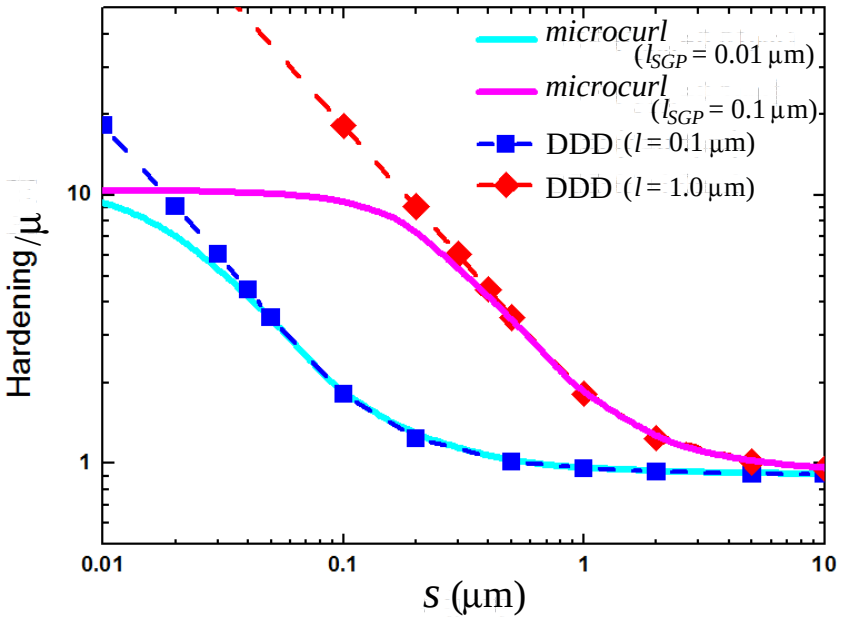

Figure III.6 : Relative work–hardening as a function of the channel width, s, in the case of single slip with slip planes orthogonal to the boundaries (described in Fig. III.2(a)) and with $\mu = 42$ GPa and $\nu = 0.31$. These results are obtained from DDD simulations with $l = 0.1$ and $1\,\mu$m and with the analytical expression from the *microcurl* model given in Eq. (III.31) with $l_{SGP} = 0.01$ and $0.1\,\mu$m. In this case, the *microcurl* model with an appropriate intrinsic length ($l_{SGP} \approx 0.1\,l$) can reproduce the work–hardening obtained from DDD simulations.

more affected by neighbouring pileups in the size–independent regime, $s/l > 1$.

The work–hardening produced by the micromorphic model, H_{SGP}, given in Eq. (III.31) has been designed to take into account both hardenings arising from pileups on single layers and from pileups on neighbouring slip planes. The hardening by pileups on single layer corresponds to the linear kinematic hardening from the *microcurl* model as described in Chapter II, while hardening–by–neighbouring slip planes corresponds to the additional hardening $\bar{H}$ introduced in Eq. (III.14). In fact, $\bar{H}$ has been considered to mimic the interaction hardening that occurs between neighbouring slip planes in DDD. This hardening is simply introduced in Eq. (III.14) as a size–independent linear hardening. In both *microcurl* model and DDD, it remains for very large microstructural sizes while the linear kinematic hardening generated by pileups on single layers vanishes. The value of the modulus $\bar{H}$ is then taken as the limit of $H_{Déprés}$ when $s \to \infty$ presented in Eq. (III.5). We have:

$$\bar{H} = \lim_{s\to\infty} H_{Déprés} = \frac{8\mu}{\pi\,(1-\nu)\,(k+2)}, \tag{III.32}$$

which gives $\bar{H} = 39$ GPa with the considered elastic properties of the channel, $\mu = 42$ GPa and $\nu = 0.31$, and the calibrated value $k = 2.0$. Figure III.6 presents the work–hardenings as a function of the channel width obtained from DDD simulations and with the analytical expression from the *microcurl* model given in Eq. (III.31). The curves from the *microcurl* model are obtained with calibrated intrinsic lengths l_{SGP} (see Eq. (III.13)) providing quantitative fittings of the results from DDD. For that, a fixed value of the coupling modulus, $H_\chi = 400$ GPa, is chosen regarding the results and discussions presented in the previous chapter. Then, the higher order modulus A is calibrated for each intrinsic length used in the

DDD simulations, l. It was found that the best quantitative fittings are obtained for moduli A verifying the correlation:

$$A \approx 0.01\, l^2\, H_\chi. \tag{III.33}$$

In what follows, the value of the coupling modulus $H_\chi = 400$ GPa remains and the correlation (III.33) is used as a guideline to calibrate the higher order modulus A for each l. The correlation (III.33) also means that l_{SGP} has to be approximately ten times smaller than l in order to yield similar results to both models:

$$l_{SGP} \approx 0.1\, l. \tag{III.34}$$

The length scales l_{SGP} and l represent very different concepts: l_{SGP} characterises the ratio of the higher order moduli A and H_χ while l represent the distance between active neighbouring slip planes. This is why considering the physically relevant characteristic length of the boundary value problem, l_{BVP}, is necessary to explain what is implied by the correlation (III.34). Indeed, l_{SGP} is associated to the thickness of the boundary layer and can be correlated to the intrinsic length of DDD from its expression given in Eq. (III.16) and the relation linking A and l given in Eq. (III.33). It follows that

$$l_{BVP} = 0.1\, l \sqrt{\frac{H_\chi + \bar{H}}{\bar{H}}} \tag{III.35}$$

which means that the thickness of the boundary layer and the distance between active neighbouring slip planes are correlated. With the values used in the present case, this gives $l_{BVP} \approx 0.3\, l$. With this correlation, it can be seen that the *microcurl* model reproduces the results obtained with DDD simulations except for very small channel widths for which the *microcurl* model saturates (see Chapter II).

III.4.1.2 Single slip case with inclined slip planes

The effects of inclined slip planes are analysed next. In DDD, as the distance between two opposite pileups of a slip plane, s_i, increases with the angle θ as shown in Fig. III.7(a), the work–hardening decreases for increasing values of θ. For example, $\theta = 90^o$ leads to $s_i \to \infty$, so that no pileup is generated in the channel and therefore no work–hardening. The relative work–hardening is presented in Fig. III.7(b) as a function of θ simulated by DDD and the *microcurl* model for various ratios s/l (and the corresponding ratios s/l_{SGP}). The smallest value of the ratio, $s/l = 0.5$, corresponds to the size–dependent regime in which single layer pileups are the main sources of work–hardening (see Fig. III.4). Increasing values of θ lead to a decreasing hardening with the two models. However, for $\theta = 90^o$, DDD simulations lead to almost no work–hardening while the *microcurl* model produces a work–hardening whose value is $H_{SGP} = \bar{H}$ (= the additional linear hardening). The two other ratios, $s/l = 2.$ and $s/l = 10.$, correspond to the regime in which the effect of neighbouring pileups is dominant. DDD simulations still exhibit a decreasing work–hardening due to inclined slip systems. This effect is very low with the *microcurl* model. The difference between the two models is in fact easy to explain. The additional work–hardening $\bar{H}$ due to the effect of neighbouring pileups has been chosen to be constant and was calculated for $\theta = 0^o$. It appears that the value of $\bar{H}$ should be calculated as a function of θ to model the work–hardening more accurately. However, to that purpose, an analytical expression or an interpolation function is needed to evaluate $\bar{H}$ as it was done with Déprés' expression. In the limiting case of $\theta = 90^o$ using DDD, no pileup is formed as dislocations move along the infinite direction of the channel so that no work–hardening develops. The kinematic hardening coming from the *microcurl* model also vanishes, but the additional linear hardening $\bar{H}$ remains. For this specific case, this additional linear hardening should be $\bar{H} = 0$.

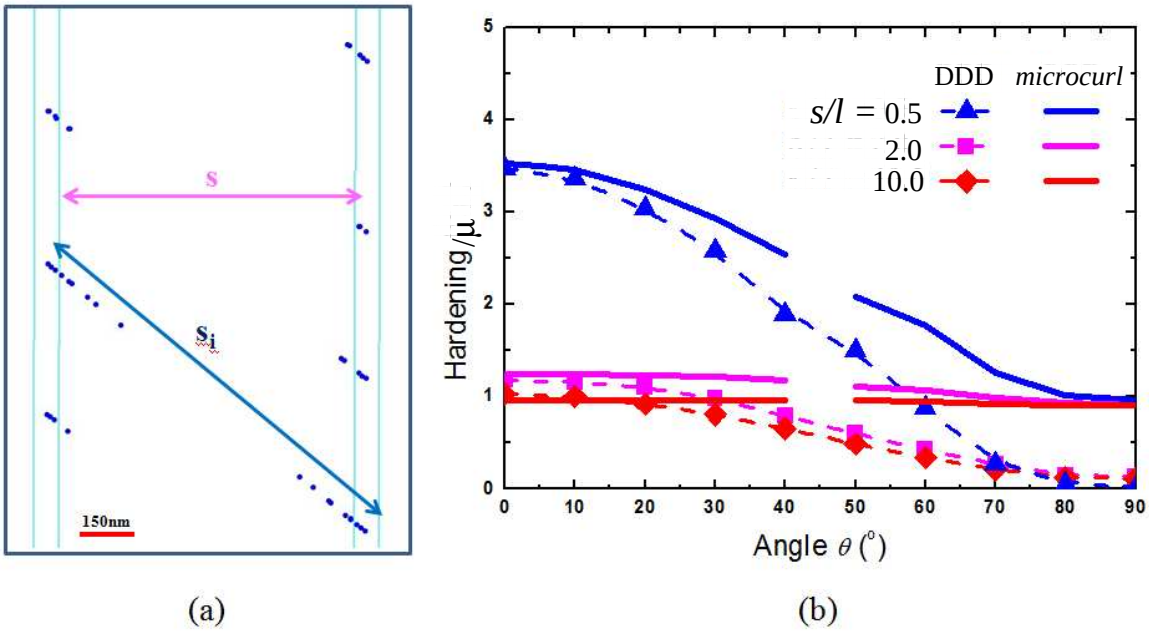

Figure III.7 : (a) Two–dimensional dislocation pileups structure on slip planes inclined of an angle $\theta = 40^o$ in a channel of width $s = 1\,\mu$m and with a intrinsic length $l = 0.5\,\mu$m (see Fig. III.2(b)). Increasing θ increases the distance between opposite pileups of a slip layer, i.e., $s_i > s$. (b) Relative work–hardening as a function of θ simulated by DDD and the *microcurl* model for various ratios s/l (and the corresponding ratios $s/l_{SGP} \approx 10.\, s/l$) and with $\mu = 42$ GPa and $\nu = 0.31$.

III.4.2 Distributions of local plastic slip

The local plastic slip distribution is also closely related to the ratio s/l. Distributions of γ along the channel width obtained with DDD in the case of single slip with slip planes orthogonal to the boundaries are presented in Fig. III.8 for different levels of the local shear stress, τ, and with two different ratios $s/l = 1.0$ and $s/l = 100.0$ leading to a size–dependent work–hardening and a size–independent work–hardening, respectively. The obtained profiles are such that γ vanishes at the boundaries of the channel (at $0.5\,\mu$m from the center of the channel) and is maximum close to the center of the channel. Small values of the ratio, $s/l \leq 1$, cause inhomogeneous plastic slip distributions while large values of the ratio, $s/l \gg 1$, provide almost homogeneous plastic slip distributions. Indeed, when work–hardening is size–independent, plastic slip distributions inside the channel are almost homogeneous. This homogeneity is broken when size effects appear. In both cases, γ increases with the local shear stress τ. Similar plastic slip distributions are presented in Baskaran *et al.* (2010). Plastic slip distributions are also obtained with the *microcurl* model and are compared with DDD results in Fig. III.9. The profiles of this figure are obtained under a local shear stress $\tau = 200$ MPa by DDD simulations and with the analytical expression of γ given in Eq. (III.12). Three ratios s/l (and again their corresponding ratios s/l_{SGP}) are analysed and the results show that the *microcurl* model reproduces quantitatively the distributions obtained with the DDD simulations. The parabolic profiles of γ obtained without additional linear hardening $\bar{H}$ and presented in Chapter II would have been very different from the present profiles. This shows that the additional hardening due to neighbouring pileups also affects significantly the plastic slip distributions. It has to be noted from Fig. III.9 that the plastic

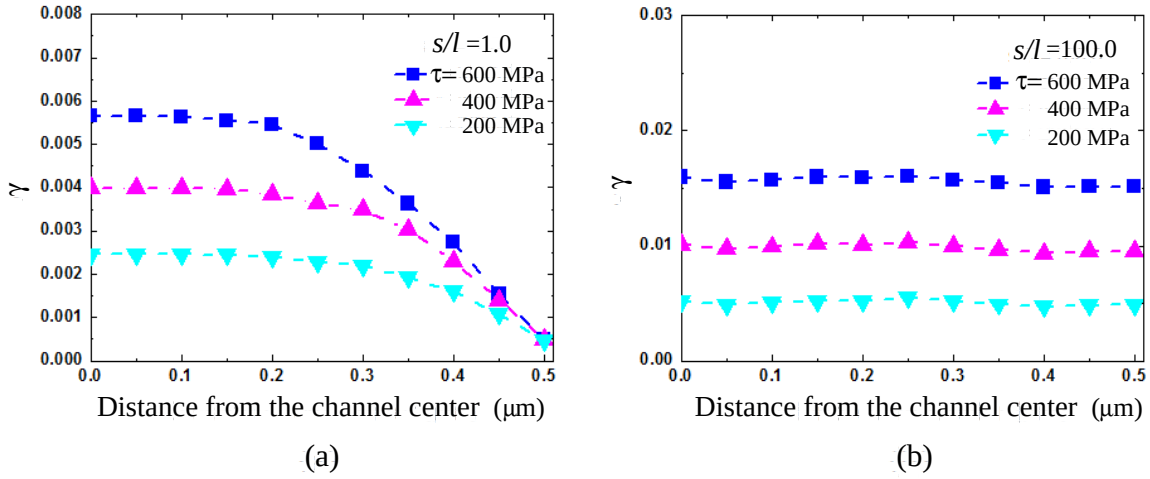

Figure III.8 : Plastic slip, γ, distributions along the channel width in the case of single slip with slip planes orthogonal to the boundaries (described in Fig. III.2(a)) for different levels of the local shear stress, τ ($\mu = 42$ GPa and $\nu = 0.31$). These profiles are obtained by DDD simulations with two different ratios $s/l = 1.0$ and $s/l = 100.0$ leading to (a) a size–dependent work–hardening and (b) a size–independent work–hardening, respectively.

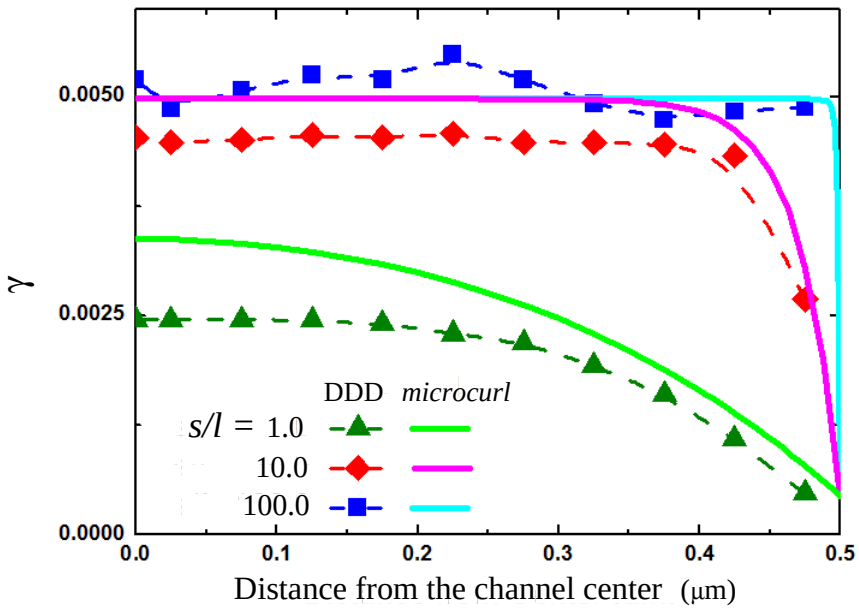

Figure III.9 : Comparison of the plastic slip distributions modelled by DDD and the *microcurl* model along the channel width in the case of single slip with slip planes orthogonal to the boundaries (described in Fig. III.2(a)) with a local shear stress of $\tau = 200$ MPa. These profiles are obtained for three different s/l ratios (and their corresponding ratios $s/l_{SGP} \approx 10.\, s/l$), and with $l = 0.1\,\mu$m and $l_{SGP} = 0.01\,\mu$m.

slip given by the *microcurl* model is not $\gamma = 0$ at the boundaries. In fact, the degrees of freedom χ_{ij}^{p} are imposed to be zero at both ends of the channel as recalled by Fig. III.3. Then, the boundary conditions needed to mimic boundaries impenetrable by dislocations as in DDD are ensured by the internal constraint between macro (γ) and micro (χ_{ij}^{p}) –variables (see Subsection II.3.3). As already shown, these variables can be more or less constrained depending on the coupling modulus and, even if they are very close to each other, γ is slightly different from χ_{12} (and consequently from zero) at the boundaries. It can finally be noted from Figs. III.8 and III.9 that the correlation between the thickness of the boundary layer, associated to l_{BVP}, and the distance l is verified: for a fixed width s, decreasing l leads to sharper profiles at the boundaries, i.e., to thinner boundary layers.

Comparing the overall behaviour and local distributions obtained from DDD simulations and from the *microcurl* model pointed out two important results. First, for a fixed coupling modulus, H_{χ}, the higher order modulus, A, of the *microcurl* model can be calibrated for each intrinsic length used in the DDD simulations so that the two models give similar results. Then, a correlation is found between the thickness of the boundary layer and the distance between active neighbouring slip planes.

References

Aifantis E.C. (1984). *On the microstructural origin of certain inelastic models.* Journal of Engineering Materials and Technology, vol. 106, pp 326–330.

Aslan O., Cordero N.M., Gaubert A., and Forest S. (2011). *Micromorphic approach to single crystal plasticity and damage.* International Journal of Engineering Science.

Baskaran R., Akarapu S., Mesarovic S.D., and Zbib H.M. (2010). *Energies and distributions of dislocations in stacked pile-ups.* International Journal of Solids and Structures, vol. 47 n° 9, pp 1144–1153.

Bassani J.L., Needleman A., and Van der Giessen E. (2001). *Plastic flow in a composite: a comparison of nonlocal continuum and discrete dislocation predictions.* International journal of solids and structures, vol. 38 n° 5, pp 833–853.

Bittencourt E., Needleman A., Gurtin M.E., and Van der Giessen E. (2003). *A comparison of nonlocal continuum and discrete dislocation plasticity predictions.* Journal of the Mechanics and Physics of Solids, vol. 51 n° 2, pp 281 – 310.

Busso E.P., Meissonier F.T., and O'Dowd N.P. (2000). *Gradient-dependent deformation of two-phase single crystal.* Journal of Mechanics and Physics of Solids, vol. 48 n° 11, pp 2333–2361.

Chang H.J. (2009). *Analysis of nano indentation size effect based on dislocation dynamics and crystal plasticity.* Thèse de Doctorat, Institut National Polytechnique de Grenoble / Seoul National University.

Chang H.J., Fivel M., Rodney D., and Verdier M. (2010). *Multiscale modelling of indentation in FCC metals: From atomic to continuum.* Comptes Rendus Physique.

Chang H.J., Gaubert A., Fivel M., Berbenni S., Bouaziz O., and Forest S. (2011). *Analysis of particle induced dislocation structures using three-dimensional dislocation dynamics and strain gradient plasticity.* Computational Materials Science.

Cleveringa H.H.M., Van der Giessen E., and Needleman A. (1997). *Comparison of discrete dislocation and continuum plasticity predictions for a composite material.* Acta materialia, vol. 45 n° 8, pp 3163–3179.

Cleveringa H.H.M., Van der Giessen E., and Needleman A. (1998). *Discrete dislocation simulations and size dependent hardening in single slip.* Le Journal de Physique IV, vol. 8 n° PR4, pp 83–92.

Cleveringa H.H.M., Van der Giessen E., and Needleman A. (1999). *A discrete dislocation analysis of residual stresses in a composite material.* Philosophical Magazine A, vol. 79 n° 4, pp 893–920.

Cordero N.M., Gaubert A., Forest S., Busso E.P., Gallerneau F., and Kruch S. (2010). *Size effects in generalised continuum crystal plasticity for two–phase laminates.* Journal of the Mechanics and Physics of Solids, vol. 58, pp 1963–1994.

Déprés C. (2004). *Modélisation physique des stades précurseurs de l'endommagement en fatigue dans l'acier inoxydable austénitique 316L.* Thèse de Doctorat, Institut National Polytechnique de Grenoble.

Déprés C., Robertson C.F., and Fivel M. (2004). *Low-strain fatigue in AISI 316L steel surface grains: a three-dimensional discrete dislocation dynamics modelling of the early cycles I. Dislocation microstructures and mechanical behaviour.* Philosophical Magazine, vol. 84 n° 22, pp 2257–2275.

Evers L.P., Brekelmans W.A.M., and Geers M.G.D. (2004a). *Non-local crystal plasticity model with intrinsic SSD and GND effects.* Journal of the Mechanics and Physics of Solids, vol. 52 n° 10, pp 2379–2401.

Evers L.P., Brekelmans W.A.M., and Geers M.G.D. (2004b). *Scale dependent crystal plasticity framework with dislocation density and grain boundary effects.* International journal of solids and structures, vol. 41 n° 18-19, pp 5209–5230.

Fivel M., Tabourot L., Rauch E., and Canova G. (1998). *Identification through mesoscopic simulations of macroscopic parameters of physically based constitutive equations for the plastic behaviour of fcc single crystals.* Journal de Physique IV, vol. 8, pp 151–158.

Forest S. and Sedláček R. (2003). *Plastic slip distribution in two–phase laminate microstructures: Dislocation–based vs. generalized–continuum approaches.* Philosophical Magazine A, vol. 83, pp 245–276.

Ghoniem N.M. and Sun L.Z. (1999). *Fast-sum method for the elastic field of three-dimensional dislocation ensembles.* Physical Review B, vol. 60, pp 128–140.

Hall E.O. (1951). *The deformation and ageing of mild steel: III discussion of results.* Proceedings of the Physical Society. Section B, vol. 64, pp 747.

Kim G.S., Fivel M., Lee H.J., Shin C., Han H.N., Chang H.J., and Oh K.H. (2010). *A discrete dislocation dynamics modeling for thermal fatigue of preferred oriented copper via patterns.* Scripta Materialia, vol. 63 n° 7, pp 788–791.

Kubin L.P., Canova G., Condat M., Devincre B., Pontikis V., and Bréchet Y. (1992). *Dislocation microstructures and plastic flow: a 3D simulation.* Solid State Phenomena, vol. 23, pp 455–472.

Madec R., Devincre B., Kubin L., Hoc T., and Rodney D. (2003). *The role of collinear interaction in dislocation-induced hardening.* Science, vol. 301 n° 5641, pp 1879–1882.

Mughrabi H. (1983). *Dislocation wall and cell structures and long-range internal stresses in deformed metal crystals.* Acta metallurgica, vol. 31 n° 9, pp 1367–1379.

Ortiz M., Repetto E.A., and Stainier L. (2000). *A theory of subgrain dislocation structures.* Journal of the Mechanics and Physics of Solids, vol. 48 n° 10, pp 2077–2114.

Petch N.J. (1953). *The cleavage strength of polystrals.* J. Iron Steel Inst, vol. 173, pp 25–28.

Schouwenaars R., Seefeldt M., and Houtte P.V. (2010). *The stress field of an array of parallel dislocation pile-ups: Implications for grain boundary hardening and excess dislocation distributions.* Acta Materialia, vol. 58 n° 13, pp 4344–4353.

Shin C.S., Fivel M., Verdier M., and Oh K.H. (2003). *Dislocation-impenetrable precipitate interaction: a three-dimensional discrete dislocation dynamics analysis.* Philosophical Magazine, vol. 83 n° 31-34, pp 3691–3704.

Shu J.Y., Fleck N.A., Van der Giessen E., and Needleman A. (2001). *Boundary layers in constrained plastic flow : comparison of non local and discrete dislocation plasticity.* Journal of the Mechanics and Physics of Solids, vol. 49, pp 1361–1395.

Weygand D., Friedman L.H., Van der Giessen E., and Needleman A. (2001). *Discrete dislocation modeling in three-dimensional confined volumes.* Materials Science and Engineering A, vol. 309, pp 420–424.

Yefimov S., Groma I., and Van der Giessen E. (2004). *A comparison of a statistical-mechanics based plasticity model with discrete dislocation plasticity calculations.* J. Mech. Phys. Solids, vol. 52, pp 279–300.

Yefimov S. and Van der Giessen E. (2005). *Multiple slip in a strain-gradient plasticity model motivated by a statistical-mechanics description of dislocations.* International Journal of Solids and Structures, vol. 42, pp 3375–3394.

Zbib H.M., Rhee M., and Hirth J.P. (1998). *On plastic deformation and the dynamics of 3D dislocations.* International journal of mechanical sciences, vol. 40 n° 2-3, pp 113–127.

Résumé

Dans ce chapitre, les effets de taille induits par les empilements de dislocations sont étudiés en termes de distribution du glissement plastique et d'écrouissage global par dynamique des dislocations discrètes (DDD) et avec le modèle *microcurl*. Pour cela, des dislocations coin sont considérées enfermées dans un couloir. Celles-ci se déplacent et s'empilent sur des plans inclinés ou non. Les effets de la taille du couloir sur le comportement mécanique obtenus avec les deux modèles sont analysés et comparés en utilisant des solutions analytiques et numériques. Les écrouissages produits par des empilements isolés et par les interactions avec les plans de glissement voisins sont pris en compte dans cette étude.

Bien que représentant des concepts physiques très différents, les longueurs intrinsèques des modèles ont toutes deux un impact majeur sur la distribution du glissement plastique et sur l'écrouissage global. Pour la DDD, la longueur intrinsèque, l, représente la distance entre plans de glissement actifs voisins alors que celle du modèle *microcurl*, l_{SGP}, caractérise le rapport des modules d'ordre supérieur, A et H_χ. Pour un module de couplage, H_χ, fixe, le module d'ordre supérieur, A, peut être calibré pour chaque longueur intrinsèque utilisée dans les simulations de DDD afin que les deux modèles produisent un comportement macroscopique et des distributions locales similaires. Ainsi, il est montré que les résultats des simulations de DDD et du modèle *microcurl* sont équivalents quand l_{SGP} est environ dix fois inférieure à l. Par ailleurs, une corrélation entre l'épaisseur de la couche limite et la distance entre les plans de glissement voisins est mise en avant.

Chapter -IV-

Grain size effects in generalised continuum crystal plasticity

Abstract

The aim of this chapter is to investigate the grain size effects in generalised continuum crystal plasticity. To that purpose, the *microcurl* model is used to study the impact of the microstructure size on the overall response of polycrystalline aggregates. Two–dimensional finite element simulations are performed for several polycrystals of 24 and 52 grains. Different sets of material parameters are used to explore their effects on the overall response. A first set of simulations shows that a wide range of scaling law exponents can be produced by the model without additional classical isotropic hardening. The simple shear response of idealised aluminium polycrystals is then simulated with material parameters chosen according to the previous results. It is shown that the grain size has a strong effect on the overall behaviour of these polycrystals. In particular, material parameters can be set to retrieve the Hall–Petch scaling law.

Contents

Preamble: The work presented in this chapter will be published in the book "*Scale transition for plastic crystalline and microstructured materials: from experiment to numerical modeling, ICACM 2010*" in the paper "*Grain size effects in generalised continuum crystal plasticity*" (Cordero *et al.*, 2010a).

IV.1 Size effects induced by grain boundaries

The *microcurl* model is now applied to simulate the response of polycrystals and the effects of the size of their microstructure.

The interface conditions at grain boundaries play a major role in the simulated size effects in the polycrystal behaviour. No special interface law is considered here, although such physically motivated interface conditions exist in the literature, see Gurtin and Anand (2008). Instead we consider the canonical interface conditions that arise from the formulation of the balance equations of the *microcurl* continuum model. These conditions are the continuity of displacement, $\underline{\boldsymbol{u}}$, and the continuity of plastic micro–deformation, $\underset{\sim}{\boldsymbol{\chi}}^p$. These conditions also include the continuity of the simple and double tractions, $\underline{\boldsymbol{t}}$ and $\underset{\sim}{\boldsymbol{M}}$, described in Eq. (II.86). Continuity of displacement excludes grain boundary cracking and sliding. Continuity of plastic micro–deformation is reminiscent of the fact that dislocations generally do not cross grain boundaries, especially for such random grain boundaries. Note that in the *microcurl* model, only the kinematic degrees of freedom $\underset{\sim}{\boldsymbol{\chi}}^p$ are continuous. This is not the case of the plastic deformation, $\underset{\sim}{\boldsymbol{H}}^p$, which is treated here as an internal variable. However, due to the internal constraint discussed in section II.3.3, $\underset{\sim}{\boldsymbol{H}}^p$ closely follows the plastic micro–deformation, so that it is quasi–continuous at grain boundaries when the penalty coefficient, H_χ, is high enough. Conversely, lower values of H_χ may allow slightly discontinuous plastic deformation, which may be tentatively interpreted as dislocation sinking inside grain boundaries. The continuity of the associated tractions expresses the transmission of classical and generalised internal forces from one grain to another through grain boundaries. Such continuum models are then able to mimic in that way the development of dislocation pile–ups at grain boundaries Forest and Sedláček (2003).

IV.1.1 Boundary value problem for polycrystals

The size effects exhibited by the solution of the boundary value problem are linked to an intrinsic length scale, l_s, introduced through the generalised moduli H_χ and A of Eq. (II.91) and defined as:

$$l_s = \sqrt{\frac{A}{H_\chi}}. \tag{IV.1}$$

This intrinsic length scale has to be consistent with the fact that plasticity effects occur at scales ranging from hundreds of nanometers to a few microns. In addition, as stated in section II.3.3, the coupling modulus, H_χ, has to be chosen high enough to ensure that $\underset{\sim}{\boldsymbol{\chi}}^p$ and $\underset{\sim}{\boldsymbol{H}}^p$ are close. H_χ also determines the scaling law exponent. These requirements are guidelines for the choice of relevant generalised moduli H_χ and A. The sets of material parameters used in this chapter are chosen in that way.

The finite element simulations have been made on periodic 2D meshes of periodic polycrystalline aggregates generated by a method based on Voronoi tessellations (Fig. IV.1(a)(b)). The integration order of elements is quadratic. The Voronoi polyhedra represent the grains, the random distribution of their centers has been controlled so that their sizes are sensibly the same, that is why we can reasonably assume that the mean grain size, d, is sufficient to characterise the microstructure of our aggregates. A random orientation is assigned to each grain and two slip systems are taken into account. In 2D, the plastic behaviour of f.c.c. crystals can be simulated with 2D planar double slip by considering two effective slip systems separated by an angle of 2ϕ (Asaro, 1983; Bennett and McDowell, 2003). Figure IV.1(c) describes the geometry. The slip system pair is oriented by the angle θ which is the grain orientation randomly fixed for each grain. For a f.c.c. crystal $\phi = 35.1°$, it corresponds to the orientation of the close–packed planes in the crystal lattice of the grain.

Periodic homogenisation for generalised continua is used to model the effective response of the polycrystal. The displacement field is assumed to be of the form

$$\underline{\boldsymbol{u}}\,(x) = \underset{\sim}{\boldsymbol{E}}.\underline{\boldsymbol{x}} + \underline{\boldsymbol{v}}\,(x), \tag{IV.2}$$

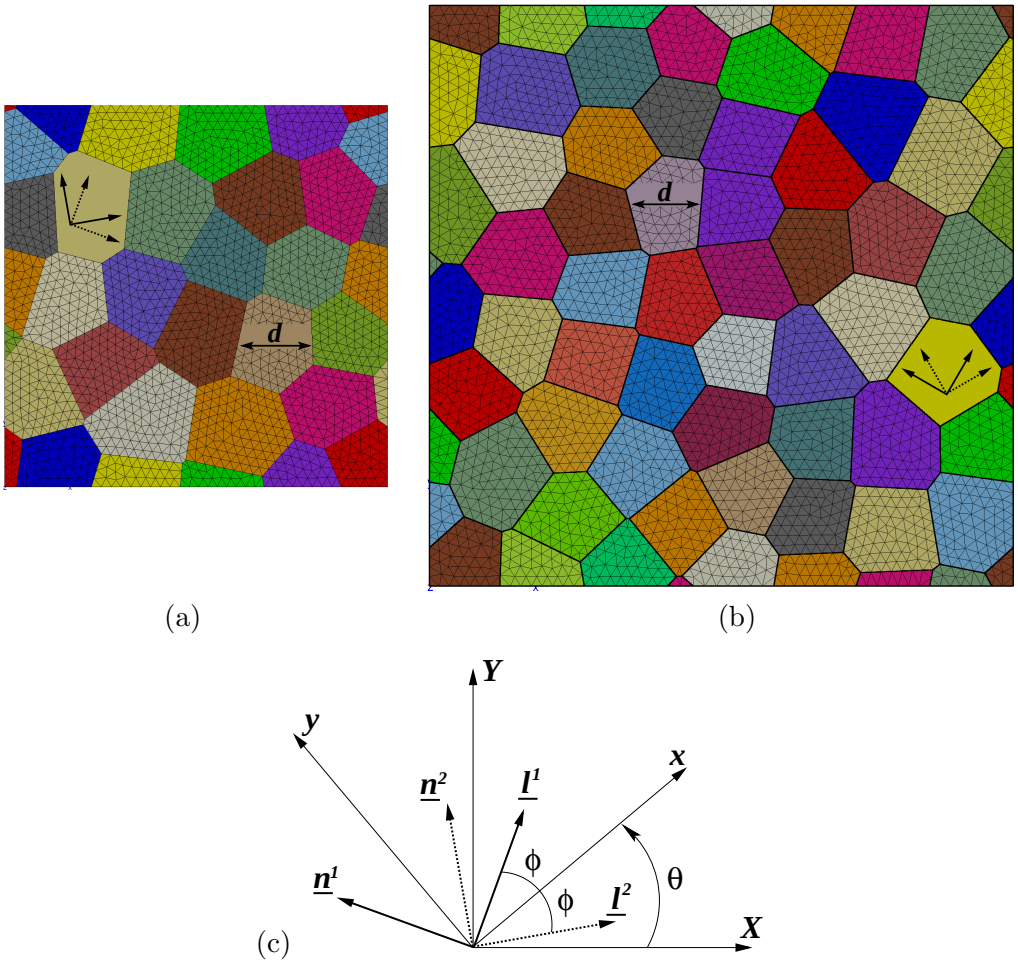

Figure IV.1 : Periodic meshes of the 2D periodic aggregates used in the finite element simulations: (a) 24 grains, (b) 52 gains. Two slip systems are taken into account in each randomly oriented grain. Various mean grain sizes, d, ranging from tens of nanometers to hundreds of microns, are investigated. (c) Description of the two effective slip systems for 2D planar double slip.

with the fluctuation $\underline{\boldsymbol{v}}$ periodic, meaning that it takes identical values at homologous points of the unit cell Forest *et al.* (2001). The plastic micro–deformation field, $\underset{\sim}{\boldsymbol{\chi}}^p$, is assumed to be periodic, meaning that no rotational macroscopic plastic deformation is imposed to the unit cell. Its components are equal at homologous opposite nodes. According to periodic homogenisation, the simple and double tractions $\underline{\boldsymbol{t}}$ and $\underset{\sim}{\boldsymbol{m}}$ are anti–periodic at homologous points of the unit cell.

Polycrystals are random materials so that the periodicity constraint may lead to a bias in the estimation of the effective properties. This boundary effect can be alleviated by considering several realisation of the microstructure and performing ensemble averaging Zeghadi *et al.* (2007).

IV.1.2 Overall stress and cyclic response of a polycrystalline aggregate

The finite element simulations of the boundary value problem presented previously have been conducted under generalised plane strain conditions on aggregates with a relatively small number of grains. The aim here is not to obtain a representative response but to catch

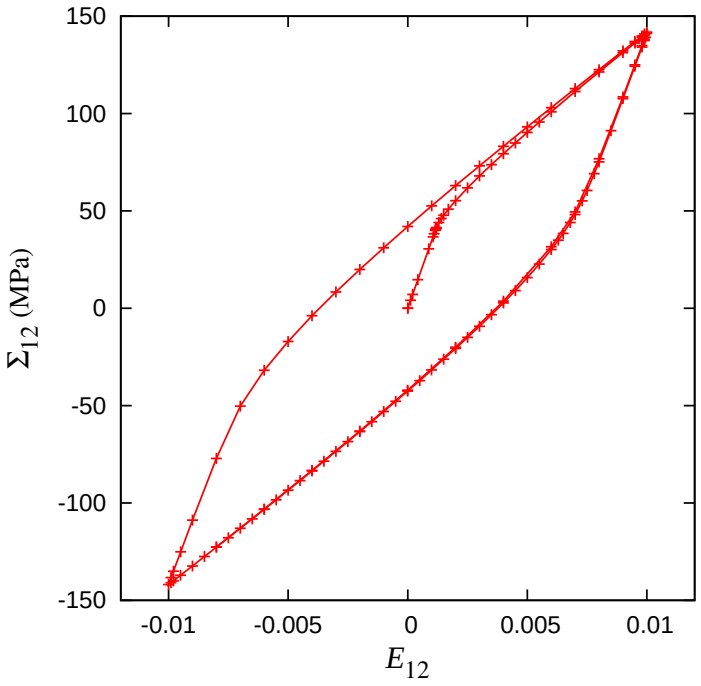

Figure IV.2 : Macroscopic stress–strain response of the 24–grain aggregate under cyclic simple shear loading conditions with a mean gain size $d \approx 0.2\mu$m. The set of material parameters used is labelled (c) in Table V.1.

the grain size effects and to explore qualitatively the impact of different sets of material parameters. In this section, a virtual material is considered with various intrinsic length scales. The macroscopic stress–strain curve shown in Fig. IV.2 is obtained by applying a cyclic simple shear loading controlled by the average stress component E_{12} on the aggregate of 24 grains with $d = 0.2\mu$m and the set of material parameters labelled (c) in Table V.1. The mean stress component Σ_{12} is then computed:

$$\Sigma_{12} = \frac{1}{V}\int_V \sigma_{12}\, dV, \quad E_{12} = \frac{1}{V}\int_V \varepsilon_{12}\, dV, \tag{IV.3}$$

where V denotes each polycrystal unit cell. The simulated response illustrates the kinematic hardening produced by the *microcurl* model. The stress–strain curves obtained in the next case (see Fig. V.1) show that this kinematic hardening is size–dependent: it increases for smaller grains. Note that the observed overall kinematic hardening has two distinct sources:

Table IV.1 : Sets of material parameters used in the 24–grain aggregate case (Fig IV.1(a)). The intrinsic length scale, $l_s = \sqrt{A/H_\chi}$, is given for each set.

Set	μ [MPa]	τ_c [MPa]	H_χ [MPa]	A [MPa mm^2]	l_s [μm]
a	35000	40	$3.0\,10^6$	$1.0\,10^{-2}$	$5.8\,10^{-2}$
b	35000	40	$1.0\,10^6$	$1.0\,10^{-2}$	$1.0\,10^{-1}$
c	35000	40	$3.5\,10^5$	$1.0\,10^{-2}$	$1.7\,10^{-1}$
d	35000	40	$8.8\,10^4$	$1.0\,10^{-3}$	$1.1\,10^{-1}$

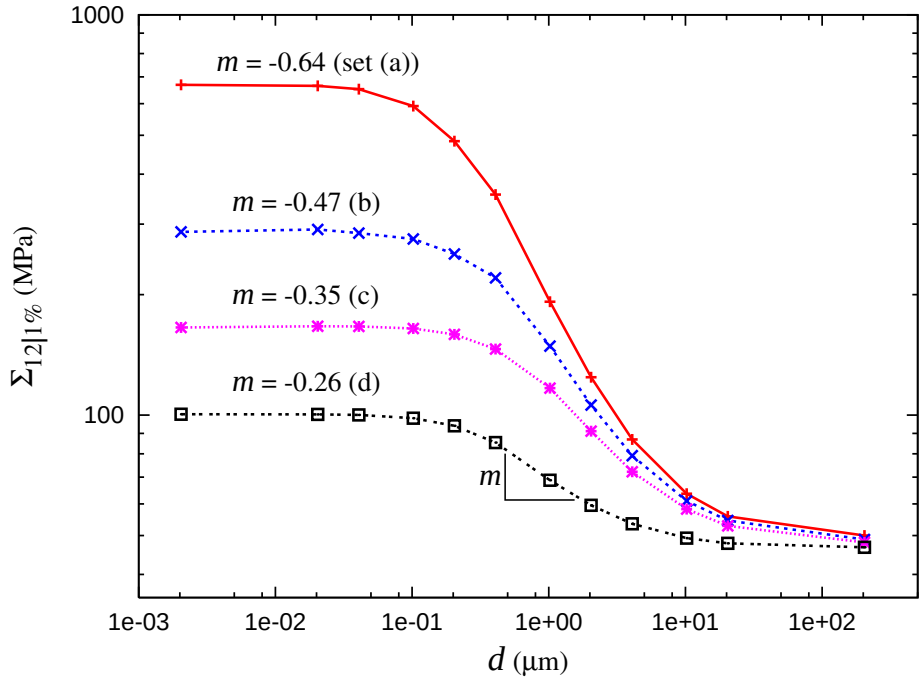

Figure IV.3 : Effect of the mean grain size, d, on the macroscopic flow stress, $\Sigma_{12|1\%}$, at 1% plastic strain. The results are obtained for the 24–grain aggregate using the different sets of material parameters given in Table V.1. The scaling law exponent, m, is identified in each case.

the intragranular back–stress induced by plastic strain gradients, and the intergranular internal stress that originate from the grain to grain plastic strain incompatibilities. The latter contribution is also predicted by classical crystal plasticity models.

Figure IV.3 presents the effect of the mean grain size, d, on the macroscopic flow stress at 1% plastic strain in the 24–grain aggregate in a log–log diagram for different intrinsic length scales, l_s, introduced through the sets of material parameters (labelled a, b, c and d) given in Table V.1. The curves exhibit two plateaus for large ($d > 20\mu$m) and small ($d < 0.1\mu$m) mean grain sizes with a transition domain in between. This *tanh*–shape indicates that when d is large compared to the intrinsic length scale, l_s, strain gradient effects are small and the kinematic hardening arising from the *microcurl* model vanishes. The model saturates when d is of the order of l_s or smaller. The transition domain exhibits a strong size–dependence, the polycrystalline aggregate becoming harder for decreasing grain sizes. The position of the transition zone, the maximum extra–stress (the distance between the two plateaus) and the scaling law exponent, m, in the size–dependent domain are controlled by the material parameters used in the model. The two latter effects are controlled by the coupling modulus, H_χ, they both increase for higher values of H_χ as shown in Fig. IV.3. The scaling exponent is defined as the slope in the log–log diagram in the inflection domain, reflecting the scaling law:

$$\Sigma_{12} \propto d^m. \tag{IV.4}$$

It is obtained with the sets of material parameters given in Table V.1. The found values range from -0.26 to -0.64 including the well–known Hall–Petch exponent $m = -0.5$. In fact it was shown in Cordero *et al.* (2010b) that values of m ranging from 0 to -2 can be simulated with the *microcurl* model in the case of two–phase microstructures. In each

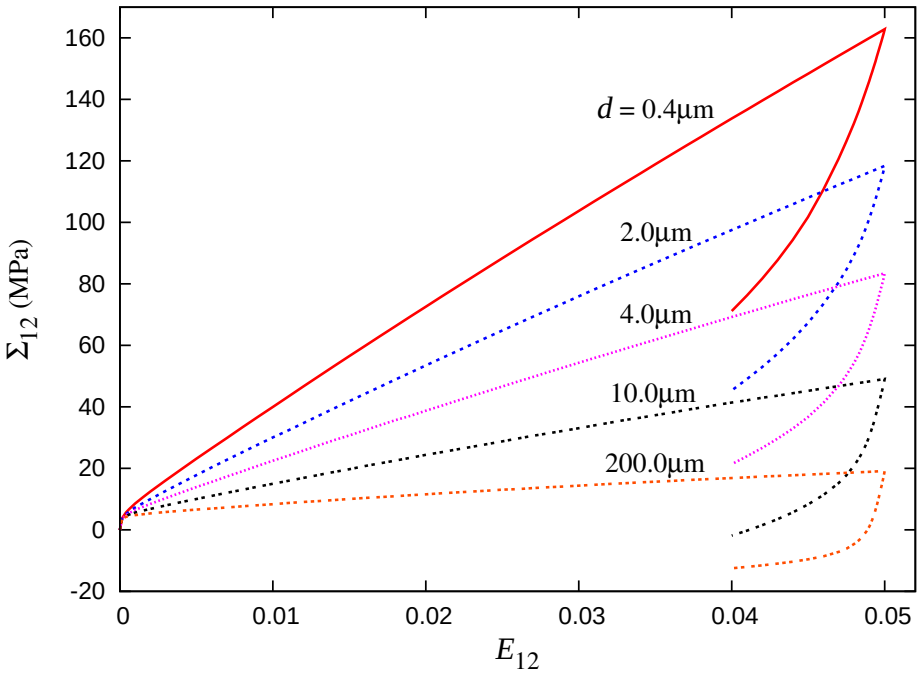

Figure IV.4 : Macroscopic stress–strain response of the 52–grain aggregate under simple shear for various mean grain sizes, d. The set of material parameters used is labelled (g) in Table IV.2.

case, these values are obtained without classical isotropic hardening, meaning that the linear kinematic hardening produced by the model is able to reproduce a wide range of scaling laws. Note that conventional strain gradient plasticity models do not lead to *tanh*–shape curves but rather to unbounded stress increase for vanishingly small microstructures Cordero *et al.* (2010b).

IV.2 Grain size effects in idealised aluminium polycrystals

Similar finite element simulations have been performed on idealised aluminium aggregates of 52 grains shown in Fig. IV.1(b). An additional isotropic hardening component is added as in Méric *et al.* (1991) to obtain a more realistic response of large aluminium grains. The size–independent hardening law reads:

$$R^{\alpha} = \tau_c + Q \sum_{\beta}^{n} h^{\alpha\beta} \left(1 - \exp\left(-b\,\gamma_{\text{cum}}^{\beta}\right)\right), \tag{IV.5}$$

where n is the number of slip systems (here $n = 2$), Q and b are material coefficients defining non–linear isotropic hardening, $h^{\alpha\beta}$ is the interaction matrix and $\gamma_{\text{cum}}^{\beta}$ is the accumulated micro–plastic slip on the slip system β. Cumulative plastic slip results from the integration of the differential equation $\dot{\gamma}_{\text{cum}}^{\beta} = |\dot{\gamma}^{\beta}|$. The material parameters used in these simulations are given in Table IV.2. The macroscopic stress–strain curves presented in Fig. V.1 are obtained by applying a simple shear loading controlled by the average strain component E_{12} on the 52–grain aggregate with various mean grain sizes, d, taken in the size–dependent domain. The chosen set of material parameters has the label (g) in Table IV.2. These parameters are

Table IV.2 : Sets of material parameters used in the 52–grain aggregate case (Fig IV.1(b)).

Set	μ [MPa]	τ_c [MPa]	Q [MPa]	b	$h^{\alpha\alpha}$	$h^{\alpha\beta,\alpha\neq\beta}$	H_χ [MPa]	A [MPa mm^2]	l_s [μm]
e	27000	0.75	7.9	10.2	1	4.4	$1.0\,10^6$	$1.0\,10^{-2}$	$1.0\,10^{-1}$
f	27000	0.75	7.9	10.2	1	4.4	$3.5\,10^5$	$1.0\,10^{-2}$	$1.7\,10^{-1}$
g	27000	0.75	7.9	10.2	1	4.4	$5.0\,10^4$	$1.0\,10^{-2}$	$4.5\,10^{-1}$

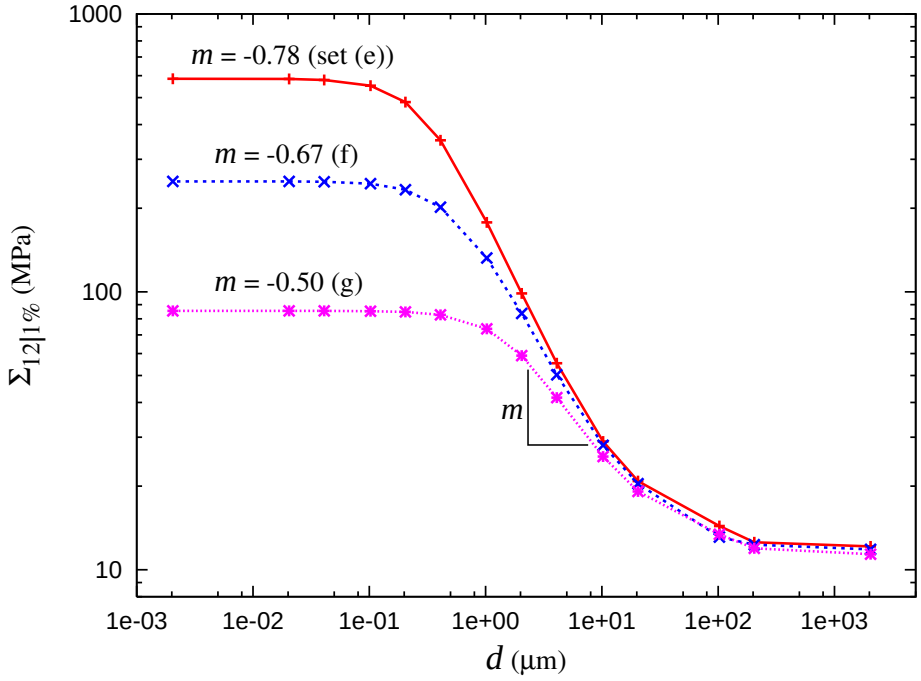

Figure IV.5 : Effect of the mean grain size, d, on the macroscopic flow stress, $\Sigma_{12|1\%}$, at 1% plastic strain. The results are obtained for the 52–grain aggregate using the different sets of material parameters given in Table IV.2. The scaling law exponent, m, is identified in each case.

such that an acceptable description of aluminium polycrystals is obtained for large grains and that a Hall–Petch–like behaviour is found in a plausible range of grain sizes. However we did not attempt to calibrate the amplitude of the extra–hardening so that simulation predictions remain qualitative. The curves of Fig. V.1 show again that the kinematic hardening produced by the model is strongly size–dependent. The evolution of the macroscopic flow stress at 1% plastic strain in the 52–grain aggregate is shown in Fig. IV.5 in the same way as it was done in Fig. IV.3. The set of material parameters (g) of Table IV.2 gives the ideal Hall–Petch scaling law exponent $m = -0.5$.

An important output of the simulations is the dependence of the stress and strain fields in the grains of the polycrystal on grain size. Figures V.3 and V.4 show the contour plots of the field of accumulated plastic slip, computed as

$$\dot{p} = \sqrt{\frac{2}{3}\underset{\sim}{\dot{\varepsilon}}^p : \underset{\sim}{\dot{\varepsilon}}^p}, \tag{IV.6}$$

where $\underset{\sim}{\varepsilon}^p$ is the symmetric part of the plastic deformation, $\underset{\sim}{\boldsymbol{H}}^p$, and the contour plots of the

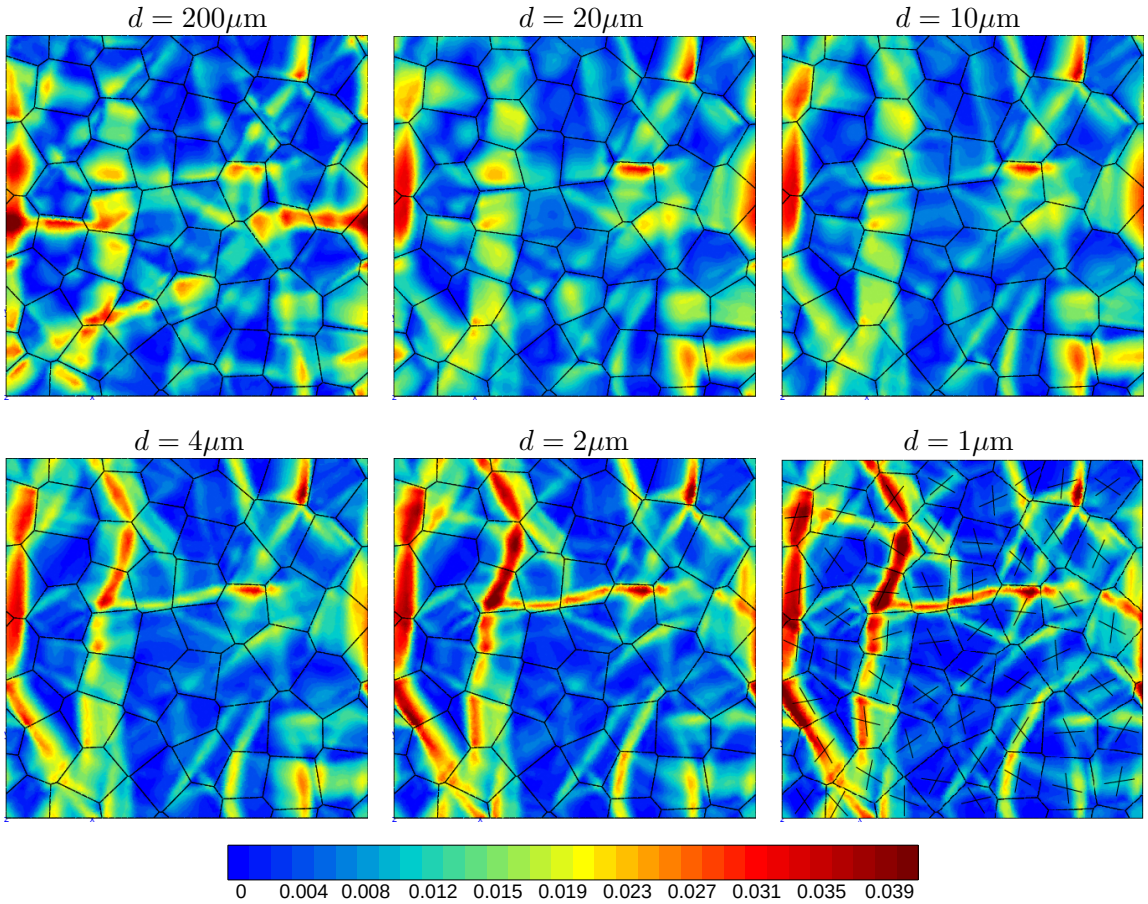

Figure IV.6 : Grain size effects on the accumulated plastic slip. These contour plots are obtained with the 52–grain aggregate for the same mean value of $p = 0.01$. The set of material parameters (g) of Table IV.2 is used. The pairs of slip plane directions are represented for each grain on the 1μm contour plot.

norm Γ of the dislocation density tensor,

$$\Gamma = \sqrt{\underset{\sim}{\boldsymbol{\Gamma}} : \underset{\sim}{\boldsymbol{\Gamma}}}, \tag{IV.7}$$

respectively. The considered grain sizes are taken in the size–dependent domain where the evolution of the fields is assumed to be physically relevant. The chosen set of material parameters has the label (g) in Table IV.2, it corresponds to an intrinsic length scale $l_s = 0.45\mu$m and gives a scaling law exponent $m = -0.5$. The mean value of the accumulated plastic slip is the same in every case, only its distribution varies with the size of the microstructure as shown in Fig. V.3.

The first contour plot of each figure is obtained for $d = 200\mu\text{m} \gg l_s = 0.45\mu$m, at the very beginning of the size–dependent behaviour domain according to Fig. IV.5. At this size, the simulated fields show that p is quite inhomogeneous and that some deformation bands appear; Γ is localised at the grain boundaries and almost vanishes in the grain cores. The contour plots obtained for $2\mu\text{m} < d < 20\mu$m show a significant evolution of both fields. One observes the progressive building of a network of strain localisation bands. These bands are slip bands as they are parallel to the slip plane directions represented on the 1μm contour plot of Fig. V.3. They compensate the larger blue zones where plastic strain cannot develop due to the higher energy cost associated with its gradient. Plastic strain becomes stronger

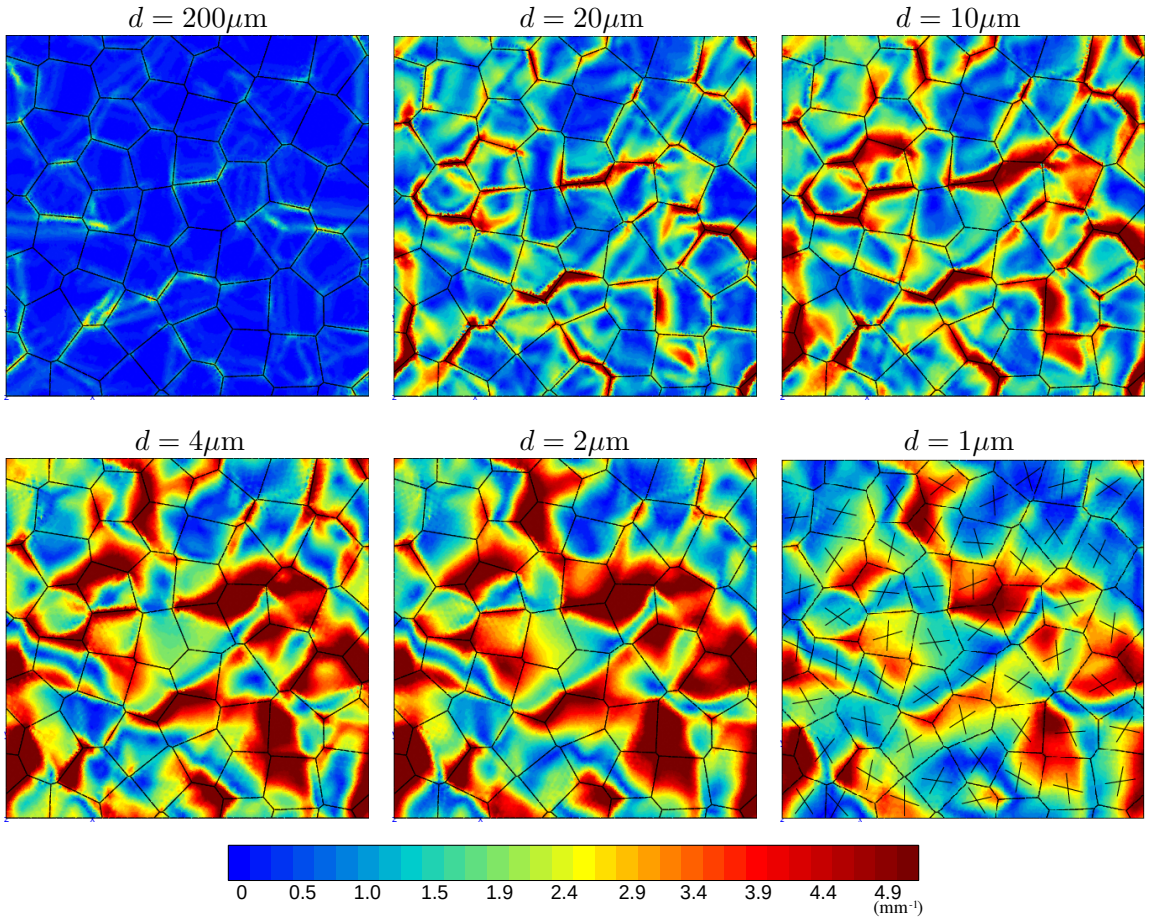

Figure IV.7 : Grain size effects on the norm of the dislocation density tensor. These contour plots are obtained with the 52–grain aggregate for the same mean value of $p = 0.01$. The set of material parameters (g) of Table IV.2 is used. The pairs of slip plane directions are represented for each grain on the 1μm contour plot.

inside the localisation bands. This is due to the fact that the contour plots are given for fixed mean value of p, which implies that the applied total strain is higher for small grain sizes as suggested by Fig. V.1. The field of the norm of the dislocation density tensor is still high close to grain boundaries and spreads over the grain cores. The last contour plot of each figure is obtained for $d = 1\mu$m, a size close to l_s. Here the model starts to saturate, which can be seen from the simulated fields. The field of p does not evolve anymore and Γ decreases. In fact, as l_s controls the strain gradient effects, strong strain gradients cannot develop because they become energetically too expensive when the microstructure size is too small.

The simple shear response of idealised aluminium aggregates of 52 grains has shown that the grain size has a strong effect on the overall behaviour of these polycrystals. In particular, material parameters were set to retrieve the Hall–Petch scaling law. A strong dependence on the size was also observed on plastic strain and dislocation density tensor fields. These fields are studied in details in next chapter.

References

Asaro R.J. (1983). *Crystal plasticity.* Journal of applied mechanics, vol. 50, pp 921.

Bennett V.P. and McDowell D.L. (2003). *Crack tip displacements of microstructurally small surface cracks in single phase ductile polycrystals.* Engineering Fracture Mechanics, vol. 70 n° 2, pp 185–207.

Cordero N.M., Forest S., Busso E.P., Berbenni S., and Cherkaoui M. (2010a). *Grain size effects in generalised continuum crystal plasticity.* In : Scale transition for plastic crystalline and microstructured materials: from experiment to numerical modeling, ICACM 2010. Hermès, Paris, in press.

Cordero N.M., Gaubert A., Forest S., Busso E. P., Gallerneau F., and Kruch S. (2010b). *Size effects in generalised continuum crystal plasticity for two–phase laminates.* Journal of the Mechanics and Physics of Solids, vol. 58, pp 1963–1994.

Forest S., Pradel F., and Sab K. (2001). *Asymptotic analysis of heterogeneous Cosserat media.* International Journal of Solids and Structures, vol. 38, pp 4585–4608.

Forest S. and Sedláček R. (2003). *Plastic slip distribution in two–phase laminate microstructures: Dislocation–based vs. generalized–continuum approaches.* Philosophical Magazine A, vol. 83, pp 245–276.

Gurtin M.E. and Anand L. (2008). *Nanocrystalline grain boundaries that slip and separate: A gradient theory that accounts for grain-boundary stress and conditions at a triple-junction.* Journal of the Mechanics and Physics of Solids, vol. 56, pp 184–199.

Méric L., Poubanne P., and Cailletaud G. (1991). *Single crystal modeling for structural calculations: part 1: Model presentation.* Journal of Engineering Materials and Technology, vol. 113, pp 162.

Zeghadi A., Forest S., Gourgues A.-F., and Bouaziz O. (2007). *Ensemble averaging stress–strain fields in polycrystalline aggregates with a constrained surface microstructure– Part 2: Crystal plasticity.* Philosophical Magazine, vol. 87, pp 1425–1446.

Résumé

Le but de ce chapitre est d'étudier les effets de la taille des grains en plasticité cristalline. Pour cela, le modèle *microcurl* est utilisé pour étudier l'influence de la taille de la microstructure sur la réponse macroscopique d'agrégats polycristallins. Des simulations par éléments finis en deux dimensions sont effectuées pour différents polycristaux de 24 et 52 grains. Différents jeux de paramètres matériau sont utilisés pour analyser leurs effets sur la réponse macroscopique. Une première série de simulations montre qu'un large éventail d'exposants peut être obtenu pour la loi d'échelle sans écrouissage isotrope classique supplémentaire. La réponse de polycristaux d'aluminium idéalisés soumis à un cisaillement simple est ensuite simulée avec des paramètres matériau choisis en fonction des résultats précédents. Il est montré que la taille des grains a un effet important sur le comportement de ces polycristaux. En particulier, les paramètres matériau peuvent être identifiés pour obtenir l'effet Hall-Petch.

Chapter -V-

Grain size effects on plastic strain and dislocation density tensor fields in metal polycrystals

Abstract

In this Chapter, the *microcurl* model is used to explore the grain size effects on the fields of plastic strain and of the dislocation density tensors in two–dimensional polycrystals. Finite element simulations are performed for several aggregates of 24 and 52 grains with a detailed description of the intragranular fields. It is found that the increasing energy cost associated with the development of GNDs leads to the formation of a network of intense slip bands accommodating the imposed deformation in ultra–fine grains polycrystals.

Contents

Preamble: The work presented in this chapter has been accepted for publication in the journal "*Computational Materials Science* in a paper entitled "*Grain size effects on plastic strain and dislocation density tensor fields in metal polycrystals*" (Cordero *et al.*, 2011).

In the same way as in Chapter IV, the *microcurl* model is applied to simulate the response of polycrystalline aggregates and the effects of their microstructure's size. In fact, the work presented in this chapter is close to what was done in the previous chapter. However, instead of comparing different sets of material parameters, only one is chosen here and used in the simulations. Moreover, in addition to the study of the overall behaviour of the polycrystalline aggregates, the grain size effects on the fields of plastic strain and of the dislocation density tensors are explored. That is why an independent chapter is dedicated to the present work.

V.1 Overall response

The set of material parameters used in this chapter are given in Table V.1 and corresponds to the set labelled (e) in the Table IV.2 of Chapter IV. It corresponds to an idealised aluminium alloy for large grains but no quantitative agreement with experimental results was sought for, due to the crystallographic simplifications in the simulations.

The finite element simulations are performed on periodic two–dimensional (2D) meshes of periodic polycrystalline aggregates randomly generated by a method based on Voronoï tessellations. Quadratic elements are used with 2 displacements and 4 micro–deformation degrees of freedom per node. The largest mesh considered contains 77,778 degrees of freedom. Note that the finite element discretisation was chosen fine enough to ensure accurate and mesh size independent results. By extension, the relative mesh size compared to the intrinsic length scale, l_s, has no impact on the results. Examples of microstructure are shown in Fig. IV.1. The grains are represented by Voronoï polyhedra, the distribution of their centers is controlled in such a way that the microstructure is characterised by a mean grain size, d. Various mean grain sizes, d, ranging from tens of nanometers to hundreds of microns, are investigated. Random orientations are assigned to the grains and two slip systems are taken into account. In 2D, the plastic behaviour of f.c.c. crystals can be simulated with 2D planar double slip by considering two effective slip systems separated by an angle of 2ϕ with $\phi = 35.1°$ (Asaro, 1983; Bennett and McDowell, 2003). The overall response of the polycrystal is predicted using periodic homogenisation for generalised continua (Forest *et al.*, 2001). The displacement field is assumed to be of the form

$$\underline{\boldsymbol{u}}\,(x) = \underset{\sim}{\boldsymbol{E}}.\underline{\boldsymbol{x}} + \underline{\boldsymbol{v}}\,(x), \tag{V.1}$$

with $\underline{\boldsymbol{v}}$ a periodic fluctuation, meaning that it takes identical values at homologous points of the unit cell. The imposed average strain tensor is $\underset{\sim}{\boldsymbol{E}}$. Periodicity is also assumed for the plastic micro–deformation field, $\underset{\sim}{\boldsymbol{\chi}}^p$, which implies that no curl of the macroscopic plastic deformation is imposed to the unit cell. According to periodic homogenization, the simple and double tractions $\underline{\boldsymbol{t}}$ and $\underset{\sim}{\boldsymbol{m}}$ are anti–periodic at homologous points of the unit cell.

Three aggregates of 24 grains and a larger one of 52 grains are studied. A better statistics would require a larger number of realisations but it will be seen that reasonable estimates are obtained in the present case. Morphology and individual grain orientations are different for each sample.

Finite element simulations of the boundary value problem have been conducted under generalised plane strain conditions on the considered aggregates of idealised aluminium. Isotropic hardening is introduced as in Méric *et al.* (1994) to obtain a realistic response of large aluminium grains. A simple size–independent hardening law is chosen:

$$\tau_c^\alpha = \tau_c + Q \sum_{\beta=1}^{N} h^{\alpha\beta} \left(1 - \exp\left(-b\,\gamma_{\text{cum}}^\beta\right)\right), \tag{V.2}$$

where Q and b are material parameters defining non–linear isotropic hardening, $h^{\alpha\beta}$ is the interaction matrix and $\gamma_{\text{cum}}^\beta$ is the accumulated plastic slip on the slip system β. The accumulated plastic slip results from the integration of the differential equation $\dot{\gamma}_{\text{cum}}^\beta = |\dot{\gamma}^\beta|$. Table V.1 gives the material parameters used in the simulations. They have been chosen to obtain an acceptable description of aluminium aggregates with large microstructures and to set a consistent intrinsic length scale $l_s = 0.1\mu$m. In this chapter we do not calibrate the amplitude of the extra–hardening and the scaling law exponent from experimental results, only one set of material parameters was investigated. The macroscopic stress–strain curves presented in Fig. V.1 give the averaged stress–strain response of the four aggregates introduced in the previous section. They are obtained by applying a simple shear loading

Table V.1 : Set of material parameters used in the finite element simulations.

μ [MPa]	τ_c [MPa]	Q [MPa]	b	$h^{\alpha\alpha}$	$h^{\alpha\beta,\alpha\neq\beta}$	H_χ [MPa]	A [MPa mm^2]	l_s [μm]
27000	0.75	7.9	10.2	1	4.4	$1.0\,10^6$	$1.0\,10^{-2}$	$1.0\,10^{-1}$

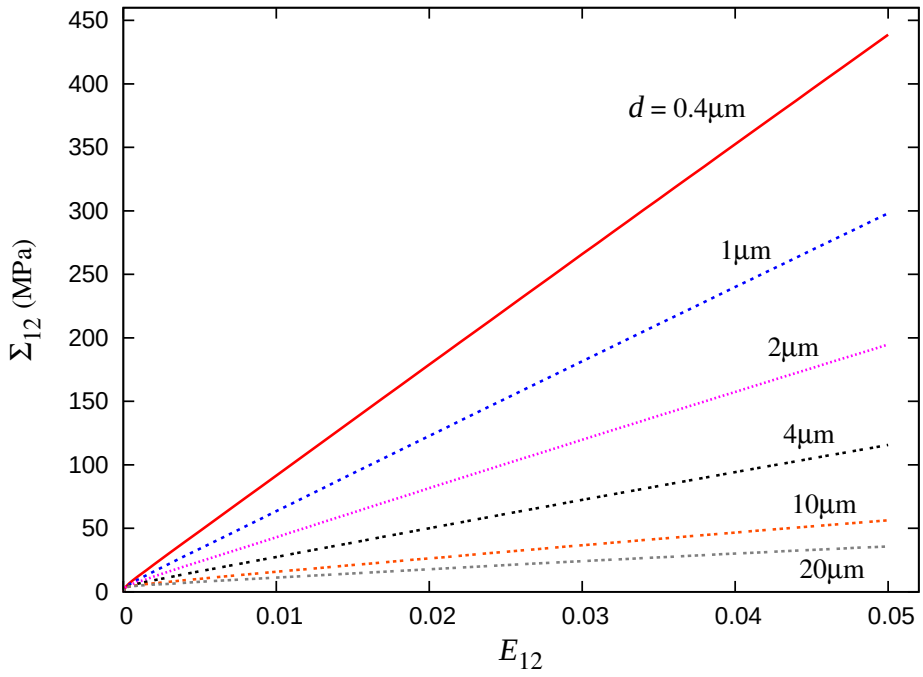

Figure V.1 : Averaged macroscopic stress–strain response of the considered aggregates of 24 and 52 grains under simple shear for various mean grain sizes, d.

controlled by the mean strain component $E_{12} =< \varepsilon_{12} >$ where $<>$ denotes volume averaging over the polycrystal unit cell, on the aggregates with various grain sizes d taken in the size–dependent domain. The mean stress component $\Sigma_{12} =< \sigma_{12} >$ is then computed from the finite element results. The curves show that the kinematic hardening produced by the model is strongly size–dependent and increases for smaller grains. This linear kinematic hardening is quite ideal and leads to values of Σ_{12} that may be surprisingly high. In future work, the constitutive framework has to be extended to include non–linear kinematic hardening. However, some experimental data available in the literature show that very high values of the mean stress can be reached with fine grain sizes (Sanders *et al.*, 1997; Wang *et al.*, 2003). Figure V.2 shows the effect of the mean grain size, d, on the macroscopic flow stress at 1% plastic strain in a log–log diagram. The solid curve is the mean curve obtained with the 24–grain aggregates, the error bars represent the standard deviation. The dashed curve is obtained with the larger aggregate of 52 grains. Both curves have a *tanh*–shape with two saturation plateaus when the grain size, d, is larger than 20μm and smaller than 0.1μm and a transition domain for intermediate sizes. When d is large compared to the intrinsic length scale, l_s, strain gradient effects are small and the kinematic hardening arising from the *microcurl* model vanishes. The model saturates when d is of the order of l_s or smaller. A strong size–dependence is observed in the transition domain, the polycrystals becoming harder for smaller microstructures. The position of the transition zone, the maximum extra–

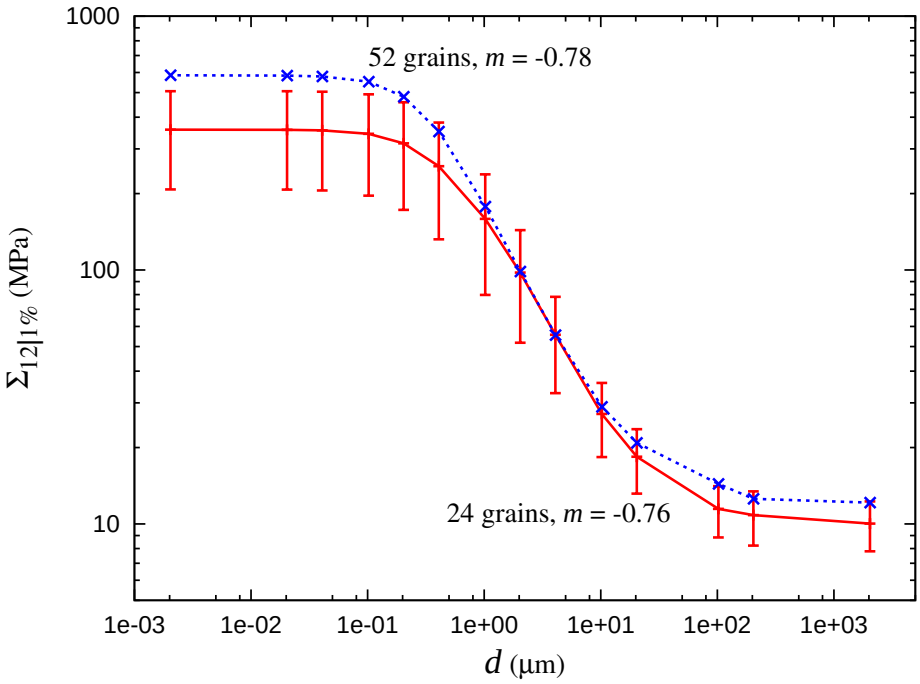

Figure V.2 : Effect of the mean grain size, d, on the macroscopic flow stress $\Sigma_{12|1\%}$ at 1% accumulated plastic slip. The results are obtained with three 24–grain aggregates and with one 52–grain aggregate under simple shear for the material parameters given in Table V.1. The solid curve is the average curve obtained with the 24–grain aggregates, the error bars give the standard deviation. The corresponding scaling law exponent, m, is identified for each case.

stress (the distance between the two plateaus) and the scaling law exponent, m, in the size–dependent domain are controlled by the material parameters used in the model. The scaling law exponent is defined as the slope in the log–log diagram in the size–dependent domain, reflecting the scaling law:

$$\Sigma_{12} \propto d^m. \tag{V.3}$$

A detailed parameter study is done in Cordero *et al.* (2010b) in the case of two–phase microstructures. It is shown in particular that m is controlled by the coupling modulus, H_χ, and that values ranging from $m = 0$ to $m = -2$ can be simulated with the *microcurl* model. In the present work, we obtain $m = -0.76$ and $m = -0.78$ for polycrystals, which are a bit higher compared to the the ideal Hall–Petch scaling law exponent $m = -0.5$. This means that the chosen value for the generalised modulus H_χ has to be re–calibrated. Such a calibration has been done in Cordero *et al.* (2010a) to obtain $m = -0.5$ but it is not presented here. The curves of Fig. V.2 show that the various realisations of the polycrystal lead to rather close stress responses, especially in the size–dependent domain.

The saturation that occurs for small microstructures is not observed with conventional strain gradient plasticity models. Instead, the stress increases infinitely for vanishingly small grain sizes (Cordero *et al.*, 2010b). However, such continuum crystal plasticity models are not expected to be relevant for nano–grains since they assume the existence of a sufficient density of dislocation sources. In particular the present model does not account for the inverse Hall–Petch behaviour, i.e, the yield stress decreases for grain sizes below a critical size, that such materials exhibit (Cherkaoui and Capolungo, 2009).

V.2 Fields of accumulated plastic slip

Grain size effects are not limited to the overall response of polycrystals. It also affects the intragranular mechanical fields. Figure V.3 shows the contour plots of the accumulated plastic slip field, computed as

$$\dot{p} = \sqrt{\frac{2}{3}\underset{\sim}{\dot{\varepsilon}}^p : \underset{\sim}{\dot{\varepsilon}}^p}, \tag{V.4}$$

where the plastic strain $\underset{\sim}{\varepsilon}^p$ is the symmetric part of the plastic deformation, $\underset{\sim}{\boldsymbol{H}}^p$. In order to catch the details of this field and to understand how it evolves with the grain size, its distribution is given in Fig. V.5(a) in the form of histograms. These histograms are obtained for each grain size by including the simulated distributions of p for all the considered realisations. The plotted frequency represents the fraction of the integration points where the accumulated plastic slip takes a value inside the interval $p \pm \Delta p$ with $2\Delta p = 0.001$. Between 11,000 and 19,000 integration points are contained in each mesh, allowing a fairly fine description of the field. One can see that the obtained curves are not bell–shaped and therefore the distributions are not Gaussian. Instead, the curves present an early peak centered at $p^{peak} \approx 0.005$, at half of the imposed overall value of p. When the grains are smaller, the value of p^{peak} is smaller and the peak is higher. The peak is followed by a long tail which becomes longer with smaller d.

The contour plots and distributions are presented for the same overall value, $< p >$, fixed at 1% so that we can compare the different cases and visualise directly the fields and their corresponding distributions. A clear dependence of the field of accumulated plastic slip, p, on the grain size can be seen in Fig. V.3. For $d = 20\mu\text{m} \gg l_s$, at the very beginning of the size–dependent domain according to Fig. V.2, the following observations can be made. Deformation bands appear in some grains, e.g., grains 1, 2, 3 and 4. In these grains, p reaches values more than twice the mean value (0.0208, 0.0232, 0.0243 and 0.0238 in grains 1, 2, 3 and 4 respectively). In the grains without such highly deformed zones, p is approximately ranging from 0.0005 to 0.0168 for a mean value of 0.0091 close to $< p >$. When d is smaller, $20\mu\text{m} \geq d \geq 0.4\mu\text{m} \approx l_s$, significant evolutions happen:

- The deformation bands initiated in some large grains, e.g., 1 and 2, intensify and propagate in neighbouring grains. A network of strain localisation bands is progressively built across the microstructure. These bands are slip bands since they are parallel to the slip plane directions represented on the 0.4μm contour plots of Fig. V.3.

- In parallel, the low deformed zones of the grains exhibiting slip bands grow and get less deformed as the slip bands intensify. For $d = 20\mu$m, the accumulated plastic slip in the grains 1 and 2 was $0.0010 \leq p \leq 0.0208$ and $0.0004 \leq p \leq 0.0232$ respectively, it becomes $0.0004 \leq p \leq 0.0502$ and $0.0002 \leq p \leq 0.0492$ with $d = 0.4\mu$m. In the grains with no slip band, p is approximately ranging from 0.0002 to 0.0209 for a mean value of 0.0051

- In other grains, a slip band observed along a slip direction in a large grain can vanish in favor of a new slip band along the other slip direction when d is smaller. This is observed, for example, in grain 3.

- A last situation is noticed, e.g. in grain 4 where the slip band formed for $d = 20\mu$m vanishes in smaller microstructures. Here, the accumulated plastic slip goes from $0.0025 \leq p \leq 0.0238$ to $0.0005 \leq p \leq 0.0170$ when d decreases from 20μm to 0.4μm.

To sum up, when the grain size gets smaller, a network of slip bands is progressively built. These bands compensate the larger low deformed zones where, probably, the plastic strain

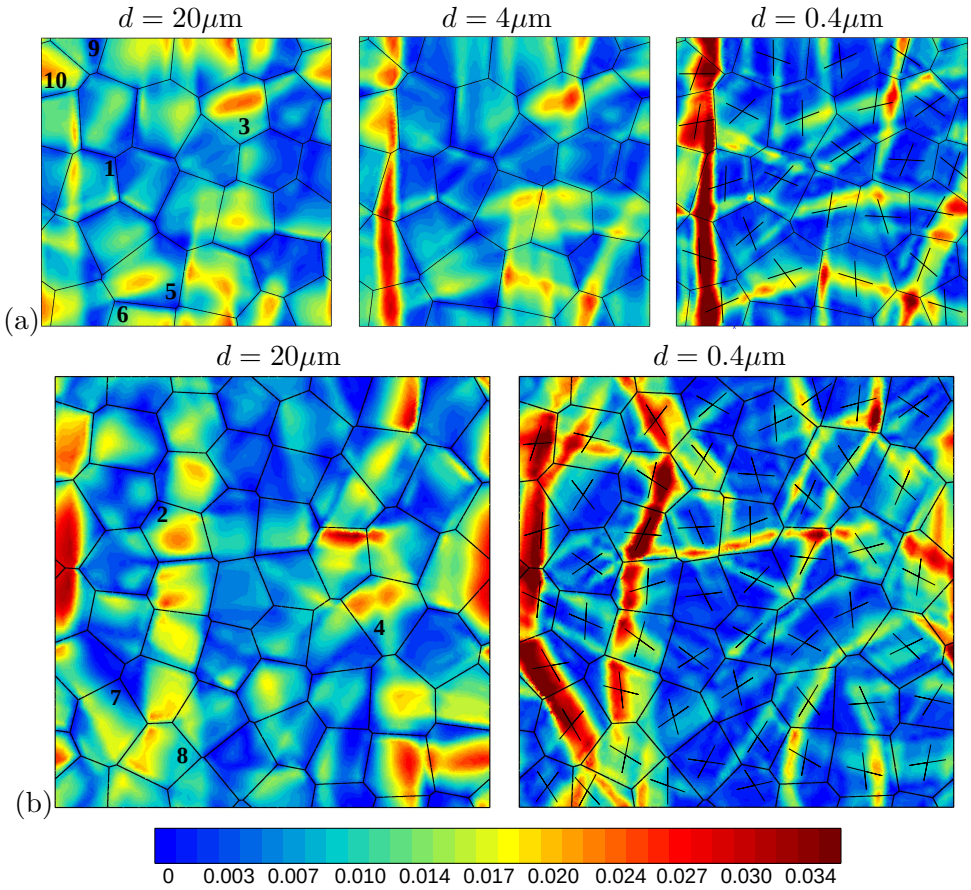

Figure V.3 : Effect of the mean grain size, d, on the accumulated plastic slip, p. These contour plots are obtained with (a) the 24–grain aggregate of Fig. IV.1 and (b) the 52–grain aggregate under simple shear for the same overall value $< p >= 0.01$. The pairs of slip plane directions are represented on the 0.4μm contour plots.

cannot develop any more due to the higher energy cost associated with its gradient. In smaller grains, the plastic strain becomes larger inside the bands. This is a result of the fact that the contour plots are obtained with a fixed mean accumulated plastic slip implying a higher applied overall strain and stress for small grain sizes.

These observations are consistent with the histograms of Fig. V.5(a). Indeed, the distributions exhibit a slightly higher peak centered at smaller values of p when the grains are smaller. That is to say, the distribution of p becomes more homogeneous in most grains and the weakly deformed zones increase. At the same time, smaller grains lead to a longer tail of the distribution denoting that p is locally higher, as observed in the localisation bands.

V.3 Grain size effect on the dislocation density tensor field

The evolution of the dislocation density field is studied in the same way as in the previous section. The dislocation density tensor can be related to the lattice curvature by means of Nye's formula. Lattice curvature can be measured experimentally with EBSD 2D misorientation mapping (Perrin *et al.*, 2010). The components of the dislocation density tensors can also be decomposed in terms of so–called geometrically necessary dislocation densities associated to the two slip systems considered in this work. However, for the sake of

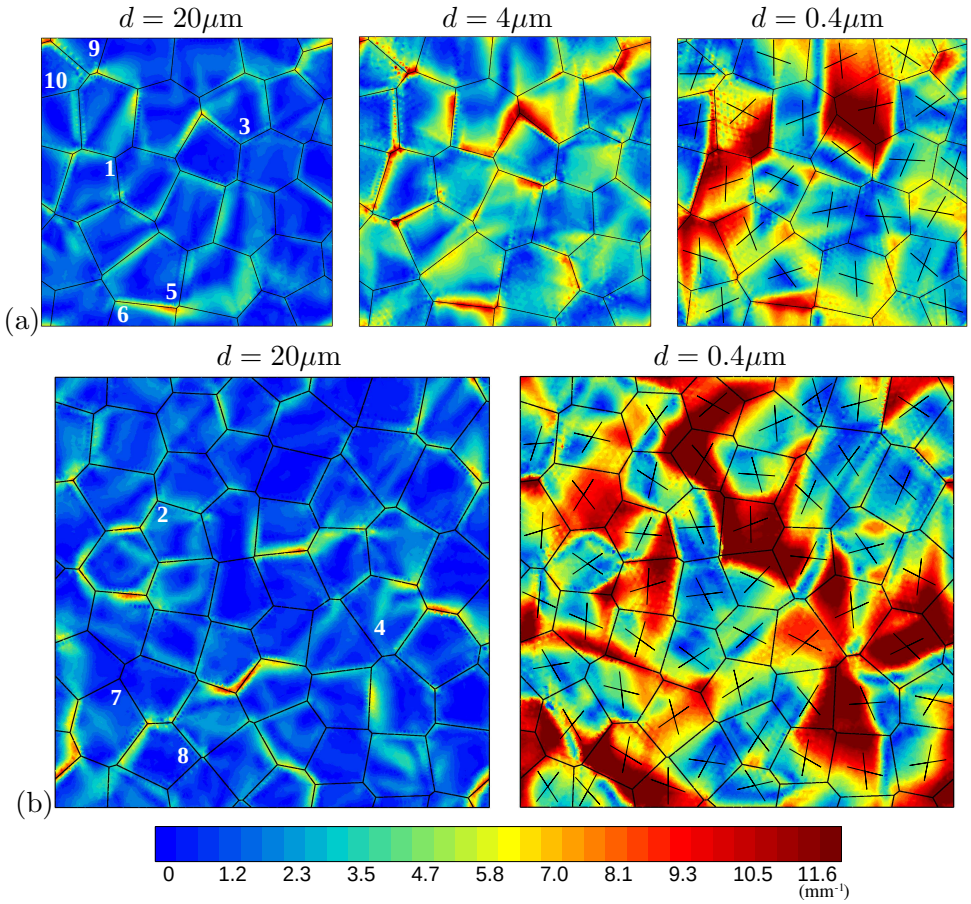

Figure V.4 : Effect of the mean grain size, d, on the norm of the dislocation density tensor, Γ. These contour plots are obtained with (a) the 24–grain aggregate of Fig. IV.1 and (b) the 52–grain aggregate under simple shear for the same overall value $< p >= 0.01$. The pairs of slip plane directions are represented on the 0.4μm contour plots.

brevity, we will consider only the field of the norm of the dislocation density tensor which is defined as

$$\Gamma = \sqrt{\underset{\sim}{\mathbf{\Gamma}} : \underset{\sim}{\mathbf{\Gamma}}} \tag{V.5}$$

and combines all present GNDs. Figure V.4 shows the contour plots of the norm Γ of the dislocation density tensor. The physical dimension of Γ in the contour plots is mm^{-1}. Figure V.5(b) describes its distributions for various grain sizes. Γ is stored at all integration points of the meshes, the plotted frequency represents the fraction of these points where Γ takes a value inside the interval $\Gamma \pm \Delta\Gamma$ with $2\Delta\Gamma = 0.25\text{mm}^{-1}$. Again, the obtained distributions are not Gaussian, they also present a strong dependence on the grain size and their evolution is very different from what was obtained for the plastic strain (Fig. V.5(a)). Decreasing peaks and longer tails are observed for smaller grains. The contour plots and distributions are still obtained with the overall value of p fixed at 1%. For $d = 20\mu\text{m} >> l_s$, one can observe that:

- Γ is localised at the grain boundaries and almost vanishes in the grain cores. See for example grains 5 and 6 or 7 and 8. For the first pair, $\Gamma = 6.75\text{mm}^{-1}$ at the grain boundary and $\Gamma = 0.10$ and 0.64mm^{-1} at the centers of grains 5 and 6 respectively. $\Gamma = 5.98\text{mm}^{-1}$ at the boundary between 7 and 8, $\Gamma = 1.34$ and 0.10mm^{-1} at their centers.

- The GND pileups appear at most grain boundaries; their existence, shape and intensity depend notably on the relative orientations of the considered grains.

When d is smaller, $20\mu\text{m} \geq d \geq 0.4\mu\text{m} \approx l_s$, the following changes happen:

- The highest values of Γ are still reached close to the grain boundaries.
- The GND pileups spreads over the grain cores (see the pair of grains 7/8 with $d = 0.4\mu$m, $\Gamma = 15.42\text{mm}^{-1}$ at the grain boundary and $2.80 \leq \Gamma \leq 8.82\text{mm}^{-1}$ in the cores of 7 and 8).
- Some pileups formed in large grains vanish in smaller microstructures. This is the case at the grain boundary between 9 and 10, where $\Gamma = 4.51$, 4.47 and 3.61mm^{-1} for $d = 20$, 4 and 0.4μm respectively.

The field of Γ is localised at the grain boundaries. When the grain size is smaller, this field spreads over the grain cores and affect entire grains. In fact, the strain gradient effects are controlled by the intrinsic length scale, l_s, so that the simulated GND affected zones is directly related to l_s. Then, decreasing the grain size amounts to increasing the relative size of these zones.

The histograms of Fig. V.5(b) confirm the previous observations. The curve obtained for $d = 20\mu$m with a high peak for small values of Γ describes a homogeneous distribution where most of the integration points exhibit a low norm of the dislocation density tensor. When d gets smaller, the peak is decreasing and is centered at higher values of Γ. This describes the spreading over the microstructure, leading to an heterogeneous field of Γ. The same distributions are obtained for $d = 1\mu$m and $d = 0.4\mu$m. As we get closer to l_s, the model starts to saturate as it was shown in Fig. V.2. The strain gradients become energetically too expensive and cannot develop so that the field does not evolve anymore.

It is remarkable that the Γ field does not correlate with the plastic strain field. In particular, the network of slip bands observed in Fig. V.3 is not systematically associated with high GND densities. It means that the slip bands form without inducing higher lattice curvature in contrast to kink bands sometimes observed in simulations (Forest, 1998). The following interpretation is proposed. The slip band network that develops in fine grained polycrystals is such that plastic strain is maximised without significant increase of GND densities. This is possible only for specific relative orientations of grains and leads to a selection of the formed slip bands.

This slip band network in ultra–fine grains is a new feature of generalised crystal plasticity. The question remains open whether such a phenomenon will still occur in the case of 3D simulations with more than 2 slip systems. On the other hand, the size of the intragranular domains affected by lattice curvature found in the simulations can be used as input to calibrate mean field models with internal length scales as in Pipard *et al.* (2009).

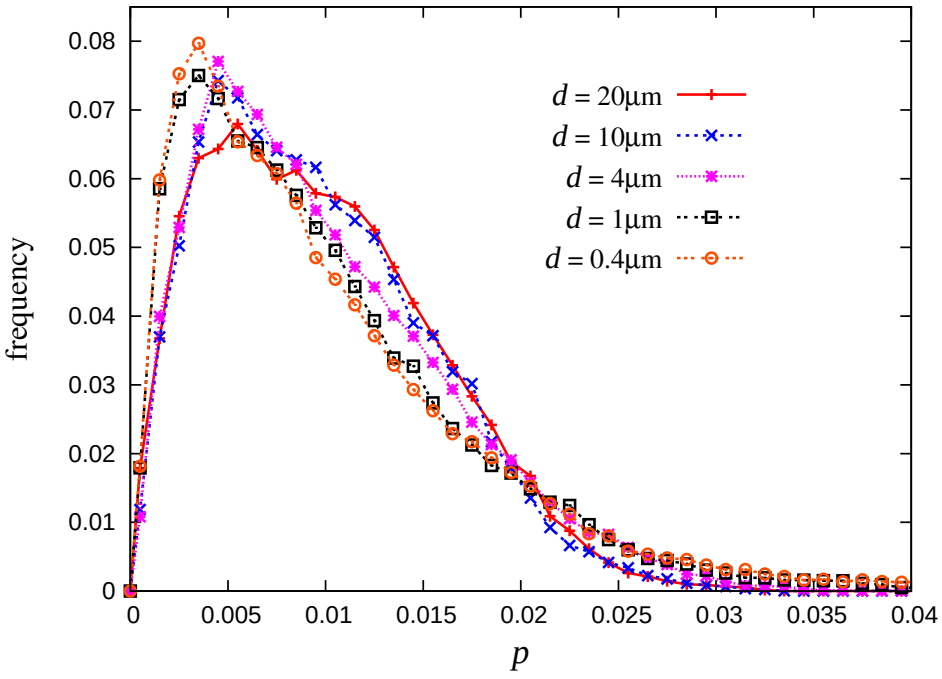

(a)

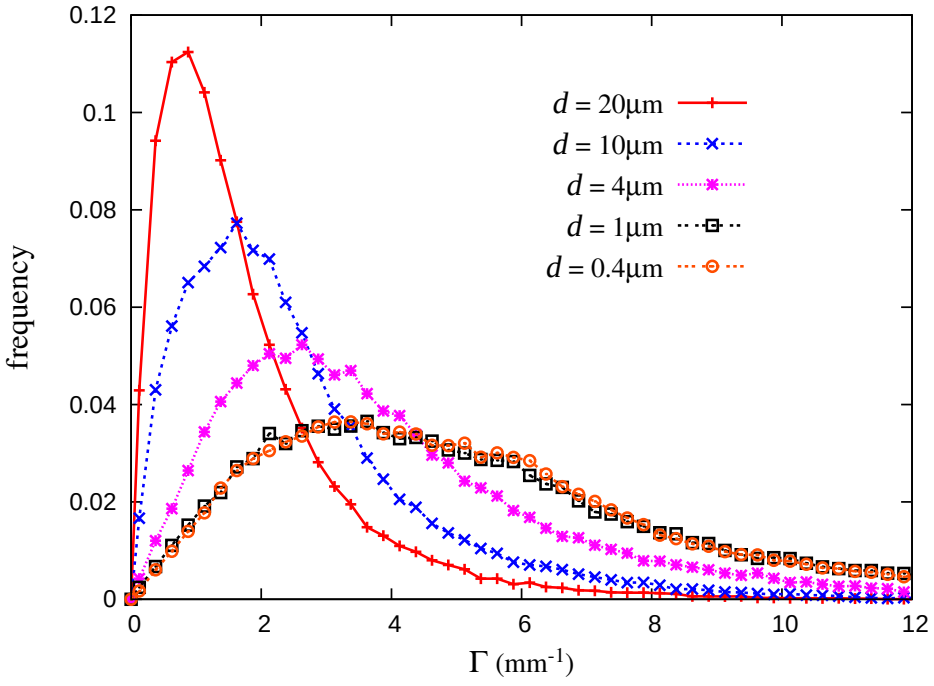

(b)

Figure V.5 : Distributions of (a) p and (b) Γ in the considered aggregates under simple shear for the same overall value $< p >= 0.001$ and for various grain sizes. The frequency represents the fraction of integration points where (a) p takes the value of $p \pm \Delta p$ or (b) Γ takes the value of $\Gamma \pm \Delta\Gamma$. These histograms are obtained by including all the values from the three realisations of the 24–grain aggregate and from the 52–grain aggregate and with interval sizes of $2\Delta p = 0.001$ and $2\Delta\Gamma = 0.25\text{mm}^{-1}$.

References

Asaro R.J. (1983). *Crystal plasticity.* Journal of applied mechanics, vol. 50, pp 921.

Bennett V.P. and McDowell D.L. (2003). *Crack tip displacements of microstructurally small surface cracks in single phase ductile polycrystals.* Engineering Fracture Mechanics, vol. 70 n° 2, pp 185–207.

Cherkaoui M. and Capolungo L. (2009). *Atomistic and Continuum Modeling of Nanocrystalline Materials: Deformation Mechanisms and Scale Transition.* Springer Verlag.

Cordero N.M., Forest S., Busso E.P., Berbenni S., and Cherkaoui M. (2010a). *Grain size effects in generalised continuum crystal plasticity.* In : Scale transition for plastic crystalline and microstructured materials: from experiment to numerical modeling, ICACM 2010. Hermès, Paris, in press.

Cordero N.M., Forest S., Busso E.P., Berbenni S., and Cherkaoui M. (2011). *Grain size effects on plastic strain and dislocation density tensor fields in metal polycrystals.* Computational Materials Science.

Cordero N.M., Gaubert A., Forest S., Busso E. P., Gallerneau F., and Kruch S. (2010b). *Size effects in generalised continuum crystal plasticity for two–phase laminates.* Journal of the Mechanics and Physics of Solids, vol. 58, pp 1963–1994.

Forest S. (1998). *Modeling Slip, Kink and Shear Banding in Classical and Generalized Single Crystal Plasticity.* Acta Materialia, vol. 46 n° 9, pp 3265–3281.

Forest S., Pradel F., and Sab K. (2001). *Asymptotic analysis of heterogeneous Cosserat media.* International Journal of Solids and Structures, vol. 38, pp 4585–4608.

Méric L., Cailletaud G., and Gaspérini M. (1994). *F.E. Calculations of Copper Bicrystal Specimens Submitted to Tension–Compression Tests.* Acta metall. mater., vol. 42, pp 921–935.

Perrin C., Berbenni S., Vehoff H., and Berveiller M. (2010). *Role of discrete intragranular slip on lattice rotations in polycrystalline Ni: Experimental and micromechanical studies.* Acta Materialia, vol. 58 n° 14, pp 4639–4649.

Pipard J.M., Nicaise N., Berbenni S., Bouaziz O., and Berveiller M. (2009). *A new mean field micromechanical approach to capture grain size effects.* Computational Materials Science, vol. 45 n° 3, pp 604–610.

Sanders P.G., Eastman J.A., and Weertman J.R. (1997). *Elastic and tensile behavior of nanocrystalline copper and palladium.* Acta materialia, vol. 45 n° 10, pp 4019–4025.

Wang Y.M., Wang K., Pan D., Lu K., Hemker K.J., and Ma E. (2003). *Microsample tensile testing of nanocrystalline copper.* Scripta materialia, vol. 48 n° 12, pp 1581–1586.

Résumé

Dans ce chapitre, le modèle microcurl est utilisé pour explorer les effets de la taille des grains sur les champs de déformation plastique et du tenseur de densité de dislocations dans des polycristaux en deux dimensions. Des simulations par éléments finis sont effectuées pour plusieurs agrégats de 24 et 52 grains avec une description détaillée des champs intragranulaires. Dans le cas de polycristaux dont les grains sont ultra-fins, le coût croissant de l'énergie associée au développement des GNDs conduit à la formation d'un réseau de bandes de glissement intenses qui accommodent la déformation imposée.

Chapter -VI-

Conclusions

The main results obtained in this work can be summarised as follows:

1. A micromorphic crystal plasticity model, called *microcurl*, has been proposed to regularise the response of a strain gradient plasticity model in the presence of an elastic phase. The "$curl H^p$" model is retrieved when the coupling modulus H_χ that arises in the *microcurl* model, becomes a Lagrange multiplier. The corresponding internal constraint states that the plastic micro–deformation $\underset{\sim}{\boldsymbol{\chi}}^p$ coincides with conventional plastic deformation $\underset{\sim}{\boldsymbol{H}}^p$.

2. A complete solution of stress, strain and plastic slip distributions could be worked out for a two–phase laminate microstructure where the behaviour of the elastic and elasto–plastic phases are described by the Cosserat or *microcurl* model. In contrast, a discontinuity remains with the "$curl H^p$" model due to the question of transmission of higher order tractions from the plastic to the elastic phase. It was also found that the Cosserat and *microcurl* solutions coincide for a certain range of values of material parameters.

3. The size effect in terms of extra–hardening amplitude, predicted by the Cosserat model is bounded. In contrast, this amplitude is linearly related to the coupling modulus H_χ in the *microcurl* model. Accordingly, the *microcurl* model can accommodate any observed amplitude of extra–hardening.

4. A size–dependent transition domain between two asymptotic regimes has been detected for both models, for small and large microstructural length scales respectively. The location of this transition domain, defined by l_c, has been determined and can be calibrated to comply with experimental results observed either at the nano or micron scales. This characteristic length is mainly controlled by the parameter A^s and A^h.

5. The power law exponents for the scaling laws were determined, ranging from $m = 0$ to -2. It comprises therefore the ideal Orowan and Hall–Petch exponents. The higher order parameters A and H_χ can be calibrated to match experimental results in a given domain of length scales. More specifically, the *microcurl* model can produce scaling laws between 0 and -2. The Cosserat model produces scaling laws from 0 to -1 depending on the volume fraction of the soft phase. In contrast, the "$curl\ H^p$" model invariably leads to an asymptotic regime with $m = -2$.

6. The formulation of the three models considered in this work is such that a back stress component arises in the soft phase and macroscopically results in linear kinematic hardening. The corresponding kinematic hardening modulus was explicitly derived as a function of higher order material parameters, volume fraction of soft phase, and microstructural length scale. It is bounded in the case of the Cosserat model, whereas it is linearly related to H_χ according to the *microcurl* model.

7. The models are applicable to multislip conditions. The analysis in the case of symmetric double slip has revealed a similar size–dependent behaviour as in single slip, and the existence of a possible discontinuity of some plastic micro–deformation components.

8. Size effects induced by multilayer pileups have been investigated in terms of plastic slip distribution and overall work–hardening using discrete dislocation dynamics (DDD) and the *microcurl* model. The comparison of these models showed that the higher order moduli of the *microcurl* model can be calibrated to obtain similar overall behaviours and local distributions to those from DDD simulations.

9. Comparing DDD and the *microcurl* model also pointed out that a correlation exists between the thickness of the boundary layer, and the distance between active neighbouring slip planes.

10. The *microcurl* model was applied to simulate polycrystalline aggregates under simple shear loading. Several sets of material parameters have been used to explore their effects on the overall response and a wide range of scaling law exponents were obtained. In particular, material parameters were set to retrieve the Hall–Petch scaling law. It was shown that the grain size has a strong effect on the overall behaviour of polycrystals.

11. A strong dependence on the size was also observed on plastic strain and dislocation density tensor fields. A network of slip bands is progressively built and the GND pileups, defined as the norm of the dislocation density tensor, spread over the grains for smaller sizes of the microstructure. The slip band network in ultra–fine grains is a new feature of generalised crystal plasticity. The question remains open whether such a phenomenon will still occur in the case of 3D simulations with more than 2 slip systems. In future work the GND pileups could be compared and identified with results obtained with internal mean field approaches as in Pipard *et al.* (2009). The simulated fields could also be compared and calibrated with fields measured with EBSD 2D misorientation mapping (Perrin *et al.*, 2010).

In the three model formulations presented in Chapter II, the double stress tensor belongs to the arguments of the free energy function only, and not of the dissipation potential. This simple framework is sufficient to illustrate the existence of a back stress and to work out explicit analytic results for the laminate problem. However, dissipative mechanisms related to generalised stresses can be introduced in a systematic manner following the work of Forest and Sievert (2003), Forest (2009) and Gurtin and Anand (2009). The theory can also be formulated assuming finite deformation kinematics following the framework proposed in Forest and Sievert (2003) for micromorphic continua. This formulation is based on the usual multiplicative decomposition of the deformation gradient into elastic and plastic parts. Such decompositions exist also for the microdeformation and its gradient. However, in the present single crystal model, there will be no need for decomposing $\underset{\sim}{\boldsymbol{\chi}}^p$ and $\underset{\sim}{\boldsymbol{\Gamma}}_\chi$ as long as no additional dissipative mechanisms are introduced. The internal constraint corresponding to equation (II.96) would then be $\underset{\sim}{\boldsymbol{\chi}}^p \equiv \underset{\sim}{\boldsymbol{F}}^p - \underset{\sim}{\mathbf{1}}$ where $\underset{\sim}{\boldsymbol{F}}^p$ is the plastic deformation in the multiplicative decomposition.

The fact that the Cosserat extra–hardening stress was found to be bounded, irrespective of the value of higher order moduli, may explain that the grain size effects for aggregates of Cosserat crystals are systematically underestimated in Forest *et al.* (2000) and Zeghadi *et al.* (2005). It is expected that predicted size–effects will be more pronounced for the *microcurl* model that with the Cosserat model.
The linear kinematic hardening predicted by the models in the laminate microstructure is quite ideal and unrealistic. A dependence of the linear kinematic hardening on total dislocation density was shown in Groma *et al.* (2003) and Forest (2008). More generally, the constitutive framework should be extended to include non linear kinematic hardening.
From the numerical point of view, the Cosserat model has the advantage that it requires only three additional degrees of freedom compared to the nine generally required in the "$curl H^p$" and *microcurl* models. Models involving the slips γ^α themselves or the dislocation densities as additional degrees of freedom, like that of Bayley *et al.* (2006), are even more expensive since the number of degrees of freedom increases proportionally to the number of slip systems. The possible discontinuity of some components of the plastic micro–deformation makes the finite element implementation of the *microcurl* model quite complex.
Under single slip conditions, the models discussed here have a sound physical basis as shown by comparison with theoretical results using statistical dislocation concepts and also simple line tension dislocation models (e.g., see Forest, 2008). In contrast, the application of the models to multislip conditions is possible in a purely phenomenological way, by identifying the material parameters from experimental data, or from comparison with dislocation dynamics simulations. This remains to be done with a view to highlight the limitations of the approach.
Interface conditions with simple continuity requirements have played a major role in the present work. However, enriched interface conditions and constitutive equations at grain boundaries, as proposed in Aifantis and Willis (2005) and Gurtin and Anand (2008), could be more realistic. Some aspects of such interface laws should even be identified from atomistic simulations (see, for instance, McDowell, 2008).

References

Aifantis K.E. and Willis J.R. (2005). *The role of interfaces in enhancing the yield strength of composites and polycrystals.* Journal of the Mechanics and Physics of Solids, vol. 53, pp 1047–1070.

Bayley C.J., Brekelmans W.A.M., and Geers M.G.D. (2006). *A comparison of dislocation induced back stress formulations in strain gradient crystal plasticity.* International Journal of Solids and Structures, vol. 43, pp 7268–7286.

Forest S. (2008). *Some links between Cosserat, strain gradient crystal plasticity and the statistical theory of dislocations.* Philosophical Magazine, vol. 88, pp 3549–3563.

Forest S. (2009). *Micromorphic Approach for Gradient Elasticity, Viscoplasticity, and Damage.* Journal of Engineering Mechanics, vol. 135, pp 117–131.

Forest S., Barbe F., and Cailletaud G. (2000). *Cosserat Modelling of Size Effects in the Mechanical Behaviour of Polycrystals and Multiphase Materials.* International Journal of Solids and Structures, vol. 37, pp 7105–7126.

Forest S. and Sievert R. (2003). *Elastoviscoplastic constitutive frameworks for generalized continua.* Acta Mechanica, vol. 160, pp 71–111.

Groma I., Csikor F.F., and Zaiser M. (2003). *Spatial correlations and higher-order gradient terms in a continuum description of dislocation dynamics.* Acta Materialia, vol. 51, pp 1271–1281.

Gurtin M.E. and Anand L. (2008). *Nanocrystalline grain boundaries that slip and separate: A gradient theory that accounts for grain-boundary stress and conditions at a triple-junction.* Journal of the Mechanics and Physics of Solids, vol. 56, pp 184–199.

Gurtin M.E. and Anand L. (2009). *Thermodynamics applied to gradient theories involving the accumulated plastic strain: The theories of Aifantis and Fleck & Hutchinson and their generalization.* Journal of the Mechanics and Physics of Solids, vol. 57, pp 405–421.

McDowell D.L. (2008). *Viscoplasticity of heterogeneous metallic materials.* Materials Science and Engineering R, vol. 62, pp 67–123.

Perrin C., Berbenni S., Vehoff H., and Berveiller M. (2010). *Role of discrete intragranular slip on lattice rotations in polycrystalline Ni: Experimental and micromechanical studies.* Acta Materialia, vol. 58 n° 14, pp 4639–4649.

Pipard J.M., Nicaise N., Berbenni S., Bouaziz O., and Berveiller M. (2009). *A new mean field micromechanical approach to capture grain size effects.* Computational Materials Science, vol. 45 n° 3, pp 604–610.

Zeghadi A., Forest S., Gourgues A.-F., and Bouaziz O. (2005). *Cosserat continuum modelling of grain size effects in metal polycrystals.* Proc. Appl. Math. Mech., vol. 5, pp 79–82.

Appendix of Part A

Appendix A.1: Notation

First–rank, second–rank and fourth–rank tensors are respectively denoted by $\underline{\underline{A}}, \underline{\underline{\underline{A}}}$ and $\underline{\underline{\underline{\underline{A}}}}$. The superscripts $\underline{\underline{\underline{A}}}^s$ and $\underline{\underline{\underline{A}}}^a$ will denote respectively the symmetric and skew-symmetric parts of the tensor. Both intrinsic and index notations are given at some places for clarity. The intrinsic definition of the curl operator applied to a tensor T of any rank in any coordinate system q^i is

$$\mathrm{curl}\, T = \frac{\partial T}{\partial q^i} \times \underline{e}^{\,i}, \tag{VI.1}$$

where $\times$ denotes the vector product. In a Cartesian frame and for a tensor of rank two, this gives:

$$\mathrm{curl}\, \underline{\underline{\underline{A}}} = \frac{\partial \underline{\underline{\underline{A}}}}{\partial x_l} \times \underline{e}_{\,l} = A_{ik,l} \underline{e}_{\,i} \otimes (\underline{e}_{\,k} \times \underline{e}_{\,l}) = \epsilon_{jkl} A_{ik,l} \underline{e}_{\,i} \otimes \underline{e}_{\,j}, \tag{VI.2}$$

where ϵ_{ijk} is the permutation tensor. Hence

$$(\mathrm{curl}\, \underline{\underline{\underline{A}}})_{ij} = \epsilon_{jkl} A_{ik,l}. \tag{VI.3}$$

Note that the definition of the curl operator chosen in Cermelli and Gurtin (2001) is the *opposite and transpose* of (VI.3).
Finally, brackets $<>$ are used to compute average values over a unit cell V:

$$< - >= \frac{1}{V} \int_V - \, dV. \tag{VI.4}$$

Appendix A.2: Strain gradient plasticity solution for a two–phase plastic laminate

A complete solution of the laminate boundary value problem can be derived for the two–phase periodic microstructure under simple shear for the "$curl H^p$" model of Section II.2 when both phases exhibit a plastic behaviour. The hard phase now admits a critical resolved shear stress τ_c^h. In both phases, under plastic loading conditions, the plastic slip has a parabolic profile:

$$\gamma^h(x_1) = a^h x_1^2 + b^h x_1 + c^h, \quad \gamma^s(x_1) = a^s x_1^2 + b^s x_1 + c^s \tag{VI.5}$$

taken over the interval $[-s/2, s/2+h]$, with six coefficients to be determined from the following conditions:

- Continuity of plastic slip at $x_1 = s/2$ and periodicity of plastic slip at $x_1 = -s/2$ and $x_1 = s/2 + h$:

$$a^s \left(\frac{s}{2}\right)^2 + b^s \frac{s}{2} + c^s = a^h \left(\frac{s}{2}\right)^2 + b^h \frac{s}{2} + c^h, \tag{VI.6}$$

$$a^s \left(\frac{s}{2}\right)^2 - b^s \frac{s}{2} + c^s = a^h \left(\frac{s}{2} + h\right)^2 + b^h (\frac{s}{2} + h) + c^h. \tag{VI.7}$$

- Continuity of double stress component $M_{13} = -A\gamma_{,1}$ at $x_1 = s/2$ and periodicity of double stress vector at $x_1 = -s/2$ and $s/2 + h$:

$$A^s (2a^s \frac{s}{2} + b^s) = A^h (2a^h \frac{s}{2} + b^h), \tag{VI.8}$$

$$A^s (-2a^s \frac{s}{2} + b^s) = A^h (2a^h (\frac{s}{2} + h) + b^h). \tag{VI.9}$$

- Plasticity criterion

$$\sigma_{12} + 2A_s a^s = \tau_c^s, \tag{VI.10}$$
$$\sigma_{12} + 2A_h a^h = \tau_c^h. \tag{VI.11}$$

- Symmetry condition at $x_1 = 0$:

$$\gamma_{,1}(0) = 0. \tag{VI.12}$$

- Periodicity condition for the perturbation u_2 translated into the following terms. The elastic law provides

$$u_{2,1} = \sigma_{12}/\mu - \bar{\gamma} + \gamma. \tag{VI.13}$$

The mean value over one unit cell of the left–hand side necessarily vanishes since u_2 is periodic:

$$\begin{aligned}
(s+h) < u_{2,1} > &= (s+h) < \sigma_{12}/\mu - \bar{\gamma} + \gamma > \\
&= \int_{-s/2}^{s/2} \left(\tau_c^s/\mu - 2A^s a^s/\mu - \bar{\gamma} + a^s x_1^2 + c^s\right) dx_1 \\
&+ \int_{s/2}^{s/2+h} \left(\tau_c^h/\mu - 2A^h a^h/\mu - \bar{\gamma} + a^h x_1^2 + c^h\right) dx_1 \\
&= (\tau_c^s/\mu - 2A^s a^s/\mu - \bar{\gamma})(s+h) + sc^s + hc^h + \frac{2a^s}{3}\left(\frac{s}{2}\right)^3 \\
&+ \frac{2a^h}{3}\left((\frac{s}{2}+h)^3 - (\frac{s}{2})^3\right) + \frac{b^h}{2}\left((\frac{s}{2}+h)^2 - (\frac{s}{2})^2 + h(s+h)\right).
\end{aligned}$$

From Eq. (VI.12) we obtain

$$b^s = 0. \tag{VI.14}$$

The combination (VI.10) - (VI.11) provides the relation

$$2(A^s a^s - A^h a^h) = \tau_c^s - \tau_c^h. \tag{VI.15}$$

From the combination of Eqs. (VI.8) and (VI.15), one finds

$$b^h = \frac{\tau_c^s - \tau_c^h}{A^h}\frac{s}{2}. \tag{VI.16}$$

The combination (VI.6) - (VI.7) yields

$$a^h = \frac{b^h}{s+h} = \frac{\tau_c^s - \tau_c^h}{A^h}\frac{s}{2(s+h)}. \tag{VI.17}$$

Finally,

$$a^s = \frac{\tau_c^s - \tau_c^h}{A^s}\frac{2s+h}{2(s+h)}. \tag{VI.18}$$

The equations (VI.6) (or (VI.7)) and (VI.14) provide a system of two equations to from which we obtain c^h and c^s.

Appendix A.3: Double traction at the interface

The purpose of this appendix is to propose a way to derive, from the microcurl model, the jump of generalised tractions presented in section II.2. It was shown that with the "$curlH^p$" model, the required continuity of the double traction tensor, $\underset{\sim}{\boldsymbol{m}}$, see Eq. (II.51), leads to a physically not relevant solution of the boundary value problem. So, the correct value of the double traction to be imposed at the interface was left undetermined. This value can be obtained as the limiting case of the *microcurl* model for which we have solved the full boundary value problem. As we want the *microcurl* model to tend to the "$curlH^p$" model, we have to consider an infinite coupling modulus, $H_\chi \to \infty$. In that case, χ_{12}^{ps} is equal to the plastic slip γ and then we have:

$$\lim_{H_\chi \to \infty} \chi_{12}^{ps}(\pm s/2) = 0, \tag{VI.19}$$

which means that the plastic micro–deformation tends to zero at the interfaces with the elastic phase.
We evaluate the double traction tensor at the interfaces:

$$\begin{aligned} \lim_{H_\chi \to \infty} m_{12}(\pm s/2) &= \lim_{H_\chi \to \infty} A^s \chi_{12,1}^{ps}(\pm s/2) \\ &= -\frac{A^s \mathcal{A} f_s l}{\mathcal{B} l^2 + \dfrac{2A^s}{\mu}} \\ &= \frac{A^s \left(\overline{\gamma} - \dfrac{\tau_c}{\mu}\right) f_s l}{\dfrac{f_s^3}{6} l^2 + \dfrac{2A^s}{\mu}}. \end{aligned} \tag{VI.20}$$

This expression can be transformed into the following expression:

$$\begin{aligned} \lim_{H_\chi \to \infty} m_{12}(\pm s/2) &= -\frac{A^s \mathcal{A}' f_s}{\mathcal{B}' l} \\ &= \frac{6A^s \langle \gamma \rangle}{f_s^2 l}. \end{aligned} \tag{VI.21}$$

Eqs. (VI.20) and (VI.21) give us the value of the double traction tensor at the interfaces in the limit case of the *microcurl* model. We can now return to the original "$curlH^p$" model and impose the appropriate value of the double traction (and double stress) component m_{12} (and M_{13}) at the interface. The corresponding boundary value problem is then well–posed and can be solved for the plastic deformation profile.

Appendix A.4: Summary of the main equations of the *microcurl* model

In order to help the reader's understanding, the main features of the *microcurl* model are summarised in this short appendix.

DOF: displacement $\underline{\boldsymbol{u}}$ (u_i)
plastic micro–deformation variable $\underset{\sim}{\boldsymbol{\chi}}^p$ (χ_{ij})

Dislocation density tensor: $\underset{\sim}{\boldsymbol{\Gamma}} = \operatorname{curl} \underset{\sim}{\boldsymbol{H}}^p$
where $\underset{\sim}{\boldsymbol{H}}^p$ is the plastic deformation tensor

Power density of internal forces: $p^{(i)} = \underset{\sim}{\boldsymbol{\sigma}} : \dot{\underset{\sim}{\boldsymbol{H}}} + \underset{\sim}{\boldsymbol{s}} : \dot{\underset{\sim}{\boldsymbol{\chi}}}^p + \underset{\sim}{\boldsymbol{M}} : \operatorname{curl} \dot{\underset{\sim}{\boldsymbol{\chi}}}^p$
where $\underset{\sim}{\boldsymbol{\sigma}}$ is the stress tensor, $\underset{\sim}{\boldsymbol{s}}$ the micro–stress tensor and $\underset{\sim}{\boldsymbol{M}}$ the double–stress tensor

Balance equations: $\operatorname{div} \underset{\sim}{\boldsymbol{\sigma}} = 0, \quad \operatorname{curl} \underset{\sim}{\boldsymbol{M}} + \underset{\sim}{\boldsymbol{s}} = 0$

Boundary conditions: $\underline{\boldsymbol{t}} = \underset{\sim}{\boldsymbol{\sigma}}.\underline{\boldsymbol{n}}\,, \quad \underset{\sim}{\boldsymbol{m}} = \underset{\sim}{\boldsymbol{M}}.\underset{\approx}{\boldsymbol{\epsilon}}.\underline{\boldsymbol{n}}$
where $\underline{\boldsymbol{t}}$ and $\underset{\sim}{\boldsymbol{m}}$ are the simple and double tractions at the boundary
$\underset{\approx}{\boldsymbol{\epsilon}}$ the permutation tensor and $\underline{\boldsymbol{n}}$ the unit normal vector to the boundary

Arguments of ψ: $\underset{\sim}{\boldsymbol{\varepsilon}}^e, \quad \underset{\sim}{\boldsymbol{e}}^p := \underset{\sim}{\boldsymbol{H}}^p - \underset{\sim}{\boldsymbol{\chi}}^p, \quad \underset{\sim}{\boldsymbol{\Gamma}}_\chi := \operatorname{curl} \underset{\sim}{\boldsymbol{\chi}}^p$

Residual intrinsic dissipation: $D = (\underset{\sim}{\boldsymbol{\sigma}} + \underset{\sim}{\boldsymbol{s}}) : \dot{\underset{\sim}{\boldsymbol{H}}}^p \geq 0$
no dissipative part is introduced for $\underset{\sim}{\boldsymbol{\Gamma}}_\chi$

Constitutive equations: $\underset{\sim}{\boldsymbol{\sigma}} = \underset{\approx}{\boldsymbol{\Lambda}} : \underset{\sim}{\boldsymbol{\varepsilon}}^e, \quad \underset{\sim}{\boldsymbol{s}} = -H_\chi\, \underset{\sim}{\boldsymbol{e}}^p, \quad \underset{\sim}{\boldsymbol{M}} = A\, \underset{\sim}{\boldsymbol{\Gamma}}_\chi$
with $\underset{\approx}{\boldsymbol{\Lambda}}$ the four–rank tensor of the elastic moduli assumed isotropic
H_χ and A the generalised moduli

Resulting back–stress: $x = -\underset{\sim}{\boldsymbol{s}} : (\underline{\boldsymbol{l}} \otimes \underline{\boldsymbol{n}}) = A \left(\operatorname{curl} \operatorname{curl} \underset{\sim}{\boldsymbol{\chi}}^p \right) : (\underline{\boldsymbol{l}} \otimes \underline{\boldsymbol{n}})$
where $\underline{\boldsymbol{l}} \otimes \underline{\boldsymbol{n}}$ is the orientation tensor

Internal constraint: in $s = -H_\chi\, \underset{\sim}{\boldsymbol{e}}^p$, the modulus H_χ is equivalent to a penalty factor it constrains $\underset{\sim}{\boldsymbol{e}}^p$ to be sufficiently small and sets a coupling between $\underset{\sim}{\boldsymbol{H}}^p$ and $\underset{\sim}{\boldsymbol{\chi}}^p$ (if $H_\chi \to \infty$, $\underset{\sim}{\boldsymbol{\chi}}^p \equiv \underset{\sim}{\boldsymbol{H}}^p$)

Intrinsic length scale: $l_s = \sqrt{A/H_\chi}$

Appendix A.5: Extension of the *microcurl* model to finite deformations

The objective of this appendix is to formulate a finite deformation extension of the *microcurl* model presented in Chapter II and in Cordero *et al.* (2010). This formulation has been accepted for publication in the International Journal of Engineering Science in the paper "*Micromorphic approach to single crystal plasticity and damage*" (Aslan *et al.*, 2011).

A.5.1 Notation

This formulation requires a specific notation. Vectors and second rank tensors are denoted by $\underline{\boldsymbol{a}}\,, \underset{\sim}{\boldsymbol{a}}$, respectively. The theory is formulated within the general finite deformation framework essentially following Eringen's choice of strain measures (Eringen, 1999). The initial and current positions of the material point are denoted by $\underline{\boldsymbol{X}}$ and $\underline{\boldsymbol{x}}$, respectively. Throughout this appendix, the initial configuration of the body is V_0 whereas V denotes the current one. The associated smooth boundaries are ∂V_0 and ∂V with normal vector $\underline{\boldsymbol{N}}$ and $\underline{\boldsymbol{n}}$. The gradient operators with respect to initial and current coordinates are called $\boldsymbol{\nabla}_X$ and $\boldsymbol{\nabla}_x$ respectively. Similarly, the divergence and curl operators are Div, div and Curl, curl whether they are computed with respect to initial or current positions, respectively. Intrinsic notation is used in general but it is sometimes complemented or replaced by the index notation for clarity. A Cartesian coordinate system is used throughout with respect to the orthonormal basis $(\underline{\boldsymbol{e}}_1, \underline{\boldsymbol{e}}_2, \underline{\boldsymbol{e}}_3)$. The notations for double contraction and gradient operations are:

$$\underset{\sim}{\boldsymbol{A}} : \underset{\sim}{\boldsymbol{B}} = A_{ij}B_{ij}, \quad \underline{\boldsymbol{u}} \otimes \boldsymbol{\nabla}_X = \frac{\partial u_i}{\partial X_j}\, \underline{\boldsymbol{e}}_i \otimes \underline{\boldsymbol{e}}_j. \tag{VI.22}$$

A.5.2 Balance equations

The degrees of freedom of the proposed theory are the displacement vector $\underline{\boldsymbol{u}}$ and the micro–deformation variable $\underset{\sim}{\hat{\boldsymbol{\chi}}}^p$, a generally non–symmetric second rank tensor. The field $\underset{\sim}{\hat{\boldsymbol{\chi}}}^p(\underline{\boldsymbol{X}})$ is generally not compatible, meaning that it does not derive from a vector field. The exponent ^{p} indicates that this variable is constitutively related to plastic deformation occurring at the material point. In particular, the microdeformation $\underset{\sim}{\hat{\boldsymbol{\chi}}}^p$ is treated as an invariant quantity with respect to rigid body motion. The constitutive model will eventually ensure this invariance property. This is in contrast to the general microdeformation degrees of freedom of the original micromorphic theory. A first gradient theory is considered with respect to the degrees of freedom. However, the influence of the microdeformation gradient is limited to its curl part because of the aimed relation to the dislocation density tensor associated with the curl of plastic distortion. The following sets of degrees of freedom and of their gradients are therefore defined:

$$DOF = \{\underline{\boldsymbol{u}}\,, \quad \underset{\sim}{\hat{\boldsymbol{\chi}}}^p\}, \quad GRAD = \{\underset{\sim}{\boldsymbol{F}} := \underset{\sim}{\boldsymbol{1}} + \underline{\boldsymbol{u}} \otimes \boldsymbol{\nabla}_X, \quad \underset{\sim}{\boldsymbol{K}} := \mathrm{Curl}\, \underset{\sim}{\hat{\boldsymbol{\chi}}}^p\}. \tag{VI.23}$$

The following definition of the Curl operator is adopted:

$$\mathrm{Curl}\, \underset{\sim}{\hat{\boldsymbol{\chi}}}^p := \frac{\partial \underset{\sim}{\hat{\boldsymbol{\chi}}}^p}{\partial X_k} \times \underline{\boldsymbol{e}}_k, \quad K_{ij} := \epsilon_{jkl} \frac{\partial \hat{\chi}^p_{ik}}{\partial X_l} \tag{VI.24}$$

where ϵ_{ijk} is the permutation tensor.
The method of virtual power is used to derive the balance and boundary conditions, following

Germain (1973). For that purpose, we define the power density of internal forces as a linear form with respect to the velocity fields and their Eulerian gradients:

$$p^{(i)} = \underset{\sim}{\boldsymbol{\sigma}} : (\dot{\underline{\boldsymbol{u}}} \otimes \boldsymbol{\nabla}_x) + \underset{\sim}{\boldsymbol{s}} : \dot{\underset{\sim}{\boldsymbol{\chi}}}^p + \underset{\sim}{\boldsymbol{M}} : \operatorname{curl} \dot{\underset{\sim}{\boldsymbol{\chi}}}^p, \quad \forall \underline{\boldsymbol{x}} \in V \tag{VI.25}$$

where the conjugate quantities are the Cauchy stress tensor $\underset{\sim}{\boldsymbol{\sigma}}$, which is symmetric for objectivity reasons, the microstress tensor, $\underset{\sim}{\boldsymbol{s}}$, and the generalised couple stress tensor $\underset{\sim}{\boldsymbol{M}}$. The curl of the microdeformation rate is defined as

$$\operatorname{curl} \dot{\underset{\sim}{\boldsymbol{\chi}}}^p := \epsilon_{jkl} \frac{\partial \dot{\chi}^p_{ik}}{\partial x_l} \underline{\boldsymbol{e}}_i \otimes \underline{\boldsymbol{e}}_j = \dot{\underset{\sim}{\boldsymbol{K}}} \cdot \underset{\sim}{\boldsymbol{F}}^{-1}. \tag{VI.26}$$

The form of the power density of internal forces dictates the form of the power density of contact forces:

$$p^{(c)} = \underline{\boldsymbol{t}} \cdot \dot{\underline{\boldsymbol{u}}} + \underset{\sim}{\boldsymbol{m}} : \dot{\underset{\sim}{\boldsymbol{\chi}}}^p, \quad \forall \underline{\boldsymbol{x}} \in \partial V \tag{VI.27}$$

where $\underline{\boldsymbol{t}}$ is the usual simple traction vector and $\underset{\sim}{\boldsymbol{m}}$ the double traction tensor. The principle of virtual power is stated in the static case and in the absence of volume forces for the sake of brevity:

$$-\int_D p^{(i)}\, dV + \int_{\partial D} p^{(c)}\, dS = 0 \tag{VI.28}$$

for all virtual fields $\dot{\underline{\boldsymbol{u}}}, \dot{\underset{\sim}{\boldsymbol{\chi}}}^p$, and any subdomain $D \subset V$. By application of Gauss divergence theorem, assuming sufficient regularity of the fields, this statement expands into:

$$\int_V \frac{\partial \sigma_{ij}}{\partial x_j} \dot{u}_i\, dV + \int_V \left(\epsilon_{kjl} \frac{\partial M_{ik}}{\partial x_l} - s_{ij} \right) \dot{\chi}^p_{ij}\, dV + \int_{\partial V} (t_i - \sigma_{ij} n_j)\, \dot{u}_i\, dS + \int_{\partial V} (m_{ik} - \epsilon_{jkl} M_{ij} n_l)\, \dot{\chi}^p_{ik}\, dS = 0, \quad \forall \dot{u}_i, \forall \dot{\chi}^p_{ij} \tag{VI.29}$$

which leads to the two field equations of balance of momentum and generalised balance of moment of momentum:

$$\operatorname{div} \underset{\sim}{\boldsymbol{\sigma}} = 0, \quad \operatorname{curl} \underset{\sim}{\boldsymbol{M}} + \underset{\sim}{\boldsymbol{s}} = 0, \quad \forall \underline{\boldsymbol{x}} \in V \tag{VI.30}$$

and two boundary conditions

$$\underline{\boldsymbol{t}} = \underset{\sim}{\boldsymbol{\sigma}} \cdot \underline{\boldsymbol{n}}, \quad \underset{\sim}{\boldsymbol{m}} = \underset{\sim}{\boldsymbol{M}} \cdot \underset{\sim}{\boldsymbol{\epsilon}} \cdot \underline{\boldsymbol{n}}, \quad \forall \underline{\boldsymbol{x}} \in \partial V \tag{VI.31}$$

the index notation of the latter relation being $m_{ij} = M_{ik} \epsilon_{kjl} n_l$.

A.5.3 Constitutive equations

The deformation gradient is decomposed into elastic and plastic parts in the form

$$\underset{\sim}{\boldsymbol{F}} = \underset{\sim}{\boldsymbol{F}}^e \cdot \underset{\sim}{\boldsymbol{F}}^p. \tag{VI.32}$$

The isoclinic intermediate configuration is defined in a unique way by keeping the crystal orientation unchanged from the initial to the intermediate configuration following Mandel (1973). The plastic distortion $\underset{\sim}{\boldsymbol{F}}^p$ is invariant with respect to rigid body motions that are carried by $\underset{\sim}{\boldsymbol{F}}^e$. The current mass density is ρ whereas the mass density of the material element in the intermediate configuration is ρ_i, such that $\rho_i/\rho = J_e := \det F^e$. The elastic strain is defined as

$$\underset{\sim}{\boldsymbol{E}}^e := \frac{1}{2} \left(\underset{\sim}{\boldsymbol{F}}^{eT} \cdot \underset{\sim}{\boldsymbol{F}}^e - \underset{\sim}{\boldsymbol{1}} \right). \tag{VI.33}$$

The microdeformation is linked to the plastic deformation via the introduction of a relative deformation measure defined as

$$\underset{\sim}{\boldsymbol{e}}^p := \underset{\sim}{\boldsymbol{F}}^{p-1} \cdot \hat{\underset{\sim}{\boldsymbol{\chi}}}^p - \underset{\sim}{\mathbf{1}}. \tag{VI.34}$$

It measures the departure of the microdeformation from the plastic deformation, which will be associated with a cost in the free energy potential. When $\underset{\sim}{\boldsymbol{e}}^p \equiv \underset{\sim}{\mathbf{1}}$, the microdeformation coincides with the plastic deformation. The state variables are assumed to be the elastic strain, the relative deformation, the curl of microdeformation and some internal variables, α:

$$STATE := \{\underset{\sim}{\boldsymbol{E}}^e, \quad \underset{\sim}{\boldsymbol{e}}^p, \quad \underset{\sim}{\boldsymbol{K}}, \quad \alpha\}. \tag{VI.35}$$

The specific Helmholtz free energy density, ψ, is assumed to be a function of this set of state variables. In particular, in this simple version of the model, the curl of microdeformation is assumed to contribute entirely to the stored energy. In more sophisticated models, as proposed in (Forest and Sievert, 2003, 2006; Forest, 2009), the relative deformation, the microdeformation and its gradient can be split into elastic and plastic parts. This is not necessary for the size effects described in the present work.
The dissipation rate density is the difference:

$$D := p^{(i)} - \rho\dot{\psi} \geq 0 \tag{VI.36}$$

which must be positive according to the second principle of thermodynamics. When the previous strain measures are introduced, the power density of internal forces takes the following form:

$$\begin{aligned} p^{(i)} &= \underset{\sim}{\boldsymbol{\sigma}} : \dot{\underset{\sim}{\boldsymbol{F}}}^e \cdot \underset{\sim}{\boldsymbol{F}}^{e-1} + \underset{\sim}{\boldsymbol{\sigma}} : \underset{\sim}{\boldsymbol{F}}^e \cdot \dot{\underset{\sim}{\boldsymbol{F}}}^p \cdot \underset{\sim}{\boldsymbol{F}}^{p-1} \cdot \underset{\sim}{\boldsymbol{F}}^{e-1} + \underset{\sim}{\boldsymbol{s}} : \left(\underset{\sim}{\boldsymbol{F}}^p \cdot \dot{\underset{\sim}{\boldsymbol{e}}}^p + \dot{\underset{\sim}{\boldsymbol{F}}}^p \cdot \underset{\sim}{\boldsymbol{e}}^p\right) + \underset{\sim}{\boldsymbol{M}} : \dot{\underset{\sim}{\boldsymbol{K}}} \cdot \underset{\sim}{\boldsymbol{F}}^{-1} \\ &= \frac{\rho}{\rho_i} \underset{\sim}{\boldsymbol{\Pi}}^e : \dot{\underset{\sim}{\boldsymbol{E}}}^e + \frac{\rho}{\rho_i} \underset{\sim}{\boldsymbol{\Pi}}^M : \dot{\underset{\sim}{\boldsymbol{F}}}^p \cdot \underset{\sim}{\boldsymbol{F}}^{p-1} + \underset{\sim}{\boldsymbol{s}} : \left(\underset{\sim}{\boldsymbol{F}}^p \cdot \dot{\underset{\sim}{\boldsymbol{e}}}^p + \dot{\underset{\sim}{\boldsymbol{F}}}^p \cdot \underset{\sim}{\boldsymbol{e}}^p\right) + \underset{\sim}{\boldsymbol{M}} : \dot{\underset{\sim}{\boldsymbol{K}}} \cdot \underset{\sim}{\boldsymbol{F}}^{-1} \end{aligned} \tag{VI.37}$$

where $\underset{\sim}{\boldsymbol{\Pi}}^e$ is the second Piola–Kirchhoff stress tensor with respect to the intermediate configuration and $\underset{\sim}{\boldsymbol{\Pi}}^M$ is the Mandel stress tensor:

$$\underset{\sim}{\boldsymbol{\Pi}}^e := J_e \underset{\sim}{\boldsymbol{F}}^{e-1} \cdot \underset{\sim}{\boldsymbol{\sigma}} \cdot \underset{\sim}{\boldsymbol{F}}^{e-T}, \quad \underset{\sim}{\boldsymbol{\Pi}}^M := J_e \underset{\sim}{\boldsymbol{F}}^{eT} \cdot \underset{\sim}{\boldsymbol{\sigma}} \cdot \underset{\sim}{\boldsymbol{F}}^{e-T} = \underset{\sim}{\boldsymbol{F}}^{eT} \cdot \underset{\sim}{\boldsymbol{F}}^e \cdot \underset{\sim}{\boldsymbol{\Pi}}^e. \tag{VI.38}$$

On the other hand,

$$\rho\dot{\psi} = \rho \frac{\partial \psi}{\partial \underset{\sim}{\boldsymbol{E}}^e} : \dot{\underset{\sim}{\boldsymbol{E}}}^e + \rho \frac{\partial \psi}{\partial \underset{\sim}{\boldsymbol{e}}^p} : \dot{\underset{\sim}{\boldsymbol{e}}}^p + \rho \frac{\partial \psi}{\partial \underset{\sim}{\boldsymbol{K}}} : \dot{\underset{\sim}{\boldsymbol{K}}} + \rho \frac{\partial \psi}{\partial \alpha} : \dot{\underset{\sim}{\boldsymbol{\alpha}}}, \tag{VI.39}$$

we compute

$$\begin{aligned} J_e D = &\left(\underset{\sim}{\boldsymbol{\Pi}}^e - \rho_i \frac{\partial \psi}{\partial \underset{\sim}{\boldsymbol{E}}^e}\right) : \dot{\underset{\sim}{\boldsymbol{E}}}^e + \left(J_e \underset{\sim}{\boldsymbol{F}}^{pT} \cdot \underset{\sim}{\boldsymbol{s}} - \rho_i \frac{\partial \psi}{\partial \underset{\sim}{\boldsymbol{e}}^p}\right) : \dot{\underset{\sim}{\boldsymbol{e}}}^p + \left(J_e \underset{\sim}{\boldsymbol{M}} \cdot \underset{\sim}{\boldsymbol{F}}^{-T} - \rho_i \frac{\partial \psi}{\partial \underset{\sim}{\boldsymbol{K}}}\right) : \dot{\underset{\sim}{\boldsymbol{K}}} \\ &+ \left(\underset{\sim}{\boldsymbol{\Pi}}^M + J_e \underset{\sim}{\boldsymbol{s}} \cdot \hat{\underset{\sim}{\boldsymbol{\chi}}}^{pT}\right) : \dot{\underset{\sim}{\boldsymbol{F}}}^p \cdot \underset{\sim}{\boldsymbol{F}}^{p-1} - \rho_i \frac{\partial \psi}{\partial \alpha} : \dot{\underset{\sim}{\boldsymbol{\alpha}}} \geq 0. \end{aligned} \tag{VI.40}$$

Assuming that the processes associated with $\dot{\underset{\sim}{\boldsymbol{E}}}^e, \dot{\underset{\sim}{\boldsymbol{e}}}^p$ and $\dot{\underset{\sim}{\boldsymbol{K}}}$ are non–dissipative, the state laws are obtained:

$$\underset{\sim}{\boldsymbol{\Pi}}^e = \rho_i \frac{\partial \psi}{\partial \underset{\sim}{\boldsymbol{E}}^e}, \quad \underset{\sim}{\boldsymbol{s}} = J_e^{-1} \underset{\sim}{\boldsymbol{F}}^{p-T} \cdot \rho_i \frac{\partial \psi}{\partial \underset{\sim}{\boldsymbol{e}}^p}, \quad \underset{\sim}{\boldsymbol{M}} = J_e^{-1} \rho_i \frac{\partial \psi}{\partial \underset{\sim}{\boldsymbol{K}}} \cdot \underset{\sim}{\boldsymbol{F}}^T. \tag{VI.41}$$

The residual dissipation rate is

$$J_e D = \left(\underset{\sim}{\boldsymbol{\Pi}}^M + J_e \underset{\sim}{\boldsymbol{s}} \cdot \hat{\underset{\sim}{\boldsymbol{\chi}}}^{pT}\right) : \dot{\underset{\sim}{\boldsymbol{F}}}^p \cdot \underset{\sim}{\boldsymbol{F}}^{p-1} - R\dot{\alpha} \geq 0, \quad \text{with} \quad R := \rho_i \frac{\partial \psi}{\partial \alpha}. \tag{VI.42}$$

Due to the specific choice of energy storage associated with relative deformation and microdeformation gradient, the higher order terms do not appear in the residual dissipation. More general constitutive frameworks can be proposed to include dissipative parts due to gradient effects (see Forest and Sievert, 2003; Gurtin and Anand, 2009; Forest, 2009).
At this stage, a dissipation potential, function of stress measures, $\Omega(\underset{\sim}{\boldsymbol{\mathcal{S}}}, R)$, is introduced in order to formulate the evolution equations for plastic flow and internal variables:

$$\dot{\underset{\sim}{\boldsymbol{F}}}^p \cdot \underset{\sim}{\boldsymbol{F}}^{p-1} = \frac{\partial \Omega}{\partial \underset{\sim}{\boldsymbol{\mathcal{S}}}}, \quad \text{with} \quad \underset{\sim}{\boldsymbol{\mathcal{S}}} := \underset{\sim}{\boldsymbol{\Pi}}^M + J_e \underset{\sim}{\boldsymbol{s}} \cdot \underset{\sim}{\hat{\boldsymbol{\chi}}}^{pT}, \tag{VI.43}$$

$$\dot{\alpha} = -\frac{\partial \Omega}{\partial R} \tag{VI.44}$$

where R is the thermodynamic force associated with the internal variable α, and $\underset{\sim}{\boldsymbol{\mathcal{S}}}$ is the effective stress conjugate to plastic strain rate, the driving force for plastic flow.
In the case of crystal plasticity, a generalised Schmid law is adopted for each slip system s in the form:

$$f^s\left(\underset{\sim}{\boldsymbol{\mathcal{S}}}, \tau_c^s\right) = |\underset{\sim}{\boldsymbol{\mathcal{S}}} : \underset{\sim}{\boldsymbol{P}}^s| - \tau_c^s \geq 0, \quad \text{with} \quad \underset{\sim}{\boldsymbol{P}}^s = \underline{\boldsymbol{l}}^s \otimes \underline{\boldsymbol{n}}^s \tag{VI.45}$$

for activation of slip system s with slip direction, $\underline{\boldsymbol{l}}^s$, and normal to the slip plane, $\underline{\boldsymbol{n}}^s$. We call $\underset{\sim}{\boldsymbol{P}}^s$ the orientation tensor. The critical resolved shear stress is τ_c^s which may be a function of R in the presence of isotropic hardening. The kinematics of plastic slip follows from the choice of a dissipation potential, $\Omega(f^s)$, that depends on the stress variables through the yield function itself, f^s:

$$\dot{\underset{\sim}{\boldsymbol{F}}}^p \cdot \underset{\sim}{\boldsymbol{F}}^{p-1} = \sum_{s=1}^{N} \frac{\partial \Omega}{\partial f^s} \frac{\partial f^s}{\partial \underset{\sim}{\boldsymbol{\mathcal{S}}}} = \sum_{s=1}^{N} \dot{\gamma}^s \underset{\sim}{\boldsymbol{P}}^s, \quad \text{with} \quad \dot{\gamma}^s = \frac{\partial \Omega}{\partial f^s} \text{sign}\left(\underset{\sim}{\boldsymbol{\mathcal{S}}} : \underset{\sim}{\boldsymbol{P}}^s\right). \tag{VI.46}$$

A possible viscoplastic potential is then:

$$\Omega(f^s) = \frac{K}{n+1} < \frac{f^s}{K} >^{n+1} \tag{VI.47}$$

where K and n are viscosity parameters associated with viscoplastic slip, and the brackets stand for $< \cdot >= Max(0, \cdot)$. The generalised resolved shear stress can be decomposed into two contributions:

$$\underset{\sim}{\boldsymbol{\mathcal{S}}} : \underset{\sim}{\boldsymbol{P}}^s = \tau^s - x^s, \quad \text{with} \quad \tau^s = \underset{\sim}{\boldsymbol{\Pi}}^M : \underset{\sim}{\boldsymbol{P}}^s \quad \text{and} \quad x^s = -\underset{\sim}{\boldsymbol{s}} \cdot \underset{\sim}{\hat{\boldsymbol{\chi}}}^{pT} : \underset{\sim}{\boldsymbol{P}}^s. \tag{VI.48}$$

The usual resolved shear stress is τ^s whereas x^s can be interpreted as an internal stress or back–stress leading to kinematic hardening. The fact that the introduction of the effect of the dislocation density tensor or, more generally, of gradient of plastic strain tensor, leads to the existence of an internal stresses induced by higher order stresses has already been noticed by Steinmann (1996) (see also Forest, 2008). The back–stress component is induced by the micro–stress $\underset{\sim}{\boldsymbol{s}}$ or, equivalently, by the curl of the generalised couple stress tensor, $\underset{\sim}{\boldsymbol{M}}$, via the balance equation (VI.30).

When deformations and rotations remain sufficiently small, the previous equations can be linearised as follows:

$$\underset{\sim}{\boldsymbol{F}} = \underset{\sim}{\boldsymbol{1}} + \underset{\sim}{\boldsymbol{H}} \simeq \underset{\sim}{\boldsymbol{1}} + \underset{\sim}{\boldsymbol{H}}^e + \underset{\sim}{\boldsymbol{H}}^p, \quad \underset{\sim}{\boldsymbol{H}}^e = \underset{\sim}{\boldsymbol{\varepsilon}}^e + \underset{\sim}{\boldsymbol{\omega}}^e, \quad \underset{\sim}{\boldsymbol{H}}^p = \underset{\sim}{\boldsymbol{\varepsilon}}^p + \underset{\sim}{\boldsymbol{\omega}}^p \tag{VI.49}$$

where $\underset{\sim}{\boldsymbol{\varepsilon}}^e, \underset{\sim}{\boldsymbol{\omega}}^e$ (resp. $\underset{\sim}{\boldsymbol{\varepsilon}}^p, \underset{\sim}{\boldsymbol{\omega}}^p$) are the symmetric and skew–symmetric parts of $\underset{\sim}{\boldsymbol{F}}^e - \underset{\sim}{\boldsymbol{1}}$ (resp. $\underset{\sim}{\boldsymbol{F}}^p - \underset{\sim}{\boldsymbol{1}}$). When microdeformation is small, the relative deformation is linearised as

$$\underset{\sim}{\boldsymbol{e}}^p = \left(\underset{\sim}{\boldsymbol{1}} + \underset{\sim}{\boldsymbol{\varepsilon}}^p + \underset{\sim}{\boldsymbol{\omega}}^p\right)^{-1} \cdot \left(\underset{\sim}{\boldsymbol{1}} + \underset{\sim}{\boldsymbol{\chi}}^p\right) - \underset{\sim}{\boldsymbol{1}} \simeq \underset{\sim}{\boldsymbol{\chi}}^p - \underset{\sim}{\boldsymbol{H}}^p, \quad \text{with} \quad \underset{\sim}{\boldsymbol{\chi}}^p = \underset{\sim}{\hat{\boldsymbol{\chi}}}^p - \underset{\sim}{\boldsymbol{1}}. \tag{VI.50}$$

When linearised, the state laws (VI.41) become:

$$\underset{\sim}{\boldsymbol{\sigma}} = \rho\frac{\partial\psi}{\partial\underset{\sim}{\boldsymbol{\varepsilon}}^e}, \quad \underset{\sim}{\boldsymbol{s}} = \rho\frac{\partial\psi}{\partial\underset{\sim}{\boldsymbol{e}}^p}, \quad \underset{\sim}{\boldsymbol{M}} = \rho\frac{\partial\psi}{\partial\underset{\sim}{\boldsymbol{K}}}. \tag{VI.51}$$

The evolution equations read then:

$$\dot{\underset{\sim}{\boldsymbol{\varepsilon}}}^p = \frac{\partial\Omega}{\partial\left(\underset{\sim}{\boldsymbol{\sigma}} + \underset{\sim}{\boldsymbol{s}}\right)}, \quad \dot{\underset{\sim}{\boldsymbol{\alpha}}} = \frac{\partial\Omega}{\partial R}. \tag{VI.52}$$

We adopt the most simple case of a quadratic free energy potential:

$$\rho\psi\left(\underset{\sim}{\boldsymbol{\varepsilon}}^e, \underset{\sim}{\boldsymbol{e}}^p, \underset{\sim}{\boldsymbol{K}}\right) = \frac{1}{2}\underset{\sim}{\boldsymbol{\varepsilon}}^e : \underset{\approx}{\boldsymbol{C}} : \varepsilon^e + \frac{1}{2}H_\chi\underset{\sim}{\boldsymbol{e}}^p : \underset{\sim}{\boldsymbol{e}}^p + \frac{1}{2}A\underset{\sim}{\boldsymbol{K}} : \underset{\sim}{\boldsymbol{K}}. \tag{VI.53}$$

The usual four–rank tensor of elastic moduli is denoted by $\underset{\approx}{\boldsymbol{C}}$. The higher order moduli have been limited to only two additional parameters: H_χ (unit MPa) and A (unit MPa.mm^2). It follows that:

$$\underset{\sim}{\boldsymbol{\sigma}} = \underset{\approx}{\boldsymbol{C}} : \underset{\sim}{\boldsymbol{\varepsilon}}^e, \quad \underset{\sim}{\boldsymbol{s}} = H_\chi\underset{\sim}{\boldsymbol{e}}^p, \quad \underset{\sim}{\boldsymbol{M}} = A\underset{\sim}{\boldsymbol{K}}. \tag{VI.54}$$

The yield condition for each slip system becomes:

$$f^s = |\tau^s - x^s| - \tau_c^s, \quad \text{with} \quad x^s = -\underset{\sim}{\boldsymbol{s}} : \underset{\sim}{\boldsymbol{P}}^s = \left(\operatorname{curl}\underset{\sim}{\boldsymbol{M}}\right) : \underset{\sim}{\boldsymbol{P}}^s = A\left(\operatorname{curl}\operatorname{curl}\underset{\sim}{\boldsymbol{\chi}}^p\right) : \underset{\sim}{\boldsymbol{P}}^s. \tag{VI.55}$$

References

Aslan O., Cordero N.M., Gaubert A., and Forest S. (2011). *Micromorphic approach to single crystal plasticity and damage.* International Journal of Engineering Science.

Cermelli P. and Gurtin M.E. (2001). *On the characterization of geometrically necessary dislocations in finite plasticity.* Journal of the Mechanics and Physics of Solids, vol. 49, pp 1539–1568.

Cordero N.M., Gaubert A., Forest S., Busso E.P., Gallerneau F., and Kruch S. (2010). *Size effects in generalised continuum crystal plasticity for two–phase laminates.* Journal of the Mechanics and Physics of Solids, vol. 58, pp 1963–1994.

Eringen A.C. (1999). *Microcontinuum field theories.* Springer, New York.

Forest S. (2008). *Some links between Cosserat, strain gradient crystal plasticity and the statistical theory of dislocations.* Philosophical Magazine, vol. 88, pp 3549–3563.

Forest S. (2009). *The micromorphic approach for gradient elasticity, viscoplasticity and damage.* ASCE Journal of Engineering Mechanics, vol. 135, pp 117–131.

Forest S. and Sievert R. (2003). *Elastoviscoplastic constitutive frameworks for generalized continua.* Acta Mechanica, vol. 160, pp 71–111.

Forest S. and Sievert R. (2006). *Nonlinear microstrain theories.* International Journal of Solids and Structures, vol. 43, pp 7224–7245.

Germain P. (1973). *The method of virtual power in continuum mechanics. Part 2 : Microstructure.* SIAM J. Appl. Math., vol. 25, pp 556–575.

Gurtin M.E. and Anand L. (2009). *Thermodynamics applied to gradient theories involving the accumulated plastic strain: The theories of Aifantis and Fleck & Hutchinson and their generalization.* Journal of the Mechanics and Physics of Solids, vol. 57, pp 405–421.

Mandel J. (1973). *Equations constitutives et directeurs dans les milieux plastiques et viscoplastiques.* Int. J. Solids Structures, vol. 9, pp 725–740.

Steinmann P. (1996). *Views on multiplicative elastoplasticity and the continuum theory of dislocations.* International Journal of Engineering Science, vol. 34, pp 1717–1735.

Part B

Nanoelasticity

Chapter -VII-

Introduction

Contents

VII.1 Context

Due to their different local environments, atoms at a free surface and atoms in the bulk of a material have different associated energy and lattice spacing. This excess of energy associated with surface atoms is called *surface free energy* and gives rise to *surface stress*. This *surface energy*, γ, is equal to the reversible work per unit area needed to create a new surface noted w_1 in Fig. VII.1. This surface quantity is a scalar and has the form

$$\gamma = \frac{w_1}{2\mathcal{A}} \tag{VII.1}$$

where $\mathcal{A}$ is the created surface area. This concept is fundamental to determine the behaviour of fluid surfaces or fluid–fluid interfaces. In the case of solids, Gibbs (1906) showed that another type of surface effect, called *surface stress*, takes place and affects the surface (or interface) behaviour (see also Cammarata, 1994, 1997; Müller and Saúl, 2004; Trimble and Cammarata, 2008). The *surface stress*, $\underset{\sim}{\boldsymbol{T}}^s$, is equal to the reversible work per unit area, noted w_2 in Fig. VII.1, needed to elastically stretch a surface that already exists. In this case, the surface quantity is a tensor. A constitutive relationship exists between γ and $\underset{\sim}{\boldsymbol{T}}^s$ and is known as the Shuttleworth's equation (Shuttleworth, 1950),

$$T^s_{ij} = \gamma\delta_{ij} + \frac{d\gamma}{d\varepsilon^s_{ij}}, \tag{VII.2}$$

where δ_{ij} is the Kronecker delta and ε^s_{ij} is the surface elastic strain tensor. Note that the term $d\gamma/d\varepsilon^s_{ij}$ vanishes in the case of fluids as there is no deformation. Then, as suggested by Eq. (VII.2), in fluids *surface stress* coincides with *surface energy* and is described by a scalar often called surface tension. *Surface energy* and *surface stress* both arise from the fact that the presence of a surface or an interface modifies locally the atomic configuration. However, they are linked to distinct physical origins and appear provided different requirements. The

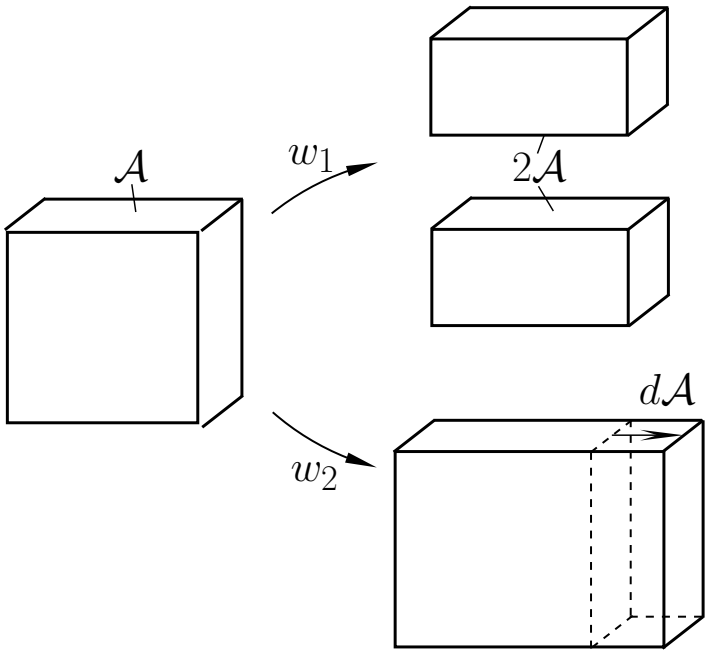

Figure VII.1 : A simple schematic representation of the two types of effects studied in this work arising at the surface or interface of fluids and solids. w_1 and w_2 are the reversible works per unit area needed to create a new surface or to elastically stretch an existing surface respectively. Then, the upper path illustrates *surface energy* and the lower path *surface stress*.

first one is linked to the broken bonds between atoms in the surface region and their missing neighbours which leads to different equilibrium interatomic distances; it appears when a new surface is created. The second one is linked to the modification of the bond strength between atoms in the surface region and appears when the surface is deformed. These two fundamental concepts can be calculated in simple configurations such as dimers or monoatomic wires (Delin and Tosatti, 2004; Zarechnaya *et al.*, 2008). For example, Fig. VII.2 presents the difference between the calculated equilibrium molecular distances for some diatomic molecules (dimers) and the calculated distances in the corresponding bulk materials. However, these differences are not clearly described and distinguished in most experimental works and remain a source of confusion. The need to distinguish *surface energy* from *surface stress* is discussed in Kramer and Weissmüller (2007) and appears unambiguously in the present work, where these effects will be addressed separately in simple analytical boundary value problems (see Sections X.1.1, X.1.2 and X.1.3).

The surface region is only a few atomic layers thin, that is why surface effects can be neglected when the characteristic length of the microstructure of the considered material is within the micrometer range or larger. In contrast, for nano-sized microstructures, the surface–to–volume ratio is much higher and the surface region behaviour can no longer be neglected. Indeed, the mechanical behaviour of this type of materials is known to be significantly dependent on the surface effects as it is observed theoretically and experimentally in the literature (see, for instance, Miller and Shenoy, 2000; Sharma *et al.*, 2003; Cuenot *et al.*, 2004; McDowell *et al.*, 2008; Sadeghian *et al.*, 2009). There are several ways to introduce the surface mechanical properties. If an interface separating two homogeneous bulk phases is considered, one can define the interfacial properties by using an inter–phase with a finite volume and assign thermodynamic properties in the usual way, as in Capolungo *et al.* (2005).

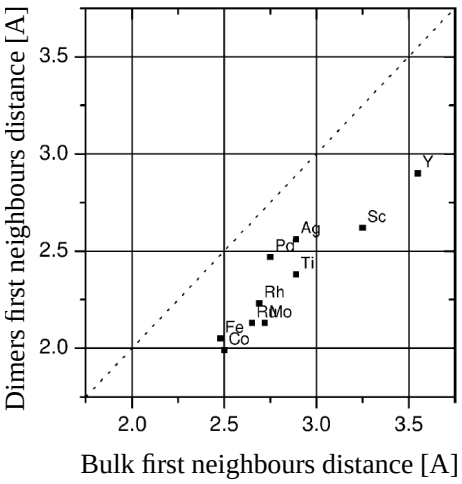

Figure VII.2 : Comparison of ab–initio calculated equilibrium distances for some diatomic molecules (dimers) with the inter–atomic distances calculated in the corresponding bulk materials (Müller and Saúl, 2004).

Three phases are considered in this approach and the boundaries of the inter–phase have to be defined more or less arbitrary.

One can also consider that the two homogeneous phases are separated by a single dividing interface; the thermodynamic properties of the interface are defined as the excess over the values obtained for both bulk phases separated by a zero–thickness surface (Müller and Saúl, 2004; Dingreville *et al.*, 2005). A continuum mechanical theory of surface/interface behaviour has been formulated by Gurtin and Murdoch (1975, 1978). It introduces a volume stress tensor in the bulk of the material and a *surface stress* tensor at the surface or interface modelled as a membrane. Both stress tensors fulfill balance of momentum equations. A specific elastic behaviour is attributed to the membrane and kinematic constraints ensure that the bulk and the surface remain coherent. The most common manifestation of surface behaviour is capillarity effects in elastic fluids. It is described by the Young–Laplace equation which states that the internal pressure, p, in a spherical droplet is proportional to the surface tension, T, multiplied by the surface curvature, $1/r$:

$$p = \frac{2T}{r}. \tag{VII.3}$$

When the size of the considered object is small enough, there is no clear way to define a sharp interface or surface. Instead, a continuum model can be used to describe a transition domain between two bulk regions, or between the bulk and the outer free surface. Such continuum theories for diffuse surface or interfaces have been developed for a refined description of capillarity in elastic fluids and solids. They are based on higher order gradient theories like the Korteweg equation which involves the gradient of a density vector, see Truesdell and Noll (1965). A more general strain gradient theory has been proposed by Casal (1963, 1972) and Casal and Gouin (1985). In an insufficiently known paper, Mindlin (1965) claims that a second gradient of strain theory or, equivalently, a third gradient of displacement theory is in fact needed to describe, in a continuous manner, capillarity and cohesion effects in isotropic linear elastic solids and fluids. Based on a simple one–dimensional atomic chain model, he identifies the higher order elasticity modulus that is responsible for the variation of lattice spacing from the free surface into the bulk in a semi–infinite crystal. This

model has not been discussed in the literature, so that there seems to be no general opinion whether a first or second strain gradient theory is needed for capillarity effects in linear elastic media. On the other hand, Mindlin's second gradient of strain theory is challenging from a computational point of view to calculate fields of lattice parameters in nano–objects like nano–particles and nanowires and in nano–structured materials like nanocrystals or nano–porous materials (Duan *et al.*, 2005, 2006). Molecular static simulation techniques enable the description of such non–homogeneous distributions of lattice spacing in crystals close to free surfaces or grain boundaries, that could be represented using a suitable continuum model.

VII.2 Aims and outline

The objective of the present work is, firstly, to discuss the need of a second gradient of strain theory to introduce surface effects without distinguishing between the properties of the surface (or interface) from those of the bulk. To that purpose, the Korteweg's equation is compared with the first and second gradient of strain theories in order to highlight the main differences, and a framework for the numerical implementation of Mindlin's second strain gradient theory is provided for fluids. Finite element implementations of the first gradient of strain theory exist in literature. They are based on the introduction of additional strain degrees of freedom in the spirit of Eringen's micromorphic approach (Shu *et al.*, 1999; Dillard *et al.*, 2006; Forest, 2009). That is why a second order micromorphic model is formulated. Then, an internal constraint must be enforced by means of Lagrange multipliers or a suitable penalisation so as to reduce the general micromorphic model to Mindlin's second gradient of strain model.

The second purpose of the present work is to apply Mindlin's theory to elastic solids and to propose an adapted micromorphic approach and its finite element implementation. Once this framework is set, it is applied to simple boundary value problems in order to illustrate its capabilities and to show how the surface effects occur. This continuum model is then used to simulate the apparent elastic properties of nanowires (Song *et al.*, 2011). Molecular simulations are widely used to study these nano–objects (Diao *et al.*, 2004; Liang *et al.*, 2005; Agrawal *et al.*, 2008; Wang *et al.*, 2010) and finite element–based approaches are also used to introduce surface effects in various ways (He and Lilley, 2009; Mitrushchenkov *et al.*, 2010; Javili and Steinmann, 2011).

This part is organised as follows. In Chapter VIII, the links between Korteweg's equation and the first strain gradient theory are presented (Section VIII.1). Then, arguments pleading for the need for a second strain gradient model are provided (Section VIII.2). A micromorphic generalisation of Mindlin's model for fluids is finally proposed (Section VIII.3), as the suitable framework for a finite element implementation of higher order gradient theories. Chapter IX is focused on the case of elastic solids. Mindlin's theory is first presented to that purpose (Section IX.1), a corresponding second order micromorphic approach is then formulated (Section IX.2) and the main features of its finite element implementation are given (Appendix B.3).

The notation used hereafter are given in Appendix B.1.

References

Agrawal R., Peng B., Gdoutos E.E., and Espinosa H.D. (2008). *Elasticity Size Effects in ZnO Nanowires- A Combined Experimental-Computational Approach.* Nano Lett, vol. 8 n° 11, pp 3668–3674.

Cammarata R.C. (1994). *Surface and interface stress effects in thin films.* Progress in surface science, vol. 46 n° 1, pp 1–38.

Cammarata R.C. (1997). *Surface and interface stress effects on interfacial and nanostructured materials.* Materials Science and Engineering A, vol. 237 n° 2, pp 180–184.

Capolungo L., Jochum C., Cherkaoui M., and Qu J. (2005). *Homogenization method for strength and inelastic behavior of nanocrystalline materials.* International Journal of Plasticity, vol. 21 n° 1, pp 67–82.

Casal P. (1963). *Capillarité interne en mecanique.* CR Acad. Sci. Paris, vol. 256, pp 3820–3822.

Casal P. (1972). *La théorie du second gradient et la capillarité.* CR Acad. Sci. Paris, vol. 274, pp 1571–1574.

Casal P. and Gouin H. (1985). *Relation entre l'équation de l'énergie et l'équation du mouvement en théorie de Korteweg de la capillarité.* Comptes-rendus des séances de l'Académie des sciences. Série 2, Mécanique-physique, chimie, sciences de l'univers, sciences de la terre, vol. 300, pp 231–234.

Cuenot S., Frétigny C., Demoustier-Champagne S., and Nysten B. (2004). *Surface tension effect on the mechanical properties of nanomaterials measured by atomic force microscopy.* Physical Review B, vol. 69 n° 16, pp 165410.

Delin A. and Tosatti E. (2004). *The electronic structure of 4d transition-metal monatomic wires.* Journal of Physics: Condensed Matter, vol. 16, pp 8061.

Diao J., Gall K., *et al.* (2004). *Atomistic simulation of the structure and elastic properties of gold nanowires.* Journal of the Mechanics and Physics of Solids, vol. 52 n° 9, pp 1935–1962.

Dillard T., Forest S., and Ienny P. (2006). *Micromorphic continuum modelling of the deformation and fracture behaviour of nickel foams.* European Journal of Mechanics A/Solids, vol. 25, pp 526–549.

Dingreville R., Qu J., and Cherkaoui M. (2005). *Surface free energy and its effect on the elastic behavior of nano-sized particles, wires and films.* Journal of the Mechanics and Physics of Solids, vol. 53 n° 8, pp 1827–1854.

Duan H.L., Wang J., Huang Z.P., and Karihaloo B.L. (2005). *Size-dependent effective elastic constants of solids containing nano-inhomogeneities with interface stress.* Journal of the Mechanics and Physics of Solids, vol. 53 n° 7, pp 1574–1596.

Duan H.L., Wang J., Karihaloo B.L., and Huang Z.P. (2006). *Nanoporous materials can be made stiffer than non-porous counterparts by surface modification.* Acta materialia, vol. 54 n° 11, pp 2983–2990.

Forest S. (2009). *The micromorphic approach for gradient elasticity, viscoplasticity and damage.* ASCE Journal of Engineering Mechanics, vol. 135, pp 117–131.

Gibbs J.W. (1906). *Scientific Papers of J. Willard Gibbs*, vol. 1. Longmans, Green and co.

Gurtin M.E. and Murdoch A.I. (1975). *A continuum theory of elastic material surfaces.* Archive for Rational Mechanics and Analysis, vol. 57 n° 4, pp 291–323.

Gurtin M.E. and Murdoch A.I. (1978). *Surface stress in solids.* Int. J. Solids Struct, vol. 14 n° 6, pp 431–440.

He J. and Lilley C.M. (2009). *The finite element absolute nodal coordinate formulation incorporated with surface stress effect to model elastic bending nanowires in large deformation.* Computational Mechanics, vol. 44 n° 3, pp 395–403.

Javili A. and Steinmann P. (2011). *A finite element framework for continua with boundary energies. Part III: The thermomechanical case.* Computer Methods in Applied Mechanics and Engineering.

Kramer D. and Weissmüller J. (2007). *A note on surface stress and surface tension and their interrelation via Shuttleworth's equation and the Lippmann equation.* Surface science, vol. 601 n° 14, pp 3042–3051.

Liang H., Upmanyu M., and Huang H. (2005). *Size-dependent elasticity of nanowires: Nonlinear effects.* Physical Review B, vol. 71 n° 24, pp 241403.

McDowell M.T., Leach A.M., and Gall K. (2008). *On the elastic modulus of metallic nanowires.* Nano letters, vol. 8 n° 11, pp 3613–3618.

Miller R.E. and Shenoy V.B. (2000). *Size-dependent elastic properties of nanosized structural elements.* Nanotechnology, vol. 11, pp 139.

Mindlin R.D. (1965). *Second gradient of strain and surface–tension in linear elasticity.* Int. J. Solids Structures, vol. 1, pp 417–438.

Mitrushchenkov A., Chambaud G., Yvonnet J., and He Q.C. (2010). *Towards an elastic model of wurtzite AlN nanowires.* Nanotechnology, vol. 21, pp 255702.

Müller P. and Saúl A. (2004). *Elastic effects on surface physics.* Surface Science Reports, vol. 54 n° 5-8, pp 157–258.

Sadeghian H., Yang C.K., Goosen J.F.L., Van der Drift E., Bossche A., French P.J., and Van Keulen F. (2009). *Characterizing size-dependent effective elastic modulus of silicon nanocantilevers using electrostatic pull-in instability.* Applied Physics Letters, vol. 94, pp 221903.

Sharma P., Ganti S., and Bhate N. (2003). *Effect of surfaces on the size-dependent elastic state of nano-inhomogeneities.* Applied Physics Letters, vol. 82 n° 4, pp 535–537.

Shu J.Y., King W.E., and Fleck N.A. (1999). *Finite elements for materials with strain gradient effects.* Int. J. Numer. Meth. Engng, vol. 44, pp 373–391.

Shuttleworth R. (1950). *The surface tension of solids.* Proceedings of the Physical Society. Section A, vol. 63, pp 444.

Song F., Huang G.L., Park H.S., and Liu X.N. (2011). *A Continuum Model for the Mechanical Behavior of Nanowires Including Surface and Surface-Induced Initial Stresses.* International Journal of Solids and Structures, vol. 48, pp 2154–2163.

Trimble T.M. and Cammarata R.C. (2008). *Many-body effects on surface stress, surface energy and surface relaxation of fcc metals.* Surface Science, vol. 602 n° 14, pp 2339–2347.

Truesdell C. and Noll W. (1965). *The non-linear field theories of mechanics.* Handbuch der Physik, edited by S. Flügge, reedition Springer Verlag 2004.

Wang Z.G., Li J.B., Gao F., and Weber W.J. (2010). *Tensile and compressive mechanical behavior of twinned silicon carbide nanowires.* Acta Materialia, vol. 58 n° 6, pp 1963–1971.

Zarechnaya E.Y., Skorodumova N.V., Simak S.I., Johansson B., and Isaev E.I. (2008). *Theoretical study of linear monoatomic nanowires, dimer and bulk of Cu, Ag, Au, Ni, Pd and Pt.* Computational Materials Science, vol. 43 n° 3, pp 522–530.

Chapter -VIII-

Strain gradients model and capillarity

Abstract

Mindlin (1965) wrote a milestone paper claiming that a second strain gradient theory is required for a continuum description of volume cohesion and surface energy in isotropic elastic media. The objective of the present chapter is to compare Mindlin's approach to more standard capillarity models based on a first strain gradient theory and Korteweg's equation. A general micromorphic model is then proposed in the case of fluids as a numerical method to implement Mindlin's theory in a finite element code.

Contents

Preamble: The work presented in this chapter has been published in the journal "*Computational Materials Science* in a paper entitled "*First vs. second gradient of strain theory for capillarity effects in an elastic fluid at small length scales*" (Forest *et al.*, 2011). It is presented here with some minor modifications needed for the consistency of the notation used in this manuscript and to allow a better integration with the chapters which follow.

VIII.1 Korteweg's equation and first strain gradient model

The Van der Waals and Korteweg equations are the first attempts to introduce capillary effects in a continuum mechanical theory. For an elastic medium, they include not only the effect of mass density, ρ, on stress but also that of the density gradient $\boldsymbol{\nabla}\rho$, in the form

$$\underset{\sim}{\boldsymbol{T}} = -p(\rho)\underset{\sim}{\mathbf{1}} - \alpha(\boldsymbol{\nabla}\rho)^2\underset{\sim}{\mathbf{1}} - \beta\boldsymbol{\nabla}\rho\otimes\boldsymbol{\nabla}\rho + \delta(\boldsymbol{\nabla}^2\rho)\underset{\sim}{\mathbf{1}} + \zeta\boldsymbol{\nabla}\otimes\boldsymbol{\nabla}\rho, \tag{VIII.1}$$

where $\underset{\sim}{\boldsymbol{T}}$ is the stress tensor and α, β, δ and ζ are material parameters, namely higher order elasticity moduli. The divergence of $\underset{\sim}{\boldsymbol{T}}$ is assumed to vanish, in the absence of volume forces. In their account of Korteweg's constitutive theory, Truesdell and Noll (1965) show how it can be used to represent a spherical non–uniform field of mass density, $\rho(r)$, thus allowing for the presence of an interface between liquid and vapor in a water droplet. The balance equation,

$$T'_{rr} + \frac{2}{r}(T_{rr} - T_{\theta\theta}) = 0, \tag{VIII.2}$$

is combined with the constitutive relation,

$$T_{rr} - T_{\theta\theta} = -\beta\rho'^2 - \zeta\frac{\rho'}{r} + \zeta\rho'', \tag{VIII.3}$$

where the prime denotes derivation with respect to r. Integrating equation (VIII.2) on the interface zone $[r_1, r_2]$ yields the relation

$$T_{rr}(r_2) - T_{rr}(r_1) = 2\zeta\left(\frac{\rho'(r_2)}{r_2} - \frac{\rho'(r_1)}{r_1}\right) - 2\int_{r_1}^{r_2}\frac{\beta\rho'^2 - \zeta\rho''}{r}dr. \tag{VIII.4}$$

In order to obtain results appropriate to a thin shell of transition, we calculate the limit of the latter relation as r_1, r_2 tend to r_0. The first term on the right hand side vanishes whereas, under suitable assumptions of smoothness, the second term is proportional to the mean curvature, $1/r_0$. Accordingly, equation (VIII.4) can be interpreted as the diffuse counterpart of the Laplace sharp interface equation.

The compatibility of such higher grade constitutive equations, formulated within the framework of classical continuum mechanics, with continuum thermodynamics has been questioned by Gurtin (1965) (see also Rocard, 1967). Gurtin (1965) argued that such higher order constitutive statements can be acceptable only if higher order stress tensors are introduced in addition to the usual Cauchy simple force stress tensor. To address this issue, Korteweg's equation will next be rephrased within the linear elasticity framework. For that purpose, we define the dilatation as the trace of the small strain tensor,

$$\Delta = \operatorname{trace}\underset{\approx}{\boldsymbol{\varepsilon}} = 1 - \frac{\rho_0}{\rho}, \quad \boldsymbol{\nabla}\Delta = \rho_0\frac{\boldsymbol{\nabla}\rho}{\rho^2} \simeq \frac{\boldsymbol{\nabla}\rho}{\rho_0}, \tag{VIII.5}$$

within the small strain approximation with respect to a reference mass density ρ_0. The Korteweg equation (VIII.1) can therefore be written as

$$\underset{\sim}{\boldsymbol{T}} = -p(\Delta)\underset{\sim}{\mathbf{1}} - \alpha(\boldsymbol{\nabla}\Delta)^2\underset{\sim}{\mathbf{1}} - \beta\boldsymbol{\nabla}\Delta\otimes\boldsymbol{\nabla}\Delta + \delta(\boldsymbol{\nabla}^2\Delta)\underset{\sim}{\mathbf{1}} + \zeta\boldsymbol{\nabla}\otimes\boldsymbol{\nabla}\Delta, \tag{VIII.6}$$

$$T_{ij} = -p(\Delta)\delta_{ij} - \alpha\Delta_{,k}\Delta_{,k}\delta_{ij} - \beta\Delta_{,i}\Delta_{,j} + \delta\Delta_{,kk}\delta_{ij} + \zeta\Delta_{,ij}. \tag{VIII.7}$$

If we neglect the quadratic terms in the previous expression, we obtain the linearised Korteweg equation

$$\underset{\sim}{\boldsymbol{T}} = -p(\Delta)\underset{\sim}{\mathbf{1}} + \delta(\boldsymbol{\nabla}^2\Delta)\underset{\sim}{\mathbf{1}} + \zeta\boldsymbol{\nabla}\otimes\boldsymbol{\nabla}\Delta. \tag{VIII.8}$$

It involves higher order gradients of the dilatation. This suggests that it could be derived from a strain gradient theory as proposed by Toupin (1962); Casal (1963) and Mindlin and Eshel (1968) in the early sixties. As shown by Toupin, the second gradient of displacement theory is equivalent to the first strain gradient theory. Such theories introduce higher order stresses, as advocated by Gurtin (1965). The link between a strain gradient theory and capillarity or surface energy in fluids or solids has been recognised by Casal (1972). The strain gradient theory can be limited to the gradient of density effects and therefore compared to Korteweg's equation, as it was done by Casal and Gouin (1985). The relation between the

stress tensor $\underset{\sim}{\boldsymbol{T}}$ in equation (VIII.1) and the higher order stress measures of strain gradient theories is discussed in the next section. More recent work has developed the concept of a fluid with internal wettability based on modified Korteweg equations within the strain gradient framework, also called Cahn–Hilliard fluid in Lanchon-Ducauquis *et al.* (2000) and Biguenet (2003).

This idea of considering higher gradients of density to describe the behaviour of a material close to its free surfaces or interfaces has been implemented for phase transformation problems such as water droplets in vapor (Dreyer and Duderstadt, 2006), as it represents a diffuse interface model for liquid–gas interfaces.

VIII.2 Second strain gradient theory

Mindlin (1965) claimed that a second strain gradient theory is necessary to account for capillarity and cohesion effects in isotropic elastic media, instead of the first strain gradient theory reported in the previous section. We recall here his arguments in order to show the fundamental difference between Mindlin's approach and the previous one. The second strain gradient theory is presented and contains the first strain gradient model as a special case. It is based on the assumption that the stress state at a material point depends on the values of the strain and of the first and the second strain gradients at that point. Following the method of virtual power (Germain, 1973a; Bertram and Forest, 2007), the virtual work density of internal forces is a linear form with respect to all strain measures:

$$w^{(i)} = \underset{\sim}{\boldsymbol{\sigma}} : \underset{\sim}{\boldsymbol{\varepsilon}} + \underset{\simeq}{\boldsymbol{S}} \therefore (\underset{\sim}{\boldsymbol{\varepsilon}} \otimes \boldsymbol{\nabla}) + \underset{\approx}{\boldsymbol{S}} :: (\underset{\sim}{\boldsymbol{\varepsilon}} \otimes \boldsymbol{\nabla} \otimes \boldsymbol{\nabla}), \tag{VIII.9}$$

where $\underset{\sim}{\boldsymbol{\sigma}}$ is the simple force stress tensor and $\underset{\simeq}{\boldsymbol{S}}, \underset{\approx}{\boldsymbol{S}}$ are the so–called hyperstress tensors as required by the mentioned thermodynamical consistency. Mindlin (1965) showed that the stresses must fulfill the following balance equation

$$\underset{\sim}{\boldsymbol{T}}.\boldsymbol{\nabla} = 0, \quad \text{with} \quad \underset{\sim}{\boldsymbol{T}} = \underset{\sim}{\boldsymbol{\sigma}} - (\underset{\simeq}{\boldsymbol{S}} - \underset{\approx}{\boldsymbol{S}}.\boldsymbol{\nabla}).\boldsymbol{\nabla} \tag{VIII.10}$$

The stress tensor $\underset{\sim}{\boldsymbol{T}}$ is an effective stress tensor whose divergence vanishes. It is expressed in terms of the stress tensors at all orders. This partial differential equation is accompanied by three sets of complex boundary conditions that involve the surface curvature and the normal and tangent derivatives of stress quantities. For the sake of conciseness, they are not recalled here and the author is referred to equations (18a,b,c) in Mindlin (1965). Corresponding expressions of the boundary conditions for the first gradient of strain theory can be found in Mindlin and Eshel (1968); Germain (1973a). The free energy density function, $\Psi(\underset{\sim}{\boldsymbol{\varepsilon}}, \underset{\sim}{\boldsymbol{\varepsilon}} \otimes \boldsymbol{\nabla}, \underset{\sim}{\boldsymbol{\varepsilon}} \otimes \boldsymbol{\nabla} \otimes \boldsymbol{\nabla})$, is then a potential from which stresses are computed:

$$\underset{\sim}{\boldsymbol{\sigma}} = \rho \frac{\partial \Psi}{\partial \underset{\sim}{\boldsymbol{\varepsilon}}}, \quad \underset{\simeq}{\boldsymbol{S}} = \rho \frac{\partial \Psi}{\partial (\underset{\sim}{\boldsymbol{\varepsilon}} \otimes \boldsymbol{\nabla})}, \quad \underset{\approx}{\boldsymbol{S}} = \rho \frac{\partial \Psi}{\partial (\underset{\sim}{\boldsymbol{\varepsilon}} \otimes \boldsymbol{\nabla} \otimes \boldsymbol{\nabla})}. \tag{VIII.11}$$

When the terms $\underset{\approx}{\boldsymbol{S}}$ and $\underset{\sim}{\boldsymbol{\varepsilon}} \otimes \boldsymbol{\nabla} \otimes \boldsymbol{\nabla}$ are dropped, the first strain gradient theory is recovered. Korteweg's stress $\underset{\sim}{\boldsymbol{T}}$ can then be interpreted as the effective stress of the first gradient of strain theory, as done in Casal and Gouin (1985).

The constitutive equations in the case of an elastic fluid should be specified. Mindlin considers that, in an elastic fluid, all stress tensors are spherical so that

$$\underset{\sim}{\boldsymbol{\sigma}} = -p\underset{\sim}{\boldsymbol{1}}, \quad \underset{\simeq}{\boldsymbol{S}} = -\underset{\sim}{\boldsymbol{1}} \otimes \underline{\boldsymbol{p}}, \quad \underset{\approx}{\boldsymbol{S}} = -\underset{\sim}{\boldsymbol{1}} \otimes \underset{\sim}{\boldsymbol{\pi}}, \tag{VIII.12}$$

where Mindlin's notation for the stress tensors p, $\underline{\boldsymbol{p}}$ and $\underset{\sim}{\boldsymbol{\pi}}$ have been kept. The notation $\underset{\approx}{\boldsymbol{S}} = -\underset{\sim}{\mathbf{1}} \otimes \underset{\sim}{\boldsymbol{\pi}}$ stands for $S_{ijkl} = -\delta_{ij}\pi_{kl}$. As a result, the effective stress is spherical and reads

$$\underset{\sim}{\boldsymbol{T}} = -(p - \underline{\boldsymbol{p}}.\boldsymbol{\nabla} + \underset{\sim}{\boldsymbol{\pi}} : (\boldsymbol{\nabla} \otimes \boldsymbol{\nabla}))\underset{\sim}{\mathbf{1}}, \tag{VIII.13}$$

the divergence of which vanishes. It is in contrast to Korteweg's medium, see equation (VIII.8), which can transmit shear stresses. The concept of an elastic fluid has been clearly defined by Noll for simple materials (Truesdell and Noll, 1965) and leads to a spherical Cauchy stress tensor. The question of the definition of a first strain gradient elastic fluid has been only tackled very recently by Fried and Gurtin (2006) and Podio-Guidugli and Vianello (2009). Clearly, Korteweg and Mindlin's definitions of an elastic first strain gradient fluid differ. Mindlin's formulation is less general than that given by equation (VIII.8). Following Mindlin's definition, the free energy potential of an isotropic second strain gradient linear elastic fluid takes the form

$$\rho\Psi(\Delta, \boldsymbol{\nabla}\Delta, \boldsymbol{\nabla}\otimes\boldsymbol{\nabla}\Delta) = \frac{\lambda}{2}\Delta^2 + a_1(\boldsymbol{\nabla}\Delta)^2 + b_0\boldsymbol{\nabla}^2\Delta + b_1(\boldsymbol{\nabla}^2\Delta)^2 + b_2(\boldsymbol{\nabla}\otimes\boldsymbol{\nabla}\Delta) : (\boldsymbol{\nabla}\otimes\boldsymbol{\nabla}\Delta) + c_1\Delta\boldsymbol{\nabla}^2\Delta. \tag{VIII.14}$$

All terms are quadratic except the linear term that involves the material parameter b_0. The stress–strain relations follow

$$p = -\rho\frac{\partial\Psi}{\partial\Delta} = -\lambda\Delta - c_1\boldsymbol{\nabla}^2\Delta, \quad \underline{\boldsymbol{p}} = -\rho\frac{\partial\Psi}{\partial\boldsymbol{\nabla}\Delta} = -2a_1\boldsymbol{\nabla}\Delta, \tag{VIII.15}$$

$$\underset{\sim}{\boldsymbol{\pi}} = -\rho\frac{\partial\Psi}{\partial(\boldsymbol{\nabla}\otimes\boldsymbol{\nabla}\Delta)} = -(b_0 + c_1\Delta + 2b_1\boldsymbol{\nabla}^2\Delta)\underset{\sim}{\mathbf{1}} - 2b_2\boldsymbol{\nabla}\otimes\boldsymbol{\nabla}\Delta. \tag{VIII.16}$$

It contains, in general, a self–equilibrated higher order stress $\underset{\sim}{\boldsymbol{\pi}} = -b_0\underset{\sim}{\mathbf{1}}$, in the absence of any external load. The effective stress then becomes

$$\underset{\sim}{\boldsymbol{T}} = -(-\lambda\Delta + 2(a_1 - c_1)\boldsymbol{\nabla}^2\Delta - 2(b_1 + b_2)\boldsymbol{\nabla}^4\Delta)\underset{\sim}{\mathbf{1}} \tag{VIII.17}$$

$$T_{ij} = -(-\lambda\Delta + 2(a_1 - c_1)\Delta_{,kk} - 2(b_1 + b_2)\Delta_{,kkll})\delta_{ij}. \tag{VIII.18}$$

The corresponding effective stress for the first strain gradient model is obtained by setting $b_1 = b_2 = 0$. It can be directly compared to Korteweg's equation (VIII.8). Both relations have the Laplacian term, $\boldsymbol{\nabla}^2\Delta$, in common. Korteweg's equation contains an additional non–spherical term, as already mentioned. Mindlin's second gradient of strain theory introduces an additional contribution of fourth order.

Combining the balance and constitutive equations, the following fourth order partial differential equation is derived

$$(1 - l_1^2\boldsymbol{\nabla}^2)(1 - l_2^2\boldsymbol{\nabla}^2)\Delta = 0, \tag{VIII.19}$$

that involves two characteristic lengths such that

$$\lambda l_i^2 = a_1 - c_1 \pm \sqrt{(a_1 - c_1)^2 - 2\lambda(b_1 + b_2)}, \quad i = 1, 2. \tag{VIII.20}$$

Note that equation (VIII.19) follows from a first integration of the fifth order balance equation (VIII.10). Accordingly, a constant term should be added in the right–hand side of the equation, leading to a homogeneous pressure field to be superimposed to the solution. The equation (VIII.19) can be referred as a bi–Helmholtz equation. It can also be derived from a non–local elasticity law as done by Lazar *et al.* (2006).

Capillary effects in a spherical homogeneous material made of a second strain gradient isotropic linear elastic fluid are now considered. We look for a dilatation field $\Delta(r)$ and

equations are solved in spherical coordinates. In that specific case, Mindlin shows that the dilatation field is then of the form

$$\Delta = \frac{C_1 l_1}{r_1} \sinh \frac{r}{l_1} + \frac{C_2 l_2}{r_2} \sinh \frac{r}{l_2}. \tag{VIII.21}$$

The integration constants C_1 and C_2 must be determined from the boundary conditions. A key point of the analysis is that the outer surface of the droplet of initial radius r_0 is assumed to be free of traction forces. Mindlin shows that these traction–free boundary conditions lead to two equations for the unknowns C_1 and C_2:

$$\sum_{i=1}^{2} C_i r_i \left(2(b_1+b_2) - (2a_1 - c_1) l_i^2\right) (r_i \cosh r_i - \sinh r_i) = 0, \tag{VIII.22}$$

$$\sum_{i=1}^{2} C_i \left(r_i \left(2b_2 (1 + \frac{2}{r_i}) + 2b_1 + c_1 l_i^2 \right) \sinh r_i - 4 b_2 \cosh r_i \right) = - b_0 r_0^2, \tag{VIII.23}$$

where $r_i = r_0/l_i$. When the radius of curvature is large in comparison with the characteristic lengths l_i (i.e., $r_i \gg 1$), Mindlin derives a relation between the mean dilatation of the droplet and its radius of curvature

$$\bar{\Delta} = \frac{3}{4\pi r_0^3} \int_V \Delta \, dV = - \frac{6 c_1}{b_0 \lambda} \frac{T}{r_0}, \tag{VIII.24}$$

where T can be identified with the surface energy in the Laplace–Young equation (VII.3) and takes the value

$$T = \frac{T_0}{1 + (8 b_2 T_0 / b_0^2 r_0)}, \quad \text{with} \quad T_0 = \frac{b_0 (l_1^2 - l_2^2)}{2\lambda (l_1 (l_2^2 + c_1^2/\lambda^2)^2 - l_2 (l_1^2 + c_1^2/\lambda^2)^2)}. \tag{VIII.25}$$

The identification between the diffuse and sharp interface models for surface energy shows that the relevant material parameters that intervene in the relation are c_1, b_2 and b_0 all of which are related to the contributions of the second strain gradient in the elastic potential (VIII.14). One should also note the key rôle of the initial higher order stress b_0. Indeed, if $b_0 = 0$, the system of equations (VIII.22)–(VIII.23) is homogeneous and leads to the trivial solution $C_1 = C_2 = 0$ and to a homogeneous mass density field. As claimed by Mindlin, the internal hyperstresses account for material cohesion which is destroyed at a free surface.

The corresponding balance equations and solution of the spherical droplet can also be obtained for the first gradient of strain theory, in the same way. For, the first strain gradient theory can be formally obtained as a special case of the second strain gradient model by setting that the fourth order stress tensor $\underset{\approx}{\boldsymbol{S}}$ vanishes in equation (VIII.9), or, equivalently, that the second characteristic length l_2 vanishes in (VIII.19). The equation (VIII.19) then reduces to

$$(1 - l^2 \boldsymbol{\nabla}^2) \Delta = 0, \quad \text{with} \quad l^2 = \frac{2a_1}{\lambda}, \tag{VIII.26}$$

which involves only one characteristic length l. There is still a solution of the form

$$\Delta = \frac{C}{r} \sinh \frac{r}{l_1} \tag{VIII.27}$$

for the problem of the spherical droplet made of an linear elastic isotropic medium. However the condition of vanishing simple and double traction at the free outer surface leads to a homogeneous equation so that the integration constant is identified as $C = 0$. This leads to the trivial solution $\Delta = 0$ and homogeneous mass density within the droplet. Accordingly, the description of capillarity effects in a linear elastic medium requires the introduction of the second derivatives of the strain in the free energy density. This fact was not mentioned in the subsequent works on the links between capillarity and strain gradient theories.

VIII.3 Micromorphic approach

Higher order strain gradient theories can be viewed as special cases of the general micromorphic medium introduced by Germain (1973b). The material point is treated as a material volume with a small, but finite, size. Additional degrees of freedom are introduced to describe more accurately the relative motion of this particle with respect to its center of mass. Following the method of virtual work, the work density of internal forces is introduced as a linear form with respect to the degrees of freedom and their first gradient:

$$w^{(i)}(\underline{\boldsymbol{u}}, \underset{\sim}{\boldsymbol{\chi}}, \underline{\underset{\sim}{\boldsymbol{\chi}}}, \underset{\approx}{\boldsymbol{K}}, \underline{\underline{\boldsymbol{K}}}) = (\underset{\sim}{\boldsymbol{\sigma}} + \underline{\underset{\sim}{\boldsymbol{s}}}) : (\underline{\boldsymbol{u}} \otimes \boldsymbol{\nabla}) - (\underline{\underset{\sim}{\boldsymbol{s}}} : \underset{\sim}{\boldsymbol{\chi}} + \underline{\underline{\boldsymbol{s}}} \therefore \underline{\underset{\sim}{\boldsymbol{\chi}}}) + \underline{\underline{\boldsymbol{S}}} \therefore \underline{\underline{\boldsymbol{K}}} + \underline{\underline{\boldsymbol{S}}} :: \underline{\underline{\boldsymbol{K}}}, \quad \text{(VIII.28)}$$

where Germain's development has been truncated after the second order micromorphic terms. In addition to the displacement $\underline{\boldsymbol{u}}$, the micro–deformation $\underset{\sim}{\boldsymbol{\chi}}$ and the second order micro–deformation $\underline{\underset{\sim}{\boldsymbol{\chi}}}$ are introduced as independent degrees of freedom, together with their first gradients,

$$\underline{\underline{\boldsymbol{K}}} = \underline{\underset{\sim}{\boldsymbol{\chi}}} \otimes \boldsymbol{\nabla}, \quad \underline{\underline{\boldsymbol{K}}} = \underline{\underline{\underset{\sim}{\boldsymbol{\chi}}}} \otimes \boldsymbol{\nabla}. \quad \text{(VIII.29)}$$

The simple force stress tensor, $\underset{\sim}{\boldsymbol{\sigma}}$, the relative stress tensors, $\underline{\underset{\sim}{\boldsymbol{s}}}$ and $\underline{\underline{\boldsymbol{s}}}$, the double and triple stress tensors, $\underline{\underline{\boldsymbol{S}}}$ and $\underline{\underline{\boldsymbol{S}}}$, are dual quantities of the strain measures in the virtual work form. They must fulfill the balance equations,

$$(\underset{\sim}{\boldsymbol{\sigma}} + \underline{\underset{\sim}{\boldsymbol{s}}}).\boldsymbol{\nabla} = 0, \quad \underline{\underline{\boldsymbol{S}}}.\boldsymbol{\nabla} + \underline{\underset{\sim}{\boldsymbol{s}}} = 0, \quad \underline{\underline{\boldsymbol{S}}}.\boldsymbol{\nabla} + \underline{\underline{\boldsymbol{s}}} = 0, \quad \text{(VIII.30)}$$

in the absence of volume forces. The corresponding three sets of boundary conditions are

$$(\underset{\sim}{\boldsymbol{\sigma}} + \underline{\underset{\sim}{\boldsymbol{s}}}).\underline{\boldsymbol{n}} = \underline{\boldsymbol{t}}, \quad \underline{\underline{\boldsymbol{S}}}.\underline{\boldsymbol{n}} = \underline{\underline{\boldsymbol{t}}}, \quad \underline{\underline{\boldsymbol{S}}}.\underline{\boldsymbol{n}} = \underline{\underline{\underline{\boldsymbol{t}}}}, \quad \text{(VIII.31)}$$

where $\underline{\boldsymbol{t}}$, $\underline{\underline{\boldsymbol{t}}}$ and $\underline{\underline{\underline{\boldsymbol{t}}}}$ are respectively contact simple, double and triple tractions. When the micro–deformation $\underset{\sim}{\boldsymbol{\chi}}$ is forced to coincide with the macrodeformation gradient, $\underset{\sim}{\boldsymbol{1}} + \underline{\boldsymbol{u}} \otimes \boldsymbol{\nabla}$, by an internal constraint, and when the second order terms are neglected, the micromorphic theory is known to reduce to the strain gradient theory (Eringen, 1999; Forest, 2009). Similarly, when $\underset{\sim}{\boldsymbol{\chi}}$ and $\underline{\underset{\sim}{\boldsymbol{\chi}}}$ are constrained to coincide with the deformation gradient, $\underset{\sim}{\boldsymbol{1}} + \underline{\boldsymbol{u}} \otimes \boldsymbol{\nabla}$, and its gradient, $\underline{\boldsymbol{u}} \otimes \boldsymbol{\nabla} \otimes \boldsymbol{\nabla}$, respectively, Germain's second order micromorphic medium degenerates into Mindlin's second strain gradient continuum. In contrast to strain gradient theories, the general micromorphic models, especially the boundary conditions (VIII.31), are quite straightforward to implement in a finite element code. Penalty factors or Lagrange multipliers can then be introduced to obtain a numerical model for strain gradient media.

We illustrate the second order micromorphic model and make the link with Mindlin's theory in the case of an elastic fluid at small deformation. The degrees of freedom are limited to the displacement, $\underline{\boldsymbol{u}}$, a microdilatation, ${}^{\chi}\Delta$, and second order microdilatation, ${}^{\chi}\underline{\boldsymbol{K}}$. The associated strains are the dilatation, Δ, the microdilatation, ${}^{\chi}\Delta$, its gradient, $\boldsymbol{\nabla}{}^{\chi}\Delta$, the second order microdilatation ${}^{\chi}\underline{\boldsymbol{K}}$ and its gradient ${}^{\chi}\underline{\boldsymbol{K}} \otimes \boldsymbol{\nabla}$. The work of internal forces (VIII.28) then reduces to

$$w^{(i)} = -p\Delta - {}^{\chi}p\,{}^{\chi}\Delta + {}^{\chi}\underline{\boldsymbol{p}}.\boldsymbol{\nabla}{}^{\chi}\Delta - {}^{\chi}\underline{\boldsymbol{\pi}}.{}^{\chi}\underline{\boldsymbol{K}} + {}^{\chi}\underset{\sim}{\boldsymbol{\pi}} : ({}^{\chi}\underline{\boldsymbol{K}} \otimes \boldsymbol{\nabla}). \quad \text{(VIII.32)}$$

The generalised pressure tensors satisfy the balance of generalised momentum in the form

$$\boldsymbol{\nabla} p = 0, \quad {}^{\chi}\underline{\boldsymbol{p}}.\boldsymbol{\nabla} + {}^{\chi}p = 0, \quad {}^{\chi}\underset{\sim}{\boldsymbol{\pi}}.\boldsymbol{\nabla} + {}^{\chi}\underline{\boldsymbol{\pi}} = 0. \quad \text{(VIII.33)}$$

The corresponding Neumann boundary conditions are

$$p = p_0, \quad {}^{\chi}\underline{\boldsymbol{p}}.\underline{\boldsymbol{n}} = {}^{\chi}p_0, \quad {}^{\chi}\underset{\sim}{\boldsymbol{\pi}}.\underline{\boldsymbol{n}} = {}^{\chi}\underline{\boldsymbol{\pi}}_0 \quad \text{(VIII.34)}$$

where $p_0, {}^{\chi}p_0$ and ${}^{\chi}\underline{\boldsymbol{\pi}}_0$ are given generalised pressures at the boundary. Dirichlet conditions can also be stated and correspond to the prescription of Δ, ${}^{\chi}\Delta$ and ${}^{\chi}\underline{\boldsymbol{K}}$ at the boundary.

The free energy potential, $\Psi(\Delta, {}^{\chi}\Delta, {}^{\chi}\underline{\boldsymbol{K}}, {}^{\chi}\underline{\boldsymbol{K}} \otimes \boldsymbol{\nabla})$, is used to formulate the state laws

$$-p = \rho\frac{\partial\Psi}{\partial\Delta}, \quad -{}^{\chi}p = \rho\frac{\partial\Psi}{\partial{}^{\chi}\Delta}, \quad {}^{\chi}\underline{\boldsymbol{p}} = \rho\frac{\partial\Psi}{\partial\boldsymbol{\nabla}{}^{\chi}\Delta} \tag{VIII.35}$$

$$-{}^{\chi}\underline{\boldsymbol{\pi}} = \rho\frac{\partial\Psi}{\partial{}^{\chi}\underline{\boldsymbol{K}}}, \quad {}^{\chi}\underset{\sim}{\boldsymbol{\pi}} = \rho\frac{\partial\Psi}{\partial({}^{\chi}\underline{\boldsymbol{K}} \otimes \boldsymbol{\nabla})}. \tag{VIII.36}$$

The free energy density is taken as an isotropic quadratic function of its arguments:

$$\begin{aligned}\rho\Psi = &\frac{\lambda}{2}\Delta^2 + \frac{{}^{\chi}\lambda}{2}(\Delta - {}^{\chi}\Delta)^2 + \frac{a_1}{2}\boldsymbol{\nabla}{}^{\chi}\Delta.\boldsymbol{\nabla}{}^{\chi}\Delta + \frac{{}^{\chi}b}{2}(\boldsymbol{\nabla}{}^{\chi}\Delta - {}^{\chi}\underline{\boldsymbol{K}})^2 \\ &+ \frac{\alpha}{2}\left(\text{trace}\,({}^{\chi}\underline{\boldsymbol{K}} \otimes \boldsymbol{\nabla})\right)^2 + \frac{\beta}{2}({}^{\chi}\underline{\boldsymbol{K}} \otimes \boldsymbol{\nabla}) : ({}^{\chi}\underline{\boldsymbol{K}} \otimes \boldsymbol{\nabla}) + \frac{\delta}{2}({}^{\chi}\underline{\boldsymbol{K}} \otimes \boldsymbol{\nabla}) : (\boldsymbol{\nabla} \otimes {}^{\chi}\underline{\boldsymbol{K}}) \\ &+ (b_0 + c_1\Delta + c_2{}^{\chi}\Delta)\text{trace}\,({}^{\chi}\underline{\boldsymbol{K}} \otimes \boldsymbol{\nabla})\end{aligned} \tag{VIII.37}$$

In the previous expression, the parameters ${}^{\chi}\lambda$ and ${}^{\chi}b$ can be regarded as penalty terms ensuring that the microdilatations ${}^{\chi}\Delta$ and ${}^{\chi}\underline{\boldsymbol{K}}$ are sufficiently close to the macrodilatations Δ and $\boldsymbol{\nabla}{}^{\chi}\Delta$, respectively. The constitutive equations follow,

$$-p = \lambda\Delta + {}^{\chi}\lambda(\Delta - {}^{\chi}\Delta) + c_1\text{trace}\,({}^{\chi}\underline{\boldsymbol{K}} \otimes \boldsymbol{\nabla}), \quad -{}^{\chi}p = -{}^{\chi}\lambda(\Delta - {}^{\chi}\Delta) + c_2\text{trace}\,({}^{\chi}\underline{\boldsymbol{K}} \otimes \boldsymbol{\nabla}), \tag{VIII.38}$$

$${}^{\chi}\underline{\boldsymbol{p}} = a_1\boldsymbol{\nabla}{}^{\chi}\Delta + {}^{\chi}b(\boldsymbol{\nabla}{}^{\chi}\Delta - {}^{\chi}\underline{\boldsymbol{K}}), \quad -{}^{\chi}\underline{\boldsymbol{\pi}} = -{}^{\chi}b(\boldsymbol{\nabla}{}^{\chi}\Delta - {}^{\chi}\underline{\boldsymbol{K}}), \tag{VIII.39}$$

$${}^{\chi}\underset{\sim}{\boldsymbol{\pi}} = (b_0 + c_1\Delta + c_2{}^{\chi}\Delta + \alpha\text{trace}\,({}^{\chi}\underline{\boldsymbol{K}} \otimes \boldsymbol{\nabla}))\underset{\sim}{\mathbf{1}} + \beta{}^{\chi}\underline{\boldsymbol{K}} \otimes \boldsymbol{\nabla} + \delta\boldsymbol{\nabla} \otimes {}^{\chi}\underline{\boldsymbol{K}} \tag{VIII.40}$$

The stress tensors ${}^{\chi}p, {}^{\chi}\underline{\boldsymbol{p}}, {}^{\chi}\underline{\boldsymbol{\pi}}$ and ${}^{\chi}\underset{\sim}{\boldsymbol{\pi}}$ can be eliminated from the previous relations by means of the balance equations (VIII.33) in order to obtain the expression of the effective pressure:

$$-p = \lambda\Delta + c_1\boldsymbol{\nabla}^2\Delta - (a_1 - c_2)\boldsymbol{\nabla}^2{}^{\chi}\Delta + (c_1 + c_2)\text{trace}\,({}^{\chi}\underline{\boldsymbol{K}} \otimes \boldsymbol{\nabla}) + (\alpha + \beta + \delta)\boldsymbol{\nabla}^2\text{trace}\,({}^{\chi}\underline{\boldsymbol{K}} \otimes \boldsymbol{\nabla}) \tag{VIII.41}$$

When the following constraints are enforced:

$${}^{\chi}\Delta \equiv \Delta, \quad {}^{\chi}\underline{\boldsymbol{K}} \equiv \boldsymbol{\nabla}\Delta, \tag{VIII.42}$$

the effective pressure (VIII.41) becomes

$$-p = \lambda\Delta - (a_1 - 2(c_1 + c_2))\boldsymbol{\nabla}^2\Delta + (\alpha + \beta + \delta)\boldsymbol{\nabla}^4\Delta. \tag{VIII.43}$$

This expression can then be identified with the effective pressure (VIII.17) in Mindlin's second gradient of strain theory. Therefore, the constrained second order micromorphic model coincides with Mindlin's theory.

The model can now be applied to the problem of the elastic spherical droplet with free outer boundary at $r = r_0$. For the sake of conciseness, the form of the solution is given here only for the first order microdilatation model, i.e. dropping the terms involving ${}^{\chi}\underline{\boldsymbol{K}}$ (see Forest and Sievert, 2006). The balance and constitutive equations reduce to the following system of equations

$$\lambda\Delta + {}^{\chi}\lambda(\Delta - {}^{\chi}\Delta) = 0, \quad {}^{\chi}\lambda(\Delta - {}^{\chi}\Delta) + a_1\boldsymbol{\nabla}^2{}^{\chi}\Delta = 0. \tag{VIII.44}$$

Elimination of dilatation leads to the following partial differential equation for the microdilatation:

$${}^{\chi}\Delta - \frac{a_1(\lambda + {}^{\chi}\lambda)}{\lambda{}^{\chi}\lambda}\boldsymbol{\nabla}^2{}^{\chi}\Delta = 0. \tag{VIII.45}$$

For the elastic droplet, a solution of the form

$$ {}^{\chi}\Delta = \frac{C}{r}\sinh\frac{r}{{}^{\chi}l} \tag{VIII.46} $$

can be worked out. The characteristic length is found to be

$$ {}^{\chi}l^2 = \frac{a_1}{\lambda}\frac{\lambda + {}^{\chi}\lambda}{{}^{\chi}\lambda}. \tag{VIII.47} $$

The macrodilatation turns out to be proportional to the microdilatation

$$ \Delta = \frac{{}^{\chi}\lambda}{\lambda + {}^{\chi}\lambda}{}^{\chi}\Delta. \tag{VIII.48} $$

When the penalty coefficient ${}^{\chi}\lambda$ tends to infinity, the macro and microdilatation coincide and the previous length becomes $l^2 = A/\lambda$. Mindlin's result (VIII.20), specified for $c_i = b_i = 0$, is retrieved in that way. The outer boundary being free of forces, the constant C is found to vanish so that the material density remains constant and uniform. Only the consideration of the second order microdilatation ${}^{\chi}\underline{\boldsymbol{K}}$ can lead to a non trivial solution due to the initial cohesion stresses associated with the material parameter b_0, in the same way as in Mindlin's original theory.

The continuum description of capillarity effects in elastic fluids is possible based on the introduction of higher order gradients of the strain tensor. It has been shown, following Mindlin's arguments, that the linear elastic isotropic first strain gradient theory is not sufficient to describe internal strains and stresses that develop close to free surfaces. To have such a surface effect, linked to surface energy, initial third order stresses accounting for cohesion forces in an isotropic elastic second gradient of strain medium are required. The proposed micromorphic approach is a suitable framework to implement this higher order gradient theory in a finite element code.

References

Bertram A. and Forest S. (2007). *Mechanics Based on an Objective Power Functional.* Technische Mechanik, vol. 27, pp 1–17.

Biguenet F. (2003). *Fluid with internal wettability.* International Journal of Non–Linear Mechanics, vol. 38, pp 255–266.

Casal P. (1963). *Capillarité interne en mecanique.* CR Acad. Sci. Paris, vol. 256, pp 3820–3822.

Casal P. (1972). *La théorie du second gradient et la capillarité.* CR Acad. Sci. Paris, vol. 274, pp 1571–1574.

Casal P. and Gouin H. (1985). *Relation entre l'équation de l'énergie et l'équation du mouvement en théorie de Korteweg de la capillarité.* Comptes-rendus des séances de l'Académie des sciences. Série 2, Mécanique-physique, chimie, sciences de l'univers, sciences de la terre, vol. 300, pp 231–234.

Dreyer W. and Duderstadt F. (2006). *On the Becker/Doring theory of nucleation of liquid droplets in solids.* Journal of Statistical Physics, vol. 123, pp 55–87.

Eringen A.C. (1999). *Microcontinuum field theories.* Springer, New York.

Forest S. (2009). *The micromorphic approach for gradient elasticity, viscoplasticity and damage.* ASCE Journal of Engineering Mechanics, vol. 135, pp 117–131.

Forest S., Cordero N.M., and Busso E.P. (2011). *First vs. second gradient of strain theory for capillarity effects in an elastic fluid at small length scales.* Computational Materials Science, vol. 50, pp 1299–1304.

Forest S. and Sievert R. (2006). *Nonlinear microstrain theories.* International Journal of Solids and Structures, vol. 43, pp 7224–7245.

Fried E. and Gurtin M.E. (2006). *Tractions, balances, and boundary conditions for nonsimple materials with application to liquid flow at small-length scales.* Arch. Rational Mech. Anal., vol. 182, pp 513–554.

Germain P. (1973a). *La méthode des puissances virtuelles en mécanique des milieux continus. Première partie: Théorie du second gradient.* Journal de mécanique, vol. 12, pp 235–274.

Germain P. (1973b). *The method of virtual power in continuum mechanics. Part 2: Microstructure.* SIAM Journal on Applied Mathematics, pp 556–575.

Gurtin M.E. (1965). *Thermodynamics and the possibility of spatial interaction in elastic materials.* Archive for Rational Mechanics and Analysis, vol. 19, pp 339–352.

Lanchon-Ducauquis H., Biguenet F., Liraud T., Csapo E., and Huemouri Y. (2000). *Modelling wetting behaviour.* In : Continuum Thermomechanics, The Art and Science of Modelling Material Behaviour, Paul Germain's Anniversary Volume, éds. Maugin G.A., Drouot R., and Sidoroff F., pp 197–2008. Kluwer Academic Publishers.

Lazar M., Maugin G.A., and Aifantis E.C. (2006). *On a theory of nonlocal elasticity of bi-Helmholtz type and some applications.* International Journal of Solids and Structures, vol. 43, pp 1404–1421.

Mindlin R.D. (1965). *Second gradient of strain and surface–tension in linear elasticity.* Int. J. Solids Structures, vol. 1, pp 417–438.

Mindlin R.D. and Eshel N.N. (1968). *On first strain gradient theories in linear elasticity.* Int. J. Solids Structures, vol. 4, pp 109–124.

Podio-Guidugli P. and Vianello M. (2009). *Hypertractions and hyperstresses convey the same mechanical information.* arXiv:0906.4199v1.

Rocard Y. (1967). *Thermodynamique.* Masson, Paris.

Toupin R.A. (1962). *Elastic materials with couple-stresses.* Archive for Rational Mechanics and Analysis, vol. 11 n° 1, pp 385–414.

Truesdell C. and Noll W. (1965). *The non-linear field theories of mechanics.* Handbuch der Physik, edited by S. Flügge, reedition Springer Verlag 2004.

Résumé

En 1965, Mindlin écrit un article remarquable dans lequel il affirme qu'une théorie du second gradient de la déformation est nécessaire pour décrire de manière continue certains effets de surface. Il montre notamment qu'une telle théorie permet de prendre en compte l'énergie de surface dans les milieux élastiques isotropes. L'objectif de ce chapitre est de comparer l'approche de Mindlin à des modèles de capillarité plus classiques basés sur une théorie du premier gradient et sur l'équation de Korteweg. Un modèle micromorphe général est proposé pour traiter le cas des fluides, il constitue une méthode numérique pour mettre en œuvre la théorie de Mindlin dans un code éléments finis.

Chapter -IX-

Second strain gradient elasticity of solids

Abstract

In this chapter, the linear theory presented in Chapter VIII in the case of elastic fluids is given for the more general case of elastic solids. In addition to the surface free energy, another type of surface effect, called surface stress, takes place and affects the surface (or interface) behaviour of solids. This surface stress is equal to the reversible work per unit area needed to elastically stretch an existing surface. Mindlin's theory is presented for the case of elastic solids. In particular, the theory is decomposed in order to explain from which feature each surface effect arise. As already discussed, the surface free energy is related to an initial higher order stress. Alternatively, the surface stress comes from the coupling between the strain and the third gradient of the displacement field. It is shown that both of these surface effects appear at the third order of the theory. A corresponding second order micromorphic approach is formulated, the main features of its finite element implementation are given in Appendix B.3.

Contents

IX.1 Mindlin's theory for elastic solids

IX.1.1 Stress equation of equilibrium and boundary conditions

The linear theory to be presented is formulated in Mindlin (1965) and was already used in Section VIII.2 in the case of elastic fluids. It is given here for the more general case of elastic solids in which the potential energy density, $\rho\Psi$, is a function of the strain and of the second and third gradients of the displacement field:

$$\rho\Psi = \rho\Psi\left(\underset{\sim}{\boldsymbol{\varepsilon}},\, \underline{\underline{\boldsymbol{\varepsilon}}},\, \underset{\approx}{\boldsymbol{\varepsilon}}\right). \tag{IX.1}$$

The theory can also be formulated in terms of the first and second gradients of the strain tensor. The third gradient of displacement theory presented in this chapter, where

$$\rho\Psi = \rho\Psi\left(\underset{\sim}{\boldsymbol{\varepsilon}},\, \underline{\boldsymbol{u}} \otimes \nabla \otimes \nabla,\, \underline{\boldsymbol{u}} \otimes \nabla \otimes \nabla \otimes \nabla\right), \tag{IX.2}$$

and the second gradient of strain theory, where

$$\rho\Psi = \rho\Psi\left(\underset{\sim}{\boldsymbol{\varepsilon}},\, \underline{\underline{\boldsymbol{\varepsilon}}} \otimes \nabla,\, \underline{\underline{\boldsymbol{\varepsilon}}} \otimes \nabla \otimes \nabla\right), \tag{IX.3}$$

are equivalent. This is due to the compatibility requirements that imply bijective relationships between the strain gradient and the second gradient of the displacement field:

$$\varepsilon_{ij,k} = \frac{1}{2}\left(u_{i,jk} + u_{j,ik}\right), \tag{IX.4a}$$

$$u_{i,jk} = \varepsilon_{ij,k} + \varepsilon_{ki,j} - \varepsilon_{jk,i}. \tag{IX.4b}$$

In the following, we present the theory in terms of strain and second and third gradients of the displacement field which are denoted by:

$$\underset{\sim}{\boldsymbol{\varepsilon}} = \frac{1}{2}\left(\underline{\boldsymbol{u}} \otimes \nabla + \nabla \otimes \underline{\boldsymbol{u}}\right), \quad \underline{\underline{\boldsymbol{\varepsilon}}} = \underline{\boldsymbol{u}} \otimes \nabla \otimes \nabla, \quad \underset{\approx}{\boldsymbol{\varepsilon}} = \underline{\boldsymbol{u}} \otimes \nabla \otimes \nabla \otimes \nabla, \tag{IX.5}$$

$$\varepsilon_{ij} = \frac{1}{2}\left(u_{i,j} + u_{j,i}\right), \quad \varepsilon_{ijk} = u_{i,jk}, \quad \varepsilon_{ijkl} = u_{i,jkl},$$

where $\underline{\boldsymbol{u}}$ is the displacement field. Alternative formulations were listed by Mindlin and Eshel (1968) for the strain gradient theory. The classical infinitesimal strain tensor, $\underset{\sim}{\boldsymbol{\varepsilon}}$, is the symmetric part of the displacement field gradient and has six independent components in three dimensions (3D). The second gradient of the displacement field, $\underline{\underline{\boldsymbol{\varepsilon}}}$, is symmetric in the last two positions and has eighteen independent components while the third gradient of the displacement field, $\underset{\approx}{\boldsymbol{\varepsilon}}$, is symmetric in the last three positions and has thirty independent components. This means that we have the following symmetry properties of tensors:

$$\varepsilon_{ij} = \varepsilon_{ji}, \quad \varepsilon_{ijk} = \varepsilon_{ikj}, \quad \varepsilon_{ijkl} = \varepsilon_{ijlk} = \varepsilon_{ikjl} = \varepsilon_{iklj} = \varepsilon_{iljk} = \varepsilon_{ilkj}. \tag{IX.6}$$

In two dimensions (2D), these tensors have four, six and eight independent components, respectively.

We consider a continuum whose power density of internal forces takes the form

$$p^{(i)} = \underset{\sim}{\boldsymbol{\sigma}} : \dot{\underset{\sim}{\boldsymbol{\varepsilon}}} + \underline{\underline{\boldsymbol{S}}} \therefore \dot{\underline{\underline{\boldsymbol{\varepsilon}}}} + \underset{\approx}{\boldsymbol{S}} :: \dot{\underset{\approx}{\boldsymbol{\varepsilon}}}, \quad p^{(i)} = \sigma_{ij}\,\dot{\varepsilon}_{ij} + S_{ijk}\,\dot{\varepsilon}_{ijk} + S_{ijkl}\,\dot{\varepsilon}_{ijkl}, \tag{IX.7}$$

where

$$\underset{\sim}{\boldsymbol{\sigma}} = \rho\frac{\partial\Psi}{\partial\underset{\sim}{\boldsymbol{\varepsilon}}}, \quad \underline{\underline{\boldsymbol{S}}} = \rho\frac{\partial\Psi}{\partial\underline{\underline{\boldsymbol{\varepsilon}}}}, \quad \underset{\approx}{\boldsymbol{S}} = \rho\frac{\partial\Psi}{\partial\underset{\approx}{\boldsymbol{\varepsilon}}}, \tag{IX.8}$$

$$\sigma_{ij} = \rho\frac{\partial\Psi}{\partial\varepsilon_{ij}}, \quad S_{ijk} = \rho\frac{\partial\Psi}{\partial\varepsilon_{ijk}}, \quad S_{ijkl} = \rho\frac{\partial\Psi}{\partial\varepsilon_{ijkl}},$$

are the generalised stress tensors and share the same symmetry properties as $\underset{\sim}{\boldsymbol{\varepsilon}}$, $\underset{\simeq}{\boldsymbol{\varepsilon}}$ and $\underset{\approx}{\boldsymbol{\varepsilon}}$, respectively. The power of internal forces in a domain V, with smooth boundary ∂V, is

$$\begin{aligned}
\mathcal{P}^{(i)} &= \int_V p^{(i)} dV = \int_V \left(\underset{\sim}{\boldsymbol{\sigma}} : \dot{\underset{\sim}{\boldsymbol{\varepsilon}}} + \underset{\simeq}{\boldsymbol{S}} \therefore \dot{\underset{\simeq}{\boldsymbol{\varepsilon}}} + \underset{\approx}{\boldsymbol{S}} :: \dot{\underset{\approx}{\boldsymbol{\varepsilon}}} \right) dV \\
&= \int_V \left[\underset{\sim}{\boldsymbol{\sigma}} : (\dot{\underline{\boldsymbol{u}}} \otimes \nabla) + \underset{\simeq}{\boldsymbol{S}} \therefore (\dot{\underline{\boldsymbol{u}}} \otimes \nabla \otimes \nabla) + \underset{\approx}{\boldsymbol{S}} :: (\dot{\underline{\boldsymbol{u}}} \otimes \nabla \otimes \nabla \otimes \nabla) \right] dV \qquad \text{(IX.9)} \\
&= - \int_V \left\{ \left[\underset{\sim}{\boldsymbol{\sigma}} - \underset{\simeq}{\boldsymbol{S}} . \nabla + \underset{\approx}{\boldsymbol{S}} : (\nabla \otimes \nabla) \right] . \nabla \right\} . \dot{\underline{\boldsymbol{u}}} \, dV + \int_{\partial V} \underline{\boldsymbol{n}} . \left[\underset{\sim}{\boldsymbol{\sigma}} - \underset{\simeq}{\boldsymbol{S}} . \nabla + \underset{\approx}{\boldsymbol{S}} : (\nabla \otimes \nabla) \right] . \dot{\underline{\boldsymbol{u}}} \, dS \\
&\quad + \int_{\partial V} \left\{ \left[\left(\underset{\simeq}{\boldsymbol{S}} - \underset{\approx}{\boldsymbol{S}} . \nabla \right) . \underline{\boldsymbol{n}} + \underset{\approx}{\boldsymbol{S}} : (\underline{\boldsymbol{n}} \otimes \underline{\boldsymbol{L}}) - \left(\underset{\approx}{\boldsymbol{S}} : (\underline{\boldsymbol{n}} \otimes \underline{\boldsymbol{n}}) \right) . \left(\underline{\boldsymbol{n}} \otimes \overset{\boldsymbol{t}}{\underline{\boldsymbol{D}}} \right) \right] . \underline{\boldsymbol{L}} \right\} . \dot{\underline{\boldsymbol{u}}} \, dS \\
&\quad + \int_{\partial V} \left[\left(\underset{\simeq}{\boldsymbol{S}} - \underset{\approx}{\boldsymbol{S}} . \nabla \right) : (\underline{\boldsymbol{n}} \otimes \underline{\boldsymbol{n}}) + \underset{\approx}{\boldsymbol{S}} \therefore (\underline{\boldsymbol{n}} \otimes \underline{\boldsymbol{L}} \otimes \underline{\boldsymbol{n}}) + \underset{\approx}{\boldsymbol{S}} \therefore (\underline{\boldsymbol{n}} \otimes \underline{\boldsymbol{n}} \otimes \underline{\boldsymbol{L}}) \right] . \overset{n}{D} \dot{\underline{\boldsymbol{u}}} \, dS \\
&\quad + \int_{\partial V} \left[\underset{\approx}{\boldsymbol{S}} \therefore (\underline{\boldsymbol{n}} \otimes \underline{\boldsymbol{n}} \otimes \underline{\boldsymbol{n}}) \right] . \overset{n}{D}{}^2 \dot{\underline{\boldsymbol{u}}} \, dS, \qquad \text{(IX.10)}
\end{aligned}$$

$$\begin{aligned}
\mathcal{P}^{(i)} = &- \int_V (\sigma_{ij,j} - S_{ijk,jk} + S_{ijkl,jkl}) \, \dot{u}_i \, dV + \int_{\partial V} (\sigma_{ij,j} - S_{ijk,jk} + S_{ijkl,jkl}) \, n_j \, \dot{u}_i \, dS \\
&+ \int_{\partial V} \left[L_j \left(S_{ijk} - S_{ijkl,l} \right) n_k + L_k L_l S_{ijkl} \, n_j - L_p S_{ijkl} \, n_j \, n_l \left(\overset{t}{D}_k n_p \right) \right] \dot{u}_i \, dS \\
&+ \int_{\partial V} \left((S_{ijk} - S_{ijkl,l}) \, n_k \, n_j + L_l S_{ijkl} \, n_j \, n_k + L_k S_{ijkl} \, n_j \, n_l \right) \left(\overset{n}{D} \dot{u}_i \right) dS \\
&+ \int_{\partial V} S_{ijkl} \, n_j \, n_k \, n_l \left(\overset{n}{D}{}^2 \dot{u}_i \right) dS, \qquad \text{(IX.11)}
\end{aligned}$$

where $\overset{n}{D}$, $\overset{\boldsymbol{t}}{\underline{\boldsymbol{D}}}$ and $\underline{\boldsymbol{L}}$ are differential operators defined below. The gradient of $\dot{\underline{\boldsymbol{u}}}$ on ∂V is decomposed into a normal gradient and a surface gradient:

$$\dot{\underline{\boldsymbol{u}}} \otimes \nabla = \left(\overset{n}{D} \dot{\underline{\boldsymbol{u}}} \right) \otimes \underline{\boldsymbol{n}} + \dot{\underline{\boldsymbol{u}}} \otimes \overset{\boldsymbol{t}}{\underline{\boldsymbol{D}}}, \quad \dot{u}_{i,j} = \overset{n}{D} \dot{u}_i \, n_j + \overset{t}{D}_j \dot{u}_i \qquad \text{(IX.12)}$$

where the normal gradient operator, $\overset{n}{D}$, is defined as

$$\overset{n}{D} \dot{\underline{\boldsymbol{u}}} := (\dot{\underline{\boldsymbol{u}}} \otimes \nabla) . \underline{\boldsymbol{n}}, \quad \overset{n}{D} \dot{u}_i := \dot{u}_{i,k} \, n_k, \qquad \text{(IX.13)}$$

$$\overset{n}{D}{}^2 \dot{\underline{\boldsymbol{u}}} := (\dot{\underline{\boldsymbol{u}}} \otimes \nabla \otimes \nabla) : (\underline{\boldsymbol{n}} \otimes \underline{\boldsymbol{n}}), \quad \overset{n}{D}{}^2 \dot{u}_i := \dot{u}_{i,kl} \, n_k \, n_l, \qquad \text{(IX.14)}$$

and the surface gradient operator, $\overset{t}{D}$, is defined as

$$\dot{\underline{\boldsymbol{u}}} \otimes \overset{\boldsymbol{t}}{\underline{\boldsymbol{D}}} := (\dot{\underline{\boldsymbol{u}}} \otimes \nabla) . \left(\underset{\sim}{\boldsymbol{I}} - \underline{\boldsymbol{n}} \otimes \underline{\boldsymbol{n}} \right), \quad \overset{t}{D}_j \dot{u}_i := \dot{u}_{i,j} - \dot{u}_{i,k} \, n_k \, n_j. \qquad \text{(IX.15)}$$

In order to clarify the notation of these operators, we also write Eq. (IX.12) in the form:

$$\begin{gathered}
\dot{\underline{\boldsymbol{u}}} \otimes \nabla = (\dot{\underline{\boldsymbol{u}}} \otimes \nabla) . (\underline{\boldsymbol{n}} \otimes \underline{\boldsymbol{n}}) + (\dot{\underline{\boldsymbol{u}}} \otimes \nabla) . \left(\underset{\sim}{\boldsymbol{I}} - \underline{\boldsymbol{n}} \otimes \underline{\boldsymbol{n}} \right), \qquad \text{(IX.16)} \\
\dot{u}_{i,j} = \dot{u}_{i,k} \, n_k \, n_j + \dot{u}_{i,j} - \dot{u}_{i,k} \, n_k \, n_j.
\end{gathered}$$

The vector operator $\underline{\boldsymbol{L}}$ is expressed as a function of the surface gradient operator, $\overset{t}{D}$, we have

$$\begin{gathered}
\int_{\partial V} \underline{\boldsymbol{L}} \cdot \underline{\boldsymbol{\phi}} \, dS = \int_{\partial V} \left[\left(\overset{\boldsymbol{t}}{\underline{\boldsymbol{D}}} \cdot \underline{\boldsymbol{n}} \right) \underline{\boldsymbol{\phi}} \cdot \underline{\boldsymbol{n}} - \overset{\boldsymbol{t}}{\underline{\boldsymbol{D}}} \cdot \underline{\boldsymbol{\phi}} \right] dS, \qquad \text{(IX.17)} \\
\int_{\partial V} L_l \phi_l \, dS = \int_{\partial V} \left[\left(\overset{t}{D}_m n_m \right) \phi_l \, n_l - \overset{t}{D}_l \phi_l \right] dS.
\end{gathered}$$

The power of internal forces as expressed in Eq. (IX.10) is the result of two successive integrations by parts applied on the initial form given in Eq. (IX.9). The whole process is given in Mindlin (1965). The chain rule of differentiation and the divergence theorem are first applied. The decomposition (IX.12) is then used in addition to the chain rule, surface integrations and the surface divergence theorem (given in Appendix B.2) in order to express $\mathcal{P}^{(i)}$ as a function of the independent variations $\dot{\underline{\boldsymbol{u}}}$, $\overset{n}{D}\dot{\underline{\boldsymbol{u}}}$ and $\overset{n}{D}{}^2\dot{\underline{\boldsymbol{u}}}$. At this point, the operators $\overset{n}{D}$, $\underline{\overset{\boldsymbol{t}}{\boldsymbol{D}}}$ and $\underline{\boldsymbol{L}}$ appear as convenient notations to carry out the different steps of the process.

The power of volume and contact forces must therefore take the form

$$\mathcal{P}^{(ext)} = \int_V \underline{\boldsymbol{f}} \,.\, \dot{\underline{\boldsymbol{u}}}\, dV + \int_{\partial V} \left(\underline{\overset{\boldsymbol{1}}{\boldsymbol{t}}} \,.\, \dot{\underline{\boldsymbol{u}}} + \underline{\overset{\boldsymbol{2}}{\boldsymbol{t}}} \,.\, \overset{n}{D}\dot{\underline{\boldsymbol{u}}} + \underline{\overset{\boldsymbol{3}}{\boldsymbol{t}}} \,.\, \overset{n}{D}{}^2\dot{\underline{\boldsymbol{u}}} \right) dS \tag{IX.18}$$

where $\underline{\boldsymbol{f}}$ is the body force per unit volume and $\underline{\overset{\boldsymbol{1}}{\boldsymbol{t}}}$, $\underline{\overset{\boldsymbol{2}}{\boldsymbol{t}}}$ and $\underline{\overset{\boldsymbol{3}}{\boldsymbol{t}}}$ are the generalised surface tractions, the stress equation of equilibrium then reads

$$\begin{gathered} \left[\underset{\sim}{\boldsymbol{\sigma}} - \underline{\underline{\boldsymbol{S}}} \,.\, \nabla + \underline{\underline{\underline{\boldsymbol{S}}}} \,:\, (\nabla \otimes \nabla) \right] . \nabla + \underline{\boldsymbol{f}} = 0 \\ \sigma_{ij,j} - S_{ijk,jk} + S_{ijkl,jkl} + f_i = 0 \end{gathered} \tag{IX.19}$$

and the traction boundary conditions are

$$\begin{aligned} \underline{\overset{\boldsymbol{1}}{\boldsymbol{t}}} = & \left[\underset{\sim}{\boldsymbol{\sigma}} - \underline{\underline{\boldsymbol{S}}} \,.\, \nabla + \underline{\underline{\underline{\boldsymbol{S}}}} \,:\, (\nabla \otimes \nabla) \right] . \underline{\boldsymbol{n}} + \left[\left(\underline{\underline{\boldsymbol{S}}} - \underline{\underline{\underline{\boldsymbol{S}}}} \,.\, \nabla \right) . \underline{\boldsymbol{n}} + \underline{\underline{\underline{\boldsymbol{S}}}} \,:\, (\underline{\boldsymbol{n}} \otimes \underline{\boldsymbol{L}}) \right. \\ & \left. - \left(\underline{\underline{\underline{\boldsymbol{S}}}} : (\underline{\boldsymbol{n}} \otimes \underline{\boldsymbol{n}}) \right) . \left(\underline{\boldsymbol{n}} \otimes \underline{\overset{\boldsymbol{t}}{\boldsymbol{D}}} \right) \right] . \underline{\boldsymbol{L}} \end{aligned} \tag{IX.20a}$$

$$\underline{\overset{\boldsymbol{2}}{\boldsymbol{t}}} = \left(\underline{\underline{\boldsymbol{S}}} - \underline{\underline{\underline{\boldsymbol{S}}}} \,.\, \nabla \right) : (\underline{\boldsymbol{n}} \otimes \underline{\boldsymbol{n}}) + \underline{\underline{\underline{\boldsymbol{S}}}} \,\therefore\, (\underline{\boldsymbol{n}} \otimes \underline{\boldsymbol{L}} \otimes \underline{\boldsymbol{n}}) + \underline{\underline{\underline{\boldsymbol{S}}}} \,\therefore\, (\underline{\boldsymbol{n}} \otimes \underline{\boldsymbol{n}} \otimes \underline{\boldsymbol{L}}) \tag{IX.20b}$$

$$\underline{\overset{\boldsymbol{3}}{\boldsymbol{t}}} = \underline{\underline{\underline{\boldsymbol{S}}}} \,\therefore\, (\underline{\boldsymbol{n}} \otimes \underline{\boldsymbol{n}} \otimes \underline{\boldsymbol{n}}) \,. \tag{IX.20c}$$

These conditions and the principle (IX.18) make it possible to prescribe the displacement and its first and second normal derivatives at the surface.

IX.1.2 Constitutive equations

If only homogeneous, centrosymmetric, isotropic materials are considered, Mindlin has shown that the free energy density function takes the form:

$$\begin{aligned} \rho\Psi = & \frac{1}{2} \lambda\, \varepsilon_{ii}\, \varepsilon_{jj} + \mu\, \varepsilon_{ij}\, \varepsilon_{ij} + a_1\, \varepsilon_{iij}\, \varepsilon_{kkj} + a_2\, \varepsilon_{ijj}\, \varepsilon_{kki} + a_3\, \varepsilon_{ijj}\, \varepsilon_{ikk} \\ & + a_4\, \varepsilon_{ijk}\, \varepsilon_{ijk} + a_5\, \varepsilon_{ijk}\, \varepsilon_{jik} + b_1\, \varepsilon_{iijj}\, \varepsilon_{kkll} + b_2\, \varepsilon_{iikl}\, \varepsilon_{jjkl} \\ & + b_3\, \varepsilon_{ijkk}\, \varepsilon_{llji} + b_4\, \varepsilon_{ijkk}\, \varepsilon_{jill} + b_5\, \varepsilon_{ijkk}\, \varepsilon_{ijll} + b_6\, \varepsilon_{ijkl}\, \varepsilon_{ijkl} \\ & + b_7\, \varepsilon_{ijkl}\, \varepsilon_{jkli} + c_1\, \varepsilon_{ii}\, \varepsilon_{jjkk} + c_2\, \varepsilon_{ij}\, \varepsilon_{kkij} + c_3\, \varepsilon_{ij}\, \varepsilon_{jikk} + b_0\, \varepsilon_{iijj}. \end{aligned} \tag{IX.21}$$

Sixteen elasticity moduli appear in this free energy density in addition to the usual Lamé constants λ and μ:

- the five a_i are the higher order elasticity moduli related to the first strain gradient, they also appear in Toupin's and Mindlin's first strain gradient theories Toupin (1962); Mindlin (1964);

Table IX.1 : Dimensions of the coefficients, strains and stresses used in the theory.

Coefficient	Dimension	Strain	Dimension	Stresses	Dimension
λ, μ	MPa $\equiv$ N.mm^{-2}	ε_{ij}	dimensionless	σ_{ij}	MPa $\equiv$ N.mm^{-2}
a_i, c_i, b_0	MPa.mm^2 $\equiv$ N	ε_{ijk}	mm^{-1}	S_{ijk}	MPa.mm $\equiv$ N.mm^{-1}
$b_{i,\,i\neq 0}$	MPa.mm^4 $\equiv$ N.mm^2	ε_{ijkl}	mm^{-2}	S_{ijkl}	MPa.mm^2 $\equiv$ N

- the seven $b_{i,\,i\neq 0}$ are the higher order elasticity moduli related to the second strain gradient;
- the three c_i are coupling moduli setting a coupling between the strain and the third gradient of the displacement field, it will be shown that this coupling is responsible for surface stress;
- the initial higher order stress or cohesion modulus b_0 related to surface energy.

It will be shown that the surface effects of interest in this work are related to the coupling moduli, c_i, and to the initial higher order stress, b_0, all appearing at the third order of the considered theory. The physical dimensions of the newly introduced moduli and of the strain and stress components are given in Table IX.1. The constitutive equations are obtained from the free energy density (IX.21) and the definitions (IX.8):

$$\sigma_{pq} = \lambda\,\varepsilon_{ii}\,\delta_{pq} + 2\,\mu\,\varepsilon_{pq} + c_1\,\varepsilon_{iijj}\,\delta_{pq} + c_2\,\varepsilon_{iipq} + \frac{1}{2}\,c_3\,(\varepsilon_{pqii} + \varepsilon_{qpii})\,, \tag{IX.22a}$$

$$\begin{aligned} S_{pqr} = {} & a_1\,(\varepsilon_{iir}\,\delta_{pq} + \varepsilon_{iiq}\,\delta_{pr}) + \frac{1}{2}\,a_2\,(\varepsilon_{rii}\,\delta_{pq} + 2\,\varepsilon_{iip}\,\delta_{qr} + \varepsilon_{qii}\,\delta_{pr}) \\ & + 2\,a_3\,\varepsilon_{pii}\,\delta_{qr} + 2\,a_4\,\varepsilon_{pqr} + a_5\,(\varepsilon_{qrp} + \varepsilon_{rqp})\,, \end{aligned} \tag{IX.22b}$$

$$\begin{aligned} S_{pqrs} = {} & \frac{2}{3}\,b_1\,\varepsilon_{iijj}\,\delta_{pqrs} + \frac{2}{3}\,b_2\,\varepsilon_{iijk}\,\delta_{jkpqrs} + \frac{1}{6}\,b_3\,((\varepsilon_{jkii} + \varepsilon_{kjii})\,\delta_{jkpqrs} + 2\varepsilon_{iijp}\,\delta_{jqrs}) \\ & + \frac{2}{3}\,b_4\,\varepsilon_{jpii}\,\delta_{jqrs} + \frac{2}{3}\,b_5\,\varepsilon_{pjii}\,\delta_{jqrs} + 2\,b_6\,\varepsilon_{pqrs} + \frac{2}{3}\,b_7\,(\varepsilon_{qrsp} + \varepsilon_{rspq} + \varepsilon_{spqr}) \\ & + \frac{1}{3}\,c_1\,\varepsilon_{ii}\,\delta_{pqrs} + \frac{1}{3}\,c_2\,\varepsilon_{ij}\,\delta_{ijpqrs} + \frac{1}{3}\,c_3\,\varepsilon_{ip}\,\delta_{iqrs} + \frac{1}{3}\,b_0\,\delta_{pqrs}, \end{aligned} \tag{IX.22c}$$

where

$$\delta_{ijkl} = \delta_{ij}\delta_{kl} + \delta_{ik}\delta_{jl} + \delta_{jk}\delta_{il}, \quad \delta_{ijklmn} = \delta_{im}\delta_{jn}\delta_{kl} + \delta_{il}\delta_{jn}\delta_{km} + \delta_{il}\delta_{jm}\delta_{kn} \tag{IX.23}$$

with δ_{ij} the Kronecker delta defined as $\delta_{ij} = 1_{i=j}$ and $\delta_{ij} = 0_{i\neq j}$.

At this point, a simple remark can be done to illustrate the effect of the modulus b_0. Let us consider a traction–free surface where the generalised surface tractions must vanish, in particular we have $\underline{\boldsymbol{t}}^{\boldsymbol{3}} = 0$ which, with Eq.(IX.20c), leads to $S_{ijkl}\,n_j\,n_k\,n_l = 0$ at the considered surface. Then, the constitutive equation (IX.22c) shows that the initial higher order stress induces deformations of the surface.

IX.1.3 Surface energy

The last term in the free energy density (IX.21), $b_0\,\varepsilon_{iijj}$, generates the components of the cohesive force, $1/3\,b_0\,\delta_{pqrs}$ in Eq. (IX.22c). This self–equilibrated force is controlled by the initial higher order stress, b_0, and was shown by Mindlin to be directly linked to surface energy defined as the energy per unit area needed to create a new surface (see Fig. VII.1 as a

reminder). In the absence of external load, i.e., when $\underline{\overset{\mathbf{1}}{\boldsymbol{t}}} = \underline{\overset{\mathbf{2}}{\boldsymbol{t}}} = \underline{\overset{\mathbf{3}}{\boldsymbol{t}}} = \underline{\boldsymbol{f}} = 0$, the point surface energy at the surface is given by

$$\gamma = \frac{1}{2}\, b_0 \;\overset{n}{D}(\underline{\boldsymbol{u}}.\nabla)\,, \quad \gamma = \frac{1}{2}\, b_0\, u_{i,ij}\, n_j \quad \text{on } \partial V \tag{IX.24}$$

and is the half product of b_0 and the normal gradient of the dilatation at the surface, $\overset{n}{D}(\underline{\boldsymbol{u}}.\nabla)$.

IX.2 Formulation of the second order micromorphic model

This section gives the main equations of the micromorphic approach which will be used for a numerical implementation of the second gradient of strain theory presented in Section IX.1. This higher order theory requires a second order micromorphic approach which is formulated following the spirit of Germain's general micromorphic medium (from Germain, 1973b). First, its balance and constitutive equations are given. The internal constraints controlling the micro–deformations and ensuring the consistency with the initial theory are then stated. The micromorphic approach presented in Section VIII.3 in the case of fluids is similar to the present one. Nevertheless, all the notations and equations are redefined here for clarity and extended to the case of elastic solids. A finite element implementation is proposed in Appendix B.3.

IX.2.1 Balance equations

We introduce two micro–deformations, $\underset{\sim}{\boldsymbol{\chi}}$ and $\underline{\underset{\sim}{\boldsymbol{\chi}}}$, as second–rank and third–rank tensors respectively in which the following symmetry properties are considered:

$$\chi_{ij} = \chi_{ji}, \quad \chi_{ijk} = \chi_{jik}. \tag{IX.25}$$

$\underset{\sim}{\boldsymbol{\chi}}$ is called the microstrain tensor. The degrees of freedom of each material point are:

$$DOF := \left\{\underline{\boldsymbol{u}}, \quad \underset{\sim}{\boldsymbol{\chi}}, \quad \underline{\underset{\sim}{\boldsymbol{\chi}}}\right\}, \quad \{u_i, \quad \chi_{ij}, \quad \chi_{ijk}\}\,, \tag{IX.26}$$

where the components of $\underset{\sim}{\boldsymbol{\chi}}$ and $\underline{\underset{\sim}{\boldsymbol{\chi}}}$ are introduced as additional independent degrees of freedom. In 2D, with the symmetry properties (IX.25), nine degrees of freedom are introduced in addition to the displacement components, u_i. This number reaches twenty–four in 3D. A continuum with a power density of internal forces of the form

$$\begin{aligned} p^{(i)} &= \underset{\sim}{\boldsymbol{\sigma}} : \dot{\underset{\sim}{\boldsymbol{\varepsilon}}} + \underset{\sim}{\boldsymbol{s}} : \left(\dot{\underset{\sim}{\boldsymbol{\varepsilon}}} - \dot{\underset{\sim}{\boldsymbol{\chi}}}\right) + \underline{\underset{\sim}{\boldsymbol{S}}} \therefore \left(\dot{\underset{\sim}{\boldsymbol{\chi}}} \otimes \nabla\right) + \underline{\underset{\sim}{\boldsymbol{s}}} \therefore \left(\dot{\underset{\sim}{\boldsymbol{\chi}}} \otimes \nabla - \dot{\underline{\underset{\sim}{\boldsymbol{\chi}}}}\right) + \underline{\underset{\approx}{\boldsymbol{S}}} :: \left(\dot{\underline{\underset{\sim}{\boldsymbol{\chi}}}} \otimes \nabla\right), \\ p^{(i)} &= \sigma_{ij}\, \dot{\varepsilon}_{ij} + s_{ij}\, (\dot{\varepsilon}_{ij} - \dot{\chi}_{ij}) + S_{ijk}\, \dot{\chi}_{ij,k} + s_{ijk}\, (\dot{\chi}_{ij,k} - \dot{\chi}_{ijk}) + S_{ijkl}\, \dot{\chi}_{ijk,l} \end{aligned} \tag{IX.27}$$

is considered. Here, $\underset{\sim}{\boldsymbol{\sigma}}$, $\underline{\underset{\sim}{\boldsymbol{S}}}$ and $\underline{\underset{\approx}{\boldsymbol{S}}}$ are the simple, double and triple stress tensors, respectively. $\underset{\approx}{\boldsymbol{s}}$ and $\underline{\underset{\approx}{\boldsymbol{s}}}$ are the relative stress tensors. The power of internal forces in a domain V, with

smooth boundary ∂V, is then

$$\begin{aligned}
\mathcal{P}^{(i)} &= \int_V p^{(i)} dV \\
&= \int_V \left[\underset{\sim}{\boldsymbol{\sigma}} : \dot{\underset{\sim}{\boldsymbol{\varepsilon}}} + \underset{\sim}{\boldsymbol{s}} : \left(\dot{\underset{\sim}{\boldsymbol{\varepsilon}}} - \dot{\underset{\sim}{\boldsymbol{\chi}}} \right) + \underset{\approx}{\boldsymbol{S}} \therefore \left(\dot{\underset{\sim}{\boldsymbol{\chi}}} \otimes \nabla \right) + \underset{\sim}{\boldsymbol{s}} \therefore \left(\dot{\underset{\sim}{\boldsymbol{\chi}}} \otimes \nabla - \dot{\underset{\approx}{\boldsymbol{\chi}}} \right) + \underset{\approx}{\boldsymbol{S}} :: \left(\dot{\underset{\approx}{\boldsymbol{\chi}}} \otimes \nabla \right) \right] dV \\
&= - \int_V \left\{ \left[\left(\underset{\sim}{\boldsymbol{\sigma}} + \underset{\sim}{\boldsymbol{s}} \right) . \nabla \right] . \dot{\underline{\boldsymbol{u}}} + \left[\underset{\sim}{\boldsymbol{s}} + \left(\underset{\approx}{\boldsymbol{S}} + \underset{\approx}{\boldsymbol{s}} \right) . \nabla \right] : \dot{\underset{\sim}{\boldsymbol{\chi}}} + \left(\underset{\approx}{\boldsymbol{s}} + \underset{\approx}{\boldsymbol{S}} . \nabla \right) \therefore \dot{\underset{\approx}{\boldsymbol{\chi}}} \right\} dV \\
&\quad + \int_{\partial V} \underline{\boldsymbol{n}} . \left[\left(\underset{\sim}{\boldsymbol{\sigma}} + \underset{\sim}{\boldsymbol{s}} \right) . \dot{\underline{\boldsymbol{u}}} + \left(\underset{\approx}{\boldsymbol{S}} + \underset{\approx}{\boldsymbol{s}} \right) : \dot{\underset{\sim}{\boldsymbol{\chi}}} + \underset{\approx}{\boldsymbol{S}} \therefore \dot{\underset{\approx}{\boldsymbol{\chi}}} \right] dS \qquad \text{(IX.28a)} \\
&= \int_{\partial V} \left(\underline{\boldsymbol{t}} . \dot{\underline{\boldsymbol{u}}} + \underset{\sim}{\boldsymbol{t}} : \dot{\underset{\sim}{\boldsymbol{\chi}}} + \underline{\underline{\boldsymbol{t}}} \therefore \dot{\underline{\underline{\boldsymbol{\chi}}}} \right) dS, \qquad \text{(IX.28b)} \\
\mathcal{P}^{(i)} &= \int_V \left[\sigma_{ij} \, \dot{\varepsilon}_{ij} + s_{ij} \left(\dot{\varepsilon}_{ij} - \dot{\chi}_{ij} \right) + S_{ijk} \, \dot{\chi}_{ij,k} + s_{ijk} \left(\dot{\chi}_{ij,k} - \dot{\chi}_{ijk} \right) + S_{ijkl} \, \dot{\chi}_{ijk,l} \right] dV \\
&= - \int_V \left[\left(\sigma_{ij} + s_{ij} \right)_{,j} \dot{u}_i + \left(s_{ij} + \left(S_{ijk} + s_{ijk} \right)_{,k} \right) \dot{\chi}_{ij} + \left(s_{ijk} + S_{ijkl,l} \right) \dot{\chi}_{ijk} \right] dV \\
&\quad + \int_{\partial V} \left[\left(\sigma_{ij} + s_{ij} \right) n_j \, \dot{u}_i + \left(S_{ijk} + s_{ijk} \right) n_k \, \dot{\chi}_{ij} + S_{ijkl} \, n_l \, \dot{\chi}_{ijk} \right] dS \\
&= \int_{\partial V} \left(t_i \dot{u}_i + t_{ij} \dot{\chi}_{ij} + t_{ijk} \dot{\chi}_{ijk} \right) dS.
\end{aligned}$$

The method of virtual power is applied and, assuming no volume forces for simplicity, we obtain the balance field equations:

$$\left(\underset{\sim}{\boldsymbol{\sigma}} + \underset{\sim}{\boldsymbol{s}} \right) . \nabla = 0, \quad \left(\sigma_{ij} + s_{ij} \right)_{,j} = 0, \qquad \text{(IX.29a)}$$

$$\underset{\sim}{\boldsymbol{s}} + \left(\underset{\approx}{\boldsymbol{S}} + \underset{\approx}{\boldsymbol{s}} \right) . \nabla = 0, \quad s_{ij} + \left(S_{ijk} + s_{ijk} \right)_{,k} = 0, \qquad \text{(IX.29b)}$$

$$\underset{\approx}{\boldsymbol{s}} + \underset{\approx}{\boldsymbol{S}} . \nabla = 0, \quad s_{ijk} + S_{ijkl,l} = 0, \qquad \text{(IX.29c)}$$

and the corresponding boundary conditions of Eq. (IX.28b) are:

$$\underline{\boldsymbol{t}} = \left(\underset{\sim}{\boldsymbol{\sigma}} + \underset{\sim}{\boldsymbol{s}} \right) . \underline{\boldsymbol{n}}, \quad t_i = \left(\sigma_{ij} + s_{ij} \right) n_j, \qquad \text{(IX.30a)}$$

$$\underset{\sim}{\boldsymbol{t}} = \left(\underset{\approx}{\boldsymbol{S}} + \underset{\approx}{\boldsymbol{s}} \right) . \underline{\boldsymbol{n}}, \quad t_{ij} = \left(S_{ijk} + s_{ijk} \right) n_k, \qquad \text{(IX.30b)}$$

$$\underline{\underline{\boldsymbol{t}}} = \underset{\approx}{\boldsymbol{S}} . \underline{\boldsymbol{n}}, \quad t_{ijk} = S_{ijkl} \, n_l. \qquad \text{(IX.30c)}$$

Note that in this micromorphic approach, the generalised surface tractions $\underline{\boldsymbol{t}}$, $\underset{\sim}{\boldsymbol{t}}$ and $\underline{\underline{\boldsymbol{t}}}$ are first, second and third order tensors, respectively. Note that in the second strain gradient theory presented in Subsection IX.1.1, the tractions are vectors. The difference comes from the fact that in the second strain gradient theory, there are no additional DOFs. The previous expressions are consistent with the ranks of the chosen micro–deformations.

IX.2.2 Constitutive equations

The free energy function is assumed to have the five following arguments,

$$\Psi \left(\underset{\sim}{\boldsymbol{\varepsilon}}, \quad \underset{\sim}{\boldsymbol{e}} := \underset{\sim}{\boldsymbol{\varepsilon}} - \underset{\sim}{\boldsymbol{\chi}}, \quad \underline{\underline{\boldsymbol{K}}} := \underset{\sim}{\boldsymbol{\chi}} \otimes \nabla, \quad \underline{\underline{\boldsymbol{e}}} := \underline{\underline{\boldsymbol{K}}} - \underline{\underline{\boldsymbol{\chi}}}, \quad \underset{\approx}{\boldsymbol{K}} := \underline{\underline{\boldsymbol{\chi}}} \otimes \nabla \right) \qquad \text{(IX.31)}$$

where $\underline{\underline{\boldsymbol{K}}}$ and $\underset{\approx}{\boldsymbol{K}}$ are introduced to describe the first gradients of the micro–deformations. $\underset{\sim}{\boldsymbol{e}}$ and $\underline{\underline{\boldsymbol{e}}}$ are relative strains measuring the difference between the elastic deformation $\underset{\sim}{\boldsymbol{\varepsilon}}$ and

the gradient $\underset{\sim}{\underset{\sim}{\boldsymbol{K}}}$ with their associated micro–deformations. In 2D, $\underset{\sim}{\underset{\sim}{\boldsymbol{K}}}$, $\underset{\approx}{\boldsymbol{K}}$, $\underset{\sim}{\boldsymbol{e}}$ and $\underset{\sim}{\underset{\sim}{\boldsymbol{e}}}$ have six, twelve, three and six independent components. With these notations, the power density of internal forces (IX.27) becomes:

$$p^{(i)} = \underset{\sim}{\boldsymbol{\sigma}} : \underset{\sim}{\dot{\boldsymbol{\varepsilon}}} + \underset{\sim}{\boldsymbol{s}} : \underset{\sim}{\dot{\boldsymbol{e}}} + \underset{\sim}{\underset{\sim}{\boldsymbol{S}}} \therefore \underset{\sim}{\underset{\sim}{\dot{\boldsymbol{K}}}} + \underset{\sim}{\underset{\sim}{\boldsymbol{s}}} \therefore \underset{\sim}{\underset{\sim}{\dot{\boldsymbol{e}}}} + \underset{\approx}{\boldsymbol{S}} :: \underset{\approx}{\dot{\boldsymbol{K}}}, \tag{IX.32}$$

$$p^{(i)} = \sigma_{ij} : \dot{\varepsilon}_{ij} + s_{ij} : \dot{e}_{ij} + S_{ijk} \therefore \dot{K}_{ijk} + s_{ijk} \therefore \dot{e}_{ijk} + S_{ijkl} :: \dot{K}_{ijkl}.$$

The state laws are obtained using the free energy function (IX.31):

$$\underset{\sim}{\boldsymbol{\sigma}} = \rho \frac{\partial \Psi}{\partial \underset{\sim}{\boldsymbol{\varepsilon}}}, \quad \underset{\sim}{\underset{\sim}{\boldsymbol{S}}} = \rho \frac{\partial \Psi}{\partial \underset{\sim}{\underset{\sim}{\boldsymbol{K}}}}, \quad \underset{\approx}{\boldsymbol{S}} = \rho \frac{\partial \Psi}{\partial \underset{\approx}{\boldsymbol{K}}}, \tag{IX.33}$$

$$\underset{\sim}{\boldsymbol{s}} = \rho \frac{\partial \Psi}{\partial \underset{\sim}{\boldsymbol{e}}}, \quad \underset{\sim}{\underset{\sim}{\boldsymbol{s}}} = \rho \frac{\partial \Psi}{\partial \underset{\sim}{\underset{\sim}{\boldsymbol{e}}}}. \tag{IX.34}$$

The simple, double and triple stress tensors, $\underset{\sim}{\boldsymbol{\sigma}}$, $\underset{\sim}{\underset{\sim}{\boldsymbol{S}}}$ and $\underset{\approx}{\boldsymbol{S}}$, and the relative stress tensors, $\underset{\sim}{\boldsymbol{s}}$ and $\underset{\sim}{\underset{\sim}{\boldsymbol{s}}}$, have the same symmetry properties as their associated strain tensors, $\underset{\sim}{\boldsymbol{\varepsilon}}$, $\underset{\sim}{\underset{\sim}{\boldsymbol{K}}}$, $\underset{\approx}{\boldsymbol{K}}$, $\underset{\sim}{\boldsymbol{e}}$ and $\underset{\sim}{\underset{\sim}{\boldsymbol{e}}}$ respectively. Note that the symmetry properties considered here (IX.25) are different from the symmetry properties (IX.6) of the second strain gradient theory. Consequently, the independent components of the strain and stress tensors of the micromorphic approach are different from those of the second strain gradient theory. Next, we consider linearised elasticity constitutive equations in the general form for the simple, double and triple stress tensors,

$$\underset{\sim}{\boldsymbol{\sigma}} = \underset{\approx}{\boldsymbol{\Lambda}} : \underset{\sim}{\boldsymbol{\varepsilon}} + \overbrace{\underset{\sim\sim}{\boldsymbol{C}} :: \underset{\approx}{\boldsymbol{K}}}^{\text{coupling}}, \quad \underset{\sim}{\underset{\sim}{\boldsymbol{S}}} = \underset{\sim\sim}{\boldsymbol{A}} \therefore \underset{\sim}{\underset{\sim}{\boldsymbol{K}}}, \quad \underset{\approx}{\boldsymbol{S}} = \underset{\approx\approx}{\boldsymbol{B}} :: \underset{\approx}{\boldsymbol{K}} + \overbrace{\underset{\sim\sim}{\boldsymbol{C}^T} : \underset{\sim}{\boldsymbol{\varepsilon}}}^{\text{coupling}} + \overbrace{b_0 \, \underset{\approx}{\boldsymbol{l}}}^{\text{initial stress}}, \tag{IX.35}$$

and for the relative stress tensors,

$$\underset{\sim}{\boldsymbol{s}} = \underset{\approx}{\boldsymbol{H}^{\boldsymbol{a}}_{\boldsymbol{\chi}}} : \underset{\sim}{\boldsymbol{e}}, \quad \underset{\sim}{\underset{\sim}{\boldsymbol{s}}} = \underset{\sim\sim}{\boldsymbol{H}^{b}_{\chi}} \therefore \underset{\sim}{\underset{\sim}{\boldsymbol{e}}}. \tag{IX.36}$$

A simplified form is adopted:

$$\underset{\sim\sim}{\boldsymbol{A}} = A \, \underset{\sim\sim}{\mathbf{1}}, \quad \underset{\approx\approx}{\boldsymbol{B}} = B \, \underset{\approx\approx}{\mathbf{1}}, \quad \underset{\approx}{\boldsymbol{H}^{\boldsymbol{a}}_{\boldsymbol{\chi}}} = H^a_\chi \, \underset{\approx}{\mathbf{1}}, \quad \underset{\sim\sim}{\boldsymbol{H}^{b}_{\chi}} = H^b_\chi \, \underset{\sim\sim}{\mathbf{1}}, \tag{IX.37}$$

where A, B, H^a_χ and H^b_χ are the generalised moduli. Only one modulus is adopted for all the components of each strain gradient instead of the a_i and $b_{i,\,i\neq 0}$ introduced in the second strain gradient theory. This simplifies the formulation of the present model as a first step. Note that, in this simplified form, no coupling is considered with respect to the relative strains. A more general isotropic formulation should be considered in the future. The coupling terms appearing in $\underset{\sim}{\boldsymbol{\sigma}}$ and $\underset{\sim}{\underset{\sim}{\boldsymbol{S}}}$ have the same origin as the coupling terms of the constitutive equations (IX.22a) and (IX.22c) from Mindlin's theory. They introduce additional terms proportional to some components K_{ijkl} in the simple stress tensor and additional terms proportional to the strain components ,ε_{ij}, in the triple stress tensor. As this coupling plays a key role in the surface stress effect, no simplification is made here. The initial stress appearing in some components S_{ijkl} is linked to the initial higher order stress, or cohesive modulus, b_0, and consequently to the surface energy. In order to define the additional terms, coming from the coupling and the initial stress, that have to be introduced in $\underset{\sim}{\boldsymbol{\sigma}}$ and $\underset{\approx}{\boldsymbol{S}}$, let us write the

Table IX.2 : Dimensions of the coefficients, strains and stresses used in the second order micromorphic model.

Coefficient	Dimension	Strain	Dimension	Stresses	Dimension
λ, μ	MPa $\equiv$ N.mm^{-2}	ε_{ij}, χ_{ij}, e_{ij}	dimensionless	σ_{ij}	MPa $\equiv$ N.mm^{-2}
A, c'_i, b_0	MPa.mm^2 $\equiv$ N	χ_{ijk}, K_{ijk}, e_{ijk}	mm^{-1}	S_{ijk}	MPa.mm $\equiv$ N.mm^{-1}
B	MPa.mm^4 $\equiv$ N.mm^2	K_{ijkl}	mm^{-2}	S_{ijkl}	MPa.mm^2 $\equiv$ N

corresponding part $\rho\Psi^{\mathrm{cpl}}(\underset{\sim}{\boldsymbol{\varepsilon}}, \underset{\approx}{\boldsymbol{K}})$ of the free energy density function. We give $\rho\Psi^{\mathrm{cpl}}$ in the case of material isotropy:

$$\begin{aligned}\rho\Psi^{\mathrm{cpl}} = {} & C_1\,\varepsilon_{ii}\,K_{kkll} + C_2\,\varepsilon_{ii}\,K_{klkl} + C_3\,\varepsilon_{ii}\,K_{kllk} + C_4\,\varepsilon_{ij}\,K_{ijkk} + C_5\,\varepsilon_{ij}\,K_{ikjk} \\ & + C_6\,\varepsilon_{ij}\,K_{ikkj} + C_7\,\varepsilon_{ij}\,K_{jikk} + C_8\,\varepsilon_{ij}\,K_{jkik} + C_9\,\varepsilon_{ij}\,K_{jkki} + C_{10}\,\varepsilon_{ij}\,K_{kkij} \\ & + C_{11}\,\varepsilon_{ij}\,K_{kikj} + C_{12}\,\varepsilon_{ij}\,K_{kijk} + C_{13}\,\varepsilon_{ij}\,K_{kkji} + C_{14}\,\varepsilon_{ij}\,K_{kjki} + C_{15}\,\varepsilon_{ij}\,K_{kjik} \\ & + \frac{1}{3}\,b_0\,(K_{kkll} + K_{klkl} + K_{kllk})\,, \end{aligned} \tag{IX.38}$$

where the symmetry property $K_{ijkl} = K_{jikl}$ is not taken into account as needed to compute the stress tensors by mean of partial derivatives. The state laws (IX.33) are used to derive the stress and relative stress tensors and the symmetry properties (IX.25) are applied on the results. The following constitutive equations are finally obtained for the stress tensors:

$$\begin{aligned}\sigma_{pq} = {} & \lambda\,\varepsilon_{ii}\,\delta_{pq} + 2\mu\,\varepsilon_{pq} + c'_1\,K_{iijj}\,\delta_{pq} + \frac{1}{2}\,c'_2\,(K_{iipq} + K_{iiqp}) + c'_3\,K_{pqii} \\ & + c'_4\,K_{ijij}\,\delta_{pq} + \frac{1}{2}\,c'_5\,(K_{piqi} + K_{iqpi}) + \frac{1}{2}\,c'_6\,(K_{piiq} + K_{iqip})\,, \end{aligned} \tag{IX.39a}$$

$$S_{pqr} = A\,K_{pqr}, \tag{IX.39b}$$

$$\begin{aligned}S_{pqrs} = {} & B\,K_{pqrs} + c'_1\,\varepsilon_{ii}\,\delta_{pq}\delta_{rs} + c'_2\,\varepsilon_{rs}\,\delta_{pq} + c'_3\,\varepsilon_{pq}\,\delta_{rs} + \frac{1}{2}\,c'_4\,\varepsilon_{ii}\,(\delta_{pr}\delta_{qs} + \delta_{qr}\delta_{ps}) \\ & + \frac{1}{2}\,c'_5\,\varepsilon_{ir}\,(\delta_{ip}\delta_{qs} + \delta_{iq}\delta_{ps}) + \frac{1}{2}\,c'_6\,\varepsilon_{is}\,(\delta_{ip}\delta_{qr} + \delta_{iq}\delta_{pr}) + \frac{1}{3}\,b_0\delta_{pqrs}, \end{aligned} \tag{IX.39c}$$

with $\delta_{ijkl} = \delta_{ij}\delta_{kl} + \delta_{ik}\delta_{jl} + \delta_{jk}\delta_{il}$, and for the relative stress tensors:

$$s_{pq} = H^a_\chi\,e_{pq}, \quad s_{pqr} = H^b_\chi\,e_{pqr}. \tag{IX.40}$$

The coefficients c'_i are the coupling moduli in the same way as the c_i of Mindlin's theory. They are related to the coefficients C_i of the non–symmetrised free energy density (IX.38) as

$$\begin{aligned} c'_1 = C_1, \quad c'_2 = C_{10} + C_{13}, \quad c'_3 = C_4 + C_7, \quad c'_4 = C_2 + C_3, \\ c'_5 = C_5 + C_8 + C_{12} + C_{15}, \quad c'_6 = C_6 + C_9 + C_{11} + C_{14}. \end{aligned} \tag{IX.41}$$

Note that the symmetry properties (IX.25) reduce the number of coupling coefficients from fifteen to six. The dimensions of the moduli and of the strain and stress tensors components of the present model are given in Table IX.2.

IX.2.3 Internal constraint

The moduli H^a_χ and H^b_χ in Eqs. (IX.36) set a constraint between $\underset{\sim}{\boldsymbol{\varepsilon}}$ and $\underset{\sim}{\boldsymbol{\chi}}$ and between the gradient of $\underset{\sim}{\boldsymbol{\chi}}$ and $\underset{\sim}{\boldsymbol{\chi}}$ respectively. These moduli, acting as penalty factors, enforce the relative

strains of the free energy function to vanish. For that, H^a_χ and H^b_χ have to be sufficiently high. This internal constraint then implies that,

$$\underset{\sim}{\boldsymbol{\chi}} \equiv \underset{\sim}{\boldsymbol{\varepsilon}}, \quad \underset{\approx}{\boldsymbol{\chi}} \equiv \underset{\approx}{\boldsymbol{K}} \equiv \underset{\sim}{\boldsymbol{\chi}} \otimes \nabla \equiv \underset{\sim}{\boldsymbol{\varepsilon}} \otimes \nabla, \tag{IX.42}$$
$$\chi_{ij} \equiv \varepsilon_{ij}, \quad \chi_{ijk} \equiv K_{ijk} \equiv \chi_{ij,k} \equiv \varepsilon_{ij,k}.$$

As mentioned in Section VIII.3, these equivalences are fundamental. Indeed, such a constrained second order micromorphic model coincides with Mindlin's second strain gradient theory.

These equivalences are now used to identify the coupling moduli c'_i that are equivalent to the c_i of Eq. (IX.21). The expression of $\underset{\sim}{\boldsymbol{\sigma}}$ can then be written as a function of the components of the strain tensor and of its second gradient:

$$\begin{aligned}\sigma_{pq} = {} & \lambda\,\varepsilon_{ii}\,\delta_{pq} + 2\mu\,\varepsilon_{pq} + c'_1\,\varepsilon_{ii,jj}\,\delta_{pq} + c'_2\,\varepsilon_{ii,pq} + c'_3\,\varepsilon_{pq,ii} \\ & + c'_4\,\varepsilon_{ij,ij}\,\delta_{pq} + \frac{1}{2}\,c'_5\,(\varepsilon_{pi,qi} + \varepsilon_{iq,pi}) + \frac{1}{2}\,c'_6\,(\varepsilon_{pi,iq} + \varepsilon_{iq,ip})\,.\end{aligned} \tag{IX.43}$$

With the compatibility equation given in 2D as

$$\varepsilon_{kk,ll} + \varepsilon_{ll,kk} = 2\,\varepsilon_{kl,kl}, \tag{IX.44}$$

this expression becomes:

$$\begin{aligned}\sigma_{pq} = {} & \lambda\,\varepsilon_{ii}\,\delta_{pq} + 2\mu\,\varepsilon_{pq} + \left(c'_1 + c'_4\right)\varepsilon_{ii,jj}\,\delta_{pq} + \left(c'_2 + \frac{c'_5 + c'_6}{2}\right)\varepsilon_{ii,pq} \\ & + \left(c'_3 + \frac{c'_5 + c'_6}{2}\right)\varepsilon_{pq,ii}.\end{aligned} \tag{IX.45}$$

In parallel, the expression of $\underset{\sim}{\boldsymbol{\sigma}}$ derived in Mindlin's theory is also written as a function of ε_{ij} and $\varepsilon_{ij,kl}$. For that purpose, the gradients of the displacement have to be expressed in terms of gradients of the strain. Toupin's relation linking gradient of strain and second gradient of displacement,

$$u_{i,jk} = \varepsilon_{ij,k} + \varepsilon_{ki,j} - \varepsilon_{jk,i}, \tag{IX.46}$$

is used and, recalling that Eq. (IX.5) gives $\varepsilon_{ijkl} = u_{i,jkl}$, Eq. (IX.22a) becomes:

$$\sigma_{pq} = \lambda\,\varepsilon_{ii}\,\delta_{pq} + 2\,\mu\,\varepsilon_{pq} + c_1\,\varepsilon_{ii,jj}\,\delta_{pq} + c_2\,\varepsilon_{ii,pq} + c_3\,\varepsilon_{pq,ii}. \tag{IX.47}$$

The identification can then be directly done:

$$c'_1 + c'_4 \equiv c_1, \quad c'_2 + \frac{c'_5 + c'_6}{2} \equiv c_2, \quad c'_3 + \frac{c'_5 + c'_6}{2} \equiv c_3. \tag{IX.48}$$

The main features of the finite element implementation of this second order micromorphic approach are given in Appendix B.3. It is then possible to simulate realistic and complex boundary value problems and to investigate how the surface effects generated by Mindlin's second gradient of strain model affect the mechanical behaviour of nano–objects.

References

GERMAIN P. (1973b). *The method of virtual power in continuum mechanics. Part 2: Microstructure*. SIAM Journal on Applied Mathematics, pp 556–575.

MINDLIN R.D. (1964). *Micro-structure in linear elasticity*. Archive for Rational Mechanics and Analysis, vol. 16 n° 1, pp 51–78.

MINDLIN R.D. (1965). *Second gradient of strain and surface–tension in linear elasticity*. Int. J. Solids Structures, vol. 1, pp 417–438.

MINDLIN R.D. AND ESHEL N.N. (1968). *On first strain gradient theories in linear elasticity*. Int. J. Solids Structures, vol. 4, pp 109–124.

TOUPIN R.A. (1962). *Elastic materials with couple-stresses*. Archive for Rational Mechanics and Analysis, vol. 11 n° 1, pp 385–414.

Résumé

Dans ce chapitre, la théorie linéaire présentée dans le chapitre VIII pour le cas des fluides élastiques est étendue pour le cas plus général des solides élastiques. En plus de l'énergie libre de surface, un autre type d'effet de surface, appelé contrainte de surface (surface stress), se produit et affecte le comportement mécanique de surface (ou d'interface) des solides. Cette contrainte de surface correspond au travail réversible par unité de surface nécessaire pour étirer une surface élastique. La théorie de Mindlin est présentée pour le cas des solides élastiques. Elle est notamment décomposée de façon à montrer clairement quels éléments de cette théorie génèrent chacun des effets de surface. Il a été vu précédemment que l'énergie de surface est liée à une contrainte initiale d'ordre supérieur. La contrainte de surface provient du couplage entre la déformation et son second gradient. Il est montré que ces deux effets n'apparaissent que si une telle théorie continue est appliquée. Dans le même esprit que ce qui a déjà été fait dans ce manuscrit, une approche micromorphe du second ordre est formulée, les principales caractéristiques de sa mise en œuvre dans un code éléments finis sont données en Annexe B.3.

Chapter -X-

Apparent elastic properties of nanowires

Abstract

Mindlin's second gradient of strain model is applied in this chapter. The two types of surface effects are first considered separately and illustrated with simple boundary value problems for which analytical solutions for the displacement of atoms are known. The surface energy effect is presented in a semi infinite case with a traction–free surface. It is found that this effect can either lead to higher or smaller interatomic distances close to the surface. The interaction of two traction–free surfaces is also presented. The shear of an infinite strip of various thicknesses is considered to illustrate the surface stress effect and the expression of the size–dependent apparent shear modulus is obtained. Then the second order micromorphic approach formulated in Chapter IX and its finite element implementation (presented in Appendix B.3) are used to simulate the size–dependent mechanical behaviour of nanowires.

Contents

X.1 Surface effects

As stated in Chapter IX, the considered theory generates two types of surface effects both linked to distinct specific higher order moduli and therefore uncorrelated. The surface energy is then related to the initial higher order stress, or cohesion modulus, b_0, while the surface stress effects are related to the coupling moduli, c_i (see Eq. (IX.21)). Next, simple analytical boundary value problems that will illustrate these surface effects will be considered.

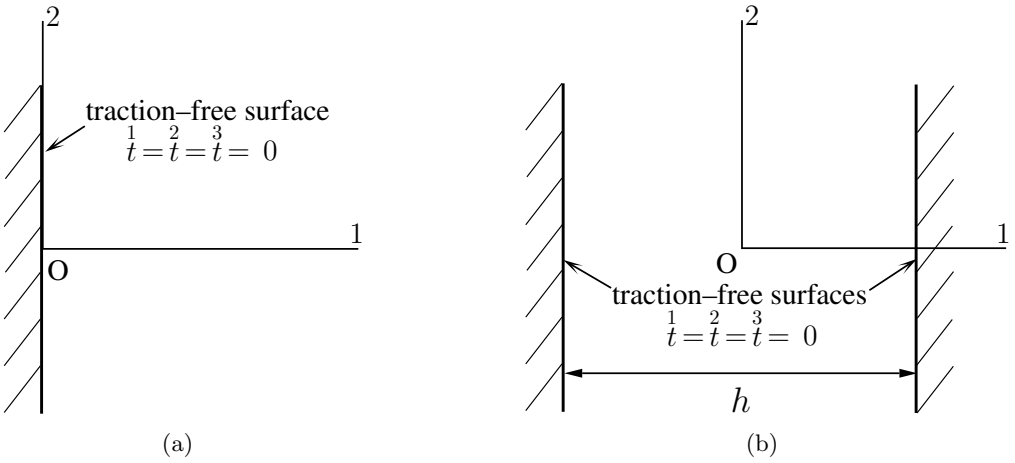

Figure X.1 : Description of (a) the half–space $x_1 \geq 0$ occupied by an elastic second strain gradient material with the plane surface $x_1 = 0$ assumed to be traction–free and of (b) the material strip located at $[-h/2, h/2]$, infinite along direction 2 and with the surfaces $x_1 = \pm h/2$ assumed to be traction–free.

X.1.1 Surface energy: half–space with a free surface

The half–space $x_1 \geq 0$ in a rectangular coordinate system x_1, x_2, x_3 is occupied by an elastic second strain gradient material as described in Fig. X.1(a). The plane surface $x_1 = 0$ is assumed to be traction–free, i.e,

$$\underline{\boldsymbol{t}}^{\mathbf{1}} = \underline{\boldsymbol{t}}^{\mathbf{2}} = \underline{\boldsymbol{t}}^{\mathbf{3}} = 0 \quad \text{at } x_1 = 0. \tag{X.1}$$

The displacement field is assumed to be of the form

$$u_1 = u_1(x_1), \quad u_2 = u_3 = 0. \tag{X.2}$$

The current problem is then 1D and the stress–equation of equilibrium (IX.19) becomes

$$\sigma_{11,1} - S_{111,11} + S_{1111,111} = 0 \tag{X.3}$$

in the absence of body forces and the boundary conditions (IX.20) are simply

$$\sigma_{11} - S_{111,1} + S_{1111,11} \; = \; S_{111} - S_{1111,1} \; = \; S_{1111} \; = \; 0 \quad \text{at } x_1 = 0 \tag{X.4}$$

as the terms with surface gradients (i.e., with the operators $\underline{\overset{\boldsymbol{t}}{\boldsymbol{D}}}$ or $\underline{\boldsymbol{L}}$) in Eqs. (IX.20) vanish for a plane surface. With the assumed displacement field (X.2), the potential energy density (IX.21) is a function of the strain components ε_{11}, ε_{111} and ε_{1111}. Then,

$$\rho\Psi\left(\varepsilon_{11},\, \varepsilon_{111},\, \varepsilon_{1111}\right) = \left(\frac{\lambda}{2} + \mu\right) \varepsilon_{11}^2 + \frac{A}{2}\, \varepsilon_{111}^2 + \frac{B}{2}\, \varepsilon_{1111}^2 + \bar{c}\, \varepsilon_{11}\, \varepsilon_{1111} + b_0\, \varepsilon_{1111} \tag{X.5}$$

with

$$A = 2\left(a_1 + a_2 + a_3 + a_4 + a_5\right), \quad B = 2\left(b_1 + b_2 + b_3 + b_4 + b_5 + b_6 + b_7\right), \quad \bar{c} = c_1 + c_2 + c_3. \tag{X.6}$$

From Table IX.1, the constants A and $\bar{c}$ have the dimension of forces (N) and B has the dimension of force times unit surface (N.mm^2). The material parameters L_1 and L_2 with the dimension of length and η and η_0 dimensionless are now defined as

$$L_1^2 = \frac{A}{\lambda/2+\mu}, \quad L_2^2 = \frac{B}{A}, \quad \eta = \frac{\bar{c}}{A}, \quad \eta_0 = \frac{b_0}{A}. \tag{X.7}$$

The purpose here is to rewrite the potential energy density (X.5) as a function of three dimensionless arguments. Hence,

$$\rho\Psi\left(\varepsilon_{11},\, \varepsilon_{111},\, \varepsilon_{1111}\right) = \rho\hat{\Psi}\left(\varepsilon_{11},\, L_1\,\varepsilon_{111},\, L_2^2\,\varepsilon_{1111}\right). \tag{X.8}$$

The stability of the local material behaviour is ensured when the function $\hat{\Psi}$ is convex with respect to its arguments, the following requirements are obtained:

$$L_1^2 \geq 0, \quad L_2^2 \geq 0, \quad 2\,\frac{L_2^2}{L_1^2} \geq \eta^2. \tag{X.9}$$

Recalling the expressions of the material parameters (X.7), these requirements impose that the moduli A and B are positive; however the modulus $\bar{c}$ can either be positive or negative. This will be used as a guideline to choose physically relevant material parameters for the theory. No condition for the initial higher order stress b_0 arises from the stability but this material parameter can be calibrated using the expression of the point surface energy given in Eq. (IX.24). The requirements (X.9) are summarised in Fig. X.2(a) where the coloured area represents the values of the material parameters η and L_2^2/L_1^2 which lead to a convex potential, $\hat{\Psi}$. The chosen notations (X.7) allow a convenient and rather clear description of the material parameters: L_1 and L_2 are related to the first and second strain gradients respectively and the ratio L_2^2/L_1^2 represents their relative weight, η describes the coupling between the strain and the third gradient of displacement and η_0 the surface energy.

From the potential energy density (X.5) and the definitions (IX.8) or alternatively from the displacement field (X.2) and the constitutive equations (IX.22), the components σ_{11}, S_{111} and S_{1111} of the stress tensors can be derived:

$$\sigma_{11} = (\lambda+2\mu)\,\varepsilon_{11} + \bar{c}\,\varepsilon_{1111}, \tag{X.10a}$$

$$S_{111} = A\,\varepsilon_{111}, \tag{X.10b}$$

$$S_{1111} = B\,\varepsilon_{1111} + \bar{c}\,\varepsilon_{11} + b_0. \tag{X.10c}$$

Substituting these expressions into the stress–equation of equilibrium (X.3) and recalling that $\varepsilon_{11} = du_1/dx_1$, $\varepsilon_{111} = d^2u_1/dx_1^2$ and $\varepsilon_{1111} = d^3u_1/dx_1^3$, the following sixth order displacement–equation of equilibrium is obtained:

$$\left(1 - l_1^2\,\frac{d^2}{dx_1^2}\right)\left(1 - l_2^2\,\frac{d^2}{dx_1^2}\right)\frac{d^2u_1}{dx_1^2} = 0. \tag{X.11}$$

The relationships,

$$l_1^2 l_2^2 = \frac{B}{\lambda+2\mu}, \quad l_1^2 + l_2^2 = \frac{A-2\bar{c}}{\lambda+2\mu}, \tag{X.12}$$

are derived and give the following expressions for the characteristic lengths l_1 and l_2:

$$l_1^2 = \frac{A-2\bar{c}+\sqrt{(A-2\bar{c})^2 - 4B\,(\lambda+2\mu)}}{2\,(\lambda+2\mu)}, \quad l_2^2 = \frac{A-2\bar{c}-\sqrt{(A-2\bar{c})^2 - 4B\,(\lambda+2\mu)}}{2\,(\lambda+2\mu)}, \tag{X.13}$$

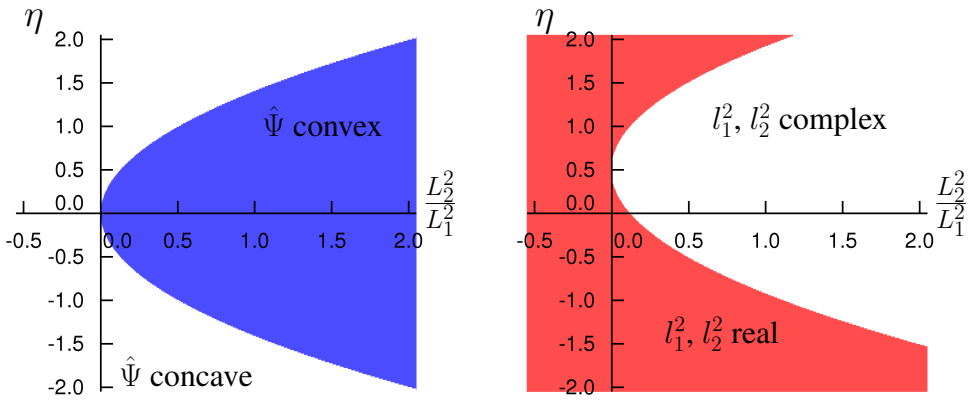

(a) (b)

Figure X.2 : Effects of the material parameters η and L_2^2/L_1^2. (a) Stability requirements: the potential $\hat{\Psi}$ is convex for the sets of material parameters taken in the coloured area. This area corresponds to the stability domain (X.9). (b) Set of l_1^2 and l_2^2: the square of the characteristic lengths l_1 and l_2 can either be complex or real depending on the sign of the part under the square root in Eqs. (X.13) or (X.14). The coloured area corresponds to the sets of material parameters for which this part is positive and then l_1^2 and l_2^2 are real.

or alternatively:

$$l_1^2 = \frac{L_1^2}{4}\left(1-2\eta+\sqrt{(1-2\eta)^2-8\frac{L_2^2}{L_1^2}}\right), \quad l_2^2 = \frac{L_1^2}{4}\left(1-2\eta-\sqrt{(1-2\eta)^2-8\frac{L_2^2}{L_1^2}}\right). \tag{X.14}$$

The solution of (X.11) has the form:

$$u_1(x_1) = \alpha_1\, e^{x_1/l_1} + \alpha_2\, e^{-x_1/l_1} + \alpha_3\, e^{x_1/l_2} + \alpha_4\, e^{-x_1/l_2} + \alpha_5\, x_1 + \alpha_6. \tag{X.15}$$

A discussion has to be made on the different possible behaviour that can be described by the theory. The characteristic lengths l_1 and l_2 have to be considered as complex numbers. Then, the exponentials $e^{\pm x_1/l_1}$ and $e^{\pm x_1/l_2}$ in the solution of the displacement–equation of equilibrium (X.15) can alternatively correspond to hyperbolic functions if l_1 and l_2 are real, trigonometric functions if l_1 and l_2 are pure imaginary or a product of these functions if the real and imaginary parts of l_1 and l_2 are both non–zero.
A study of the expressions of these characteristic lengths (X.13) or (X.14) is needed to know the shape of the solution for a given set of material parameters and then to fully understand the 1D material behaviour. For that purpose, it should first be pointed out the sign of the part $(A-2\bar{c})^2 - 4B\,(\lambda+2\mu)$ or alternatively $(1-2\eta)^2 - 8L_2^2\ L_1^2$ under the square root in both of the expressions (X.13) or (X.14): if it is positive, l_1^2 and l_2^2 are real; if not, l_1^2 and l_2^2 are complex. These two possibilities are represented in Fig. X.2(b). In the same way, the sign of the real part of l_1^2 and l_2^2, represented in Fig. X.3, has a strong impact on the resulting behaviour. The various cases arising from the combination of the previous conclusions are summarised in Fig. X.4:

1. If l_1^2 and l_2^2 are real (i.e., $\Im(l_1^2, l_2^2) = 0$) and if l_1^2 and l_2^2 are positive, then l_1 and l_2 are real and the solution of the displacement–equation of equilibrium (X.15) becomes:

$$u_1(x_1) = \alpha_2\, e^{-x_1/l_1} + \alpha_4\, e^{-x_1/l_2} \tag{X.16}$$

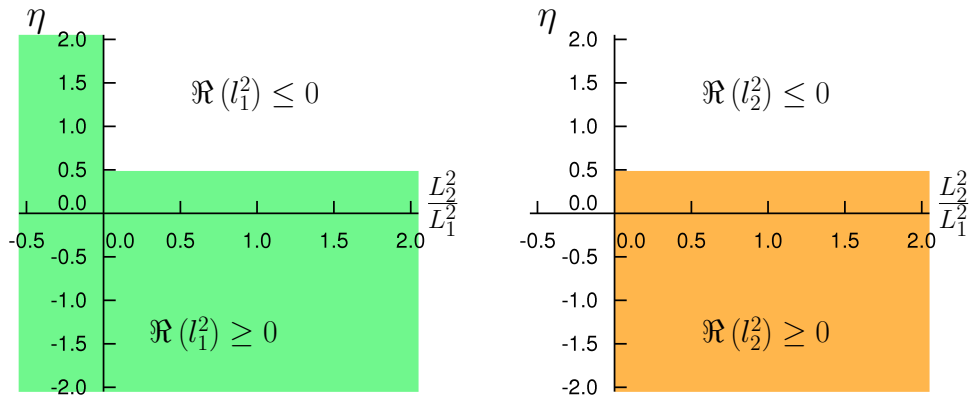

Figure X.3 : Sign of (a) $\Re\left(l_1^2\right)$ and (b) $\Re\left(l_2^2\right)$. The coloured areas correspond to the sets of material parameters for which the real part of the square of the lengths l_1 and l_2 is positive. These results are obtained with L_1^2 positive.

as the considered case is semi–infinite and therefore requires a solution vanishing at infinity. Eq. (X.16) is given in the case of positive characteristic lengths l_1 and l_2, the exponentials vanishing at infinity being e^{-x_1/l_1} and e^{-x_1/l_2}. With negative l_1 and l_2, the two remaining terms of the solution of the displacement–equation of equilibrium would be the terms with α_1 and α_3 with the vanishing exponentials e^{x_1/l_1} and e^{x_1/l_2}. Eq. (X.16) can also be written as:

$$u_1(x_1) = \alpha_2 \left[\cosh\left(\frac{x_1}{l_1}\right) - \sinh\left(\frac{x_1}{l_1}\right)\right] + \alpha_4 \left[\cosh\left(\frac{x_1}{l_2}\right) - \sinh\left(\frac{x_1}{l_2}\right)\right]. \tag{X.17}$$

It describes an exponential decrease of the surface effects as the distance from the traction–free surface increases. This case corresponds to area "1" of Fig. X.4.

2. If l_1^2 and l_2^2 are real and if l_1^2 and l_2^2 are negative, then l_1 and l_2 (and consequently, α_1, α_2, α_3 and α_4) are pure imaginary (i.e., $\Re(l_1, l_2) = 0$, $\Im(l_1, l_2) \neq 0$) and (X.15) can be written as:

$$\begin{aligned} u_1(x_1) =& \Re\left\{\alpha_1 \left[\cos\left(\frac{ix_1}{l_1}\right) - i\sin\left(\frac{ix_1}{l_1}\right)\right] + \alpha_2 \left[\cos\left(\frac{ix_1}{l_1}\right) + i\sin\left(\frac{ix_1}{l_1}\right)\right]\right. \\ &\left. + \alpha_3 \left[\cos\left(\frac{ix_1}{l_2}\right) - i\sin\left(\frac{ix_1}{l_2}\right)\right] + \alpha_4 \left[\cos\left(\frac{ix_1}{l_2}\right) + i\sin\left(\frac{ix_1}{l_2}\right)\right]\right\}, \qquad \text{(X.18a)} \\ =& \Im(\alpha_1)\sin\left(\frac{x_1}{\Im(l_1)}\right) - \Im(\alpha_2)\sin\left(\frac{x_1}{\Im(l_1)}\right) + \Im(\alpha_3)\sin\left(\frac{x_1}{\Im(l_2)}\right) \\ &- \Im(\alpha_4)\sin\left(\frac{x_1}{\Im(l_2)}\right). \qquad \text{(X.18b)} \end{aligned}$$

This solution which oscillates is not vanishing at infinity and has no physical meaning. The sets of material parameters, corresponding to area "2" of Fig. X.4, have to be avoided.

3. If l_1^2 and l_2^2 are complex (i.e., $\Re(l_1, l_2) \neq 0$, $\Im(l_1, l_2) \neq 0$), l_1 and l_2 are complex as well

and (X.15) can be written as:

$$u_1(x_1) = e^{\frac{-x_1\Re(l_1)}{\Re(l_1)^2+\Im(l_1)^2}}\left[\Re(\alpha_2)\,\cos\left(\frac{x_1\Im(l_1)}{\Re(l_1)^2+\Im(l_1)^2}\right)-\Im(\alpha_2)\,\sin\left(\frac{x_1\Im(l_1)}{\Re(l_1)^2+\Im(l_1)^2}\right)\right] + e^{\frac{-x_1\Re(l_2)}{\Re(l_2)^2+\Im(l_2)^2}}\left[\Re(\alpha_4)\,\cos\left(\frac{x_1\Im(l_2)}{\Re(l_2)^2+\Im(l_2)^2}\right)-\Im(\alpha_4)\,\sin\left(\frac{x_1\Im(l_2)}{\Re(l_2)^2+\Im(l_2)^2}\right)\right], \tag{X.19}$$

with $\Re(l_1)$ and $\Re(l_2)$ positive ensuring that $u_1(x_1)$ vanishes at infinity. A similar solution exists with $\Re(l_1)$ and $\Re(l_2)$ negative, the remaining terms are then the terms with α_1 and α_3 of Eq. (X.15). Here the oscillating solution decreases exponentially so that the surface effects remain localised at the traction–free surface. This case corresponds to material parameters taken in area "3" of Fig. X.4.

4. The last case corresponds to area "4". It is obtained with l_1^2 and l_2^2 real and of opposite signs leading to l_1 real and l_2 pure imaginary. The solution takes the form of a sum of an exponential function and a trigonometric function,

$$u_1(x_1) = \Re(\alpha_1)\,e^{x_1/l_1} + \Re(\alpha_2)\,e^{-x_1/l_1} + \Re(\alpha_3)\cos\left(\frac{x_1}{\Im(l_2)}\right) + \Im(\alpha_3)\sin\left(\frac{x_1}{\Im(l_2)}\right) + \Re(\alpha_4)\cos\left(\frac{x_1}{\Im(l_2)}\right) - \Im(\alpha_4)\sin\left(\frac{x_1}{\Im(l_2)}\right), \tag{X.20}$$

and has no physical meaning.

Figure X.4 summarises the four cases just described. As it has been shown, only the sets of material parameters taken in areas "1" and "3" lead to physically relevant behaviour. The stability requirements initially presented in Fig. X.2(a) are also recalled, the hatched area representing the material parameters leading to a convex potential energy density. This convex domain is associated with both exponential and aperiodic physically relevant behaviour. In the following, the solution of the displacement–equation of equilibrium is supposed to have the general form vanishing at infinity given in Eq. (X.16). Recalling the discussions made in cases 1 and 3, this implies that l_1^2 and l_2^2 or $\Re(l_1)$ and $\Re(l_2)$ are positive.

Successive derivations of $u_1(x_1)$ give the expressions of $\varepsilon_{11}(x_1)$, $\varepsilon_{111}(x_1)$ and $\varepsilon_{1111}(x_1)$. By using the components of the stress tensors as expressed in (X.10), the two last boundary conditions of (X.4) become

$$(A-\bar{c})\,\varepsilon_{111} - B\,\varepsilon_{1111,1} = 0, \quad B\,\varepsilon_{1111} + \bar{c}\,\varepsilon_{11} = -b_0 \qquad \text{at } x_1 = 0. \tag{X.21}$$

The two constants α_2 and α_4 of the solution (X.16) then follow:

$$\alpha_2 = l_0^2\,\frac{l_1^2\left(l_2^2+l_c^2\right)}{l_1\left(l_2^2+l_c^2\right)^2 - l_2\left(l_1^2+l_c^2\right)^2}, \quad \alpha_4 = -\alpha_2\,\frac{l_2^2\left(l_1^2+l_c^2\right)}{l_1^2\left(l_2^2+l_c^2\right)}, \tag{X.22}$$

with the new characteristic lengths

$$l_c^2 = \frac{\bar{c}}{\lambda+2\mu} = \frac{1}{2}\,\eta\,L_1^2 \tag{X.23}$$

and

$$l_0^2 = \frac{b_0}{\lambda+2\mu} = \frac{1}{2}\,\eta_0\,L_1^2. \tag{X.24}$$

It clearly appears that no surface effects occur without initial higher order stress, i.e., when $b_0 = 0$. Indeed, if the modulus b_0 or its associated dimensionless material parameter η_0 related

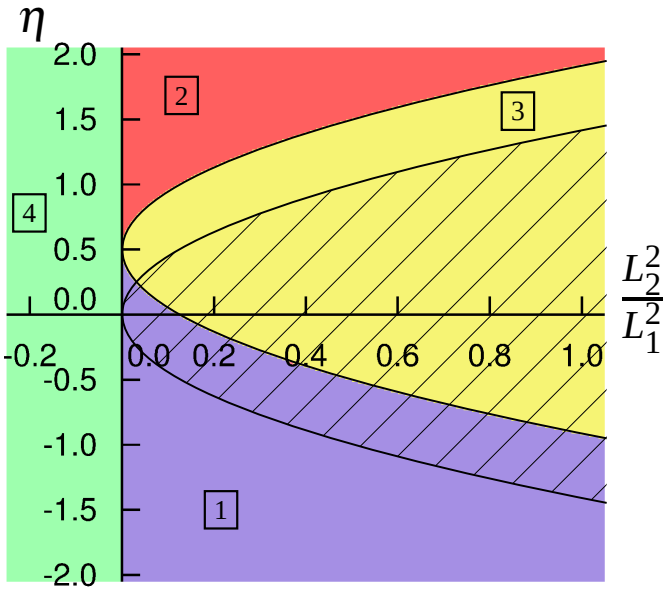

Figure X.4 : Summary of the four main cases simulated by the theory. Only the sets of material parameters taken in areas "1" and "3" lead to solutions vanishing at infinity. The hatched area represents the convex domain described by the stability requirements (X.9). This convex domain is associated with both exponential and aperiodic physically relevant behaviour (i.e., convex domain $\subset 1 \cup 3$).

to surface energy vanishes, the characteristic length l_0 and the constants α_2 and α_4 vanish and, finally, $u_1(x_1) = 0$. Note that this complete solution of the boundary value problem is valid for both physically relevant cases 1 and 3.

The corresponding displacement, strain and stress profiles close to the traction–free surface are presented in Fig. X.5. These profiles are obtained for $L_1 = 0.3$ nm, a fixed ratio $L_2^2/L_1^2 = 1$, $\eta_0 = 0.1$ and for four different values of η. These sets of material parameters correspond to the first three cases simulated by the theory: $\eta = -3.0$ and $\eta = -1.2$ correspond to the Area "1" in Fig. X.4 and to u_1 hyperbolic as in Eq. (X.17); note that $\eta = -3.0$ is not in the convex domain. In the same way, $\eta = 1.3$ and $\eta = 1.9$ correspond to Areas "2" and "3" and to u_1 as in Eqs. (X.18) and (X.19), respectively. The profiles presented in Fig. X.5 show that the surface energy effects produced by the theory can either lead to higher or smaller interatomic distances close to the free surface. This free surface can also be either in tension or compression. In this figure, $\eta = -3.0$ and $\eta = -1.2$ correspond to area "1" in Fig. X.4 and $\eta = 1.2$ to area "3". These parameters are physically relevant; note that $\eta = -3.0$ is not in the convex domain. $\eta = 1.9$ is taken in area "2" and leads to an irrelevant oscillating solution.

In this configuration, the expression of the surface energy (IX.24) at the plane traction–free surface of the half–space becomes:

$$\gamma = -\frac{1}{2} b_0 \, \varepsilon_{111} = -\frac{1}{2} b_0 \left(\frac{\alpha_2}{l_1^2} + \frac{\alpha_4}{l_2^2} \right) = \frac{1}{2} \frac{l_0^4 \left(\lambda + 2\mu\right) \left(l_1^2 - l_2^2\right)}{l_1 \left(l_2^2 + l_c^2\right)^2 - l_2 \left(l_1^2 + l_c^2\right)^2} \quad \text{at } x_1 = 0. \tag{X.25}$$

The initial higher order stress, b_0, (or alternatively its corresponding dimensionless material parameter, η_0) only appears in the constants α_2 and α_4 (X.22) through the characteristic length, l_0^2, it has then no effect on the shape of the simulated behaviour. However, as suggested by Eq. (X.25), b_0 controls the amplitude of the surface energy.

The effect of the modulus $\bar{c}$ that enables, in the present case, the coupling between the strain, ε_{11}, and the third gradient of the displacement field, ε_{1111}, is presented and discussed in detail in Section X.1.3. At this point, a first remark can be made from the solution of the displacement–equation of equilibrium (X.16), the expressions of the constants (X.22) and the expression of $l_c = \bar{c}/(\lambda + 2\mu)$. When $\bar{c} = 0$, there is no displacement of the traction–free surface and no volume variation even with a non–zero initial higher order stress, b_0, i.e., $u_1(0) = 0, \forall\, b_0$. However, displacements of internal material points occur close to the traction–free surface, i.e., $u_1(x_1 > 0) \neq 0$. This specific case is described in Fig. X.6.

X.1.2 Surface energy: interaction between two free surfaces

We consider now a material strip located at $[-h/2, h/2]$ and infinite along the direction 2 as described in Fig. X.1(b). Both surfaces at $x_1 = \pm h/2$ are assumed to be traction–free:

$$\underline{\boldsymbol{t}}^{\mathbf{1}} = \underline{\boldsymbol{t}}^{\mathbf{2}} = \underline{\boldsymbol{t}}^{\mathbf{3}} = 0 \quad \text{at } x_1 = \pm\frac{h}{2}, \tag{X.26}$$

h being the distance between the two plane surfaces. The purpose here is to show the interaction of the effects of these surfaces when they are getting closer. The same steps as in the previous example are followed, then Eqs. (X.2) to (X.14) remain valid and lead to a displacement of the same form as in Eq. (X.15). The two last boundary conditions of Eqs. (X.4) and (X.26) are in this case:

$$(A - \bar{c})\,\varepsilon_{111} - B\,\varepsilon_{1111,1} = 0, \quad B\,\varepsilon_{1111} + \bar{c}\,\varepsilon_{11} = -b_0 \qquad \text{at } x_1 = \pm\frac{h}{2}. \tag{X.27}$$

They are used to derive the constants α_1 to α_6 of the solution (X.15):

$$\alpha_1 = -\frac{1}{2}\,l_0^2\,l_1^2\left(l_2^2 + l_c^2\right)\left\{\sinh\left(\frac{h}{2l_1}\right)\left[l_1\left(l_2^2 + l_c^2\right)^2\coth\left(\frac{h}{2l_1}\right) - l_2\left(l_1^2 + l_c^2\right)^2\coth\left(\frac{h}{2l_2}\right)\right]\right\}^{-1}, \tag{X.28a}$$

$$\alpha_2 = -\,\alpha_1, \tag{X.28b}$$

$$\alpha_3 = -\,\alpha_1\,l_2^2\left(l_1^2 + l_c^2\right)\sinh\left(\frac{h}{2l_1}\right)\left[l_1^2\left(l_2^2 + l_c^2\right)\sinh\left(\frac{h}{2l_2}\right)\right]^{-1}, \tag{X.28c}$$

$$\alpha_4 = -\,\alpha_3, \tag{X.28d}$$

$$\alpha_5 = 0, \tag{X.28e}$$

$$\alpha_6 = 0. \tag{X.28f}$$

Here, the solution is not meant to vanish at infinity, that is why four constants are non–zero. However, α_5 and α_6 vanish as the solution does not exhibit linear or constant parts. The obtained expressions of $u_1(x_1)$, its derivative and its constants are similar to those obtained in the previous case where only one free surface is considered. Additional hyperbolic terms depending on the relative distance between the free surfaces, h, and the characteristic lengths, l_1 and l_2, appear. If h is large compared to l_1 and l_2, these terms vanish and each free surface can be considered alone as in the half–space case. When h decreases, the surface energy effects arising at each free surface start to interfere and the solution is then modified. The profiles of the displacement component u_1 and of stress component σ_{11} are presented in

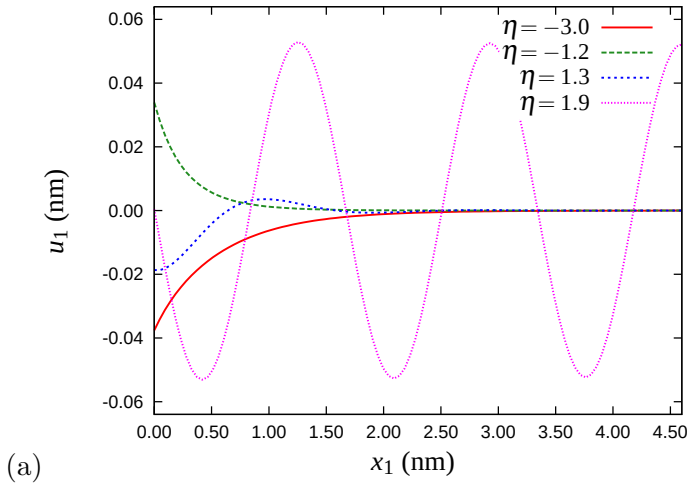

(a)

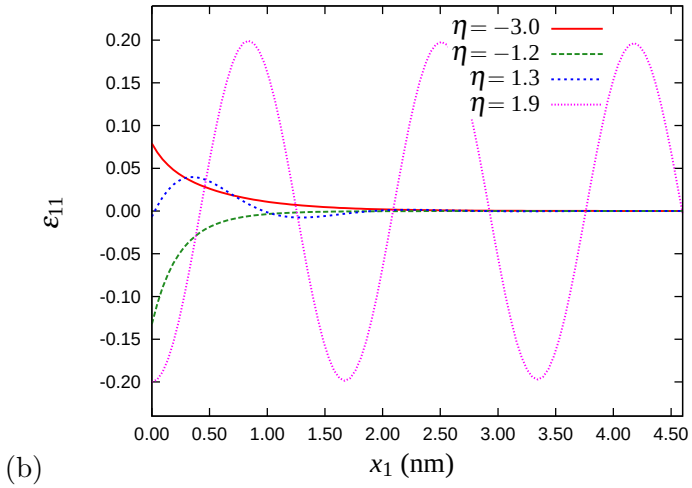

(b)

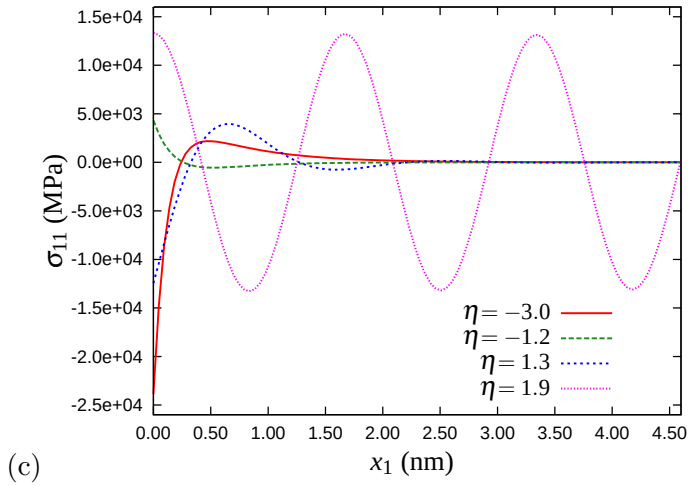

(c)

Figure X.5 : Profiles of (a) the displacement component u_1, (b) the strain component ε_{11} and (c) the stress component σ_{11} close to the traction–free surface (at $x_1 = 0$). Four sets of material parameters are considered: $E = 140$ GPa, $\nu = 0.3$, $L_1 = 0.3$ nm and a fixed ratio $L_2^2/L_1^2 = 1$ are chosen, the surface energy related parameter $\eta_0 = 0.1$ and four values of η are used in order to illustrate the four different cases arising in the theory.

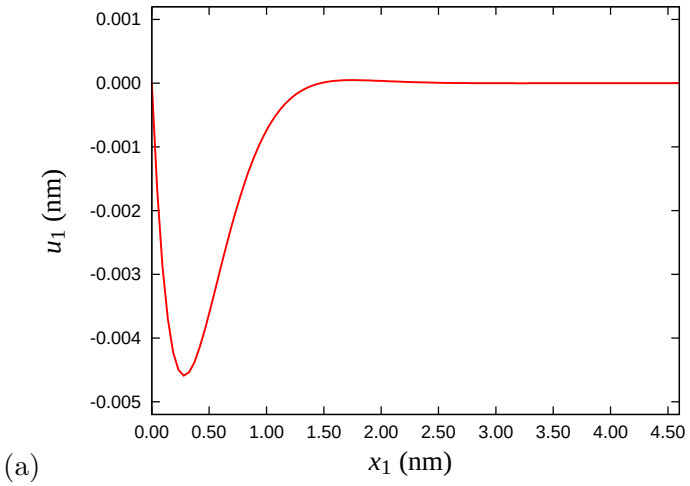

(a)

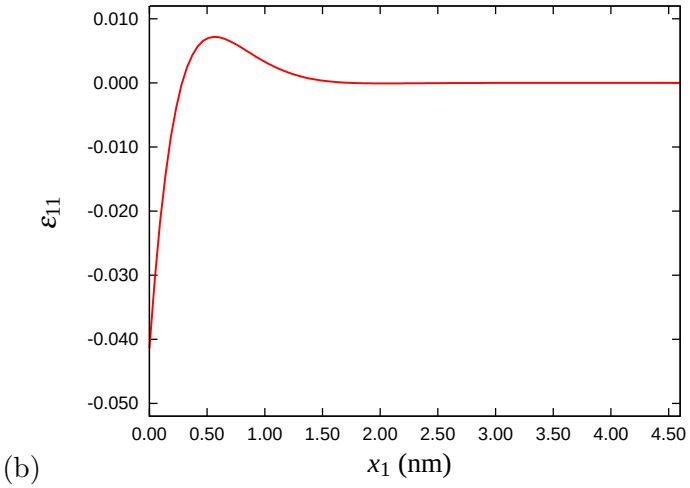

(b)

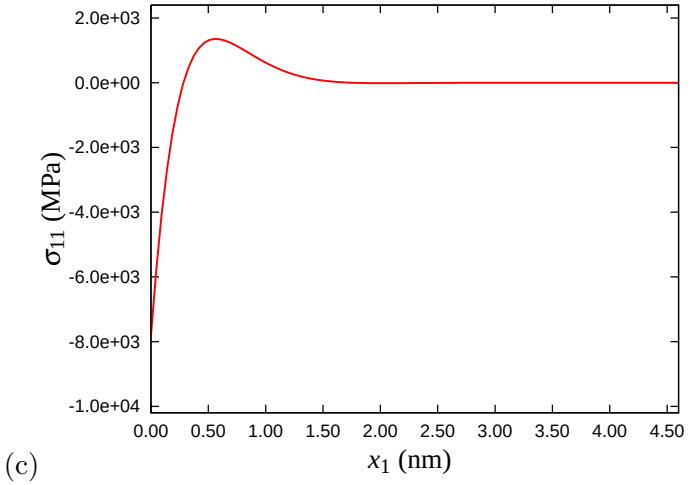

(c)

Figure X.6 : Profiles of (a) the displacement component u_1, (b) the strain component ε_{11} and (c) the stress component σ_{11} close to the traction–free surface (at $x_1 = 0$). $E = 140$ GPa, $\nu = 0.3$, $L_1 = 0.3$ nm and a fixed ratio $L_2^2/L_1^2 = 1$ are chosen, the surface energy related parameter $\eta_0 = 0.1$ and the coupling parameter $\eta = 0$, i.e., $\bar{c} = 0$.

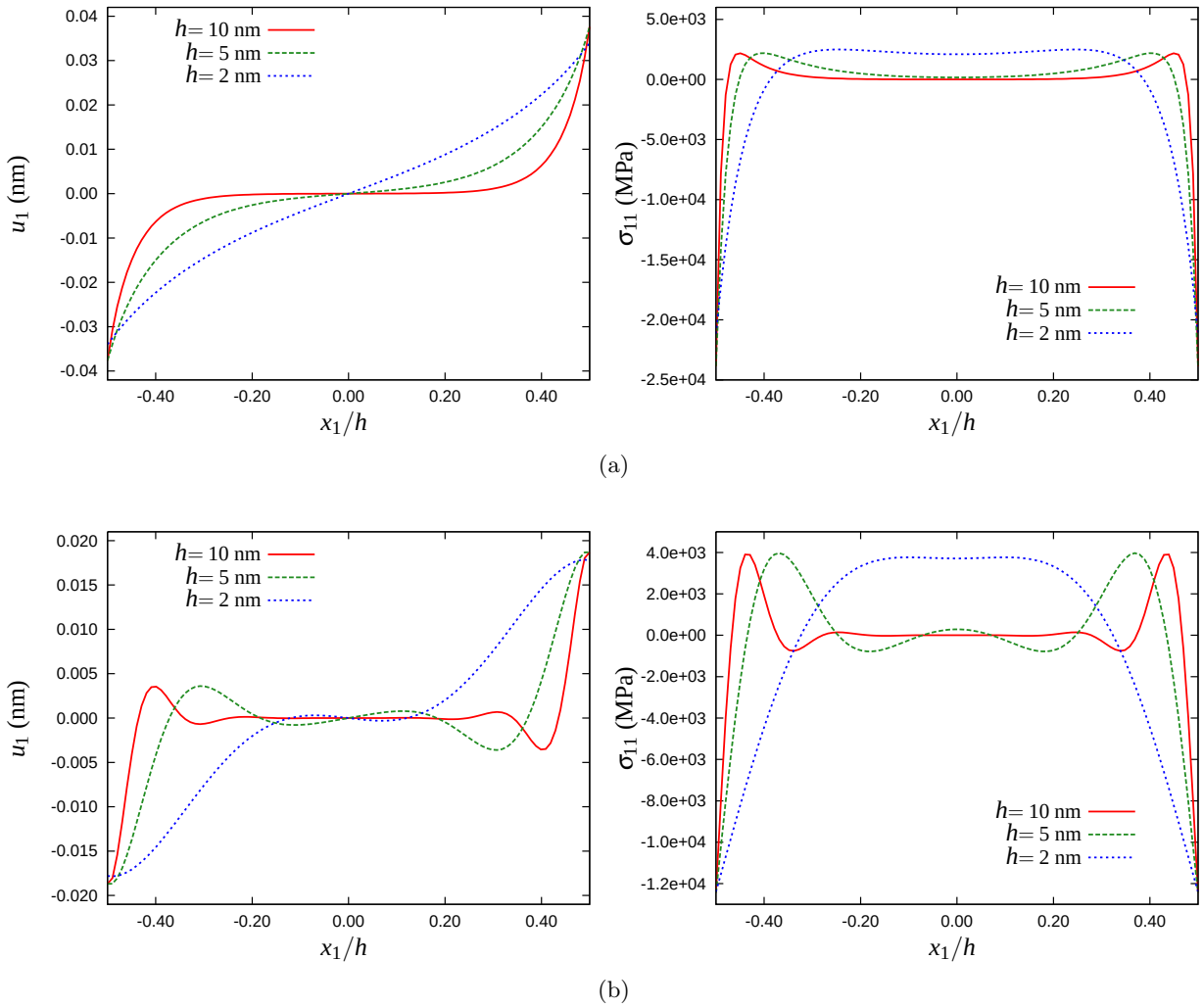

Figure X.7 : Profiles of the displacement component u_1 and of stress component σ_{11} for distances between the two traction–free surfaces $h = 10$, 5 and 2 nm and for material parameters leading to (a) exponential profiles ($E = 140$ GPa, $\nu = 0.3$, $L_1 = 0.3$ nm, $L_2^2/L_1^2 = 1$, $\eta_0 = 0.1$ and $\eta = -3$) and to (b) aperiodic profiles ($E = 140$ GPa, $\nu = 0.3$, $L_1 = 0.3$ nm, $L_2^2/L_1^2 = 1$, $\eta_0 = 0.1$ and $\eta = 1.3$). The free surfaces are located at $x_1/l = \pm 0.5$.

Fig. X.7 for different distances h and for sets of material parameters giving hyperbolic and aperiodic solutions as discussed in Section X.1.1. These profiles illustrate the conclusions made previously. Indeed, for larger values of h, e.g., $h = 10$ nm, the profiles close to the free surfaces are the same as in the half–space case, see Fig. X.5. When h gets smaller, the zones affected by the surface energy effects start to overlap and the resulting profiles are modified. This case appears to be of great interest as it can be retrieved in nano–sized objects such as nanowires or nano–porous materials where surfaces are very close to each other. A discussion could have been done here about the different possible behaviour that can be described by the theory as it was done in Section X.1.1. However, as it would have led to similar remarks, the solution of the boundary value problem was directly given for the general case.

In the previous section and in the present one, it has been shown that the initial higher order stress, b_0, generates surface energy. This surface effect will noticeably affect the overall behaviour when the material will exhibit sizes of the order of some tens of nanometers or

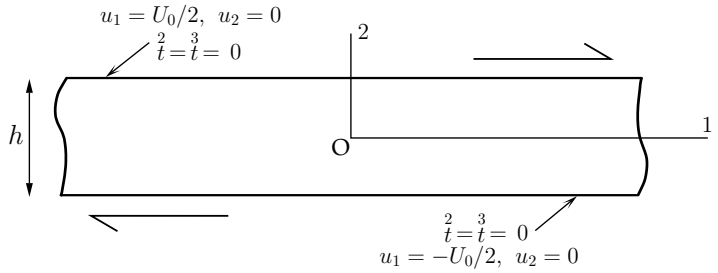

Figure X.8 : Shear of an infinite strip of thickness h. The upper and lower surfaces are traction–free with respect to the higher order stresses.

smaller. It is shown here that for smaller sizes, i.e., a few nanometers depending on the material parameters, an additional interaction effect arises modifying the overall behaviour. A two–stage size–dependent behaviour is consequently expected and nano–sized objects with smaller sizes are likely to have different behaviour.

X.1.3 Surface stress: shear of an infinite strip

The purpose of this section is to illustrate the surface stress effects produced by the theory. This surface effects come from the coupling between the components of the strain, $\underset{\sim}{\varepsilon}$, and the components of the third gradient of the displacement field, $\underset{\approx}{\underset{\sim}{\varepsilon}}$, and are controlled by the coupling moduli c_i. The shear of an infinite strip of thickness h is considered as described in Fig. X.8. The upper and lower surfaces are traction–free with respect to the higher order stresses, i.e.,

$$\underline{\overset{\mathbf{2}}{\boldsymbol{t}}} = \underline{\overset{\mathbf{3}}{\boldsymbol{t}}} = 0 \quad \text{at } x_2 = \pm\frac{h}{2}, \tag{X.29}$$

and are subjected to a displacement u_1 as

$$u_1(h/2) = \frac{U_0}{2}, \quad u_1(-h/2) = -\frac{U_0}{2}. \tag{X.30}$$

In addition, in order to focus exclusively on the surface stress effects, no surface energy is considered at these surfaces. In other words, in this specific case, the initial higher order stress, b_0, related to surface energy is taken equal to zero. The displacement field is assumed to be of the form:

$$u_1 = u_1(x_2), \quad u_2 = u_3 = 0. \tag{X.31}$$

The stress–equation of equilibrium (IX.19) becomes

$$\sigma_{12,2} - S_{122,22} + S_{1222,222} = 0 \tag{X.32}$$

and the two last boundary conditions (IX.20) are

$$S_{122} - S_{1222,2} \;=\; S_{1222} \;=\; 0 \quad \text{at } x_2 = \pm\frac{h}{2}. \tag{X.33}$$

Considering the displacement field (X.31), the potential energy density (IX.21) is a function of the strain components ε_{12}, ε_{122} and ε_{1222}:

$$\rho\Psi\left(\varepsilon_{12},\, \varepsilon_{122},\, \varepsilon_{1222}\right) = \mu\,\varepsilon_{12}^2 + \frac{A}{2}\,\varepsilon_{122}^2 + \frac{B}{2}\,\varepsilon_{1222}^2 + c_3\,\varepsilon_{12}\,\varepsilon_{1222} \tag{X.34}$$

where the following moduli are adopted

$$A = 2\,(a_3 + a_4)\,, \quad B = 2\,(b_5 + b_6)\,. \tag{X.35}$$

In the same way as in Sections X.1.1 and X.1.2, the following material parameters are introduced

$$L_1^2 = \frac{A}{\mu}, \quad L_2^2 = \frac{B}{A}, \quad \eta = \frac{c_3}{A}, \tag{X.36}$$

allowing an alternative way to express the potential energy density (X.34) as a function of dimensionless arguments:

$$\rho\Psi\left(\varepsilon_{12},\, \varepsilon_{122},\, \varepsilon_{1222}\right) = \rho\hat{\Psi}\left(\varepsilon_{12},\, L_1\,\varepsilon_{122},\, L_2^2\,\varepsilon_{1222}\right). \tag{X.37}$$

The following stability requirements can then be obtained to ensure a convex potential,

$$L_1^2 \geq 0, \quad L_2^2 \geq 0, \quad 2\,\frac{L_2^2}{L_1^2} \geq \eta^2. \tag{X.38}$$

These stability requirements imply that the moduli A and B have to be positive and that c_3 can be either positive or negative. The components σ_{12}, S_{122} and S_{1222} of the stress tensors are obtained from Eqs. (X.34) and (IX.8) or alternatively from Eqs. (X.40) and (IX.22):

$$\sigma_{12} = 2\mu\,\varepsilon_{12} + c_3\,\varepsilon_{1222}, \tag{X.39a}$$

$$S_{122} = A\,\varepsilon_{122}, \tag{X.39b}$$

$$S_{1222} = B\,\varepsilon_{1222} + c_3\,\varepsilon_{12}. \tag{X.39c}$$

Substituting these expressions into the stress–equation of equilibrium (X.32) and recalling that $\varepsilon_{12} = 0.5\,u_{1,2}$, $\varepsilon_{122} = 0.5\,u_{1,22}$ and $\varepsilon_{1222} = 0.5\,u_{1,222}$, the following displacement–equation of equilibrium is obtained:

$$\left(1 - l_1^2\,\frac{d^2}{dx_2^2}\right)\left(1 - l_2^2\,\frac{d^2}{dx_2^2}\right)\frac{d^2u_1}{dx_2^2} = 0. \tag{X.40}$$

The relationships,

$$l_1^2 l_2^2 = \frac{B}{2\mu}, \quad l_1^2 + l_2^2 = \frac{A - 2c_3}{2\mu}, \tag{X.41}$$

are derived and give the following expressions for the lengths l_1 and l_2:

$$l_1^2 = \frac{A - 2c_3 + \sqrt{(A-2c_3)^2 - 8B\mu}}{4\mu}, \quad l_2^2 = \frac{A - 2c_3 - \sqrt{(A-2c_3)^2 - 8B\mu}}{4\mu}, \tag{X.42}$$

or alternatively:

$$l_1^2 = \frac{L_1^2}{4}\left(1 - 2\eta + \sqrt{(1-2\eta)^2 - 8\frac{L_2^2}{L_1^2}}\right), \quad l_2^2 = \frac{L_1^2}{4}\left(1 - 2\eta - \sqrt{(1-2\eta)^2 - 8\frac{L_2^2}{L_1^2}}\right). \tag{X.43}$$

It can be noted that the chosen notations for the material parameters L_1, L_2 and η lead to the same expressions of the stability requirements (X.9) and of the characteristic lengths (X.14) as in Subsections X.1.1 and X.1.2.

The solution of (X.40) takes the form:

$$u_1(x_2) = \alpha_1\,e^{x_2/l_1} + \alpha_2\,e^{-x_2/l_1} + \alpha_3\,e^{x_2/l_2} + \alpha_4\,e^{-x_2/l_2} + \alpha_5\,x_2 + \alpha_6, \tag{X.44}$$

and the boundary conditions (X.33) become

$$(A - c_3)\,\varepsilon_{122} - B\,\varepsilon_{1222,2} = 0, \quad B\,\varepsilon_{1222} + c_3\,\varepsilon_{12} = 0 \qquad \text{at } x_2 = \pm\frac{h}{2}, \tag{X.45}$$

and are used to find the expressions of the constants α_1 to α_6:

$$\begin{aligned}\alpha_1 =& U_0\, l_c^2\, l_1^2\, \left(l_2^2 + l_c^2\right) \left\{ \sinh\left(\frac{h}{2l_1}\right) \left[4\, l_c^4 \left(l_1^2 - l_2^2\right) - 2h \left(l_1 \left(l_2^2 + l_c^2\right)^2 \coth\left(\frac{h}{2l_1}\right) \right.\right.\right. \\ & \left.\left.\left. - l_2 \left(l_1^2 + l_c^2\right)^2 \coth\left(\frac{h}{2l_2}\right) \right) \right] \right\}^{-1}, \end{aligned} \tag{X.46a}$$

$$\alpha_2 = -\,\alpha_1, \tag{X.46b}$$

$$\alpha_3 = -\,\alpha_1\, l_2^2 \left(l_1^2 + l_c^2\right) \sinh\left(\frac{h}{2l_1}\right) \left[l_1^2 \left(l_2^2 + l_c^2\right) \sinh\left(\frac{h}{2l_2}\right) \right]^{-1}, \tag{X.46c}$$

$$\alpha_4 = -\,\alpha_3, \tag{X.46d}$$

$$\alpha_5 = -\,2\alpha_1\, \sinh\left(\frac{h}{2l_1}\right) \left[l_1 \left(l_2^2 + l_c^2\right)^2 \coth\left(\frac{h}{2l_1}\right) - l_2 \left(l_1^2 + l_c^2\right)^2 \coth\left(\frac{h}{2l_2}\right) \right] \left[l_c^2\, l_1^2 \left(l_2^2 + l_c^2\right) \right]^{-1}, \tag{X.46e}$$

$$\alpha_6 = 0, \tag{X.46f}$$

with the new characteristic length,

$$l_c^2 = \frac{c_3}{2\mu} = \frac{1}{2}\,\eta\, L_1^2. \tag{X.47}$$

Recall that the initial higher order stress, b_0, and its related characteristic length, l_0^2, do not appear in these expressions as the surface energy is purposely not considered in this case. By observing Eqs. (X.46), it appears that surface stress effects only occur if a coupling exists between the component of the strain ε_{12} and the component of the third gradient of the displacement field ε_{1222}: if the coupling modulus $c_3 = 0$, $l_c = 0$ and then $\alpha_1 = \alpha_2 = \alpha_3 = \alpha_4 = 0$ and $\alpha_5 = U_0/h$. Finally, the homogeneous solution of a classical continuum is retrieved: $u_1(x_2) = U_0 x_2/h$. The same remark can be made on the imposed displacement at the upper and lower surfaces. Indeed, if $U_0 = 0$ all the constants α_i vanish and then $u_1(x_2) = 0$. This is not the case in the presence of surface energy which, as shown is Section X.1.1, arises even in the absence of external loading at traction–free surfaces. The profiles of the displacement component u_1 and of stress component σ_{12} are shown in Fig. X.9 for different thicknesses h of the infinite strip and for sets of material parameters leading to usual hyperbolic and aperiodic solutions. This figure shows that for larger thicknesses h of the strip, the profiles are almost linear and close to the solution for a classical continuum; the surface stress effects being localised at the upper and lower surfaces, the affected zones remain small compared to h. The surface stress effects become relatively more important when the strip becomes thinner, i.e., when the higher order traction–free surfaces get closer.

The apparent shear modulus μ^{app} is defined by averaging the stress component σ_{12} and the strain component ε_{12} along the thickness of the infinite strip as:

$$\int_{-h/2}^{h/2} \sigma_{12}\, dx_2 = 2\,\mu^{app} \int_{-h/2}^{h/2} \varepsilon_{12}\, dx_2. \tag{X.48}$$

The following expression of the apparent shear modulus is then obtained:

$$\mu^{app} = \mu\, \frac{l_1 \left(l_2^2 + l_c^2\right)^2 \coth\left(\frac{h}{2l_1}\right) - l_2 \left(l_1^2 + l_c^2\right)^2 \coth\left(\frac{h}{2l_2}\right)}{l_1 \left(l_2^2 + l_c^2\right)^2 \coth\left(\frac{h}{2l_1}\right) - l_2 \left(l_1^2 + l_c^2\right)^2 \coth\left(\frac{h}{2l_2}\right) - \frac{2}{h}\, l_c^4 \left(l_1^2 - l_2^2\right)}. \tag{X.49}$$

Equivalently, the ratio μ^{app}/μ is:

$$\frac{\mu^{app}}{\mu} = \frac{1}{1 - \dfrac{2}{h} \dfrac{l_c^4 \left(l_1^2 - l_2^2\right)}{l_1 \left(l_2^2 + l_c^2\right)^2 \coth\left(\dfrac{h}{2l_1}\right) - l_2 \left(l_1^2 + l_c^2\right)^2 \coth\left(\dfrac{h}{2l_2}\right)}}. \tag{X.50}$$

It turns out that μ^{app} is size–dependent, the effect of the thickness h on its value is plotted for different sets of material parameters in Fig. X.10. For large values of h the surface stress effects are negligible and the bulk shear modulus μ is retrieved,

$$\lim_{h\to\infty} \mu^{app} = \mu. \tag{X.51}$$

When the size decreases, the apparent elastic property progressively differs from the one of the bulk and tends to

$$\lim_{h\to 0} \mu^{app} = \mu \frac{l_1^2 l_2^2 - l_c^4}{l_1^2 l_2^2}. \tag{X.52}$$

Figure X.10 shows that μ^{app} can either increase or decrease for smaller h. This only depends on the material parameter related to the coupling, η. This also appears in the limit presented in Eq. (X.52) where the ratio μ^{app}/μ depends on the difference between the characteristic lengths $l_1^2 l_2^2 - l_c^4$. In this figure, the horizontal line corresponds to the classical solution obtained without coupling or, equivalently, without surface stress effects.

Some specific cases can be investigated to fully understand the surface stress effects. For example, if $l_1 = l_2$ (i.e., $(1-2\eta)^2 = 8\, L_2^2/L_1^2$), no effect is produced and then

$$\mu^{app}_{(l_1=l_2)} = \mu. \tag{X.53}$$

This is the specific case of the double root of the differential equation (X.40). It corresponds to the parabola of Fig. X.2(b) separating the two domains in which l_1^2 and l_2^2 are real or complex. Moreover, if the generalised modulus related to the second strain gradient, B, vanishes, we have $L_2 \to 0$, $l_2 \to 0$ and finally:

$$\lim_{B\to 0} \mu^{app} = \mu \frac{h \coth\left(\dfrac{h}{2l_1}\right)}{h \coth\left(\dfrac{h}{2l_1}\right) - 2l_1}. \tag{X.54}$$

This means that the theory generates size–dependent surface stress effects even if B vanishes. This enforces the fact that, as mentioned before, the surface stress effects only depend on the coupling set between the strain component, ε_{12}, and the third gradient of the displacement field component, ε_{1222}.

X.2 Application to nanowires

Now that the capabilities of the theory and, more particularly, the generated surface effects, have been presented, more realistic and complex boundary value problems will be considered. This section focuses on the size–dependent mechanical behaviour of nanowires. These nano–objects have been widely investigated due to their key role in nano–electromechanical systems (NEMS) (Craighead, 2000; Feng *et al.*, 2007; Sanii and Ashby, 2010). In particular, their size–dependent elastic properties are studied experimentally using different methods (see, for example, Agrawal *et al.*, 2008; McDowell *et al.*, 2008; Sadeghian

Table X.1 : Set of material parameters used in the finite element simulations.

E [GPa]	ν	A [N]	B [N.nm^2]	c_1 [N]	$c_{i\neq 1}$ [N]	b_0 [N]
140	0.3	$9.4\,10^{-8}$	$4.7\,10^{-8}$	$-2.8\,10^{-7}$	0	0

or equivalently:

E [GPa]	ν	L_1 [nm]	L_2^2/L_1^2	η_1	$\eta_{i\neq 1}$	η_0
140	0.3	1.0	0.5	-3	0	0

et al., 2009). Nanowires exhibit a very high surface area to volume ratio and therefore their behaviour is highly affected by surface effects. Using the previous results as a guideline to define the materials parameters, their overall behaviour and local profiles are studied using finite element simulations. To that purpose, the second gradient of strain theory presented in Section IX.1 is implemented using the second order micromorphic approach formulated in Section IX.2. The micromorphic model is constrained through the moduli H_χ^a and H_χ^b of Eqs. (IX.36) and coincides with Mindlin's theory. In what follows, H_χ^a and H_χ^b are taken sufficiently high to ensure this internal constraint. The main features of the finite element implementation are given in Appendix B.3.

The finite element simulations are performed on the boundary value problem described in Fig. X.11(a) under plane strain conditions. Tensile tests of nanowires with various diameters, d, and an infinite length (as a result of the periodic boundary conditions set at the top and bottom ends of the computed wire sections) are simulated. In these tests, the nano–objects remain elastic as the considered micromorphic model and the initial theory only generate elasticity surface effects affecting elastic behaviour. A displacement, U, is imposed at the top of the wire sections while the bottom end is kept fixed. The outer surface of the nanowires is traction–free, which means that in the present case

$$\underline{\boldsymbol{t}}^{\mathbf{1}} = \underline{\boldsymbol{t}}^{\mathbf{2}} = \underline{\boldsymbol{t}}^{\mathbf{3}} = 0 \quad \text{at } x_1 = \pm\frac{h}{2}, \tag{X.55}$$

at the vertical sides of the 2D geometry presented in Fig. X.11(a). Moreover, the finite element simulations are conducted under generalised plane strain conditions.

The contour plots of Fig. X.11(b) and the corresponding profiles across the wire diameter of Fig. X.11(c) describe the simulated fields of the strain and stress components ε_{11} and σ_{22} obtained for three diameters and with the material parameters given in Table X.1. These material parameters are presented using the notation (X.7) introduced in Section X.1 and the corresponding generalised moduli A, B, c_i and b_0 are also given. The coupling moduli c_i' used in the micromorphic model are defined using the equivalences between c_i and c_i' (IX.48). The results given in Fig. X.11 reveal that the surface stress effects are localised at the surface of the larger nanowire of diameter $d = 50$ nm. The fields and profiles of ε_{11} and σ_{22} are close to those that can be obtained with a classical continuum. However, for smaller d, the surface stress effects become more significant and the affected zone spreads across the wires. These results agree with the previous observations made in the infinite strip shear case.

Recalling that generalised plane strain conditions are used, the apparent Poisson's ratio, ν^{app}, and the apparent Young's modulus, E^{app}, are calculated as

$$\nu^{app} = \frac{\varepsilon_{11}}{\varepsilon_{11} - \varepsilon_{22}} \tag{X.56}$$

and

$$E^{app} = \frac{\sigma_{22}(1 - \nu^{app^2})}{\varepsilon_{22}}, \tag{X.57}$$

where ε_{11}, ε_{22} and σ_{22} come from the finite element simulations. These apparent elastic constants are found to be size–dependent. Figure X.12 shows the effect of the nanowire diameter, d, on the evolution of the apparent Young's modulus, E^{app}, for the material parameters given in Table X.1. These parameters have been identified in order to reproduce a similar size–dependent behaviour to the one described by the experimental data obtained with tensile tests of single crystal ZnO nanowires having a [0001] oriented wurtzite structure from Agrawal *et al.* (2008). This identification is done using the results from the previous sections as a guideline. Indeed, the value of the material parameter related to the coupling is first set at $\eta = -3$ regarding the previous results where satisfying amplitudes of the surface displacement were simulated. Then, the only dimensional parameter, L_1, is calibrated to obtain a size dependent zone for a range of diameters that corresponds to the experimental results. Finally, the ratio L_2/L_1 is calibrated to refine the fitting. The identified material parameters are of the same order of magnitude as those used in the simple cases treated earlier in this chapter. Note that this identification is quite idealised as the proposed theory has been formulated for isotropic materials. In the same way, Fig. X.13, shows the effect of d on the evolution of the apparent Poisson's ratio, ν^{app}.

The second gradient of strain theory presented in Section IX.1 is then able to simulate the size–dependent elastic properties of nanowires. Their mechanical behaviour is affected by surface effects that occur in a surface region of a few nanometers. The obtained results show that these surface effects can be neglected when the wire diameter is equal to some tens of nanometers or larger. For such sizes, the elastic properties of the bulk material are retrieved.

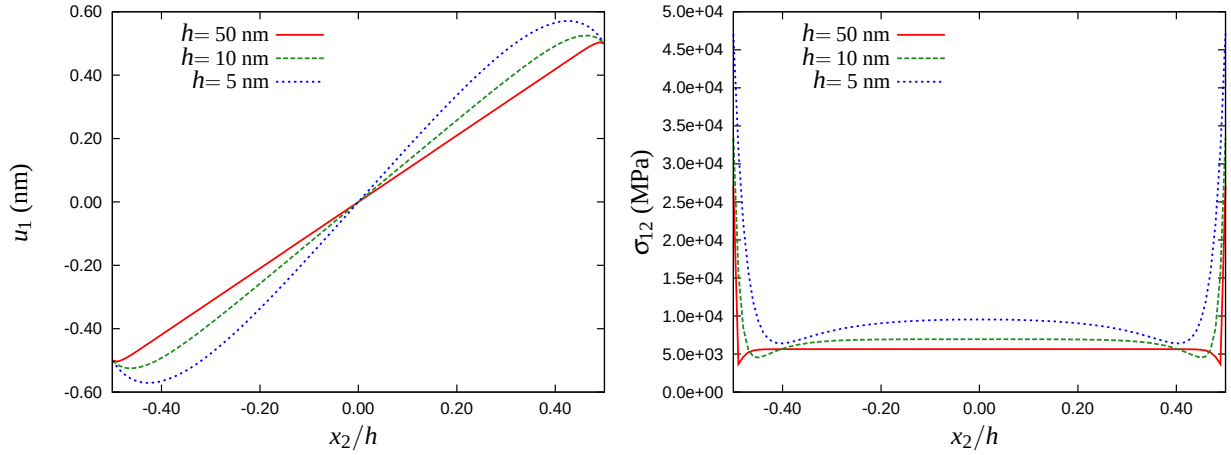

(a)

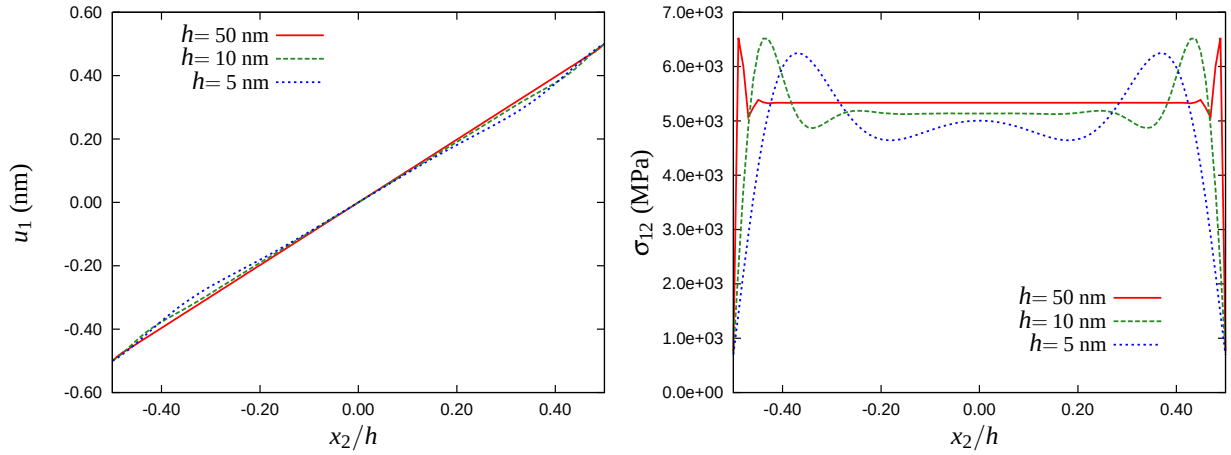

(b)

Figure X.9 : Profiles of the displacement component u_1 and of stress component σ_{12} for thicknesses of the infinite strip, $h = 50$, 10 and 5 nm, and for material parameters leading to (a) exponential profiles ($E = 140$ GPa, $\nu = 0.3$, $L_1 = 0.3$ nm, $L_2^2/L_1^2 = 1$ and $\eta = -3$) and to (b) aperiodic profiles ($E = 140$ GPa, $\nu = 0.3$, $L_1 = 0.3$ nm, $L_2^2/L_1^2 = 1$ and $\eta = 1.3$). In both cases, the surface energy is not considered, i.e., $b_0 = \eta_0 = 0$.

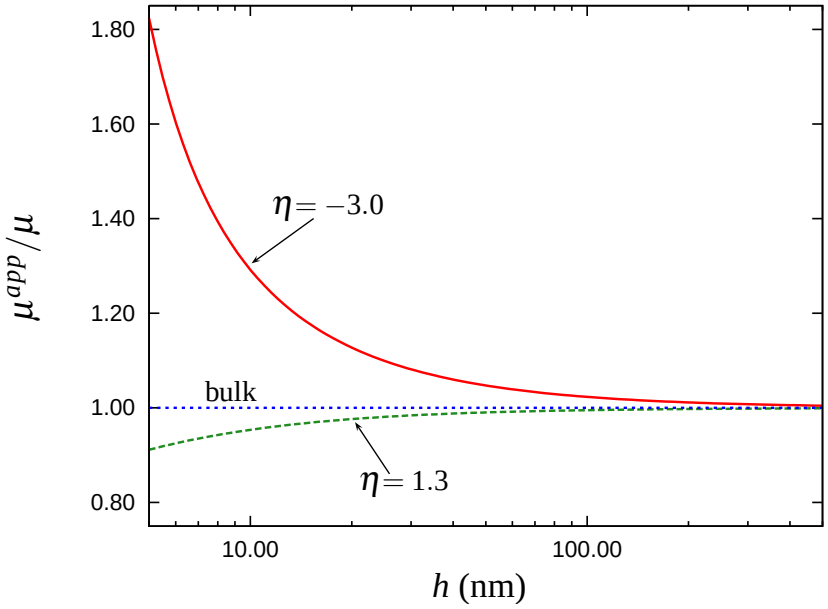

Figure X.10 : Effect of the thickness of the infinite strip, h, on the evolution of the apparent shear modulus, μ^{app}, for $E = 140$ GPa, $\nu = 0.3$, $L_1 = 0.3$ nm, $L_2^2/L_1^2 = 1$ and for two different η. The horizontal line corresponds to the classical solution obtained without coupling ($\eta = 0$) or equivalently without surface stress effects. In all of these cases, the surface energy is not considered, i.e., $b_0 = \eta_0 = 0$.

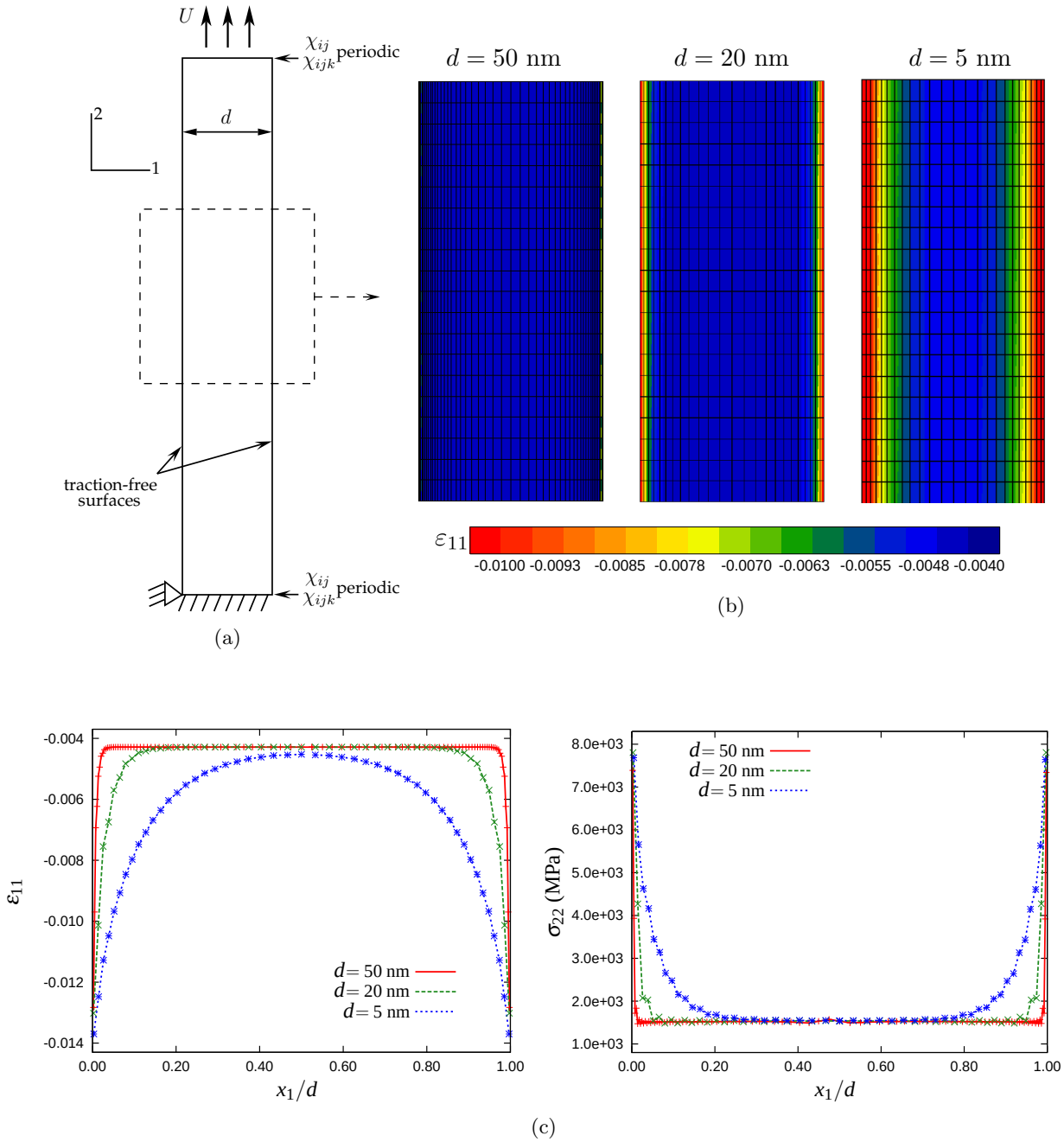

Figure X.11 : Finite element simulations of tensile tests of nanowires with material parameters given in Table X.1. (a) Description of the boundary value problem. (b) Contour plots of the strain component ε_{11}. (c) Profiles of the strain component ε_{11} and stress component σ_{22} across the nanowires diameter.

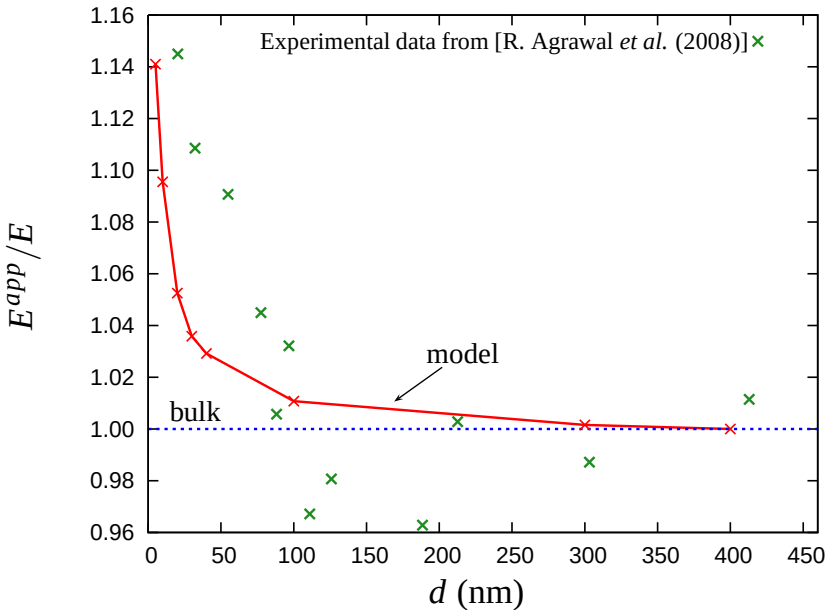

Figure X.12 : Effect of the nanowire diameter, d, on the evolution of the apparent Young's modulus, E^{app}, for the material parameters given in Table X.1. The horizontal line corresponds to the classical solution obtained without surface effects or equivalently to the bulk Young's modulus. The plotted experimental data come from Agrawal *et al.* (2008) and are obtained with tensile tests of single crystal ZnO nanowires having a [0001] oriented wurtzite structure.

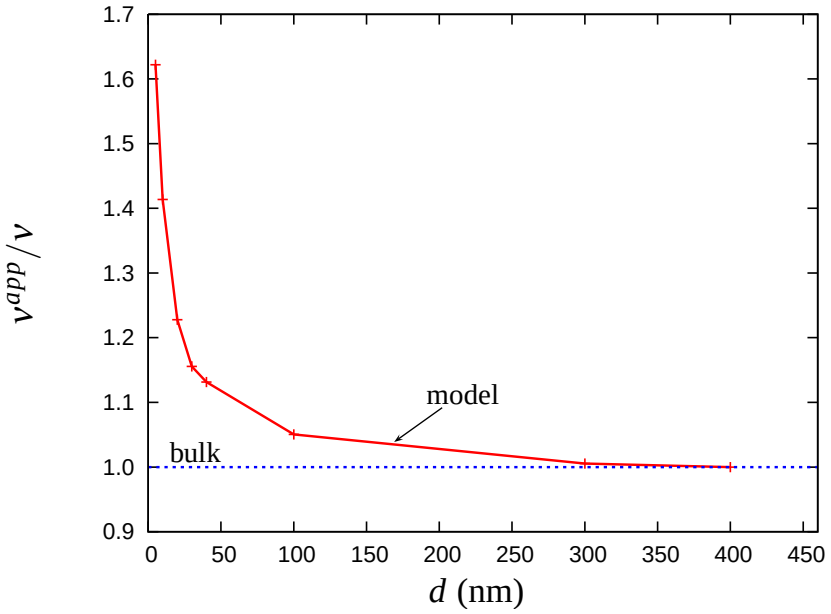

Figure X.13 : Effect of the nanowire diameter, d, on the evolution of the apparent Poisson's ratio, ν^{app}, for the material parameters given in Table X.1. The horizontal line corresponds to the classical solution obtained without surface effects or equivalently to the bulk Poisson's ratio.

References

Agrawal R., Peng B., Gdoutos E.E., and Espinosa H.D. (2008). *Elasticity Size Effects in ZnO Nanowires- A Combined Experimental-Computational Approach.* Nano Lett, vol. 8 n° 11, pp 3668–3674.

Craighead H.G. (2000). *Nanoelectromechanical systems.* Science, vol. 290 n° 5496, pp 1532–1535.

Feng X.L., He R., Yang P., and Roukes M.L. (2007). *Very high frequency silicon nanowire electromechanical resonators.* Nano Letters, vol. 7 n° 7, pp 1953–1959.

McDowell M.T., Leach A.M., and Gall K. (2008). *Bending and tensile deformation of metallic nanowires.* Modelling and Simulation in Materials Science and Engineering, vol. 16, pp 045003.

Sadeghian H., Yang C.K., Goosen J.F.L., Van der Drift E., Bossche A., French P.J., and Van Keulen F. (2009). *Characterizing size-dependent effective elastic modulus of silicon nanocantilevers using electrostatic pull-in instability.* Applied Physics Letters, vol. 94, pp 221903.

Sanii B. and Ashby P.D. (2010). *High sensitivity deflection detection of nanowires.* Physical review letters, vol. 104 n° 14, pp 147203.

Résumé

Le modèle du second gradient de la déformation de Mindlin est appliqué dans ce chapitre. Les deux types d'effet de surface précédemment décrits, énergie de surface et contrainte de surface, sont, dans un premier temps, traités séparément et illustrés par des problèmes aux limites simples dont le déplacement des atomes près d'une surface peut être décrit analytiquement. L'effet de l'énergie de surface est présenté dans un espace semi infini avec une surface libre. Il est montré que cet effet peut conduire à des distances interatomiques contractées ou étirées près de la surface. De la même manière, le cas où deux surfaces libres proches interagissent est traité. Le cisaillement d'une bande infinie dont l'épaisseur varie est considéré afin d'illustrer l'effet de la contrainte de surface. L'expression analytique du module de cisaillement apparent en fonction de la taille est ainsi obtenu. Après avoir traité ces cas simples (mais instructifs), l'approche micromorphe du second ordre formulée dans le chapitre IX est appliquée pour simuler le comportement mécanique de nanofils par éléments finis. Les résultats obtenus sont en accord avec les observations précédentes et montrent que les propriétés apparentes de ces fils nanométriques dépendent de leur diamètre.

Chapter -XI-

Conclusions

The first part of the present work was dedicated to elastic fluids. It was shown that the continuum description of capillarity effects in elastic bodies is possible based on the introduction of higher order gradients of the strain tensor in the continuum theory. The Korteweg equation can be incorporated into the framework of a first strain gradient theory and can be used to model capillarity effects at the interface between two phases of different densities like droplets in vapor, particularly when it is embedded in phase field like simulations. However we have shown, following Mindlin's arguments, that the linear elastic isotropic first strain gradient theory is not sufficient to describe internal strains and stresses that develop close to free surfaces. Their existence requires initial third order stresses in order to account for cohesion forces. The cohesion material behaviour in an isotropic elastic second gradient of strain medium is fully characterised by a single parameter, the initial higher order stress b_0, that can be linked to the surface energy when converging towards the sharp interface limiting case.

It has been shown that the special case of elastic fluids was a first step to investigate Mindlin's second strain gradient theory. In fact, this theory exists for the more general case of elastic solids at small strains and was presented in the second part of this work. Such a situation is encountered for instance in single crystalline nano–particles, as computed from molecular statics simulations (Ferrando *et al.*, 2009). Indeed, in such small atomic aggregates, the lattice parameter field is strongly inhomogeneous due to the small distance between the particle core and its free surface. A surface energy model would be inappropriate since, at that size, the capillary effect is not confined to an infinitesimal surface. That is the reason why Mindlin's second strain gradient theory appeared to be suitable. It was shown that Mindlin's theory generates two types of surface effects linked to distinct physical origins:

- *Surface energy* appears when a new surface is created. It is linked to the broken bonds between atoms in the surface region and their missing neighbours which leads to different equilibrium interatomic distances. Surface energy is related to an initial higher order stress, or cohesive modulus b_0.

- *Surface stress* appears when a surface is deformed. It is linked to the modification of the bond strength between atoms in the surface region. This surface effect is linked to the coupling set between the strain and the third gradient of the displacement field. It is then related to the coupling moduli c_i.

The higher order stress and the coupling just mentioned appear at the third order of Mindlin's theory. This means that such a higher order theory is required to account for the surface effects of interest.

It has been discussed that finite element simulations based on strain gradient theories are quite challenging, especially because of the complex boundary conditions. In contrast, Eringen's micromorphic theory is based on the introduction of independent deformation degrees of freedom and their gradients (Eringen, 1999), leading to significantly simpler boundary conditions. The numerical implementation merely relies on the introduction of additional degrees of freedom and the computation of their first gradient. Lagrange multipliers or penalisation method can then be used to retrieve the strain gradient formulation. Such an implementation has already been done for the first order micromorphic model in Shu *et al.* (1999) and Dillard *et al.* (2006). The present work went further by setting a second order micromorphic framework suitable to implement the second strain gradient theory. A second order micromorphic model was formulated and constrained to coincide with Mindlin's second strain gradient theory. Then, finite element computations of nanowires have been performed and their size–dependent apparent elastic properties have been investigated. The resulting strain distribution could be directly compared to atomistic computations. In particular the higher order elasticity moduli could be identified in that way from the discrete computations, as Mindlin did for the one–dimensional atomic chain. Mindlin's theory and the general micromorphic simulations could also be used to represent grain boundary stresses in nanocrystals (Müller and Kern, 2004), or in nano–objects like layers (Villain *et al.*, 2004). This will require extension of the theory to anisotropic cases.

References

Dillard T., Forest S., and Ienny P. (2006). *Micromorphic continuum modelling of the deformation and fracture behaviour of nickel foams.* European Journal of Mechanics A/Solids, vol. 25, pp 526–549.

Eringen A.C. (1999). *Microcontinuum field theories.* Springer, New York.

Ferrando R., Rossi G., Levi A.C., Kuntova Z., Nita F., Jelea A., Mottet C., Barcaro G., Fortunelli A., and Goniakowski J. (2009). *Structures of metal nanoparticles adsorbed on MgO(001). I. Ag and Au.* Journal of Chemical Physics, vol. 130, pp 174702.

Müller P. and Kern R. (2004). *Equilibrium shape changes of nanocrystals induced by strain.* Surface Science Reports, vol. 54, pp 157–258.

Shu J.Y., King W.E., and Fleck N.A. (1999). *Finite elements for materials with strain gradient effects.* Int. J. Numer. Meth. Engng, vol. 44, pp 373–391.

Villain P., Beauchamp P., Badawi K.F., Goudeau P., and Renault P. (2004). *Atomistic calculation of size effects on elastic coefficients in nanometre–sized tungsten layers and wires.* Scripta materialia, vol. 50, pp 1247–1251.

Appendix of Part B

Appendix B.1: Notation

For the sake of conciseness, a small strain framework is adopted. Volume forces are not considered throughout the work and the analysis is limited to static conditions. Mindlin's notation is followed as closely as possible. However, an intrinsic notation is adopted where zeroth, first, second, third and fourth order tensors are denoted by $a, \underline{\boldsymbol{a}}, \underset{\sim}{\boldsymbol{a}}, \underline{\underline{\boldsymbol{a}}}$ and $\underset{\approx}{\boldsymbol{a}}$ respectively. The simple, double, triple and quadruple contractions are written $.$, $:$, $\therefore$ and $::$ respectively. In index form with respect to an orthonormal Cartesian basis $(\underline{\boldsymbol{e}}_1, \underline{\boldsymbol{e}}_2, \underline{\boldsymbol{e}}_3)$, this notation corresponds to

$$\underline{\boldsymbol{a}} . \underline{\boldsymbol{b}} = a_i b_i, \quad \underset{\sim}{\boldsymbol{a}} : \underset{\sim}{\boldsymbol{b}} = a_{ij} b_{ij}, \quad \underline{\underline{\boldsymbol{a}}} \therefore \underline{\underline{\boldsymbol{b}}} = a_{ijk} b_{ijk}, \quad \underset{\approx}{\boldsymbol{a}} :: \underset{\approx}{\boldsymbol{b}} = a_{ijkl} b_{ijkl}, \tag{XI.1}$$

where repeated indices imply the sum. The tensor product is denoted by $\otimes$ and the nabla operator with respect to the reference configuration by $\boldsymbol{\nabla}$. For example, the component ijk of $\underset{\sim}{\boldsymbol{a}} \otimes \boldsymbol{\nabla}$ is $a_{ij,k}$. In particular, $\boldsymbol{\nabla}^2$ is the Laplace operator. As the formulated theories involve operations on tensors of order up to eight that may be unusual for the reader, both intrinsic and index notations are given to clarify some equations. For instance, we give the chosen intrinsic and index notations for the second gradient of a scalar field and of a second rank tensor:

$$\boldsymbol{\nabla} \otimes \boldsymbol{\nabla} \rho = \rho_{,ij}\, \underline{\boldsymbol{e}}_i \otimes \underline{\boldsymbol{e}}_j, \quad \underset{\sim}{\boldsymbol{\varepsilon}} \otimes \boldsymbol{\nabla} \otimes \boldsymbol{\nabla} = \varepsilon_{ij,kl}\, \underline{\boldsymbol{e}}_i \otimes \underline{\boldsymbol{e}}_j \otimes \underline{\boldsymbol{e}}_k \otimes \underline{\boldsymbol{e}}_l. \tag{XI.2}$$

Appendix B.2: Surface divergence theorem

For a smooth surface ∂V bounded by a smooth closed curve, the contact line γ, the surface divergence theorem states that:

$$\int_{\partial V} \overset{\boldsymbol{t}}{\underline{\boldsymbol{D}}} . \underline{\boldsymbol{v}}\, dS = \int_{\gamma} \underline{\boldsymbol{v}} . \underline{\boldsymbol{m}}\, d\gamma - \int_{\partial V} \frac{2}{R} (\underline{\boldsymbol{v}} . \underline{\boldsymbol{n}})\, dS, \tag{XI.3}$$

with $\overset{\boldsymbol{t}}{\underline{\boldsymbol{D}}} . \underline{\boldsymbol{v}}$ the surface divergence of $\underline{\boldsymbol{v}}$ (i.e., the trace of the surface gradient $\underline{\boldsymbol{v}} \otimes \overset{\boldsymbol{t}}{\underline{\boldsymbol{D}}}$ on ∂V), $1/R = -1/2\, \overset{\boldsymbol{t}}{\underline{\boldsymbol{D}}} . \underline{\boldsymbol{n}}$ the surface mean curvature, and $\underline{\boldsymbol{m}}$ the outward unit vector binormal to γ, i.e, $\underline{\boldsymbol{m}}$ normal to γ and $\underline{\boldsymbol{n}} . \underline{\boldsymbol{m}} = 0$ on γ.

If ∂V is a smooth closed surface, it is not bounded anymore and then the surface divergence theorem reduces to:

$$\int_{\partial V} \overset{\boldsymbol{t}}{\underline{\boldsymbol{D}}} . \underline{\boldsymbol{v}}\, dS = - \int_{\partial V} \frac{2}{R} (\underline{\boldsymbol{v}} . \underline{\boldsymbol{n}})\, dS. \tag{XI.4}$$

Appendix B.3: Main features of the finite element implementation

The purpose of this appendix is to give the main features of the finite element implementation of the second order micromorphic model presented in Section IX.2. For the sake of simplicity and in order to present matrices of reasonable sizes, the finite element implementation presented here is limited to 2D.

The chosen elements are isoparametric, i.e., the same shape functions are used to interpolate nodal coordinates and degrees of freedom. These elements are quadratic with reduced integration and have two displacement and nine micro–deformation degrees of freedom,

$$[\,DOF\,]^T = [u_1 \quad u_2 \quad \chi_{11} \quad \chi_{22} \quad \chi_{12} \quad \chi_{111} \quad \chi_{221} \quad \chi_{122} \quad \chi_{222} \quad \chi_{112} \quad \chi_{121}]\,. \tag{XI.5}$$

The B–matrix is the transformation matrix computed to calculate the components of the strain tensors (ε_{ij}, K_{ijk} and K_{ijkl}) and relative strain tensors (e_{ij} and e_{ijk}) from the degrees of freedom as:

$$[\,STRAIN\,] = [\,\mathrm{B}_{\mathrm{matrix}}\,]\,[\,DOF\,]\,. \tag{XI.6}$$

This matrix is given in Fig. XI.1. The shape function N is such as, for example, $\varepsilon_{11} = N_{,1}\,u_1 = u_{1,1}$ and $e_{11} = N_{,1}\,u_1 - N\,\chi_{11} = u_{1,1} - \chi_{11}$.

$$\begin{bmatrix} \varepsilon_{11} \\ \varepsilon_{22} \\ \varepsilon_{33} \\ \sqrt{2}\varepsilon_{12} \\ \\ e_{11} \\ e_{22} \\ \sqrt{2}e_{12} \\ \\ K_{111} \\ K_{221} \\ \sqrt{2}K_{122} \\ K_{222} \\ K_{112} \\ \sqrt{2}K_{121} \\ \\ e_{111} \\ e_{221} \\ \sqrt{2}e_{122} \\ e_{222} \\ e_{112} \\ \sqrt{2}e_{121} \\ \\ K_{1111} \\ K_{2211} \\ \sqrt{2}K_{1221} \\ K_{2222} \\ K_{1122} \\ \sqrt{2}K_{1212} \\ K_{1112} \\ K_{2212} \\ \sqrt{2}K_{1222} \\ K_{2221} \\ K_{1121} \\ \sqrt{2}K_{1211} \end{bmatrix} = \begin{bmatrix} N_{,1} & 0 & & & & & & & & & & \\ 0 & N_{,2} & & & & & & & & & & \\ 0 & 0 & & & & & & & & & & \\ N_{,2}/\sqrt{2} & N_{,1}/\sqrt{2} & & & & & & & & & & \\ \\ N_{,1} & 0 & -N & 0 & 0 & & & & & & & \\ 0 & N_{,2} & 0 & -N & 0 & & & & & & & \\ N_{,2}/\sqrt{2} & N_{,1}/\sqrt{2} & 0 & 0 & -\sqrt{2}N & & & & & & & \\ \\ & & N_{,1} & 0 & 0 & & & & & & & \\ & & 0 & N_{,1} & 0 & & & & & & & \\ & & 0 & 0 & \sqrt{2}N_{,2} & & & & & & & \\ & & 0 & N_{,2} & 0 & & & & & & & \\ & & N_{,2} & 0 & 0 & & & & & & & \\ & & 0 & 0 & \sqrt{2}N_{,1} & & & & & & & \\ \\ & & N_{,1} & 0 & 0 & -N & 0 & 0 & 0 & 0 & 0 & \\ & & 0 & N_{,1} & 0 & 0 & -N & 0 & 0 & 0 & 0 & \\ & & 0 & 0 & \sqrt{2}N_{,2} & 0 & 0 & -\sqrt{2}N & 0 & 0 & 0 & \\ & & 0 & N_{,2} & 0 & 0 & 0 & 0 & -N & 0 & 0 & \\ & & N_{,2} & 0 & 0 & 0 & 0 & 0 & 0 & -N & 0 & \\ & & 0 & 0 & \sqrt{2}N_{,1} & 0 & 0 & 0 & 0 & 0 & -\sqrt{2}N & \\ \\ & & & & & N_{,1} & 0 & 0 & 0 & 0 & 0 & \\ & & & & & 0 & N_{,1} & 0 & 0 & 0 & 0 & \\ & & & & & 0 & 0 & \sqrt{2}N_{,1} & 0 & 0 & 0 & \\ & & & & & 0 & 0 & 0 & N_{,2} & 0 & 0 & \\ & & & & & 0 & 0 & 0 & 0 & N_{,2} & 0 & \\ & & & & & 0 & 0 & 0 & 0 & 0 & \sqrt{2}N_{,2} & \\ & & & & & N_{,2} & 0 & 0 & 0 & 0 & 0 & \\ & & & & & 0 & N_{,2} & 0 & 0 & 0 & 0 & \\ & & & & & 0 & 0 & \sqrt{2}N_{,2} & 0 & 0 & 0 & \\ & & & & & 0 & 0 & 0 & N_{,1} & 0 & 0 & \\ & & & & & 0 & 0 & 0 & 0 & N_{,1} & 0 & \\ & & & & & 0 & 0 & 0 & 0 & 0 & \sqrt{2}N_{,1} & \end{bmatrix} \begin{bmatrix} u_1 \\ u_2 \\ \chi_{11} \\ \chi_{22} \\ \chi_{12} \\ \chi_{111} \\ \chi_{221} \\ \chi_{122} \\ \chi_{222} \\ \chi_{112} \\ \chi_{121} \end{bmatrix}$$

Figure XI.1 : B–matrix computed in the finite element code to calculate the components of the strain and relative strain tensors from the degrees of freedom.

The components of the stress tensors (σ_{ij}, S_{ijk} and S_{ijkl}) and relative stress tensors (s_{ij}

and s_{ijk}) are computed as:

$$[\,STRESS\,] = [\,D\,] [\,STRAIN\,] + [\,b_0\,], \tag{XI.7a}$$

$$\begin{bmatrix} [\,\underset{\sim}{\boldsymbol{\sigma}}\,] \\ [\,\underset{\sim}{\boldsymbol{s}}\,] \\ \left[\,\underset{\approx}{\boldsymbol{S}}\,\right] \\ \left[\,\underset{\approx}{\boldsymbol{s}}\,\right] \\ \left[\,\underset{\approx}{\boldsymbol{S}}\,\right] \end{bmatrix} = \begin{bmatrix} [\,\Lambda\,] & & & & [\,C\,] \\ & [\,H^a_\chi\,] & & & \\ & & [\,A\,] & & \\ & & & [\,H^b_\chi\,] & \\ [\,C\,]^T & & & & [\,B\,] \end{bmatrix} \begin{bmatrix} [\,\underset{\sim}{\boldsymbol{\varepsilon}}\,] \\ [\,\underset{\sim}{\boldsymbol{e}}\,] \\ \left[\,\underset{\approx}{\boldsymbol{K}}\,\right] \\ \left[\,\underset{\approx}{\boldsymbol{e}}\,\right] \\ \left[\,\underset{\approx}{\boldsymbol{K}}\,\right] \end{bmatrix} + \begin{bmatrix} \\ \\ \\ \\ b_0 \left[\,\underset{\approx}{\boldsymbol{l}}\,\right] \end{bmatrix}. \tag{XI.7b}$$

where the simple, double and triple stress tensors and the relative stress tensors are computed as follow

$$\begin{gathered} \left[\,\underset{\sim}{\boldsymbol{\sigma}}\,\right]^T = \begin{bmatrix} \sigma_{11} & \sigma_{22} & \sigma_{33} & \sqrt{2}\,\sigma_{12} \end{bmatrix}, \quad \left[\,\underset{\sim}{\boldsymbol{S}}\,\right]^T = \begin{bmatrix} S_{111} & S_{221} & \sqrt{2}\,S_{122} & S_{222} & S_{112} & \sqrt{2}\,S_{121} \end{bmatrix}, \\ \left[\,\underset{\approx}{\boldsymbol{S}}\,\right]^T = \begin{bmatrix} S_{1111} & S_{2211} & \sqrt{2}\,S_{1221} & S_{2222} & S_{1122} & \sqrt{2}\,S_{1212} & S_{1112} & S_{2212} & \sqrt{2}\,S_{1222} & S_{2221} & S_{1121} & \sqrt{2}\,S_{1211} \end{bmatrix}, \\ \left[\,\underset{\sim}{\boldsymbol{s}}\,\right]^T = [\,s_{11} \quad s_{22} \quad s_{12}\,], \quad \left[\,\underset{\approx}{\boldsymbol{s}}\,\right]^T = [\,s_{111} \quad s_{221} \quad s_{122} \quad s_{222} \quad s_{112} \quad s_{121}\,]. \end{gathered} \tag{XI.8}$$

The strain and relative strain tensors are computed in the same way:

$$\begin{gathered} \left[\,\underset{\sim}{\boldsymbol{\varepsilon}}\,\right]^T = \begin{bmatrix} \varepsilon_{11} & \varepsilon_{22} & \varepsilon_{33} & \sqrt{2}\,\varepsilon_{12} \end{bmatrix}, \quad \left[\,\underset{\sim}{\boldsymbol{K}}\,\right]^T = \begin{bmatrix} K_{111} & K_{221} & \sqrt{2}\,K_{122} & K_{222} & K_{112} & \sqrt{2}\,K_{121} \end{bmatrix}, \\ \left[\,\underset{\approx}{\boldsymbol{K}}\,\right]^T = \begin{bmatrix} K_{1111} & K_{2211} & \sqrt{2}\,K_{1221} & K_{2222} & K_{1122} & \sqrt{2}\,K_{1212} & K_{1112} & K_{2212} & \sqrt{2}\,K_{1222} & K_{2221} & K_{1121} & \sqrt{2}\,K_{1211} \end{bmatrix}, \\ \left[\,\underset{\sim}{\boldsymbol{e}}\,\right]^T = [\,e_{11} \quad e_{22} \quad e_{12}\,], \quad \left[\,\underset{\approx}{\boldsymbol{e}}\,\right]^T = [\,e_{111} \quad e_{221} \quad e_{122} \quad e_{222} \quad e_{112} \quad e_{121}\,]. \end{gathered} \tag{XI.9}$$

The invertible matrix $[\,D\,]$ is the matrix of the elastic moduli in which four distinct parts can be noted. $[\,\Lambda\,]$ contains the classical elastic moduli. $[\,A\,]$ and $[\,B\,]$ are the diagonal matrices of the generalised moduli A and B that are related to the first and second strain gradients respectively and defined as:

$$[\,A\,] = \begin{bmatrix} A & & \\ & \ddots & \\ & & A \end{bmatrix}, \quad [\,B\,] = \begin{bmatrix} B & & \\ & \ddots & \\ & & B \end{bmatrix}. \tag{XI.10}$$

$[\,A\,]$ and $[\,B\,]$ are the matrix forms of a sixth rank tensor and a eighth rank tensor respectively. The blocks $[\,C\,]$ and $[\,C\,]^T$ ensure the coupling between the components ε_{ij} and K_{ijkl}. The

specific matrix $[\,C\,]$ is computed as follow

$$[\,C\,]^T = \begin{bmatrix} (c'_1+..+c'_6) & (c'_1+c'_4) & (c'_1+c'_4) & & & \\ (c'_1+c'_2) & (c'_1+c'_3) & c'_1 & & & \\ (c'_4+c'_6)/\sqrt{2} & (c'_4+c'_5)/\sqrt{2} & c'_4/\sqrt{2} & & & \\ (c'_1+c'_4) & (c'_1+..+c'_6) & (c'_1+c'_4) & & & \\ (c'_1+c'_3) & (c'_1+c'_2) & c'_1 & & & \\ (c'_4+c'_5)/\sqrt{2} & (c'_4+c'_6)/\sqrt{2} & c'_4/\sqrt{2} & & & \\ & & & (c'_2+c'_6)/\sqrt{2} & & \\ & & & (c'_2+c'_5)/\sqrt{2} & & \\ & & & c'_3+(c'_5+c'_6)/\sqrt{2} & & \\ & & & (c'_2+c'_6)/\sqrt{2} & & \\ & & & (c'_2+c'_5)/\sqrt{2} & & \\ & & & c'_3+(c'_5+c'_6)/\sqrt{2} & & \end{bmatrix}. \tag{XI.11}$$

Finally, $[\,H^a_\chi\,]$ and $[\,H^b_\chi\,]$,

$$[\,H^a_\chi\,] = \begin{bmatrix} H^a_\chi & & \\ & \ddots & \\ & & H^a_\chi \end{bmatrix}, \quad [\,H^b_\chi\,] = \begin{bmatrix} H^b_\chi & & \\ & \ddots & \\ & & H^b_\chi \end{bmatrix}, \tag{XI.12}$$

are the diagonal matrices setting the internal constraint, presented in Subsection IX.2.3, ensuring the equivalences (IX.42) and that the second order micromorphic model coincides with Mindlin's second strain gradient theory.

The last element that has to be discussed about the relation (XI.7b) is the term $b_0[\,\underset{\approx}{\boldsymbol{l}}\,]$ appearing on the left–hand side. It has been shown in Chapter IX that the initial higher order stress, or cohesion modulus, b_0, appears in some components of the triple stress tensor $\underset{\approx}{\boldsymbol{S}}$. These components are identified in Eq. (IX.39c) as S_{kkll}, S_{klkl} and S_{kllk}, then

$$b_0 \left[\,\underset{\approx}{\boldsymbol{l}}\,\right]^T = \left[b_0 \quad \frac{1}{3}\,b_0 \quad \frac{\sqrt{2}}{3}\,b_0 \quad b_0 \quad \frac{1}{3}\,b_0 \quad \frac{\sqrt{2}}{3}\,b_0 \quad 0 \quad 0 \quad 0 \quad 0 \quad 0 \quad 0 \right]^T. \tag{XI.13}$$

The principle of virtual work in the absence of body forces is, for all $[\,DOF^*\,]$,

$$\int_V \left[\underset{\sim}{\boldsymbol{\sigma}} : \underset{\sim}{\boldsymbol{\varepsilon}}^* + \underset{\sim}{\boldsymbol{s}} : \underset{\sim}{\boldsymbol{e}}^* + \underset{\simeq}{\boldsymbol{S}} \therefore \underset{\simeq}{\boldsymbol{K}}^* + \underset{\sim}{\boldsymbol{s}} \therefore \underset{\simeq}{\boldsymbol{e}}^* + \underset{\approx}{\boldsymbol{S}} :: \underset{\approx}{\boldsymbol{K}}^* \right] dV = \int_{\partial V} \left(\underline{\boldsymbol{t}} \,.\underline{\boldsymbol{u}}^* + \underline{\boldsymbol{t}} : \underset{\sim}{\boldsymbol{\chi}}^* + \underline{\underline{\boldsymbol{t}}} \therefore \underset{\simeq}{\boldsymbol{\chi}}^* \right) dS. \tag{XI.14}$$

$$\int_V [\,STRESS\,]^T\,[\,STRAIN^*\,]\,dV = \int_{\partial V} [\,t\,]^T\,[\,DOF^*\,]\,dS \tag{XI.15}$$

$$\int_V [\,STRAIN\,]^T\,[\,D\,]\,[\,STRAIN^*\,]\,dV = \int_{\partial V} [\,t\,]^T\,[\,DOF^*\,]\,dS \tag{XI.16}$$

$$\int_V [\,DOF\,]^T\,[\,\mathrm{B}_{\mathrm{matrix}}\,]^T\,[\,D\,]\,[\,\mathrm{B}_{\mathrm{matrix}}\,]\,[\,DOF^*\,]\,dV = \int_{\partial V} [\,t\,]^T\,[\,DOF^*\,]\,dS. \tag{XI.17}$$

Then, we have,

$$[\,F\,] = [\,K\,]\,[\,DOF\,], \tag{XI.18}$$

with the stiffness matrix,

$$[\,K\,] = \int_V [\,\mathrm{B}_{\mathrm{matrix}}\,]^T\,[\,D\,]\,[\,\mathrm{B}_{\mathrm{matrix}}\,]\;dV, \tag{XI.19}$$

and

$$[\,F\,] = \int_{\partial V} [\,t\,]^T\;dS. \tag{XI.20}$$

Note that in the derivation we have used the fact that our formulation is incremental, so that $\Delta[\,STRESS\,] = [\,D\,]\;\Delta[\,STRAIN\,]$ and b_0 does not arise in Eq. (XI.16).

The $\sqrt{2}$ in $[\,STRESS\,]$ and $[\,STRAIN\,]$ are such that the chosen form of the power density of internal forces given in Eq. (IX.27) is respected,

$$[\,STRESS\,]^T\,[\,STRAIN^*\,] = \sigma_{ij}\,\varepsilon^*_{ij} + s_{ij}\,e^*_{ij} + S_{ijk}\,K^*_{ijk} + s_{ijk}\,e^*_{ijk} + S_{ijkl}\,K^*_{ijkl}, \tag{XI.21}$$

this is the reason why several coefficients of the matrices $[\,\mathrm{B}_{\mathrm{matrix}}\,]$, $[\,C\,]$ and $b_0[\,\underset{\approx}{\boldsymbol{l}}\,]$ were multiplied by $(\sqrt{2})^{\pm 1}$ in order to fit this chosen form and to end up with the same relations as formulated in the second order micromorphic model. For example, the strains given in Eq. (IX.31) remain

$$\varepsilon_{ij} = \frac{1}{2}\,(u_{i,j} + u_{j,i})\,, \quad e_{ij} = \varepsilon_{ij} - \chi_{ij}, \quad K_{ijk} = \chi_{ij,k}, \quad e_{ijk} = K_{ijk} - \chi_{ijk}, \quad K_{ijkl} = \chi_{ijk,l}, \tag{XI.22}$$

and more particularly, as the modified coefficients are related to ε_{ij}, e_{ij}, K_{ijk}, e_{ijk} and K_{ijkl} when $i \neq j$, we do have

$$\sqrt{2}\,\varepsilon_{12} = \frac{u_{1,2}}{\sqrt{2}} + \frac{u_{2,1}}{\sqrt{2}} \;\equiv\; \varepsilon_{12} = \frac{1}{2}\,(u_{1,2} + u_{2,1})\,, \tag{XI.23}$$

$$\sqrt{2}\,e_{121} = \sqrt{2}\,\chi_{12,1} - \sqrt{2}\,\chi_{121} = \sqrt{2}\,K_{121} - \sqrt{2}\,\chi_{121} \;\equiv\; e_{121} = K_{121} - \chi_{121}, \tag{XI.24}$$

or

$$\sqrt{2}\,K_{1221} = \sqrt{2}\,\chi_{122,1} \;\equiv\; K_{1221} = \chi_{122,1}. \tag{XI.25}$$

It can also be shown that the constitutive equations (IX.39) are verified by this finite element implementation.

Conclusions – Recommendations for future work

Conclusions

In this thesis, a theoretical framework to study the deformation behaviour of polycrystalline materials with ultra–fine or nano–sized microstructures has been developed. Continuum models able to model size effects arising from mechanisms that are predominant at interfaces (i.e., grain boundaries) or surfaces have been formulated and applied. The scales of the structures and objects have been considered starting from the macroscale to the nanoscale. The conclusions from the two parts of this top–down approach are presented separately.

Sizes ranging from hundreds of microns to tens of nanometers were first treated in the microplasticity part (Part A). The most significant results obtained in this first part are recalled:

- A micromorphic crystal plasticity model, the *microcurl* model, has been proposed to regularise the response of a Gurtin–type strain gradient plasticity model, referred to as the "*curl* H^p" model (Gurtin, 2002), in the presence of material interfaces.

- The "*curl* H^p" model, which constitutes a limiting case of the *microcurl* model, has been shown to generate invariably an evolution of the macroscopic flow stress as a function of the microstructural length scale with a fixed scaling law exponent $m = -2$.

- The *microcurl* model is able to simulate the size–dependent response of polycrystalline aggregates and, depending on the chosen sets of material parameters, a wide range of scaling law exponents can be obtained. In particular, material parameters were set to retrieve the Hall–Petch scaling law.

- A network of slip bands is built in ultra–fine grains and the GND pileups, defined as the norm of the dislocation density tensor, spread over the grains. Such slip band network is a new feature of generalised crystal plasticity.

- Size effects induced by multilayer pileups have been investigated in terms of plastic slip distributions and overall work–hardening using discrete dislocation dynamics (DDD) and the *microcurl* model. The comparison of these models showed that the higher order moduli of the *microcurl* model can be calibrated so as to obtain a similar overall behaviour and local distributions to that obtained from DDD simulations.

The nanoelasticity part (Part B) focused on effects that are localised at a few nanometers from the surface (or interface). This second step leads to the following significant results:

- Following the arguments from Mindlin (1965), it was shown that a second gradient of strain theory or, equivalently, a third gradient of displacement theory is needed to describe, in a continuous manner, capillarity and cohesion effects in isotropic linear elastic solids and fluids.

- Two types of surface effects generated by Mindlin's theory have been described and analysed using simple analytical boundary value problems:

  - *Surface energy*, which appears when a new surface is created, was shown to be related to an initial higher order stress.
  - *Surface stress*, which appears when a surface is deformed, was shown to be linked to the coupling that exists between the strain and the third gradient of the displacement field.

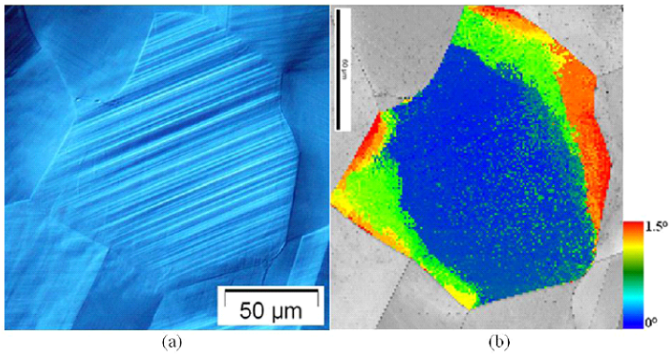

Figure XI.2 : EBSD 2D misorientation mapping (Perrin *et al.*, 2010)

.

One of the main original contribution of this work has been to demonstrate that these surface effects can only be modelled at least with a third order theory, such as Mindlin's.

- A second order micromorphic model was formulated and constrained to implement the second strain gradient theory into a finite element code.
- The size–dependent mechanical behaviour of nanowires have been investigated and it was shown that surface effects significantly affect their apparent elastic properties.

Recommendations for future work

It should first be pointed out that the models formulated in this thesis rely on the introduction of higher order moduli. These material parameters have to be calibrated as it was done with discrete dislocation dynamics (Chapter III), using experimental data (Chapters II and X) or by fitting a scaling law exponent (Chapters IV and V). In future work, a more systematic and robust method should be carried out where, for instance, the higher order moduli are identified from atomistic simulations of the deformation mechanisms observed at grain boundaries or surfaces (McDowell, 2008). A simple example is proposed in Mindlin (1965) where the higher order elasticity moduli are identified using a one–dimensional atomic chain.

Another possible calibration of the plasticity model presented in Part A could be made from the prediction of the internal stress at GND pileups using, e.g., internal mean field approaches as in Pipard *et al.* (2009). The simulated fields could also be compared and calibrated with fields measured with EBSD 2D misorientation mapping, see Fig. XI.2 (Perrin *et al.*, 2010).

The proposed constitutive frameworks should be extended to provide more accurate predictions. For example, the double stress tensor of the *microcurl* model affects only the free energy function, and not the dissipation potential. This is sufficient to point out the existence of a back stress and to derive explicit analytic results for the laminate problem treated in Chapter II. It is however possible to introduce dissipative mechanisms related to generalised stresses in a systematic manner (Forest and Sievert, 2003; Forest, 2009; Gurtin and Anand, 2009). Moreover, the linear kinematic hardening modelled by this model is quite idealised and unrealistic and non linear kinematic hardening should be included.

In the same way, Mindlin's theory and the corresponding micromorphic approach could also be used to represent grain boundary stresses in either nanocrystals (Müller and Kern,

2004) or in nano–objects like layers (Villain *et al.*, 2004). However, to do that an extension of the theory to anisotropic cases should be considered.

Three–dimensional finite element simulations of polycrystalline aggregates should be conducted with the *microcurl* model in order to verify the simulated scaling law exponent and see if the Hall–Petch scaling law is still retrieved. These simulations should also be used to verify if the slip band network observed in two–dimensional ultra–fine grains with planar double slip systems still occur in more realistic configurations. Three–dimensional finite element simulations should also be conducted to simulate the size–dependent elastic behaviour of nano–objects such as nano–particles. Improved and more robust finite element implementations should then be considered to optimise these calculations.

Predicting the mechanical behaviour of nanocrystalline materials requires more realistic continuum crystal plasticity models with an improved representation of the grain boundary behaviour. It is well known that, for such microstructural length scales, grain boundary effects such as grain boundary motion or grain boundary sliding are predominant and result in a breakdown of the Hall–Petch relation. Indeed, the interface–to–volume ratio of nanocrystalline materials is very high and therefore these materials can be seen as two–phase materials with a grain core phase and a grain boundary (and triple junction) phase. A phase field approach could then be developed to represent the mechanical behaviour of nanocrystalline materials. whereby the grain boundary phase could exhibit a specific behaviour and reproduce the motions and slidings observed experimentally. Moreover, a coupled crystal plasticity–phase field formulation has already been proposed by Abrivard (2009) to describe microstructural evolution in polycrystalline aggregates. This latter work should be considered and extended to couple the *microcurl* model proposed in this thesis with phase field.

References

Abrivard G. (2009). *A coupled crystal plasticity – phase field formulation to describe microstructural evolution in polycrystalline aggregates.* Thèse de Doctorat, Mines ParisTech / Centre des Matériaux.

Forest S. (2009). *Micromorphic Approach for Gradient Elasticity, Viscoplasticity, and Damage.* Journal of Engineering Mechanics, vol. 135, pp 117–131.

Forest S. and Sievert R. (2003). *Elastoviscoplastic constitutive frameworks for generalized continua.* Acta Mechanica, vol. 160, pp 71–111.

Gurtin M.E. (2002). *A gradient theory of single–crystal viscoplasticity that accounts for geometrically necessary dislocations.* Journal of the Mechanics and Physics of Solids, vol. 50, pp 5–32.

Gurtin M.E. and Anand L. (2009). *Thermodynamics applied to gradient theories involving the accumulated plastic strain: The theories of Aifantis and Fleck & Hutchinson and their generalization.* Journal of the Mechanics and Physics of Solids, vol. 57, pp 405–421.

McDowell D.L. (2008). *Viscoplasticity of heterogeneous metallic materials.* Materials Science and Engineering R, vol. 62, pp 67–123.

Mindlin R.D. (1965). *Second gradient of strain and surface–tension in linear elasticity.* Int. J. Solids Structures, vol. 1, pp 417–438.

Müller P. and Kern R. (2004). *Equilibrium shape changes of nanocrystals induced by strain.* Surface Science Reports, vol. 54, pp 157–258.

Perrin C., Berbenni S., Vehoff H., and Berveiller M. (2010). *Role of discrete intragranular slip on lattice rotations in polycrystalline Ni: Experimental and micromechanical studies.* Acta Materialia, vol. 58 n° 14, pp 4639–4649.

Pipard J.M., Nicaise N., Berbenni S., Bouaziz O., and Berveiller M. (2009). *A new mean field micromechanical approach to capture grain size effects.* Computational Materials Science, vol. 45 n° 3, pp 604–610.

Villain P., Beauchamp P., Badawi K.F., Goudeau P., and Renault P. (2004). *Atomistic calculation of size effects on elastic coefficients in nanometre–sized tungsten layers and wires.* Scripta materialia, vol. 50, pp 1247–1251.

Gradients de Déformation en Mécanique des Micro et Nanocristaux

Résumé :

L'influence de la taille de grain sur le comportement des matériaux à grains ultrafins et nanocristallins est l'objet de nombreuses études scientifiques. Cependant, malgré les progrès réalisés dans ce domaine, il n'est pas encore possible de prédire et de modéliser avec précision leur comportement en déformation. Peu de données fiables sont disponibles dans la littérature en raison de la complexité des expériences requises et de la forte densité de défauts que peuvent présenter ces matériaux. Par ailleurs, les techniques de modélisation discrètes telles que les approches atomistiques sont d'une utilité limitée. En effet, leurs échelles temporelle et spatiale sont souvent inadaptées pour simuler les phénomènes physiques réels intervenant dans ce travail.

Dans cette thèse, un cadre théorique est proposé pour étudier le comportement en déformation de matériaux polycristallins ayant des microstructures ultrafines ou nanométriques. Pour ce faire, des modèles continus capables de reproduire les effets de taille provenant de mécanismes apparaissant aux interfaces (joints de grains) ou près des surfaces sont proposés. Ces modèles permettent d'étudier des éléments de volume représentatifs. Ils sont formulés de manière à être calibrés en utilisant des résultats obtenus par des simulations atomistiques et de dynamique des dislocations discrètes ou par des travaux expérimentaux.

Mots clés :

Gradients de déformation, Modèle micromorphe, Milieux d'ordre supérieur, Effets de taille, Effets de surface, Plasticité cristalline, Matériaux à grains ultrafins, Matériaux nanocristallins

A Strain Gradient Approach to the Mechanics of Micro and Nanocrystals

Abstract:

The influence of grain size on the strength of ultra-fine grained and nanocrystalline materials is the subject of an increasing number of scientific studies. However, despite the progress made in this field, it is not yet possible to predict accurately and model the deformation behaviour of this type of materials. Few reliable data are available in the literature due to the complexity of the required experiments and to the high defect densities that some of these materials are known to contain. Moreover, the use of discrete modeling techniques such as atomistic approaches has a limited utility as the temporal and spatial scales are often unsuitable to address the real physical phenomena of interest in this work.

In this doctoral thesis, a theoretical framework is proposed to study the deformation behaviour of polycrystalline materials with ultra-fine or nano-sized microstructures. To that purpose, continuum models able to model size effects arising from mechanisms that are predominant at interfaces (i.e., grain boundaries) or surfaces are proposed. These models, which enable the study of large representative volume elements, have been formulated so as to be calibrated using results from atomistic and discrete dislocation dynamics simulations and experimental work.

Keywords:

Strain gradient approach, Micromorphic model, Higher order continua, Size effects, Surface effects, Crystal plasticity, Ultra-fine grained materials, Nanocrystalline materials

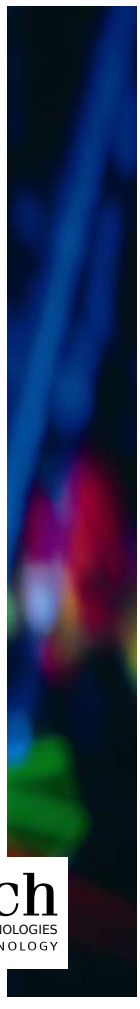

MINES ParisTech

ParisTech
INSTITUT DES SCIENCES ET TECHNOLOGIES
PARIS INSTITUTE OF TECHNOLOGY